Mid-Infrared Optical Absorption in Undoped Lamellar Copper Oxides

by

John Dillard Perkins
A.B., Harvard University
1985

Submitted to the Department of Physics
in partial fulfillment of the requirements for the degree of

Doctor of Philosophy

at the

MASSACHUSETTS INSTITUTE OF TECHNOLOGY
February 1994

Author ....
Department of Physics
December 10, 1993

Certified by ....
John M. Graybeal
Associate Professor of Physics
Thesis Supervisor

Accepted by ....
George F. Koster
Chairman, Departmental Committee

Mid-Infrared Optical Absorption in Undoped Lamellar Copper Oxides

by
John Dillard Perkins
Submitted to the Department of Physics on December 22, 1993
in partial fulfillment of the requirements for the Degree of
Doctor of Philosophy

The mid-infrared optical excitations of undoped lamellar copper oxide High-T_c host materials are studied in the energy range of ~ 0.2 - 1.7 eV using optical transmission measurements. Experiments on ~ 100 μm thick high quality single crystal samples of antiferromagnetic La_2CuO_4, $Sr_2CuO_2Cl_2$, Nd_2CuO_4 and Pr_2CuO_4 show similar absorption spectra in the energy range of ~ 0.4 to 1.3 eV. For all four compounds, the spectra display a sharp low-energy line near 0.4 eV and a set of broader bands extending to higher energies. The absorption coefficient is weak, roughly 10^3 times smaller than in heavily doped materials. Absorption occurs only with the electric field polarized parallel to the CuO_2 plane. The similarity of the spectra and the polarization dependence demonstrate that the absorption results from intrinsic electric-dipole excitations of the CuO_2 layers. In ~ 10 μm thick samples of $Sr_2CuO_2Cl_2$ an additional band is seen near 1.5 eV.

The absorption spectra are explained in terms of multimagnon sidebands to an electric-dipole forbidden excitation at ~ 0.4 eV. The magnon sideband selection rules show that if the ~ 0.4 eV excitation is a Cu d-d exciton, then it must be either the Cu $d_{x^2-y^2} \rightarrow d_{3z^2-r^2}$ or $d_{x^2-y^2} \rightarrow d_{xy}$ transition in hole terminology. Only the assignment of the $d_{x^2-y^2} \rightarrow d_{3z^2-r^2}$ transition to the ~ 0.4 eV exciton is consistent with a variety of other experiments including the recent electroreflectance experiments of Falck *et al.* which show a transition of $d_{x^2-y^2} \rightarrow d_{xy}$ symmetry at ~ 1.5 eV. Hence, the absorption band observed in $Sr_2CuO_2Cl_2$ at ~ 1.5 eV may be associated with the $d_{x^2-y^2} \rightarrow d_{xy}$ exciton.

However, the similarity in energy of the sharp line and the peak in the 2-magnon Raman scattering spectra suggests that the ~ 0.4 eV excitation may be more complex. Both the $d_{x^2-y^2} \rightarrow d_{3z^2-r^2}$ exciton and the 2-magnon excitation are B_{1g} symmetry excitations. Hence if the exciton really is at ~ 0.4 eV, it will mix with the 2-magnon excitations and both should contribute to the Raman scattering spectra. Further work is needed to determine whether the observed spectra are actually multimagnon sidebands to a Cu d-d exciton, a 2-magnon pair or a more complex excitation. In either case, the excellent agreement of the sideband features with multimagnon energy shifts strongly suggests that magnon sidebands are primarily responsible for the mid-infrared absorption in the undoped lamellar copper oxides. Presently the electric-dipole nature of the sharp line at ~ 0.4 eV is not understood.

A comparison of the spectra measured in the undoped crystals with that measured in lightly oxygen doped La_2CuO_{4+y} by Thomas *et al.* as well as the absorption induced by photo-injected carriers suggests that the magnon sideband absorption mechanism is responsible for the doping enhanced mid-infrared absorption which has been widely observed in the doped lamellar copper oxides.

Thesis Supervisor : John M. Graybeal
Title: Associate Professor of Physics

Acknowledgements

On the twisted path to graduation I have benefited from my interactions with many people. Now that I am at the end of that path, I would like to thank them before embarking upon further adventures in science and life.

The contributions of John Graybeal, my thesis advisor, to my education are too innumerable to list in detail. He has always been willing to provide explanations or patiently listen to mine. He established a research environment where hard work and open communication were the norm. He is not only my advisor, but a friend.

For the past three years Marc Kastner has essentially been a second advisor. I have benefited enormously from my frequent discussions with him. All of the optics experiments presented in this thesis were done in his lab. In the past year, Bob Birgeneau has also played an important role in this research and my education.

The optical absorption spectra which form the core of this thesis would not have been possible without the single crystal samples grown by others and generously made available to me. Arlete Cassanho, Bernard Keimer, and Ady Levy grew the Top-Seeded Solution growth crystals of La_2CuO_4, Nd_2CuO_4 and Pr_2CuO_4. Martin Greven grew the $Sr_2CuO_2Cl_2$ crystals. Hans Jenssen grew the Floating-Zone grown La_2CuO_4 crystals. Having myself spent two years learning to grow Nd_2CuO_4 thin films, I realize how fortunate I have been to have access to such a variety of high quality samples.

Jens Falck and I have shared an optics table for the past three years. He got me started in the details of optical spectroscopy, was reasonable in resolving the inevitable conflicts which arise over shared equipment and made valuable contributions to the science presented in this thesis.

Prior to joining John Graybeal's group I spent a year at the Plasma Fusion Center with Earl Marmar and then a year at the National Magnet Laboratory with Peter Wolff. Both Earl and Peter were excellent advisors.

The research adventure which culminated in this thesis began with the growth of Nd_2CuO_4 thin films. Although this aspect of my graduate career is only briefly mentioned in my thesis, it was important in my education and research. In retrospect, one might think I could have skipped this portion of my graduate experience, but in reality it was the beginning of a continuous research effort which eventually led to the single crystal measurements presented in this thesis. Terry Orlando and David Rudman welcomed me into their film growth collaboration with John Graybeal. I have enjoyed and profited from my interactions with them.

The development of the sputtering system would have been impossible without the efforts of several fellow graduate students: John Kucera, Lenny Rubin, Mary Matthiesen and David Steel. John Kucera, Kuni Uwai, a visiting scientist from NTT, and I spent an amazingly productive summer developing the ozone still and the *in-situ* deposition process. It was John Kucera who instigated this effort. Ken Ellis, an undergraduate working primarily with myself and John Graybeal, made contributions more typical of a graduate student. John Chervinsky, at Harvard, was invaluable in helping me with Rutherford Backscattering.

The four years I have spent in John Graybeal's group have been shared with his other students: Stefan Anderson, David Steel, and Gee Rittenhouse. Although we all worked on different research projects, we collaborated where possible on science and became friends in general. Stefan and I enjoyed many cups of coffee and the accompanying conversations together. David entertained me with his distinctly British sense of humor and amazed me with his ability to do things other than science while in graduate school. Gee has that special relaxed intensity I strive for. No matter how much he had to do, he always had time to share a story and a laugh.

Because of the collaborative nature of my research I spent many long days in Marc Kastner's lab, where I shared stories, frustrations, and successes with his students: David Abusch, Nathan Belk, Paul Belk, Pam Blakeslee, Jens Falck, Ethan Foxman, Danielle Kleinberg and Ady Levy. Nathan helped me with various electronics problems and Paul provided valued consultation when I developed my data acquisition software.

John Kucera and I have shared many lengthy conversations on the pursuit of success in science and life, and whether the two are mutually compatible. Barry Wells and Mike Yoo have also enriched my Building 13 experience with their friendship. Frank Payne, who is in charge of the student machine shop, provided valuable guidance with regards to design and machining. More importantly, we shared many friendly conversations and a few bike rides.

Largely through Marla Dowell, now my wife, I managed to meet people at MIT outside of Building 13. I have enjoyed the friendship of Wilson Fong, Alan Thompson, and Sarah Wayland. Peggy Berkovitz was always helpful and friendly.

The love and support of my family has been a constant in my life and has helped enormously in all that I have achieved. My parents, by their example, showed me the importance of education and hard work. More importantly, they shared their time with me. My father taught me how to hit a baseball and my mother launched me on my first solo bicycle ride. My brother is my best male friend. My sister was only ten when I left for college. We have become much closer in the past few years while she was an undergraduate at Harvard, and I a graduate student at MIT.

On the first day of class in 1987, I met Marla Dowell. We both grew up in Princeton, N.J., but had not known each other. We became the best of friends and now we are married. Meeting her was the most important thing which happened to me while at MIT. Her love and support not only made graduate school more bearable, but will continue to enrich the rest of my life no matter where the twisted path leads.

Table of Contents

List of Figures

List of Tables

Chapter 1: Introduction

The discovery by Bednorz and Muller [1] in 1986 of superconductivity at T ~ 30K in the layered copper oxide $La_{2-x}Ba_xCuO_4$ initiated an enormous amount of research. Efforts to synthesize related materials quickly led to higher transition temperatures. In 1987, Wu *et al* [2] discovered $YBa_2Cu_3O_{7-\delta}$ with $T_c \sim 90K$. In 1988, Parkin *et al* [3] along with Sheng and Hermann [4] increased T_c to ~ 125 K in $Tl_2Ba_2Ca_2Cu_3O_x$. These materials all contain layers of copper and oxygen atoms. Within a layer, the Cu atoms form a two dimensional square lattice with an O atom linking nearest neighbor Cu atoms. $La_{2-x}Ba_xCuO_4$, has one layer per formula unit where as $YBa_2Cu_3O_{7-\delta}$ has two and $Tl_2Ba_2Ca_2Cu_3O_x$ three layers per formula unit. In general, the higher transition temperature materials have multiple Cu-O layers per formula unit. The aforementioned materials, along with the vast majority of copper oxide superconductors, have hole type carriers. In 1989 Tokura *et al.* [5] discovered a class of electron doped copper oxide superconductors which includes $Nd_{2-x}Ce_xCuO_{4-y}$ with $T_c \sim 24$ K. Earlier this year Putilin *et al* [6] discovered $HgBa_2CuO_{4+\delta}$, a single layer material, with $T_c \sim 94K$. Soon thereafter, Schilling *et al* [7] synthesized the related three layer material $HgBa_2Ca_2Cu_3O_{8+\delta}$ with $T_c \sim 133$ K. Recently, reports of transition onset temperatures as high as 164 K in $HgBa_2Ca_2Cu_3O_{8+\delta}$ at 31 GPa of hydrostatic pressure [8] suggest that with further materials work, the record T_c may continue to increase.

In spite of the large number of copper oxide superconductors which have been discovered and the enormous amount of work invested in trying to understand them, the basic mechanism responsible for the superconductivity is not yet known. For conventional superconductors, such as Pb, Bardeen, Cooper, and Schreiffer [9] showed that the electron-phonon interaction causes the electrons to form pairs, which as bosons, then condense into the superconducting state. In the copper oxide superconductors, magnetic flux quantization experiments [10] show that the carriers are also bound in pairs. However, the pairing mechanism is not yet known. Whether the carriers are paired with S-wave or D-wave symmetry is still an open question [11]. The difficulty in understanding these materials stems from their complexity. The unit cells for La_2CuO_4 and Nd_2CuO_4, two of the simpler host materials, contain 14 atoms apiece. The superconductors, such as $La_{1.85}Sr_{0.015}CuO_4$ with $T_c \sim 33$ K, are derived from a semiconducting host material, such as La_2CuO_4, by chemical doping. As will be discussed, the host materials are S = 1/2 antiferromagnetic insulators with an optical absorption edge at ~ 2 eV. The zone-boundary magnons have energies of ~ 250 meV [12]. This is much higher than in previously studied antiferromagnets such as MnF_2, in which the zone boundary magnon energies are ~ 7 meV [13]. Phonons provide another low energy excitation with energies up to ~ 100 meV [14]. This thesis will show that there is strong reason to believe that other low-energy excitations exist. The optical absorption spectra presented in this thesis show that magnon sidebands to an electric-dipole forbidden excitation account for most of the absorption from about 0.4 - 1.2 eV in the undoped materials. In the undoped lamellar copper oxides there is one hole per copper ion with a ground state of primarily Cu $3d_{x^2-y^2}$ origin. If the electric-dipole forbidden excitation associated with the magnon sidebands is a Cu d-d exciton, then the Cu $3d_{x^2-y^2} \rightarrow 3d_{3z^2-r^2}$ exciton exists at ~ 0.4 eV. However, as will be discussed, the exact nature of the ~ 0.4 eV excitation is still not certain. Understanding the basic excitations of the host materials will probably be necessary in order to understand the onset of superconductivity upon doping. For that reason, this thesis focuses on the optical properties of the simplest, undoped, single layer materials.

New optical absorption spectra for undoped single-crystal samples of La_2CuO_4, $Sr_2CuO_2Cl_2$, Nd_2CuO_4 and Pr_2CuO_4 in the energy range of ~ 0.2 - 1.7 eV constitute the core data for this thesis. The optical properties of the doped lamellar copper oxides in this energy range have been the subject of intense interest [15-17] since the discovery of high temperature superconductivity. In the doped materials, both electron and hole doped, a broad absorption band peaked near 0.5 eV is observed together with additional absorption in the vicinity of 1.5 eV. While much speculation has appeared, the absence of sharp spectral features has made a definitive interpretation of the excitations difficult. The optical transmission experiments, conducted on thin single-crystals, presented in this thesis represent the first observation of mid-infrared absorption in the undoped cuprates. Unlike the spectra for doped samples, the spectra for the undoped samples show clearly resolved optical excitations which are centered near ~ 0.5 eV but with an absorption strength roughly 10^3 times smaller than in the doped materials. Similar spectra are observed in all four materials, appearing only for the electric field polarized parallel to the CuO_2 planes. The similarity of the spectra among materials along with the polarization dependence of the absorption demonstrate that the absorption bands result from intrinsic electric dipole excitations of the CuO_2 layers. In order to understand the explanation of the spectra in terms of joint exciton-magnon absorption, a simple introduction to the basic properties of these materials is needed. La_2CuO_4 will be used as an example.

Introduction to La_2CuO_4

Crystal Structure

The four materials studied share two-dimensional approximately square-planar CuO_2 layers. However, the out-of-plane structures have important differences. Figure 1.1 shows the crystal structure for La_2CuO_4 and Nd_2CuO_4. At high temperature, La_2CuO_4 is tetragonal with octahedrally coordinated Cu sites. Below ~ 530 K, La_2CuO_4 acquires a slight orthorhombic distortion. In this thesis, La_2CuO_4 will

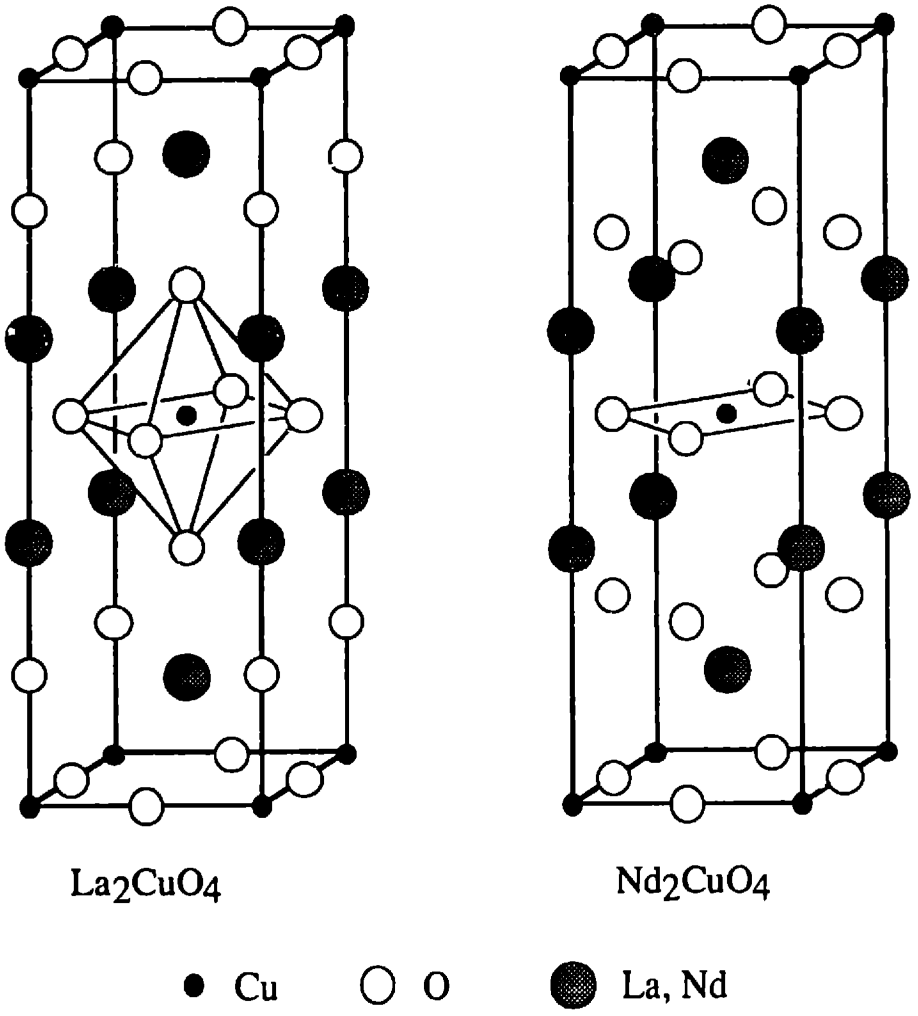

Figure 1.1: The crystal structure for La_2CuO_4 (T-phase) and Nd_2CuO_4 (T'-phase). In $Sr_2CuO_2Cl_2$, which has the same structure La_2CuO_4, the La is replaced with Sr and the apical O with Cl. Pr_2CuO_4 has the same structure as Nd_2CuO_4 but with the Nd replaced by Pr. Drawing after Tokura *et al* [5].

be treated in a tetragonal approximation. Tetragonal $Sr_2CuO_2Cl_2$ resembles La_2CuO_4, but with the La replaced by Sr and the apical O by Cl. Nd_2CuO_4 and Pr_2CuO_4 are both tetragonal with square-planar coordinated Cu sites and no apical ions. The out-of-plane oxygen ions in Nd_2CuO_4 and Pr_2CuO_4 are collected in a single oxygen layer with twice ion density of the two such layers in La_2CuO_4. With the differing chemical compositions and out-of-plane structures, the only common element among these four materials is the CuO_2 layer. Hence, it is natural to associate the common absorption features seen with excitations of the CuO_2 layer.

Electronic Configuration

The first step towards understanding the electronic structure is to count the valence charges. In La_2CuO_4, the La ions would like to be La^{+3} and the O ions O^{-2}. Hence the Cu ion, which can be either Cu^{+1} or Cu^{+2} must be Cu^{+2}. A Cu^{+2} ion has nine electrons in the 3d-shell. The top portion of figure 1.2 shows polar plots for the five d-states. In La_2CuO_4, the nearest neighbor ions are negatively charged O^{-2} ions lying along the x, y, and z directions. Electrons in the $d_{x^2-y^2}$ and $d_{3z^2-r^2}$ states, which have lobes along the principle axis, are repelled from the negative ions and hence have a higher energy. Because the O^{-2} ions in the x-y plane are closer to the Cu^{+2} ion than the apical O^{-2} ions, the $d_{x^2-y^2}$ state is higher in energy than the $d_{3z^2-r^2}$ state. These energy splittings, known as crystal field splittings, are shown in the bottom portion of figure 1.2 for the cases of cubic and tetragonal symmetry. In the ground state, the Cu^{+2} ion has one hole in the Cu $3d_{x^2-y^2}$ state. This brings us to the first unusual property of the lamellar copper oxides. In simple band theories, materials with an odd number of electrons per band are always metals. Yet La_2CuO_4 is a semiconductor. This is easily established by resistivity measurements as a function of temperature. Furthermore, such measurements on La_2CuO_4 single crystals by Preyer *et al* [18] show that conductivity is highly anisotropic. At room temperature the in-plane conductivity is 500 times greater than the out-of-plane conductivity.

Simple visual inspection shows that the crystals are opaque. An opaque insulator must have a band gap near or below the visible. Figure 1.3 shows reflectivity data for La_2CuO_4 at T = 122 K from Falck *et al* [19]. The top panel shows the reflectivity for light polarized parallel and perpendicular to the Cu-O plane. The spectra for light polarized perpendicular to the plane shows no features, again showing the two dimensional nature of these materials. For light polarized parallel to the Cu-O plane there is a sharp

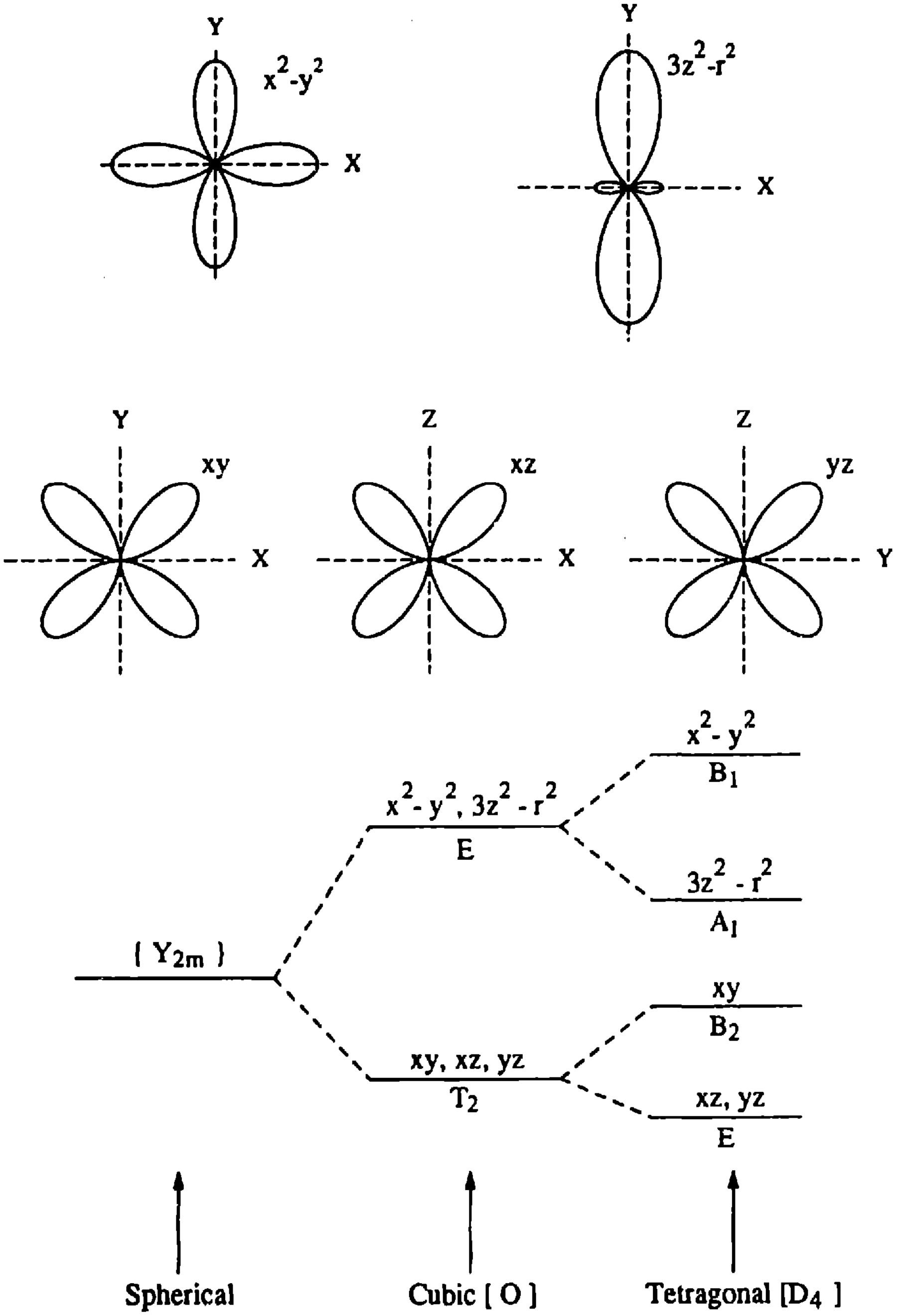

Figure 1.2: Top: Polar plots of d-state electron density. Bottom: Splitting of d-states in non-spherical symmetries.

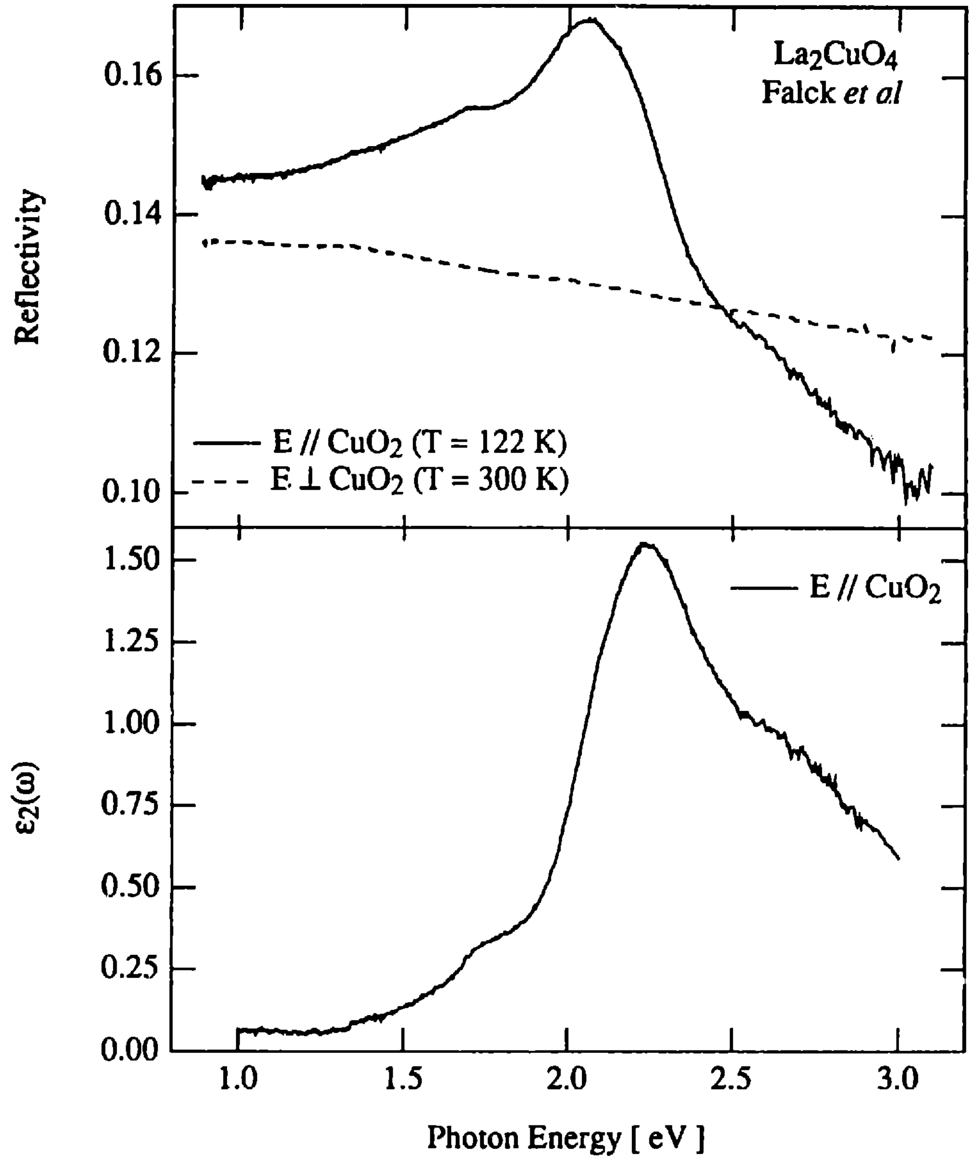

Figure 1.3: Top: Reflectivity of La_2CuO_4 for light polarized parallel and perpendicular to the Cu-O layers. Bottom: Im[ε(ω)] for light polarized in the plane. From Falck *et al* [19].

feature at ~ 2 eV. The bottom panel shows the associated imaginary part of the dielectric constant as a function of photon energy. The absorption edge at ~ 2 eV is the band gap. The excitation involves the in-plane transfer of an electron from an O ion to the Cu $d_{x^2-y^2}$ hole and is hence known as a charge-transfer excitation. This will be discussed in more detail later.

Although the first principles calculation of the energy levels in materials such as La_2CuO_4 is a current research problem, the fact that La_2CuO_4 is not metallic can be qualitatively understood as follows. Consider two hydrogen atoms. If they are close together, they form molecular hydrogen with each electron spread across both protons. If they are far apart, they exist as separate hydrogen atoms with one electron per atom. Yet, a tight binding band theory solution for the two atoms far apart has a 50% chance of finding both electrons on one proton. This is because the tight binding model ignores the electron-electron repulsion. When the protons are far enough apart the energy cost for double occupancy of a proton due to electron-electron repulsion is larger than the energy gained by letting the electron delocalize, and hence the electrons are localized with one electron per proton. The transition from extended conducting states to localized insulating states is called the Mott transition. In La_2CuO_4, the copper ions are far enough apart so that the one hole per copper ion is localized on the copper sites. However, as will be apparent when the magnetism of La_2CuO_4 is discussed, there are still important interactions between the holes on adjacent copper sites.

The Hubbard Model

In an effort to understand the crossover from localized to extended states the following model was created by Hubbard [20] in the 1960's. As variants of the model are widely used to study High-T_c copper oxides and form the basis for much of the language used in discussing the electronic structure, it will be briefly discussed. The model begins with a lattice, such as the two dimensional square lattice formed by the Cu^{+2} ions in the Cu-O layer. At each lattice site, there are a small number of localized orbitals. The simplest case has only one orbital per site, such as the Cu $d_{x^2-y^2}$. The Hubbard Hamiltonian is:

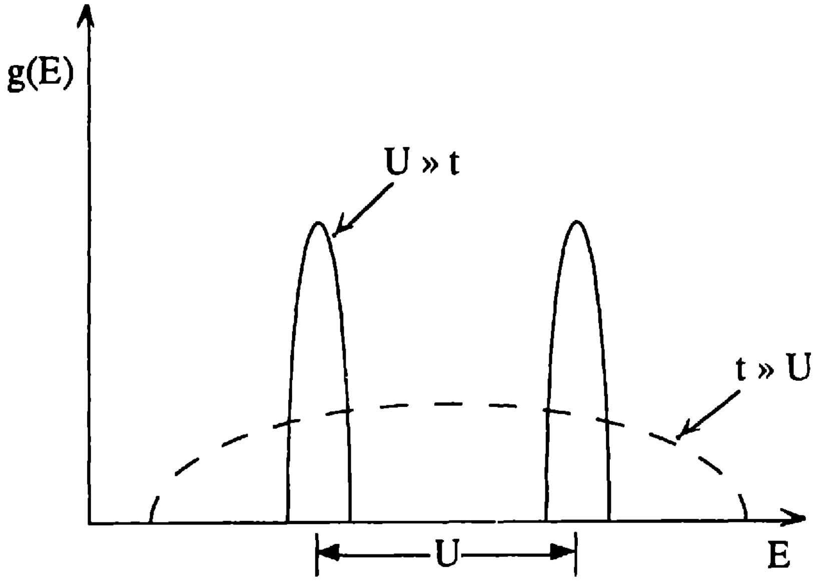

Figure 1.4: Schematic of density of states vs. energy for a one band Hubbard model including hopping, t, and on-site repulsion, U. In the case of strong on-site repulsion (U >> t) the electrons are localized.

$$H = \varepsilon_0 \sum_{i,\sigma} n_{i,\sigma} + t \sum_{i,k,\sigma} c^{\dagger}_{i,\sigma} c_{k,\sigma} + U \sum_{i} n_{i,\sigma} n_{i,-\sigma} . \tag{1.1}$$

The subscripts i and k denote lattice sites and the subscript σ denotes the spin. The first term is simply the sum of the single particle energies. For a model of the undoped crystal with only one orbital per site it can be ignored. In the second term the sum is restricted to nearest neighbors and the operators $c^{\dagger}$ and c create and destroy particles in the state given by the subscripts. This allows for hopping of particles between sites. This can be generalized to non-nearest neighbor hopping but then additional hopping parameters, t, must be introduced. The final term approximates the electron-electron repulsion as simply an energy cost, U, for a site to be doubly occupied. Ignoring the single particle energy term, this model has only two parameters, t and U. Even so, it is not easy to solve for all values of t and U. Figure 1.4 shows the schematic density of states versus energy for the two extreme cases. When t >> U, the solution is a band

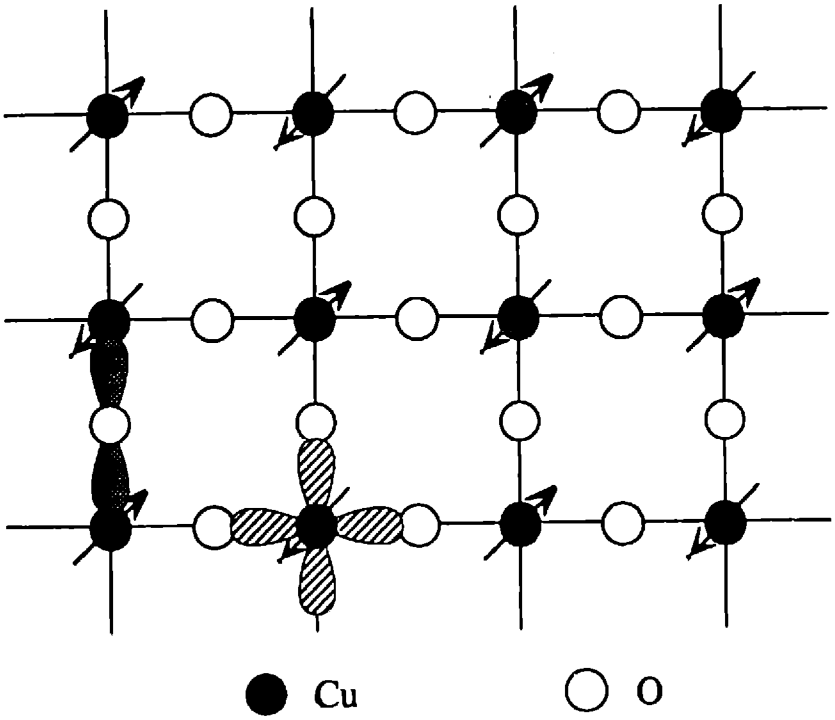

Figure 1.5: The Neel state spin orientation for a Cu-O layer. The arrows denote the spin orientation. The Cu $3d_{x^2-y^2}$ and the O2p$_\sigma$ orbitals important in the superexchange are shown pictorially. After Birgeneau [21].

of extended states, like the molecular orbitals in molecular hydrogen. For U >> T, the particles are localized one per lattice site, and the band splits in two. The excited states consist of a particle hopping to a neighbor and creating a doubly occupied site. Hence the energy gap, U, shown in the figure. Materials such as La_2CuO_4 represent an intermediate case, with U > t. This is responsible for many of their novel properties, as well as the difficulties in calculating the energy levels.

In La_2CuO_4, the nearest neighbor Cu ions within the CuO_2 layer are linked by an intermediate oxygen ion. This is shown schematically in figure 1.5. The arrows indicate the orientation of the Cu site spins. The origin of the antiferromagnetism will be discussed shortly. First, there is the question of the relative energy of the Cu ion d-states and O ion p-states. Recall from the simple valence counting argument that the

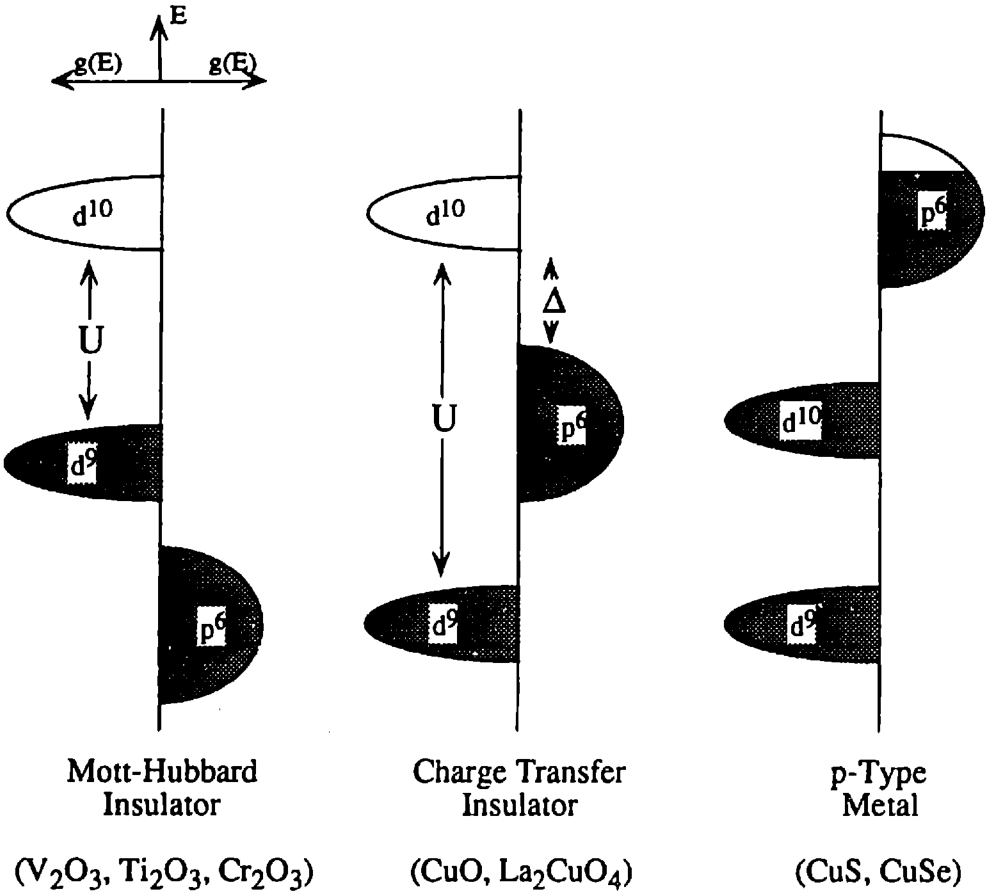

Figure 1.6: Schematic density of states vs. energy diagrams for transition metal compounds with one hole per metal ion and different ligand p-state energies relative to the metal d-states. Based on Zaanen *et al* [22].

oxygen p-states are fully occupied in an electron picture. The principle experiments used to examine the relative energy levels are X-Ray Photo-electron Spectroscopy (XPS) and Inverse XPS (IXPS). In XPS spectroscopy x-ray energy photons are used to eject electrons. The spectral shapes allow electrons from Cu and O ions to be distinguished and hence probes the energy differences of states occupied by electrons. In IXPS, the incident electrons are captured by high energy states and then emit photons when they decay to the unfilled electron states. The spectral shapes for XPS applied to core electrons such as Cu 2p or O 1s provide additional information about whether the states are extended or localized and in the case of localized

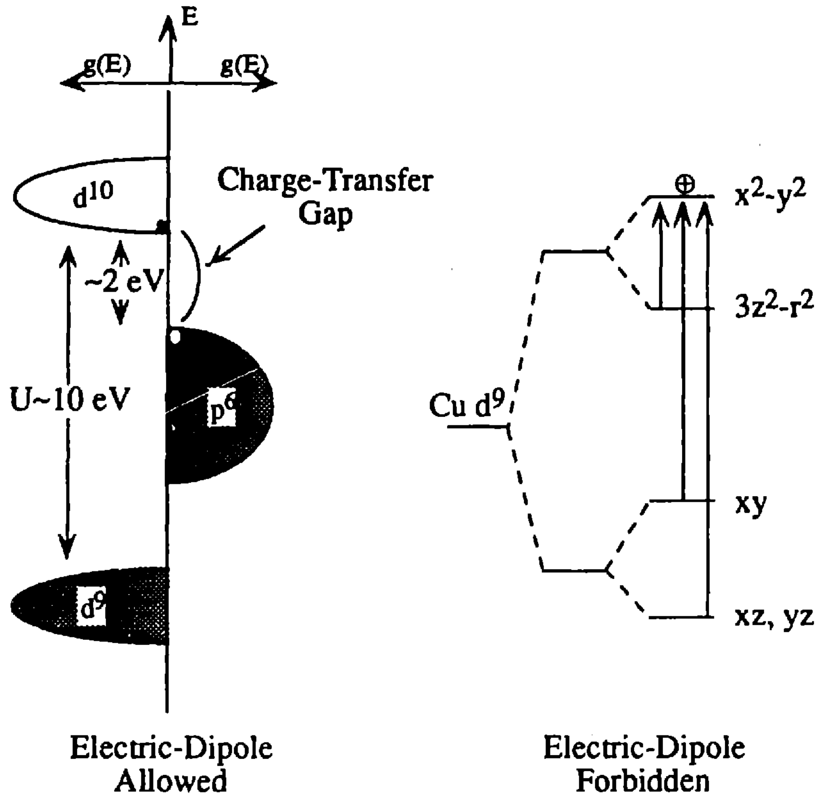

Figure 1.7: Basic electronic excitations for undoped lamellar copper oxides. Left: Electric dipole allowed charge transfer excitation. Right: Electric dipole forbidden crystal field excitations. The energy scale for the crystal field excitation drawing is roughly an order of magnitude smaller than that for the charge transfer drawing.

metal ion states, about the degree of hybridization . A good review of this is provided by Sawatzky in reference [23]. A classic comparison of Cu_2O, a band like semiconductor, and CuO, an insulator with localized states is presented by Ghijsen *et al* [24]. A general scheme for classifying transition metal compounds is described by Zaanen, Sawatzky, and Allen (ZAS) [22]. Figure 1.6, which is based on ZAS, shows three possible types of compounds for materials with one hole per metal ion, depending on the location of the ligand p-states with respect to the metal d-states. Two intermediate cases discussed by ZAS are not shown. In La_2CuO_4, a charge-transfer insulator, the filled O p-states lie between the lower and upper Hubbard bands as shown in the middle picture. The band gap, Δ, is about 2 eV in La_2CuO_4 and corresponds to the transfer of an electron from a O 2p state to the empty Cu 3 $d_{x^2-y^2}$ state.

XPS and IXPS are based on the addition or removal of an electron. The Hubbard gap U, can be thought of as the removal of an electron from one Cu ion and the addition of that electron to another Cu ion. However, in a Cu^{+2} ion, another type of electronic excitation exists. The ground state has one hole in the $d_{x^2-y^2}$ state. The excited states created by promoting this hole to one of the other d-states of the same ion conserves the Cu ion valence and is not probed by XPS or IXPS. As mentioned before, these are called crystal-field excitations. Due to the inversion symmetry of the Cu site in La_2CuO_4, these Cu d-d excitations are electric dipole forbidden. The charge-transfer excitation is electric dipole allowed. These two distinct types of excitations are summarized in figure 1.7. Note that the energy scales in the diagram are not the same. As will be demonstrated by this thesis, the crystal-field excitations play an important role in understanding the mid-infrared optical properties of the undoped lamellar copper oxides.

Magnetism

As has been mentioned several times, the undoped lamellar copper oxides are antiferromagnetic insulators. Figure 1.5 shows the spin configuration in the antiferromagnetic Neel state. Figure 1.8 shows the phase diagram for $La_{2-x}Sr_xCuO_4$ as a function of temperature and doping. Note that the diagram is not to scale. The phase boundary which runs from T ~ 325 and x = 0 to T = 0 and x ~ 0.02 gives the Neel temperature as a function of doping. Below this boundary there is true long range antiferromagnetic order. Above this boundary the spins are still correlated over large regions in the two dimensional Cu-O planes but are not correlated between the planes [25]. The distinction between these two states will not be important to the explanation of the spectra presented in this thesis. In $Sr_2CuO_2Cl_2$ crystals, with T_N ~ 256 K [26], no abrupt change is seen in the absorption spectra upon cooling through the Neel temperature. Figure 1.9 shows the two magnon Raman scattering spectra for several single layer undoped lamellar copper oxides at T = 300 K from Tokura *et al* [12]. The peak corresponds to excitation of two zone boundary

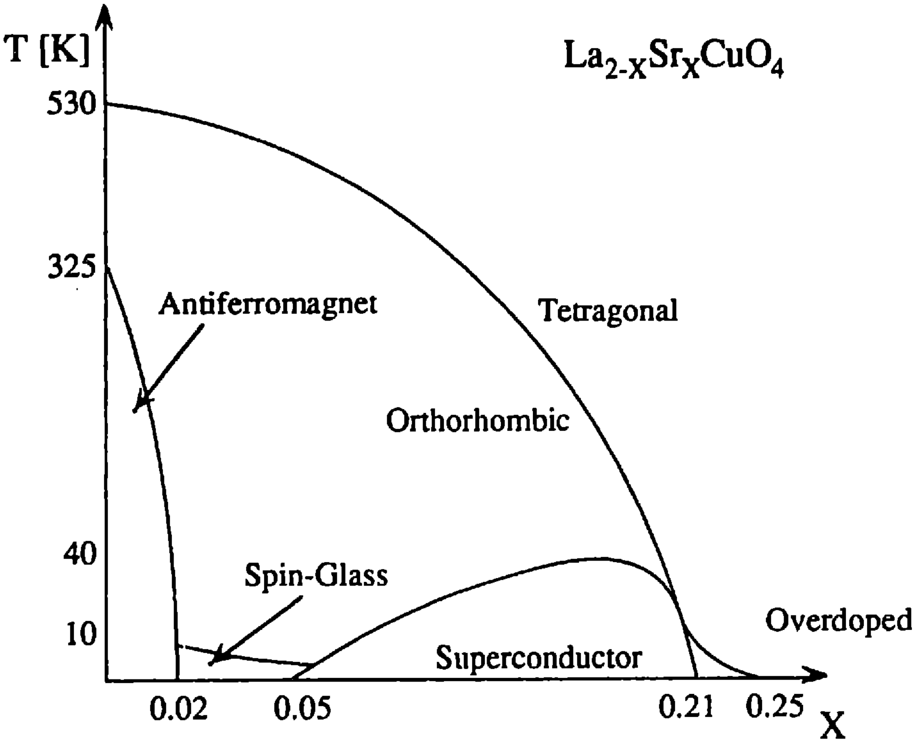

Figure 1.8: Schematic phase diagram of $La_{2-x}Sr_xCuO_4$. The diagram is not to scale. Drawing adapted from Ph.D. thesis of J. Falck [27].

magnons. Due to magnon-magnon interactions and quantum effects, the energy of the peak is about 33% lower than twice the zone boundary energy. The peak is at ~ 3000 cm^{-1} or ~ 370 meV, showing that the zone boundary magnons have an energy of roughly 250 meV. The important point here is the remarkably large energy scale for magnon excitations in the High-T_c host materials. This large energy scale is due to the strong exchange interaction between holes on neighboring copper sites. Nearest neighbor Cu site holes interact with each other by hopping though the oxygen site. Figure 1.5 shows pictorial representations of the important Cu $d_{x^2-y^2}$ and O p_σ states. Because the exchange interaction takes place via an intermediate state it is often referred to as superexchange. The magnitude of the exchange is so large because of the large overlap of the Cu $d_{x^2-y^2}$ and O p_σ wave functions as well as the small energy difference between them. The energy difference is essentially the charge transfer gap of ~ 2 eV.

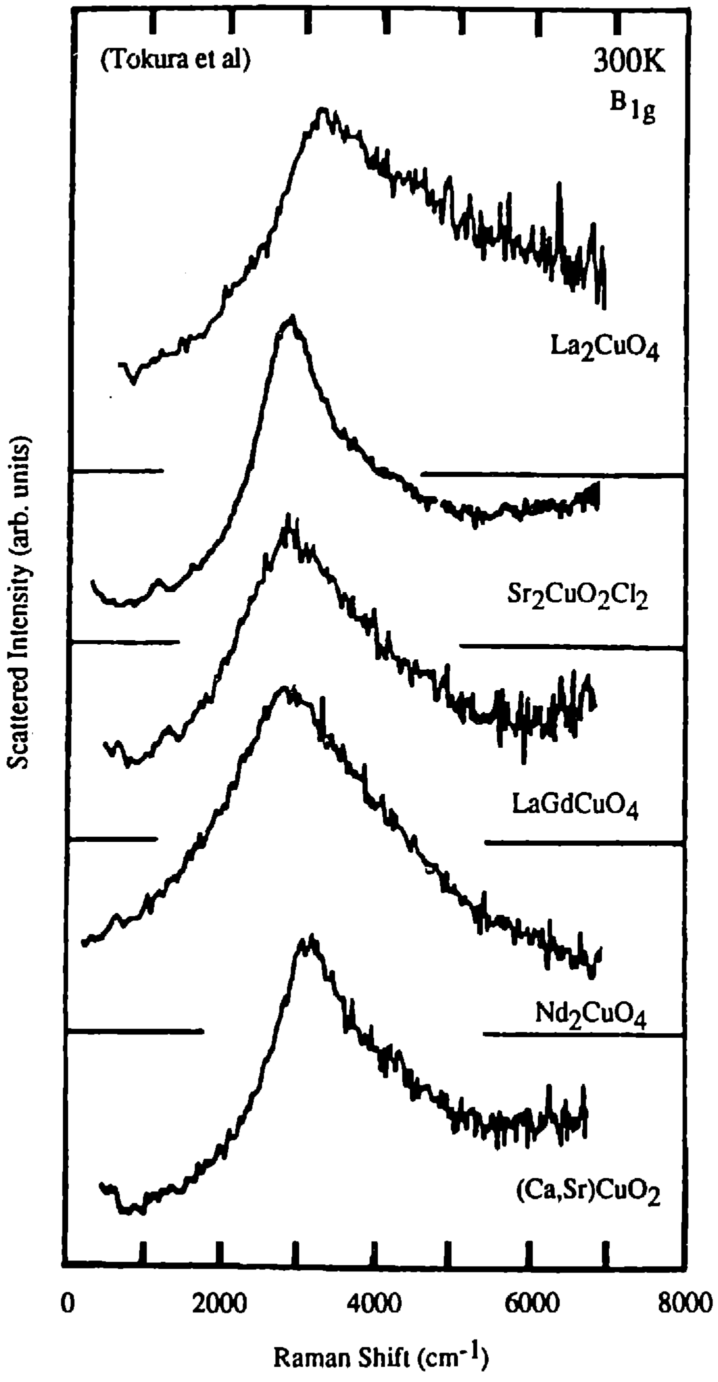

Figure 1.9: Raman spectra, at T = 300 K, for B_{1g} 2-magnon excitations in single CuO_2 layer compounds. From Tokura *et al* [12]

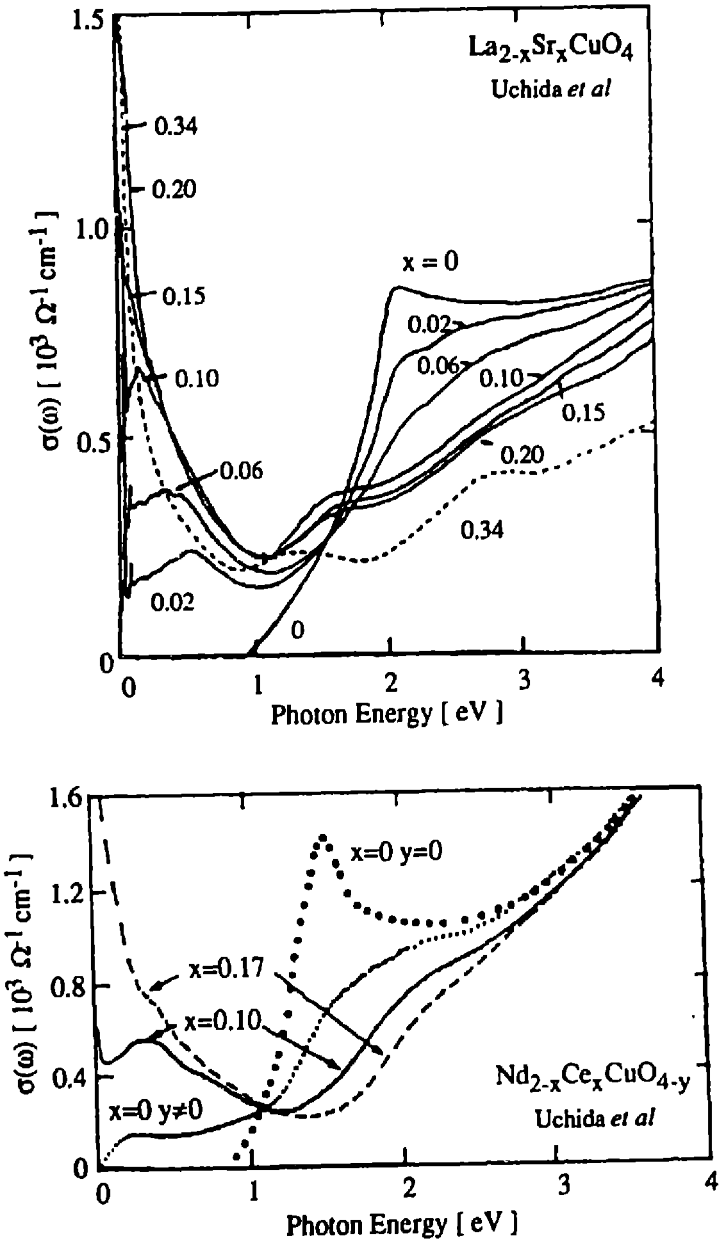

Figure 1.10: Doping dependence of optical conductivity, σ(ω), for $La_{2-x}Sr_xCuO_4$ (top) and $Nd_{2-x}Ce_xCuO_{4-y}$ (bottom) from Uchida *et al* [17]. Note the transfer of spectral weight from the charge-transfer excitation to the infrared upon doping.

When La_2CuO_4 is doped with Sr, the Sr ions donate an extra hole to the Cu-O layer. These holes occupy oxygen sites and hence frustrate the antiferromagnetic ordering. This is responsible for the rapid decline in the Neel temperature as a function of doping shown in figure 1.8. In the undoped materials, the spin-spin interactions are well described by the Hamiltonian for a S = 1/2 Heisenberg antiferromagnet in two dimensions:

$$H = J\sum_{nn}\bar{S}_i \cdot \bar{S}_j . \tag{1.2}$$

The coupling parameter, J, is known as the exchange constant and is roughly 130 meV in the undoped lamellar copper oxides.

Evolution of Optical Spectra with Doping

For Sr doping levels between x ~ 0.05 and x ~ 0.21, $La_{2-x}Sr_xCuO_4$ has a superconducting phase as shown in figure 1.8. The frustration of the magnetism and development of a superconducting phase are not the only interesting changes induced by doping. The optical spectra show dramatic and unusual evolution with doping. Figure 1.10 shows the optical conductivity as a function of photon energy for $La_{2-x}Sr_xCuO_4$ (top) and $Nd_{2-x}Ce_xCuO_4$ (bottom) at several different doping levels. When Nd_2CuO_4 and Pr_2CuO_4 are doped with Ce they also develop a superconducting phase, but the carriers are electrons instead of holes as in $La_{2-x}Sr_xCuO_4$ [5]. The spectra show a clear transfer of spectral weight from above the charge transfer gap to the infrared, below the charge transfer gap. Figure 1.11 from Thomas *et al* [28] shows the optical conductivity for lightly oxygen doped La_2CuO_{4+y}, Nd_2CuO_{4-y} and $YBa_2Cu_3O_{6+y}$. In these lightly doped materials, two distinct absorption peaks can be seen above the sharp phonon lines and below the tail of the charge transfer gap. Neither of these can be explained by the Drude free carrier absorption that would develop in a lightly doped conventional semiconductor. The peak at ~ 0.15 eV has recently been shown by Falck *et al* [27] to be the photo-ionization of impurity bound holes.

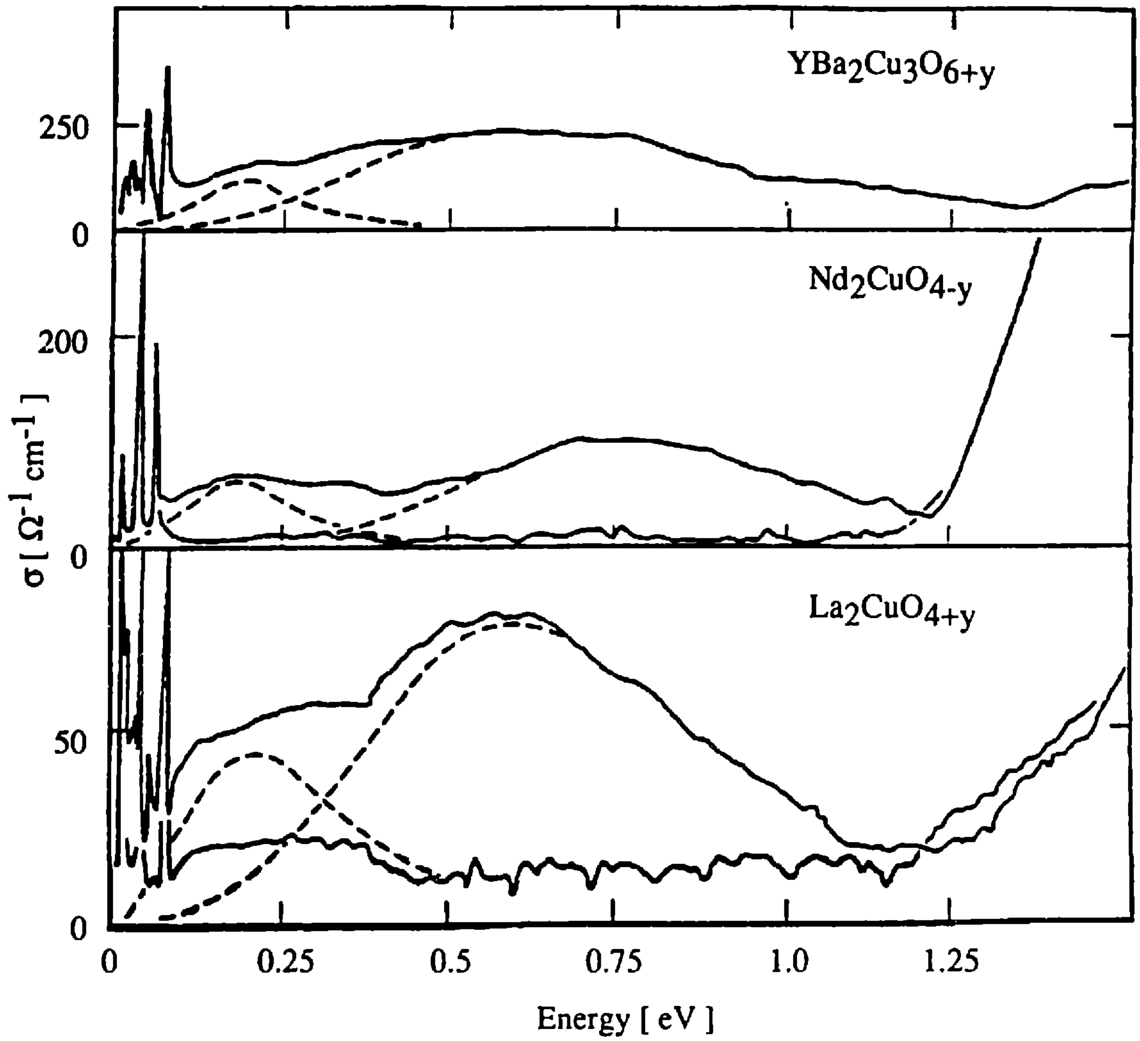

Figure 1.11: Comparison of the optical conductivity, σ, for several different materials. The YBCO is measured at 300 K, the rest at 10 K. The lower curves for Nd_2CuO_4 and La_2CuO_4 are undoped. From Thomas *et al* [28].

The absorption process for the peak centered at ~ 0.6 eV in La_2CuO_{4+y} is the focus of this thesis. In the nomenclature of the High-T_c materials, it is the referred to as the mid-infrared absorption even though many spectroscopists would consider it to be in the near-infrared.

Structure of This Thesis

This chapter has provided a brief introduction to the electronic structure of the undoped High-T_c materials and has identified the charge-transfer excitation, the crystal-field excitations and the magnons as important excitations. The phonons are also a fundamental low energy excitation, but they will not be important in the explanation of the mid-infrared absorption in the undoped lamellar copper oxides. The optical spectra presented in this introduction will provide a valuable reference with which to compare the strength and spectral features of the mid-infrared absorption in the undoped copper oxides. The brief introduction to the Hubbard model will be useful in understanding the matrix elements for the joint exciton-magnon sidebands, as well as some simple calculations of crystal field exciton energies.

This thesis is organized as follows. Chapter 2 details the sample preparation and the experimental methods used in the optical transmission measurements. In Chapter 3, the measured spectra for the undoped lamellar copper oxides are presented. The polarization experiments show that the absorption is an electric-dipole process polarized in the Cu-O plane. Along with the data presented in Chapter 3, Chapter 4 is the core of this thesis. It examines the absorption spectra in terms of a Cu d-d exciton with multimagnon sidebands. If a Cu d-d exciton is involved, the magnon sideband selection rules along with information from other experiments show that the exciton must be the Cu $d_{x^2-y^2} \rightarrow d_{3z^2-r^2}$ exciton in hole terminology. However, the exact nature of the excitation at ~ 0.4 eV on which the magnon sidebands ride is not yet certain. Two of the questions raised by the Cu d-d exciton explanation are the lack of variation in the exciton energy with the out-of-plane crystal structure and the unexpectedly low energy of the exciton. These questions are addressed in Chapter 5. Chapter 6 discusses some preliminary photo-induced absorption experiments which suggest that the mid-infrared absorption measured in the undoped crystals does indeed increase with doping. Finally, Chapter 7 summarizes the mid-infrared absorption in the undoped lamellar copper oxides and discusses the potential for future work, both experimental and theoretical.

Chapter 2: Experimental Procedures

This chapter describes the experimental procedures used to obtain the optical spectra presented in this thesis. First, the sample preparation is described, then the measurement of basic transmission spectra and finally, the photo-induced absorption measurements. The importance to this work of readily available, high quality, single crystal samples of La_2CuO_4, $Sr_2CuO_2Cl_2$, Nd_2CuO_4 and Pr_2CuO_4 can not be overstated. I am deeply indebted to those who grew the samples. I began this research studying photo-induced absorption in epitaxial Nd_2CuO_4 thin films which I made. The unusual time-decay observed led to the transmission measurements of the thin single crystals and the subsequent discovery of intrinsic mid-infrared absorption in the undoped lamellar copper oxides, upon which this thesis focuses. The existence and availability of the single crystal samples made this redirection of my research possible.

Sample Preparation

Single Crystals

All the single crystals studied in this thesis were grown at the MIT Crystal Physics Laboratory. The La_2CuO_4, Nd_2CuO_4, and Pr_2CuO_4 crystals were grown by top-seeded solution growth in Pt crucibles using CuO flux [29,30]. The specific samples used were grown by Arlete Cassanho, Bernard Keimer, and

Ady Levy. Martin Greven grew the $Sr_2CuO_2Cl_2$ crystals by cooling a stoichiometric melt in a Pt crucible [31,32]. Additional La_2CuO_4 crystals were grown by Hans Jenssen using the floating-zone technique. This last method uses no crucible, hence these crystals are free of Pt impurities.

For optical transmission experiments thin samples with large lateral dimensions are desired. The normal to the polished surface is used to indicate the orientation of the sample in a tetragonal notation where the <001> axis is perpendicular to the Cu-O layers. Hence, the Cu-O layers are parallel to the polished face in a <001> sample and perpendicular to the polished face in a <100> sample. The <100> orientation allows the incident electric field to be polarized either parallel or perpendicular to the Cu-O layers. Due to the layered nature of these materials, <001> flakes with lateral dimensions of 1-3 mm are common. Such flakes of Nd_2CuO_4 and Pr_2CuO_4 were used. The La_2CuO_4 crystals grown by the top-seeded-solution method form square Cu-O layers parallel to the surface of the melt. The resultant crystals have large <001> faces, about 1 cm on a side, and are several millimeters thick. These crystals are easily oriented by eye and from them <001> and <100> samples were cut. The float-zone grown La_2CuO_4 crystal, which had no obvious orientation, was oriented using Laue X-Ray diffraction prior to cutting <100> samples.

The as grown La_2CuO_4 crystals contain excess oxygen resulting in a hole doping level of ~ 5×10^{19} cm^{-3} or ~ 0.5 holes per copper site [18,33,34]. The excess holes frustrate the antiferromagnetism and thereby lower the Neel temperature. In La_2CuO_4, a slight canting of the spins out of the Cu-O plane results in a net paramagnetic moment per plane and a sharp ferromagnetic like peak in the magnetization at the Neel temperature [33,35]. This allows the Neel temperature to be measured with a SQUID magnetometer. Room temperature Hall measurements have shown that the Neel temperature varies linearly with doping [34]. The Neel temperature of the as grown La_2CuO_4 crystals is 240 K. To remove the excess holes, the La_2CuO_4 samples were annealed for 45 minutes at 900° C in a vacuum of $P \leq 4\times10^{-6}$ Torr [19]. Figure 2.1 shows the magnetization versus temperature for a float-zone grown La_2CuO_4 sample in an applied field of B = 5 kG,. The Neel temperature is greater than 320 K. Due to mistakes in

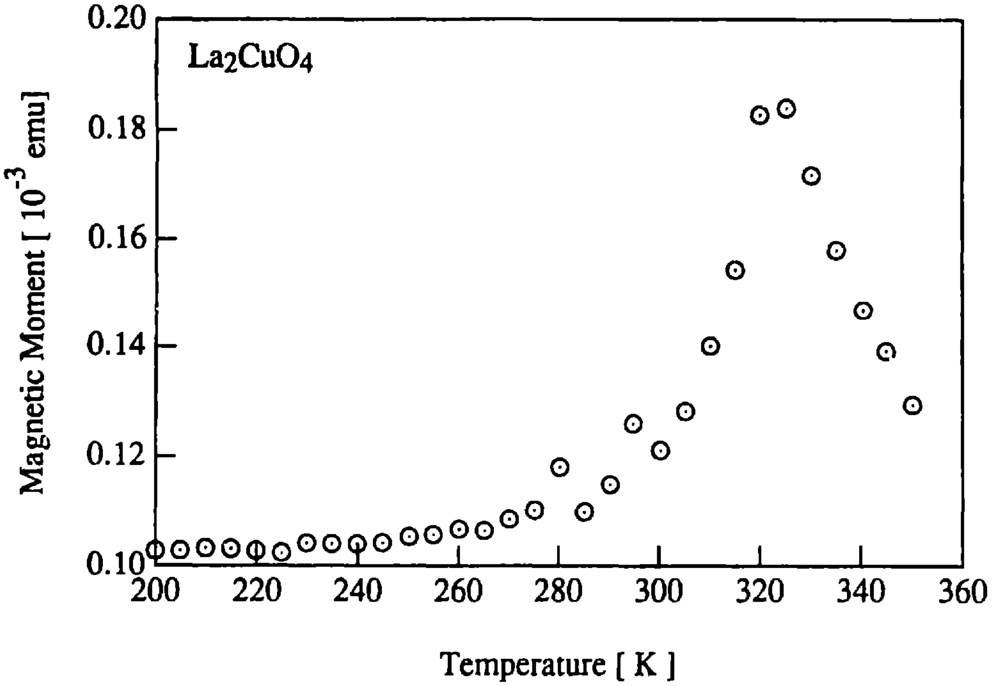

Figure 2.1: Magnetic moment vs. temperature showing a Neel temperature of greater than 320 K. The float-zone grown La_2CuO_4 crystal was annealed at $P \leq 4\times10^{-6}$ Torr and T = 900 °C for a total of 180 minutes. The applied magnetic field is B = 5 kG.

measuring the Neel temperature, this sample, which is part of the first float-zone grown La_2CuO_4 at MIT, was annealed several times for a total of 180 minutes. Presumably the additional annealing was not necessary. The Nd_2CuO_4, Pr_2CuO_4, and $Sr_2CuO_2Cl_2$ samples were measured as grown. $Sr_2CuO_2Cl_2$ is stoichiometric as grown and can not be readily doped.

The Pr_2CuO_4 and the annealed La_2CuO_4 samples were polished using diamond grit on tin laps which had been turned on a lathe. To avoid fracturing the crystals, this was done very slowly and typically took several days to a week.. Sample thicknesses of ~ 100 µm were readily obtained. At sample thicknesses below ~ 50 µm, the samples tend to crumble. At this point the samples are very delicate and have lateral dimensions of 1-3 mm. They were floated off the polishing block using acetone. The Nd_2CuO_4 flake was about ~ 200 µm thick with shiny surfaces as found and was not polished. PMMA, a common photoresist, was used to glue the samples to ~ 1/4" square copper backing plates. In each plate an appropriately sized hole was drilled to allow transmission measurements. This mounting scheme prevented light from leaking around the crystal and allowed the samples to be handled.

The reflectivity measurements of Falck *et al* [19] show that after polishing, the etching of La_2CuO_4 crystals in 1% Br in methanol sharpens the charge transfer edge for etching times up to 20 minutes. Such etching also dramatically increased the photo-induced absorption measured in Pr_2CuO_4 crystals, again showing that etching improves the as polished surface. Therefore the La_2CuO_4, Nd_2CuO_4, and Pr_2CuO_4 were etched in 1% Br in isopropyl alcohol for 20 minutes. Isopropanol was used in place of methanol to avoid degrading the PMMA.

The $Sr_2CuO_2Cl_2$ crystals were much easier to prepare for transmission measurements. Since the material grows on stoichiometry, no annealing was necessary. Due to their micaceous nature, $Sr_2CuO_2Cl_2$ crystals are easily cleaved with Scotch tape resulting in smooth optical quality surfaces. Furthermore, repeated cleaving allows samples as thin as ~ 10 µm to be easily made. However, only <001> samples can be made. The $Sr_2CuO_2Cl_2$ samples were also mounted with PMMA, but not etched. Whereas it typically took a week or more to prepare a La_2CuO_4 sample, the $Sr_2CuO_2Cl_2$ samples can be prepared in several hours. The differing mechanical properties of La_2CuO_4 and $Sr_2CuO_2Cl_2$ provided complimentary experimental possibilities. The 10 µm thick $Sr_2CuO_2Cl_2$ samples allowed measurements to higher energies, where the absorption is stronger. The more isotropic mechanical properties of La_2CuO_4 allowed both <100> and <001> samples to be prepared and hence made the polarization experiments possible.

Nd_2CuO_4 Thin Films

Epitaxial <001> oriented Nd_2CuO_4 thin films on $SrTiO_3$ substrates were used in the time-resolved photo-induced absorption measurements presented in Chapter 6. The films were grown *in-situ* by co-sputtering from elemental metallic targets in the presence of pure ozone. The substrate temperature during growth was about 800 °C. The relative deposition rates of the metallic elements was monitored with quartz crystal rate monitors and actively controlled. The ozone was purified by distilling liquid ozone prior to the deposition. Although the growth of these films represents a lot of work on my part, they are not central to the focus of this thesis and I will not discuss their fabrication at length. The details of the deposition process and a detector for measuring ozone fluxes are published elsewhere [36,37].

Optical Transmission Measurements

The absorption spectra presented in this thesis are based on optical transmission measurements. This section describes the basic experimental setup and techniques used in these measurements. In a simple view, the transmission, T, is given by:

$$T = (1 - R)e^{-\alpha d}, \tag{2.1}$$

where R is the reflectivity and α the absorption coefficient. For weak absorption processes the reflection due to the dielectric mismatch will be essentially wavelength independent. In undoped La_2CuO_4, the reflectivity in the mid-infrared is nearly wavelength independent with R ~ 15% [27]. The effect of multiple internal reflections will be discussed later. The basic quantity extracted from the transmission measurements is the absorption coefficient:

$$\alpha = \frac{-\ln(T)}{d} + \frac{\ln(1-R)}{d}. \tag{2.2}$$

The wavelength independent reflectivity simply creates a constant offset. The linear background subtraction discussed in chapter 3 automatically accounts for the reflectivity offset as well as any offsets due to aperturing of the beam by the small sample size. Therefore, the reflectivity term will simply be ignored.

In terms of the dielectric function, ε, the absorption coefficient is given by:

$$\alpha(\omega) = \frac{2\omega}{c}\,\mathrm{Im}\left(\sqrt{\varepsilon(\omega)}\right). \tag{2.3}$$

For the case of weak absorption, where $|\varepsilon_2| << |\varepsilon_1|$, with $\varepsilon_2 = \mathrm{Im}(\varepsilon)$ and $\varepsilon_1 = \mathrm{Re}(\varepsilon)$, the square root can be expanded giving:

$$\mathrm{Im}\left(\sqrt{\varepsilon}\right)=\frac{\varepsilon_2}{2\sqrt{\varepsilon_1}}\left[1-\frac{1}{8}\left(\frac{\varepsilon_2}{\varepsilon_1}\right)^2+\cdots\right]. \tag{2.4}$$

In this approximation, the absorption coefficient is directly related to the imaginary dielectric function and hence also the optical conductivity:

$$\alpha(\omega)=\frac{\omega}{c\sqrt{\varepsilon_1}}\varepsilon_2(\omega)=\frac{4\pi}{c\sqrt{\varepsilon_1}}\sigma_1(\omega). \tag{2.5}$$

The typical absorption coefficient measured is ~ 100 cm^{-1} and in La_2CuO_4 ε_1 ~ 5 [19]. From equation 2.5 this gives $\varepsilon_2 \sim 10^{-2}$. Therefore, the relative correction to the first order result in equation 2.4 is of order 10^{-4} and hence the approximation made to obtain equation 2.5 is justified. Equation 2.5 is extremely useful in comparing data obtained by transmission measurements with that from reflectivity measurements which are usually presented in terms of $\varepsilon_2(\omega)$ or $\sigma_1(\omega)$.

Optical Setup

Figure 2.2 shows the basic layout of the optics table used for the transmission measurements. The flat mirrors, although extremely useful, simply redirect the probe beam and hence will be ignored in the following description. A broad band light source is focused into a model 218 McPherson grating monochromator. A tuning fork chopper located inside the monochromator and before the diffraction grating modulates the probe beam at ~ 400 Hz allowing a lock-in amplifier to be used to extract the signal proportional to the probe beam. The light is dispersed by a diffraction grating. The wavelength resolution is set by the ratio of the input and output slit size to the grating spacing. A toroidal mirror collects the expanding beam and refocuses it through a filter which rejects the shorter wavelength light, λ/n, generated by higher order diffraction. Because of the need to reject the higher order diffraction, no single scan can span more that a factor of two in wavelength. After the filter, the expanding beam is collected by another

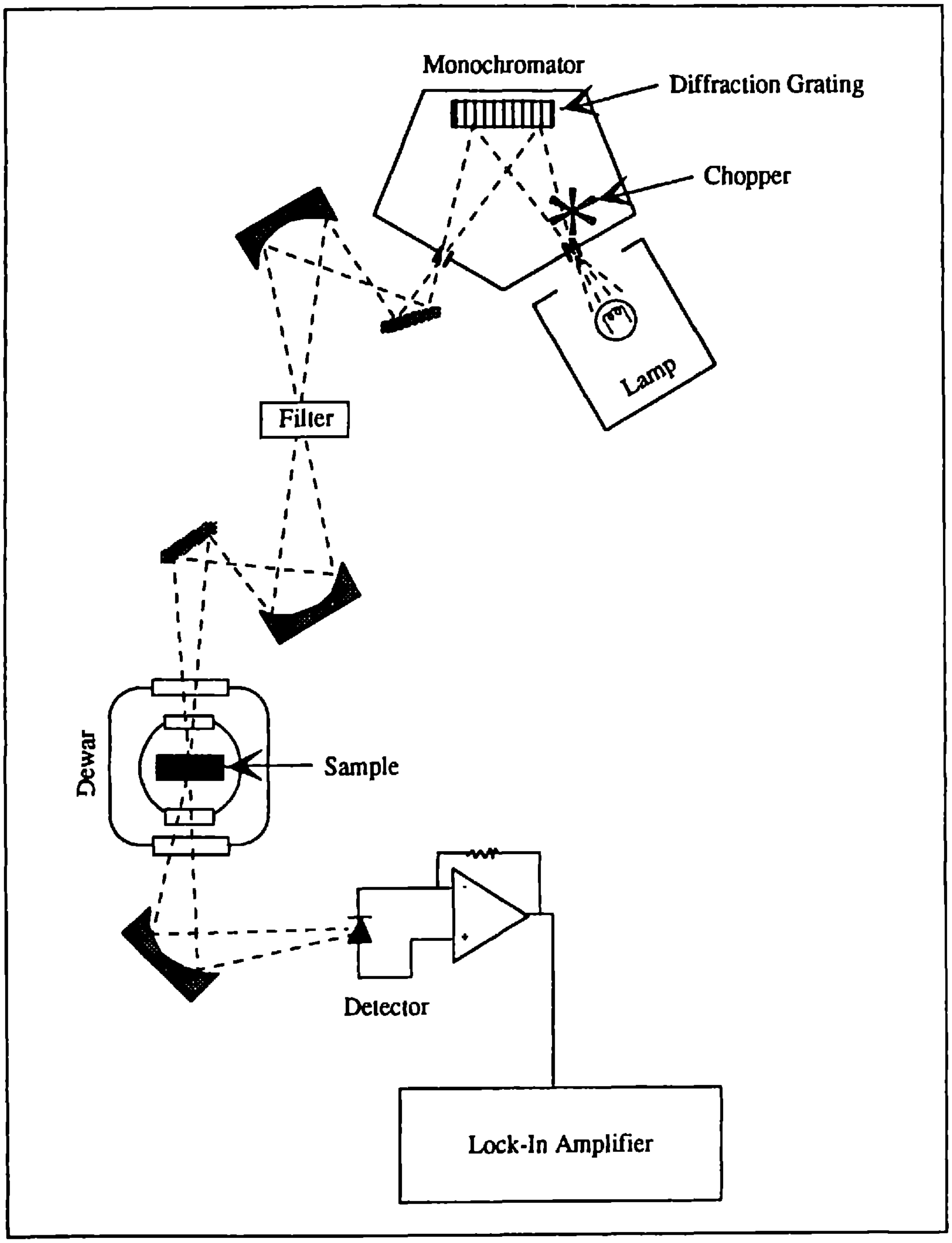

Figure 2.2: Optics table setup for basic transmission experiments. The filter is needed to block higher order diffraction components. Mirrors are used to obtain wavelength independent focusing.

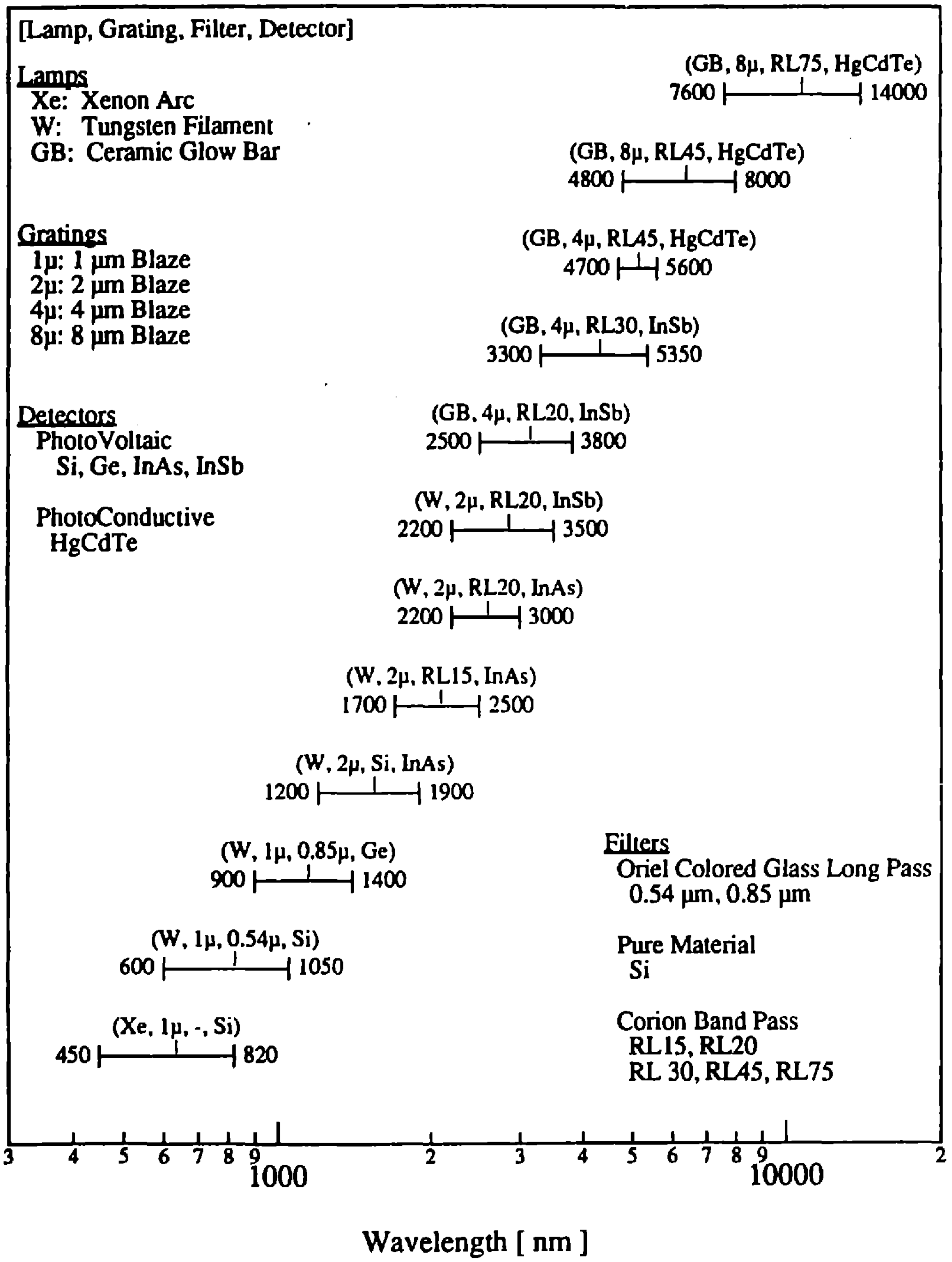

Figure 2.3: Optimum combinations of optical components for wavelength segments from 450 nm to 14 µm.

toroidal mirror and focused onto the sample. The sample resides in a Janus Supervaritemp optical dewar. The outer windows are made of BaF2 and the inner ZnS. After the light passes through the sample and out of the dewar it is collected by an elliptical mirror and focused onto the detector, typically a photodiode detector. A current to voltage preamplifier collects the detector current. A lock-in amplifier is used to extract the signal proportional to the probe beam. Standard Keithley and Hewlett-Packard multimeters are used to digitize the signal.

By using various combinations of lamps, gratings, filters and detectors this basic setup allows measurements from about 400nm to 13 μm or 3.1 to 0.095 eV. Figure 2.3 shows the optimum combination of elements for different wavelength segments. The long wavelength, low energy, cut off for each detector is set by the band gap of the material. The short wavelength cut off is not well defined for any given detector. In general, the larger the band gap, the smaller the dark current due to thermally generated carriers and the better the signal to noise ratio. When the signal to noise ratio is not a problem, the smaller band gap detectors may be used to higher energies than shown in figure 2.3. In particular, for simple transmission measurements, the InSb detector has been used to wavelengths as short as 900 nm. This allows the InAs and Ge detectors to be skipped, resulting in less time spent realigning the optics. All of the detectors except the Si detector are cooled with liquid nitrogen to reduce the dark current.

Mirrors are used as focusing elements instead of lenses to provide wavelength independent focusing. The toroidal mirrors provide one to one focusing, while the elliptical mirror reduces the beam spot to concentrate it on the detector. For the infrared polarization experiments, a BaF_2 double wire-grid polarizer with an average combined extinction ratio of ~ 10^4 is used to polarize the probe beam. The energy resolution used ranged from ~ 0.02 eV at 1.4 eV to ~ 0.001 eV at 0.1 eV. Improving the resolution by a factor of two showed no changes in the measured spectra except for a sharpening of the interference fringes arising from internal reflections within the sample.

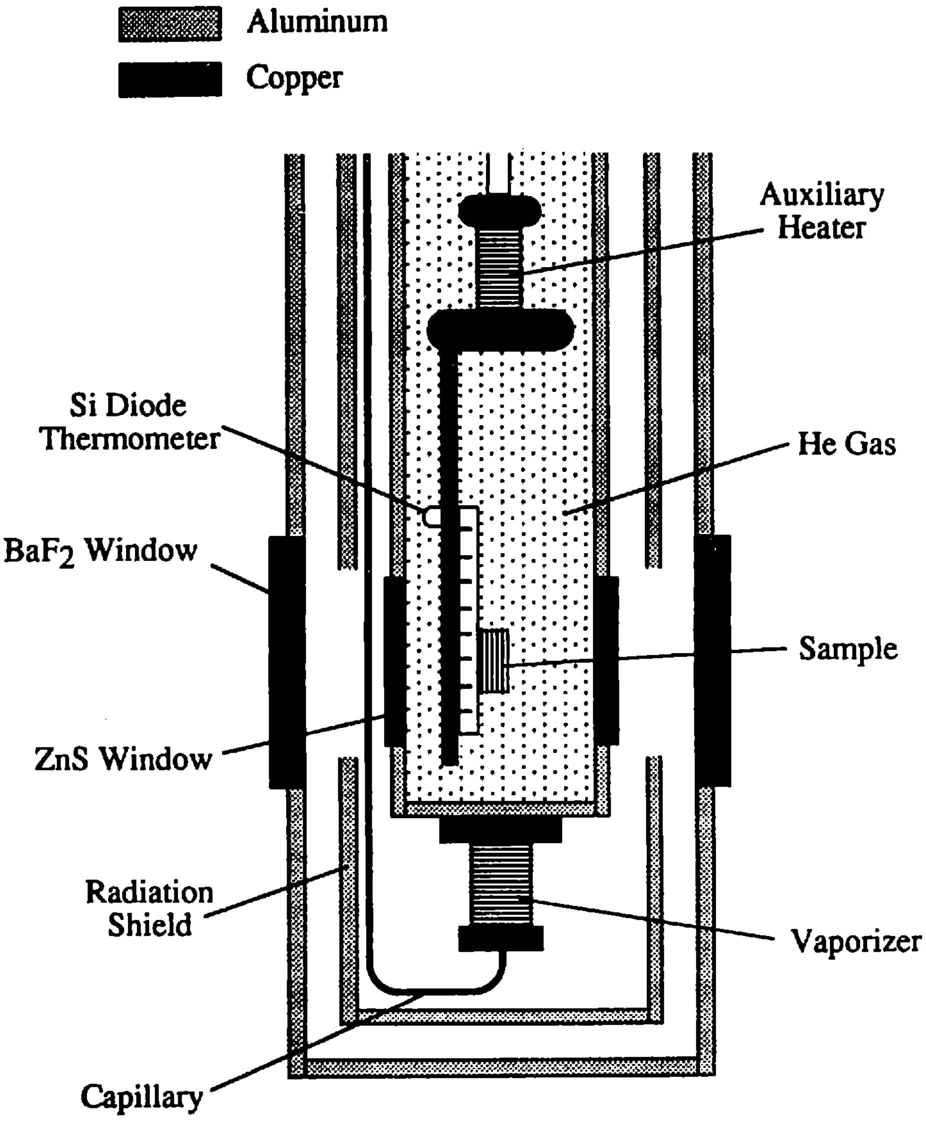

Figure 2.4: Conceptual drawing of the tail of the Janis Model 10DT Supervaritemp Optical Cryostat used for these transmission experiments.

The placement of the chopper before the diffraction grating is essential for work in the infrared. If the chopper is placed after the monochromator, the black body radiation from the case of the monochromator, which is also collected by the detector, will be modulated. Although the ceramic glow bar used for measurements below ~ 0.4 eV is hot compared to the monochromator case, only a small slice of the power is sent down beam path. The HgCdTe detector is sensitive enough to the room temperature black body radiation that if the chopper is placed after the diffraction grating the modulated signal due to the non-diffracted room temperature black body radiation will be an order of magnitude larger than that due to the dispersed probe beam. It is important that all the modulated light be wavelength resolved.

Figure 2.4 shows a conceptual drawing of the tail of the Janis Supervaritemp dewar used. The central sample space is thermally isolated by a vacuum space between the BaF_2 and the ZnS windows. Liquid He flows down the capillary tube to a wire coil heater where it is vaporized. The resulting cold He gas flows past the sample and cools it. A Si diode thermometer mounted on the copper sample block measures the temperature. An additional heater exists above the sample block but it is not used. The samples themselves are poor thermal conductors and for transmission measurements only their edges touch the small copper mounting plates used. Furthermore, a plastic chip carrier separates the small copper mounting plate from the large copper sample block on the probe. All of this results in poor thermal coupling, through the sample mounting, of the sample and large copper sample block on the probe. Therefore no heat is applied through the auxiliary heater. All temperature control is accomplished by heating the He gas at the vaporizer. The copper sample block on the probe and the sample both come to equilibrium with the He gas. A standard Lakeshore temperature controller is used to maintain the desired temperature. This setup allows the temperature to be varied from ~ 5K to 300K. For measurements above room temperature a small oven with quartz windows is used in place of the dewar.

Normalization of Data

All of the optical components used have wavelength dependent transmission or reflection. To determine the transmission of the sample two spectra are taken. The transmission is simply the detector signal with the sample in place divided by the detector signal with the sample removed. For the thin film samples a bare substrate is used for the reference. Sample and normalization spectra are taken one right after the other. The only change made is to move the sample either in to or out of the beam path. The top panel of figure 2.5 shows the measured detector signal as a function of wavelength for a $Sr_2CuO_2Cl_2$ sample and the corresponding normalization scan. The strong dip at ~ 4250 nm is an H_20 absorption due to the water in the air. The absorption coefficient calculated from this data is shown as a function of energy in the bottom panel of figure 2.5. The strong water line is at ~ 0.29 eV and is barely visible in the normalized spectra. The pronounced periodic oscillations, which are interference fringes due to the thickness of the sample, demonstrate the high quality of the sample surfaces and facilitate determining the sample thickness. The resolved fringes also clearly show that the width of the absorption peak just above 0.35 eV is not resolution limited. The thickness is given by:

$$d[\mu m] = \frac{1.24}{2\sqrt{\varepsilon_1}}\left(\frac{1}{\Delta E[eV]}\right), \tag{2.6}$$

where ΔE is the period of oscillation. In La_2CuO_4, the optical dielectric constant below the charge transfer gap is $\varepsilon_1 \sim 5$ [15,16,19]. For $Sr_2CuO_2Cl_2$, the measured interference fringes combined with mechanical thickness measurements allow determination of the optical dielectric constant at $\varepsilon_1=3.6\pm0.4$.

The expected size of the interference fringes can be estimated by explicitly considering the multiple internal reflections. For an absorbing dielectric slab the intensity transmission is given by:

$$T = \frac{(tt')^2 e^{-\alpha d}}{\left|1-(r')^2\left(e^{i2kd}\right)e^{-\alpha d}\right|^2}. \tag{2.7}$$

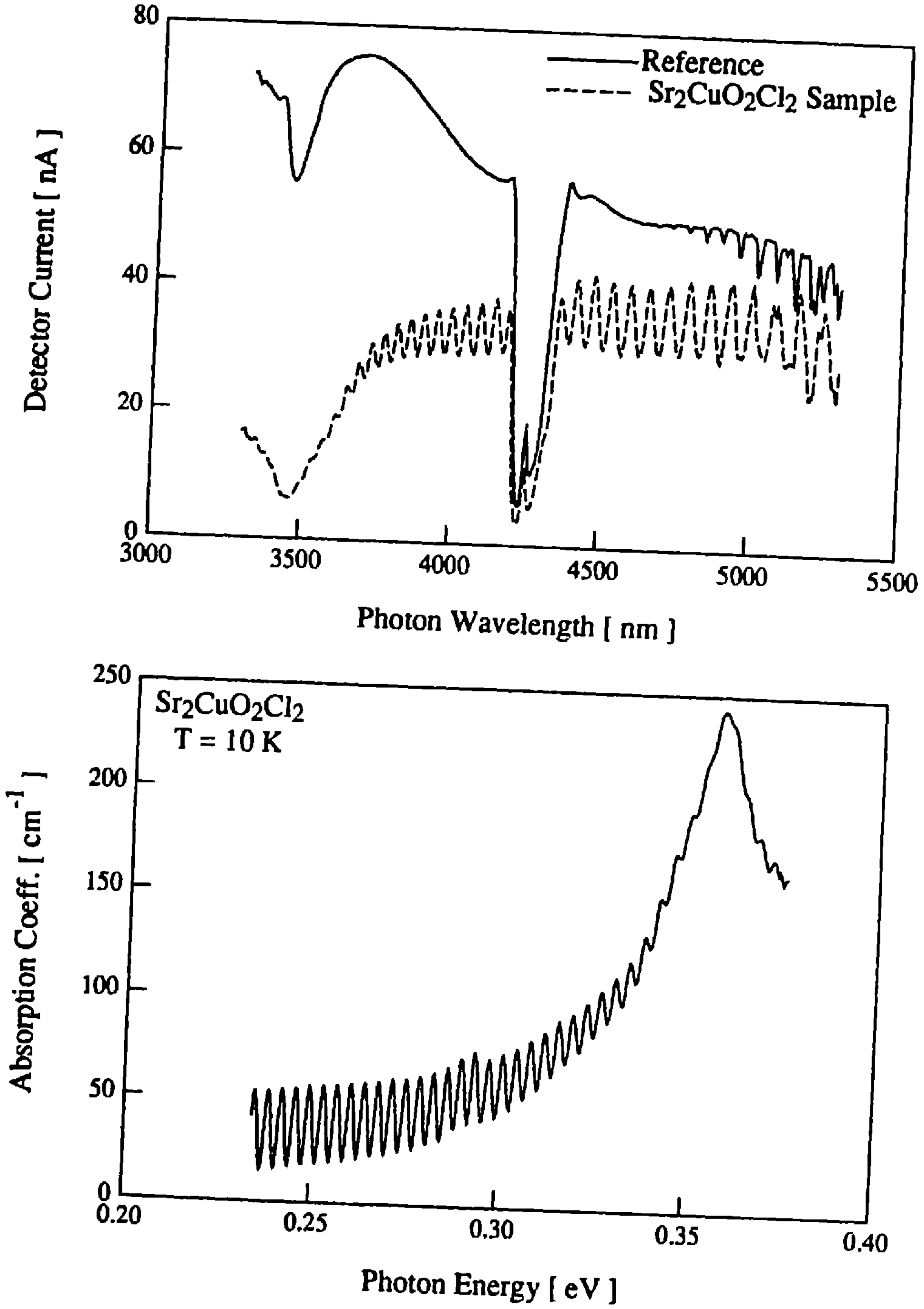

Figure 2.5: Top: Detector signal vs. probe wavelength for both a $Sr_2CuO_2Cl_2$ sample and the associated reference scan. The large dip at ~ 4250 nm is an H_2O absorption. Bottom: The corresponding absorption coefficient vs. photon energy. The periodic oscillations are interference fringes which facilitate determining the sample thickness. The strong H_2O absorption at ~ 0.29 eV is barely evident in the normalized spectra.

The electric field amplitude transmission from air to dielectric is t, from dielectric to air, t', and the internal reflection is r'. For plane waves normally incident on a dielectric slab, the values are:

$$t = \frac{2}{1+\sqrt{\varepsilon}} \qquad t' = \frac{2\sqrt{\varepsilon}}{1+\sqrt{\varepsilon}} . \qquad r' = \frac{\sqrt{\varepsilon}-1}{\sqrt{\varepsilon}+1} \tag{2.8}$$

The resulting intensity transmission is given by:

$$T = \underbrace{\frac{16\varepsilon}{\left(1+\sqrt{\varepsilon}\right)^4}}_{(1-R)} e^{-\alpha d} \frac{1}{\left|1 - e^{i2kd}\left(\frac{\sqrt{\varepsilon}-1}{\sqrt{\varepsilon}+1}\right)^2 e^{-\alpha d}\right|^2} . \tag{2.9}$$

A dielectric constant of ε ~ 3.6 yields about 20% reflection from the term labeled (1-R). The oscillatory term e^{i2kd} yields the interference fringes. Using the limiting values of ±1, the magnitude of the fringes is given by:

$$|\Delta\alpha| \approx 4\left(\frac{\sqrt{\varepsilon}-1}{\sqrt{\varepsilon}+1}\right)^2 e^{-\alpha d} . \tag{2.10}$$

Using ε = 3.6 to calculate the front surface reflection losses and evaluate equation 2.10 the low energy fringes in figure 2.5 should be about 36 cm^{-1} high, which is in agreement with the data. When the oscillatory term in equation 2.9 is zero, the internal reflections have no effect on the transmission. Hence, the mid points of the oscillations give the natural line shape.

After collecting the data and calculating the absorption coefficient for each scan segment, the different segments must be patched together to form one absorption spectra. Due to the small lateral dimensions of the samples studied the probe beam is partially apertured. Typically this rejects less than 10% of the probe beam. This aperturing appears as a wavelength independent offset in the absorption coefficient. Slight variations in the position of the sample between scans results in offsets between the overlapping scans. Enough of a spectral overlap is measured to make it clear the spectra are simply shifted with respect to each other. Therefore, the separate scans are patched together with additive corrections in the absorption coefficient which is the same as a multiplicative correction in the transmission. The uncertainty of the correct zero as for the entire spectrum as well as the wavelength independent reflection losses are removed by the linear background subtraction described in Chapter 3.

Photo-induced absorption measurements

The photo-induced absorption measurements presented in Chapter 6 may be separated into two distinct types, time-resolved and non-time-resolved measurements. For the non-time-resolved measurements the sample is pumped with an Helium-Neon laser which is chopped with a mechanical shutter at 5 Hz. This modulates the absorption of the film at 5 Hz. If the probe beam is chopped at ~ 400 Hz, the induced absorption will appear as a 5 Hz modulation of the amplitude of the 400 Hz signal. If a short time constant is used on the lock-in amplifier which extracts the 400 Hz signal, then a second lock-in amplifier can extract the 5 Hz variation in the output of the first lock-in amplifier. Since the relevant quantity is $\Delta T/T$ and both signals are proportional to the probe beam intensity, the measurement is self normalizing and no normalization scan needs to be taken. This set up is very convenient because it allows the induced absorption to be measured while scanning the wavelength of the probe beam. This type of measurement was used to determine the probe energy dependence of the photo-induced absorption.

For the time-resolved photo-induced absorption measurements, the probe beam wavelength is fixed. All the data reported in this thesis were taken at a probe wavelength of 1750 nm using the InAs detector. The wavelength of 1750 nm corresponds to the peak in the induced absorption in the Nd_2CuO_4 films at ~ 0.7 eV. This is a particularly easy spectral range in which to do time-resolved photo-induced absorption. The InAs detector has a large enough band gap that a DC probe beam may be used. However, it is not very sensitive to the visible pump . Nevertheless it is important to prevent scattered laser light from getting into the detector. In particular, light scattered by the sample is focused onto the detector by the collection mirror. A filter must be used. A particularly convenient setup is to use a prism monochromator as a tunable band pass filter. The transient responses were recorded using a Nicolet digital oscilloscope in a signal averaging mode. Signals were averaged till an acceptable signal to noise ratio was observed. The times for this ranged from several seconds to several hours depending on the pump intensity and repetition rate, as well as the sample temperature.

Chapter 3: Absorption Spectra for Undoped Single Crystals

This chapter presents and discusses the data which forms the core of this thesis. Optical absorption experiments were conducted on single crystals of four undoped lamellar copper oxides: La_2CuO_4, Nd_2CuO_4, Pr_2CuO_4 and $Sr_2CuO_2Cl_2$. As discussed in Chapter 1, these materials all have two-dimensional CuO_2 layers, but with differing out-of-plane structures. Hence, it will be natural to associate common absorption features with excitations of the CuO_2 plane. For uniaxial crystals there are three distinct polarizations, as shown in figure 3.1[38]. The electric field is parallel to the CuO_2 plane in both the α and σ-polarization. In the π-polarization, it is perpendicular to the layers. Optical transmission spectra were obtained in the photon energy range 0.1 to 2 eV. All four materials were measured in the α-polarization. Additional La_2CuO_4 samples were polished perpendicular to the layer for σ and π-polarized measurements. The sample thickness (~ 10-200 μm) was determined both by mechanical measurements and when possible from the observed interference fringes. Consistent thicknesses are obtained for an optical dielectric constant of $\varepsilon = 5$ for La_2CuO_4 [16,19] . For $Sr_2CuO_2Cl_2$, comparison of the mechanical and optical measurements yields $\varepsilon = 3.6 \pm 0.4$. In the Nd_2CuO_4 and Pr_2CuO_4 samples no interference fringes were observed. The samples measured, their thickness, the growth method and the polarizations used are summarized in table 3.1. The spectra, presented as plots of absorption coefficient

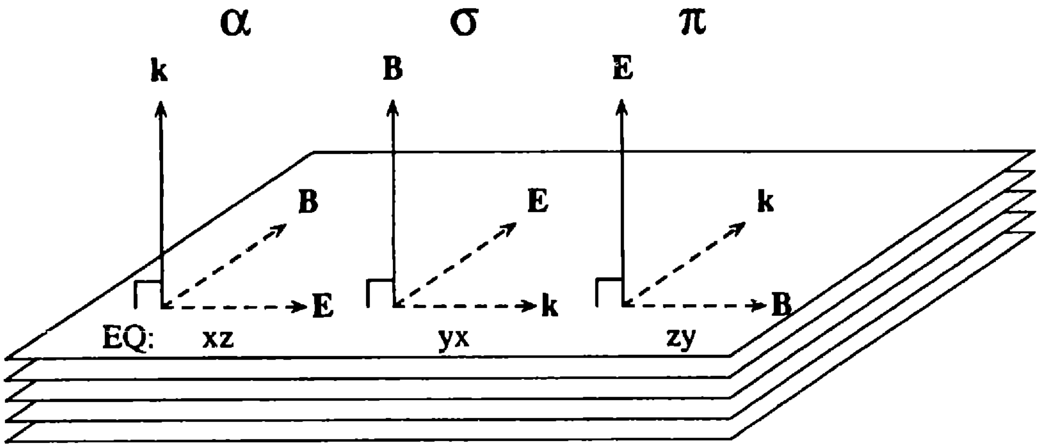

Figure 3.1: The three distinct optical polarizations for a uniaxial crystal. For α and σ-polarization, the electric field lies in the CuO_2 plane, but it is perpendicular for the π-polarization. The dashed axes lie in the plane, the solid axes are perpendicular to the plane. The electric quadruple transformation is listed below each set of axes (see section: Selection Rules for Uniaxial Crystals).

versus photon energy, are derived from transmission measurements as described in Chapter 2. The results of experiments done at T = 10K are presented and discussed first. Then the temperature dependence of the absorption spectra is presented. The discussion in this chapter is restricted to the model-independent conclusions which can be drawn from the data. Previous reflectivity experiments including those of Uchida *et al* [17] shown in figure 1.10 show that the mid-infrared absorption increases with doping. Prior to the experiments presented in this thesis, no optical absorption was expected in the undoped cuprates below the charge-transfer gap at ~ 2 eV and above the phonons at ~ 100 meV. The 2-magnon Raman spectra shown in figure 1.9 are peaked at about 3000 cm^{-1} or 0.37 eV but show scattering and hence excitations up to ~ 7000 cm^{-1} or ~ 0.87 eV. However, these excitations should not be visible in direct optical absorption experiments.

Material	Sample Name	Thickness [μm]	Growth Method	Polariztions
La_2CuO_4	LCO1	220	Top Seeded Sol'n	α
La_2CuO_4	LCO2	70	Top Seeded Sol'n	σ,π
La_2CuO_4	LCOFZ1	218	Float Zone	σ,π
$Sr_2CuO_2Cl_2$	SCOC1	86	Stoichiometric Melt	α
$Sr_2CuO_2Cl_2$	SCOC2	9	Stoichiometric Melt	α
$Sr_2CuO_2Cl_2$	SCOC3	27	Stoichiometric Melt	α
$Sr_2CuO_2Cl_2$	SCOC5	90	Stoichiometric Melt	α
Nd_2CuO_4	NCOX1	200	Top Seeded Sol'n	α
Pr_2CuO_4	PCO2	50	Top Seeded Sol'n	α

Table 3.1: The thickness and growth method for the samples measured, along with the polarizations in which measurements were made.

Absorption Spectra at 10K.

As Measured Absorption Spectra.

Figure 3.2 shows the absorption coefficients for the four materials in the α-polarization as a function of photon energy, measured at 10K. Common absorption features are seen in the range 0.2 to 0.7 eV. The absorption coefficient is weak, roughly 10^3 times smaller than in heavily doped samples [17]. The features below ~ 0.15 eV are associated with optic phonons [14]. The additional narrow lines present in the Nd- and Pr_2CuO_4 spectra arise from intra-f-shell transitions [39], which are electric-dipole allowed as the rare-earth sites do not possess inversion symmetry. Such transitions are the basis for Nd:YAG lasers. The σ and π-polarized spectra for La_2CuO_4 at T = 10K are shown in Figure 3.3. The structure seen in

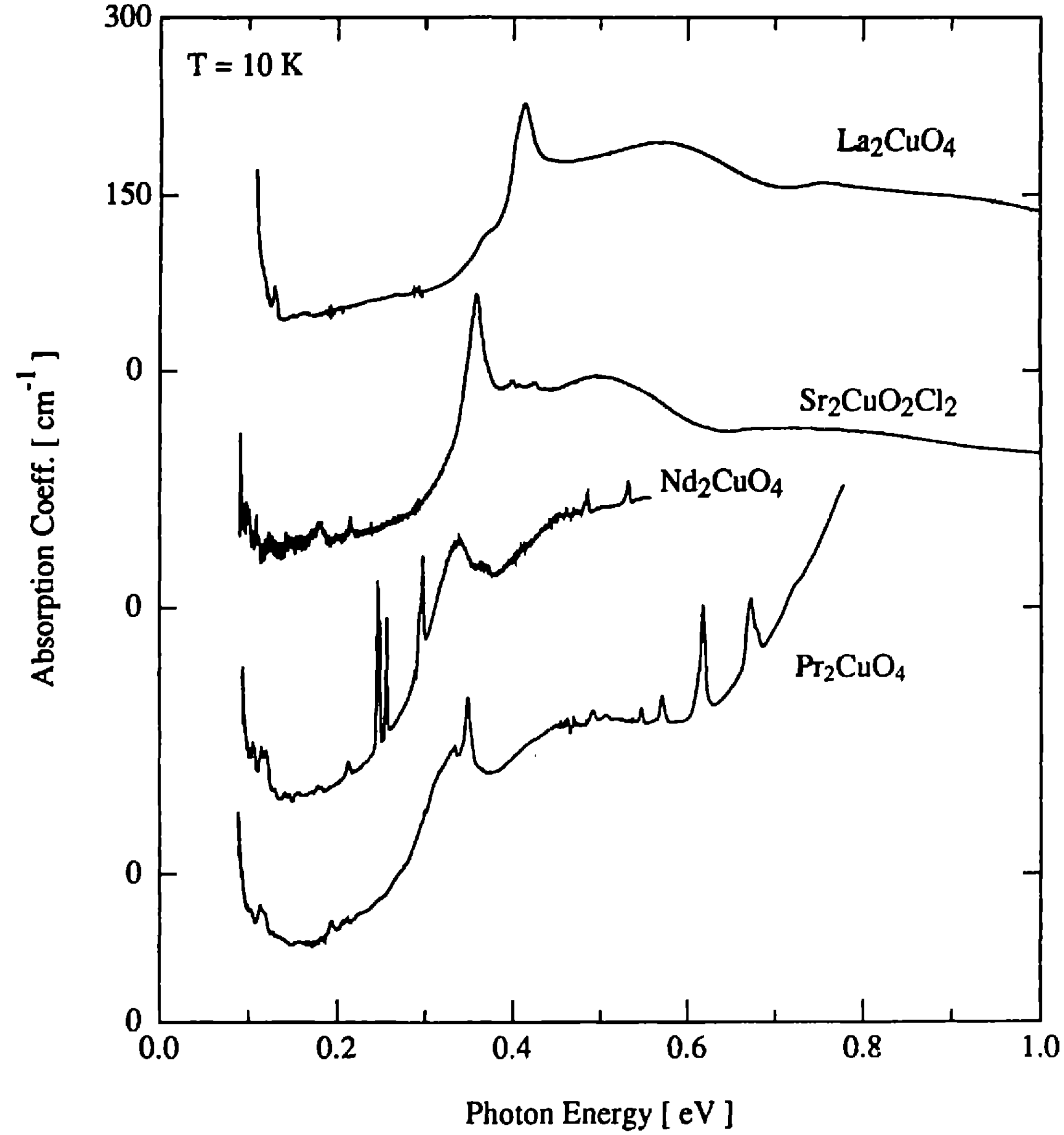

Figure 3.2: Absorption coefficient vs. photon energy in α-polarization for La_2CuO_4, $Sr_2CuO_2Cl_2$, Nd_2CuO_4 and Pr_2CuO_4 at T = 10K. Note the left axis offsets and the intra-f-shell transitions in Nd- and Pr_2CuO_4.

α-polarization appears in σ-polarization, but is absent in π-polarization. Thus, the absorption bands only appear when the electric field vector lies in the CuO_2 layer. For all four compounds, the spectra display a sharp low-energy line centered near 0.4 eV and a set of broader bands extending to higher energies.

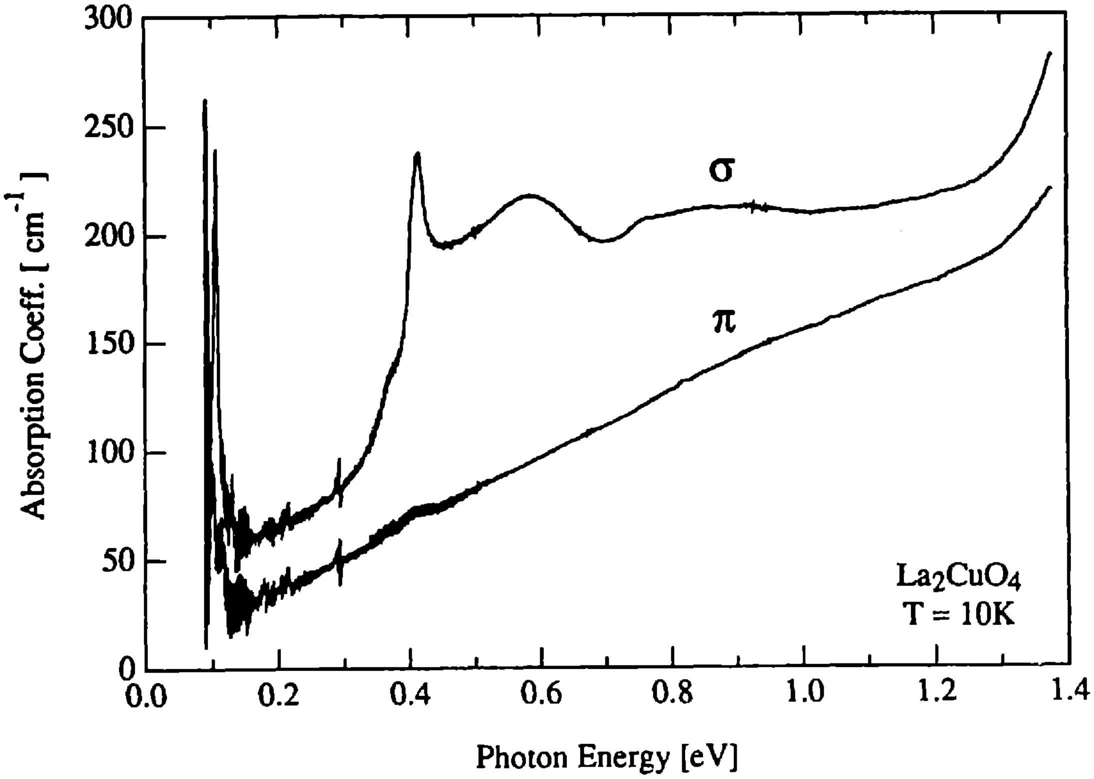

Figure 3.3: La_2CuO_4 absorption coefficient vs. photon energy for σ and π-polarizations at T = 10K. The crystal was grown by the Top-Seeded Solution Growth method.

Figure 3.4 shows the absorption spectra in σ and π-polarization for a La_2CuO_4 crystal grown by the floating zone technique. Figure 3.5 shows this crystal measured with the same energy resolution at photon fluxes differing by a factor of 15. This was accomplished using two different light sources, a tungsten filament lamp and a ceramic glow bar. The standard neutral density filters typically used in the visible have strong absorption features in the spectral range of figure 3.5. The identical spectra, obtained with different probe beam intensities, indicate that the absorption is a single photon process. For a two photon process the absorption coefficient would be quadratic in the incident intensity. In figure 3.4 a small π polarized peak is seen at ~ 0.4 eV. The absence of this peak in figure 3.5 shows that its presence in figure 3.4 is simply due to imperfect alignment of the crystal with respect to the probe beam polarization.

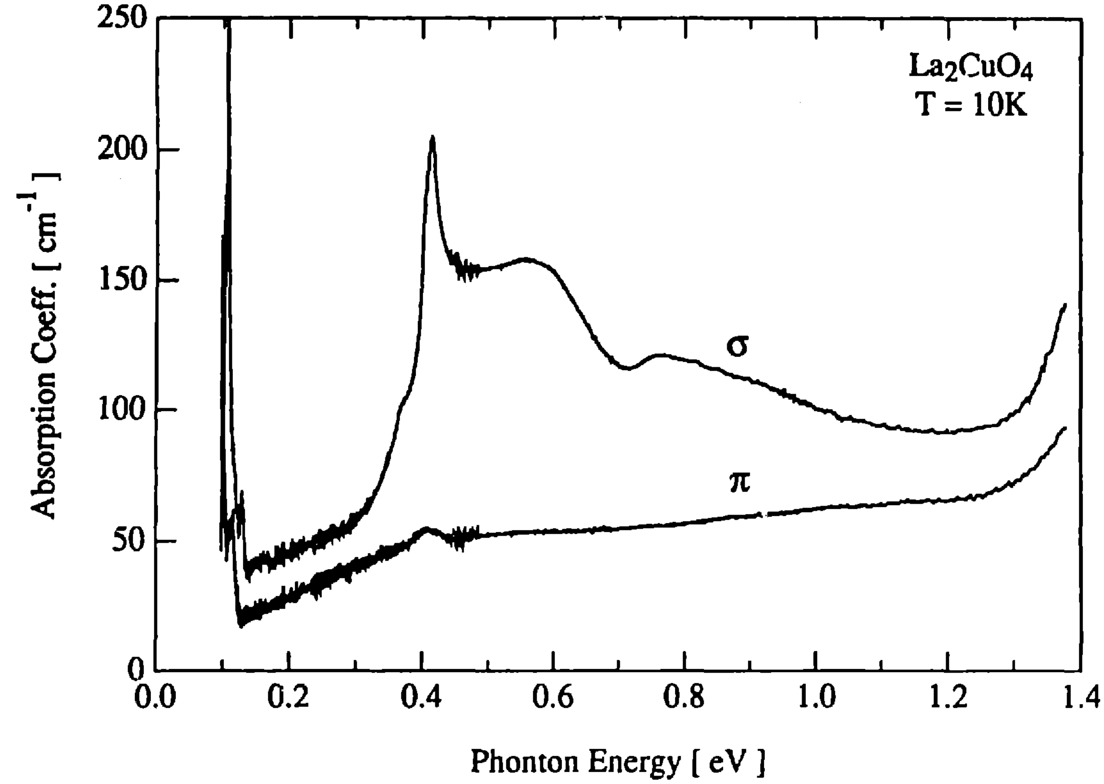

Figure 3.4: La_2CuO_4 absorption coefficient vs. photon energy for σ and π-polarizations at T = 10K. The crystal was grown by the Floating-Zone method.

The absorption spectra for an additional $Sr_2CuO_2Cl_2$ crystal is shown in figure 3.6. This crystal was grown from different starting materials than the crystal shown in figure 3.2. The strong interference fringes demonstrate the high quality of the tape cleaved surface. To look at the stronger absorption present at higher energies, thinner samples of $Sr_2CuO_2Cl_2$ were prepared by cleaving. Figure 3.7 shows the absorption spectra for samples 9 and 27 μm thick. Note that the left axis scale is now thousands of cm^{-1} compared to hundreds of cm^{-1} of the spectra presented so far. The arrow shows the 0.36 eV peak which stands out as the sharpest feature of figures 3.2 and 3.6. The sharp absorption edge at 1.65 eV is the tail of the charge-transfer gap [12]. Of interest to this work is the absorption band between 1.4 and 1.6 eV.

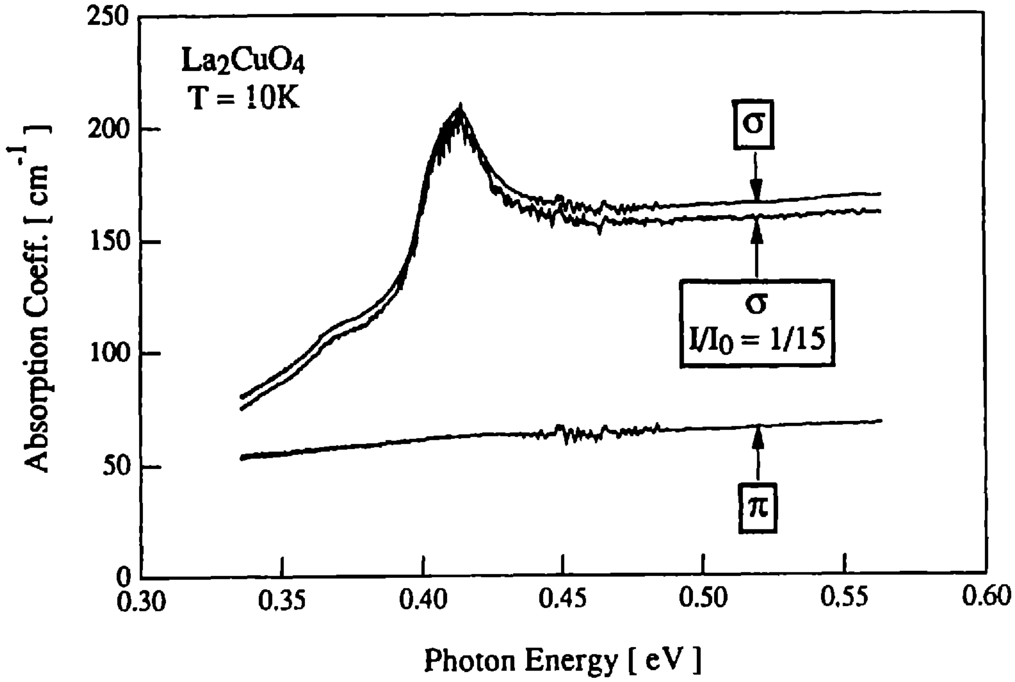

Figure 3.5: La_2CuO_4 absorption coefficient vs. photon energy for σ and π-polarizations at T = 10K. For the two σ-spectra, the probe intensity differs by a factor of 15. In the π spectra, better alignment of the crystal with respect to the beam eliminates the residual peak seen in Figure 3.4, for the same sample.

Background Subtracted Absorption Spectra.

Comparison of the σ and π-spectra for La_2CuO_4 shown in figure 3.3 suggests that a nearly linear, polarization independent, background exists. While not fully understood, this background is believed to be extrinsic in origin. In humid weather the normally reflective surfaces of the $Sr_2CuO_2Cl_2$ crystals tarnish in a few days. The measured absorption spectra of such crystals is dominated by a large linear background, suggesting that the background is largely a surface effect. To more clearly display the absorption features of interest and to facilitate comparison between crystals a linear background is subtracted as shown in figure 3.8. This method is used for all the α-polarized spectra. The σ and π-spectra for the float zone grown La_2CuO_4, shown in figure 3.4, suggest that the π-spectra may provide the best energy dependent background for the σ-spectra. This method of background subtraction is shown in figure 3.9, with an

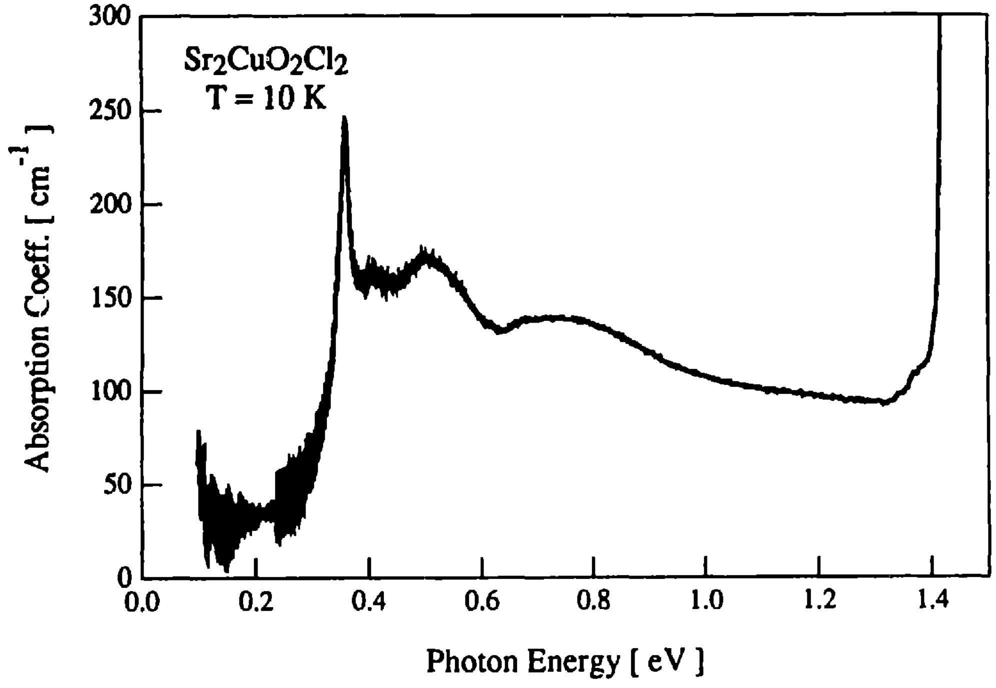

Figure 3.6: Absorption coefficient vs. photon energy in α– polarization at T = 10K for a second $Sr_2CuO_2Cl_2$ crystal. The strong interference fringes demonstrate the high quality of the tape cleaved surface.

additional DC component subtracted to pull the flat region around 0.2 eV to zero. This operationally well-defined method is used for all σ-spectra where applicable. In the as measured spectra shown in figures 3.2 through 3.6 the desired spectra dominate the background in the α and σ-polarizations. Furthermore, the analysis of the spectra presented in Chapter 4, which is based primarily on the absorption peak energies and the polarization dependence, is not sensitive to the background subtraction.

Figure 3.10 shows α, σ, and π background subtracted spectra for La_2CuO_4 at T = 10K. Identical features are seen in α and σ but not π-polarization, indicating an electric dipole absorption process, as will be discussed in the next section. The σ polarized absorption spectra of a float zone and a top seeded solution grown crystal of La_2CuO_4 are compared in panel (a) of figure 3.11. Panel (b) compares two $Sr_2CuO_2Cl_2$ crystals grown from different starting materials in α polarization. As the impurity species and concentration, although low, clearly vary between the measured samples, the observed sample-to-sample

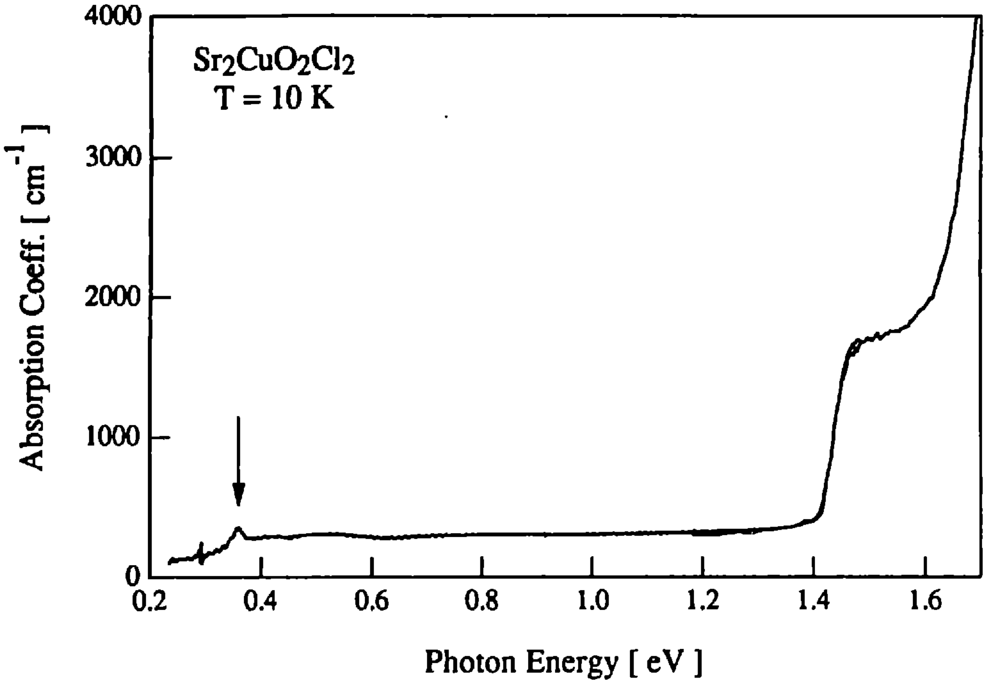

Figure 3.7: $Sr_2CuO_2Cl_2$ absorption coefficient vs. photon energy in α-polarization at T = 10K. Two samples, 27 and 9 μm thick, were measured from 0.2 to 1.5 and 1.2 to 1.7 eV respectively. An absorption band is seen at ~1.5 eV. The tail of the charge-transfer absorption edge begins at 1.65 eV. The arrow indicates the sharp, 0.36 eV, peak shown in Figures 3.2 and 3.6.

uniformity indicates that these excitations must be intrinsic. Further evidence that these excitations are intrinsic will be presented in Chapter 4, when joint exciton-magnon absorption is discussed. The $Sr_2CuO_2Cl_2$ comparison shown in figure 3.11 (b) is expanded about the low energy peak in figure 3.12. The interference fringes are particularly strong in one sample.

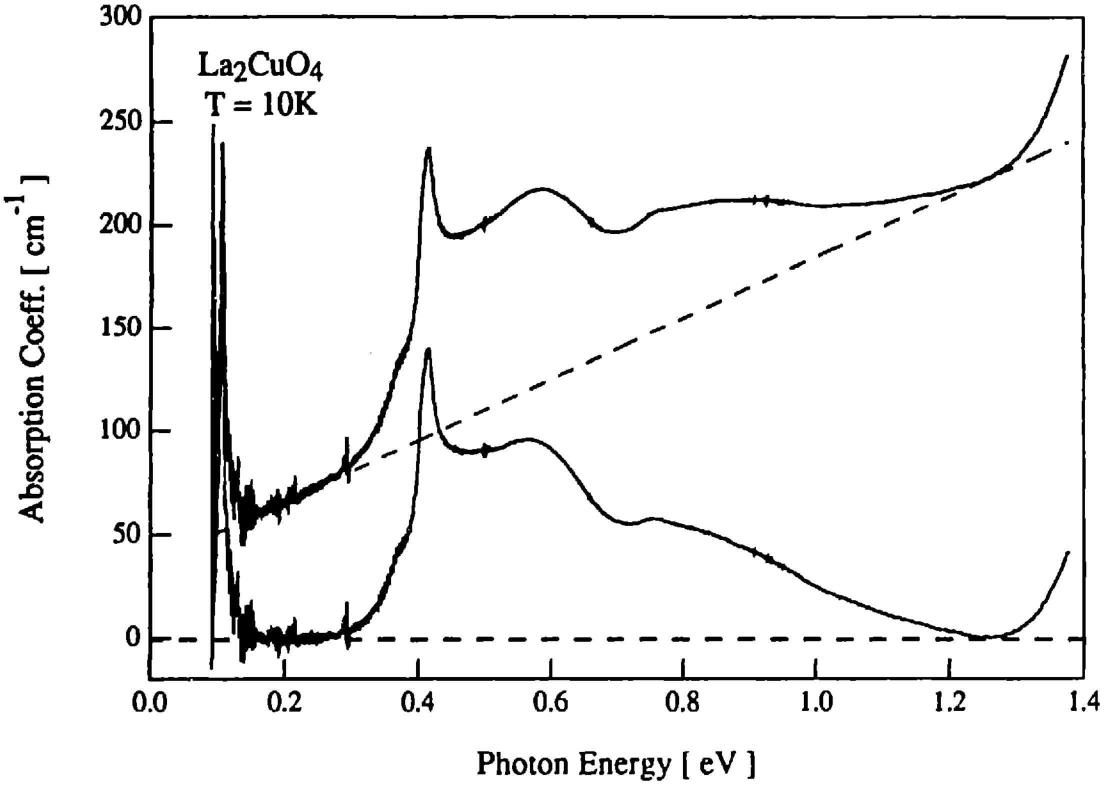

Figure 3.8: La_2CuO_4 absorption coefficient vs. photon energy in α-polarization at T = 10K. A linear background is subtracted. to more clearly display the structure near 0.5 eV.

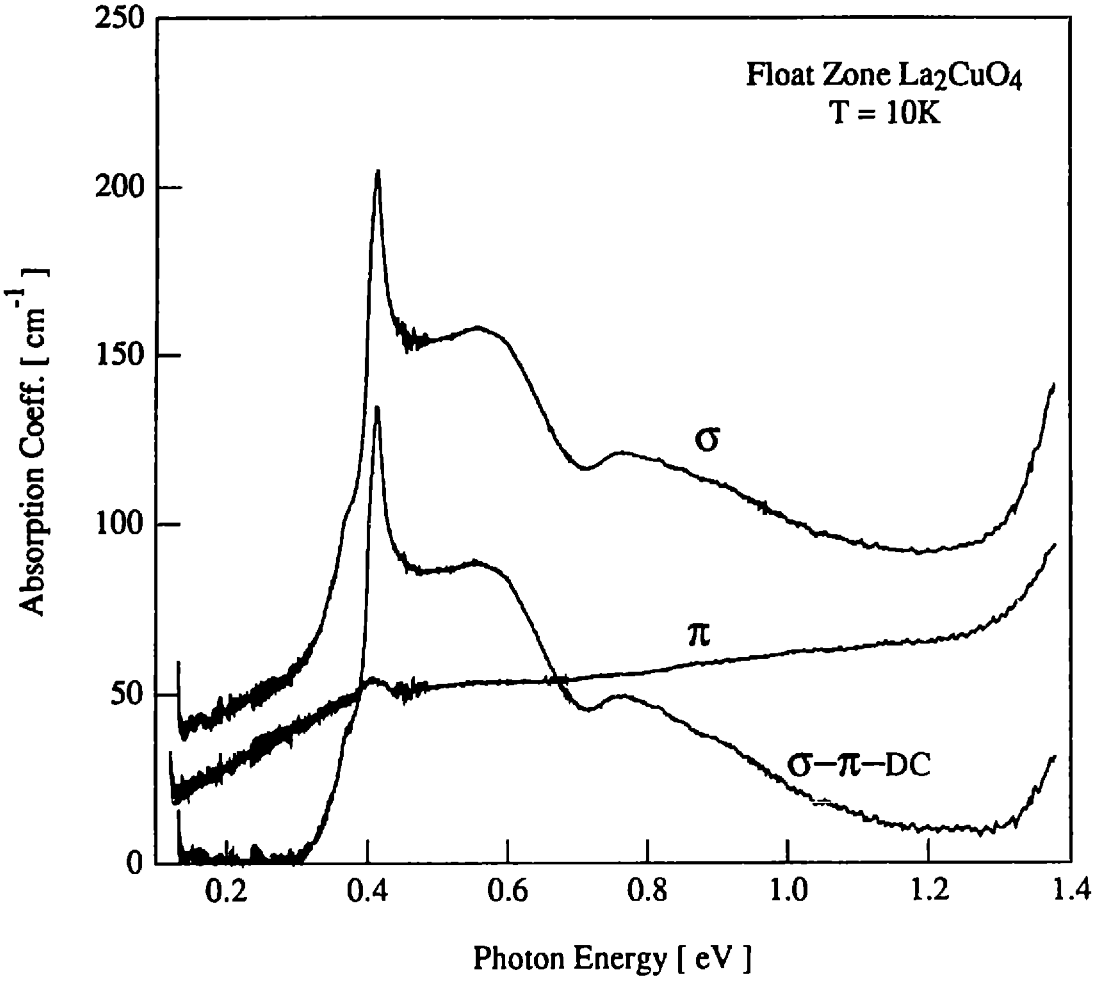

Figure 3.9: La_2CuO_4 absorption coefficient vs. photon energy in σ and π-polarization at T = 10K. The π-spectra plus a DC offset is used as the background for the σ-spectra.

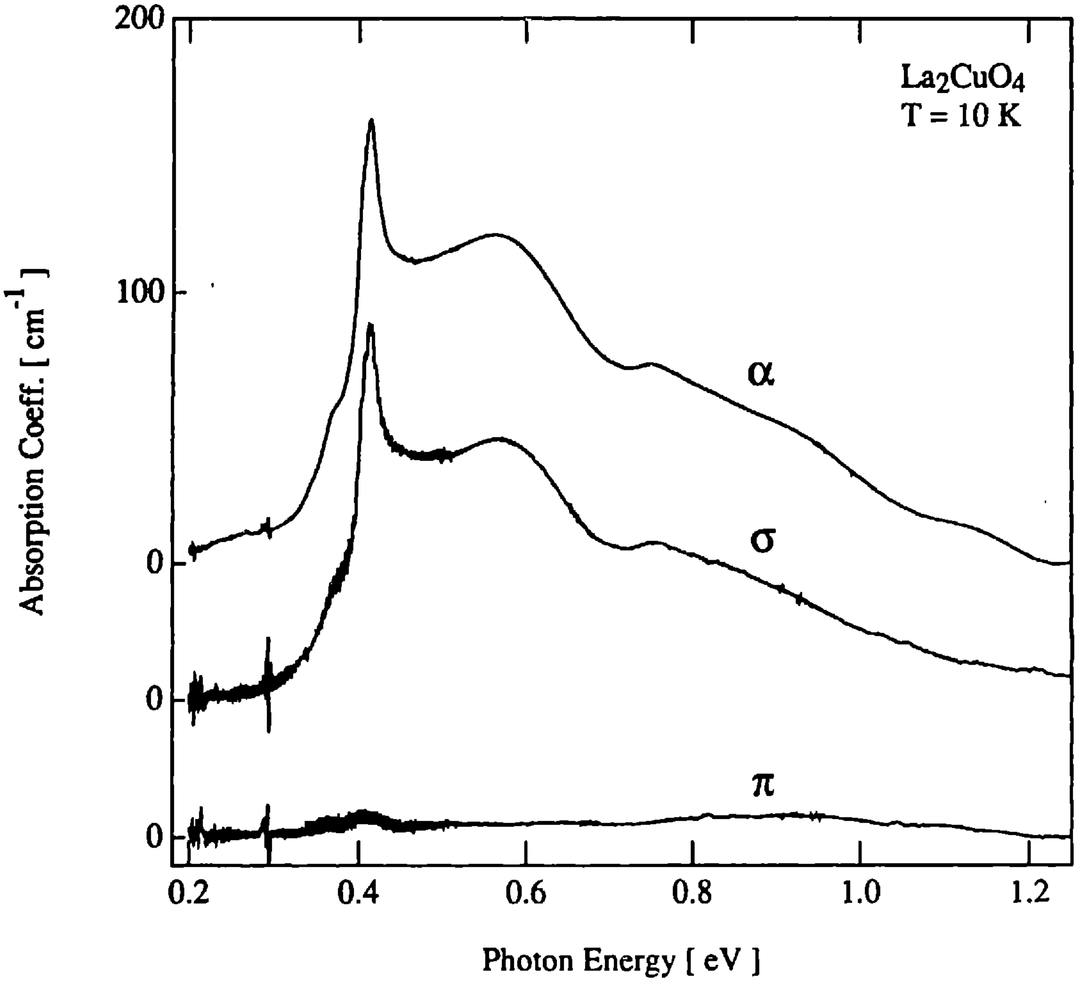

Figure 3.10: La_2CuO_4 absorption coefficient vs. photon energy for α, σ, and π-polarizations, after subtracting the linear background. The additional σ–trace (dashed line) is for a floating-zone grown crystal. The apparent structure at the top of the sharp peak in the σ-polarized spectra arises from the interference fringes in the π-polarized spectra used to subtract the background as shown in figure 3.9.

Selection Rules for Uniaxial Crystals.

For uniaxial crystals, measurements in the three distinct polarizations α, σ and π (see figure 3.1) can distinguish between electric dipole and magnetic dipole or electric quadrupole absorption processes. This can be understood quite simply. Treating the incident light as a classical perturbation, Fermi's Golden rule gives the absorption cross section for one photon absorption as:[40]

$$\sigma = \frac{4\pi^2\hbar}{m_e^2\omega}\frac{e^2}{\hbar c}\left|\langle f|e^{i\vec{k}\cdot\vec{r}}\vec{\varepsilon}\cdot\vec{p}|i\rangle\right|^2\delta(E_f - E_i - \hbar\omega) \tag{3.1}$$

The selection rules are determined by the matrix element between the initial and final state $< f|e^{i\bar{\mathbf{k}}\cdot\bar{\mathbf{r}}}\,\bar{\varepsilon}\cdot\bar{\mathbf{p}}|i >$, ε is the electric field polarization, **k** the wave vector, **p** and **r** the electron momentum and position. Expanding the exponential yields:

$$\langle f|e^{i\vec{k}\cdot\vec{r}}\vec{\varepsilon}\cdot\vec{p}|i\rangle = \underbrace{\langle f|\vec{\varepsilon}\cdot\vec{p}|i\rangle}_{\substack{\text{Electric}\\ \text{Dipole}}} + i\langle f|(\vec{k}\cdot\vec{r})(\vec{\varepsilon}\cdot\vec{p})|i\rangle \tag{3.2}$$

The first term generates electric dipole absorption. The second term contains magnetic dipole and electric quadruple absorption. This is clearer when the second term is rewritten as:

$$\langle f|(\vec{k}\cdot\vec{r})(\vec{\varepsilon}\cdot\vec{p})|i\rangle = \frac{|k|}{2}\underbrace{\langle f|\hat{B}\cdot\vec{L}|i\rangle}_{\substack{\text{Magnetic}\\ \text{Dipole}}} + \underbrace{\frac{im\omega_{fi}}{2}\langle f|(\vec{\varepsilon}\cdot\vec{x})(\vec{k}\cdot\vec{x})|i\rangle}_{\substack{\text{Electric}\\ \text{Quadrupole}}} \tag{3.3}$$

Now the electric dipole, magnetic dipole and electric quadrupole character of the absorption is clear. The polarization dependence of the absorption is determined by the vectors associated with the incident radiation. That is:

$$\begin{array}{c}\text{Electric Dipole} \sim \hat{E}\\ \text{Magnetic Dipole} \sim \hat{B}\\ \text{Electric Quadrupole} \sim \hat{E}\times\hat{k}\end{array} \tag{3.4}$$

For electric-dipole or magnetic-dipole transitions in a uniaxial crystal, the only pertinent directions are parallel to the axis and perpendicular to the axis. This is the same as perpendicular and parallel to the CuO_2 plane. Consider the case of electric dipole absorption. The electric field, **E**, lies in the plane for α and σ and out of the plane for π. If the dipole moment associated with the transition lies in the CuO_2 plane then absorption will occur in the α and σ-polarizations but not in the π-polarization. If the transition dipole moment lies perpendicular to the plane then absorption will occur in π-polarization but not α or σ-polarization. Hence an electric dipole process is characterized by absorption in both α and σ but not π or in π only. Similarly, the polarization dependence of a magnetic-dipole process depends on the direction of the magnetic field, **B**, which lies in the plane for α and π and out of the plane for σ. Hence an magnetic-dipole process is characterized by absorption in both α and π but not σ or in σ only. The product of **E**×**k** governs electric quadrupole absorption. As shown in figure 3.1 this transforms as xz for α and π and as xy for σ. Since the product **E**×**k** is the same in α and π and different for σ, an electric-quadrupole process which is absorbs in α or π will not absorb in σ. The product nature of the electric quadrupole term, E×k, has additional polarization dependence that allows it to be distinguished from magnetic-dipole absorption, but that is not important here. The principle result here is that an absorption process which occurs in α and σ but not π-polarization is an electric dipole process and not a magnetic-dipole or electric-quadrupole process.

Summary

As seen most clearly in figure 3.10, the absorption features appear in α and σ but not π polarization. Hence, it is an electric dipole process polarized along the CuO_2 layers. As previously discussed, figure 3.11 shows that the absorption is intrinsic, not impurity induced. The only common structural element of the four materials studied is the CuO_2 layer. Therefore, we conclude that the observed absorption features are intrinsic electric dipole excitations of the CuO_2 layer. The nature of the absorption mechanism is the subject of Chapter 4.

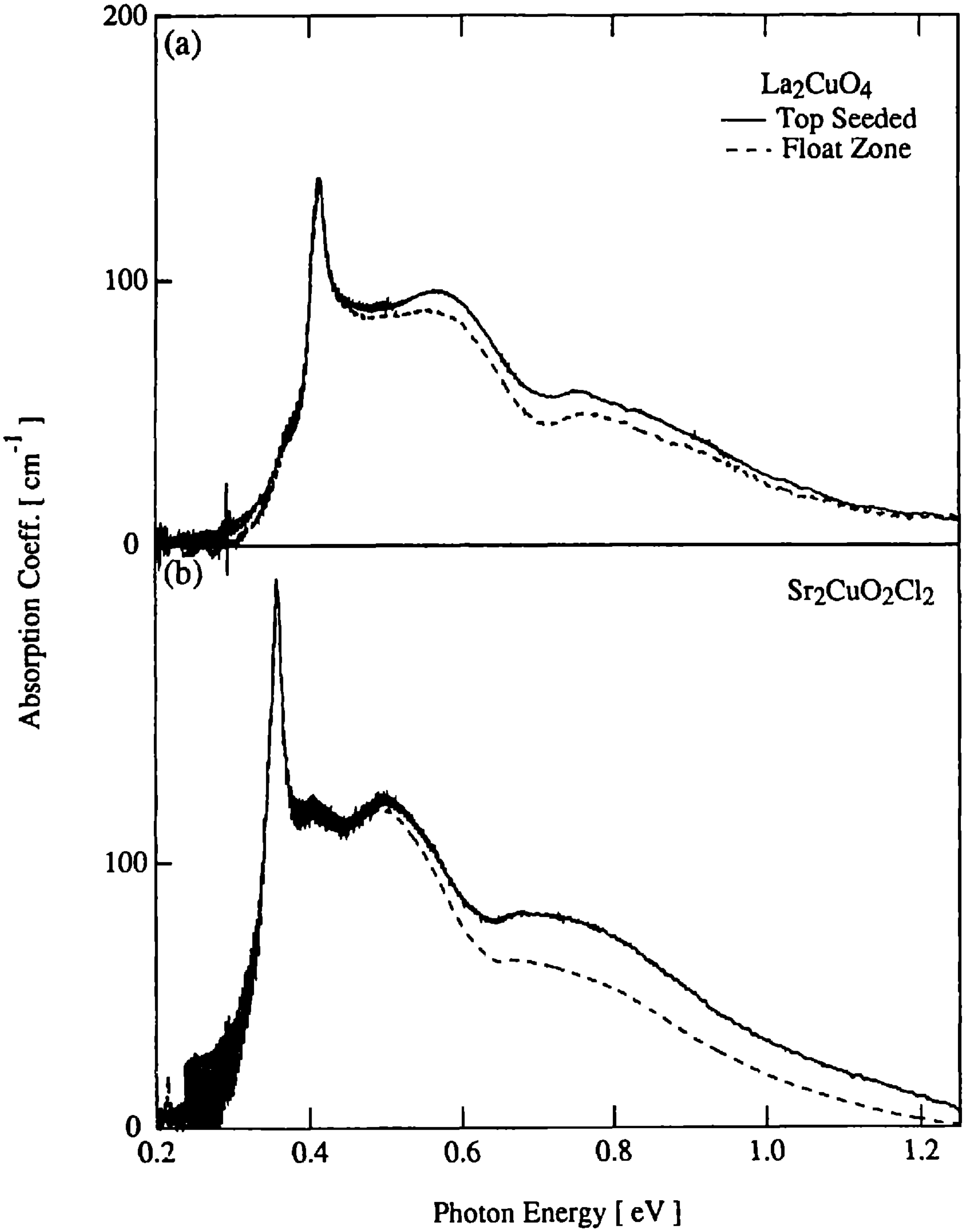

Figure 3.11: Absorption coefficient vs. photon energy at T = 10K for several crystals. Panel (a) compares top-seeded and float-zone grown La_2CuO_4 crystals in the σ-polarization. Panel (b) compares two $Sr_2CuO_2Cl_2$ crystals grown from different starting materials in the α-polarization The difference in the absorption in the $Sr_2CuO_2Cl_2$ crystals at ~ 0.8 eV probably arises from the background subtraction.

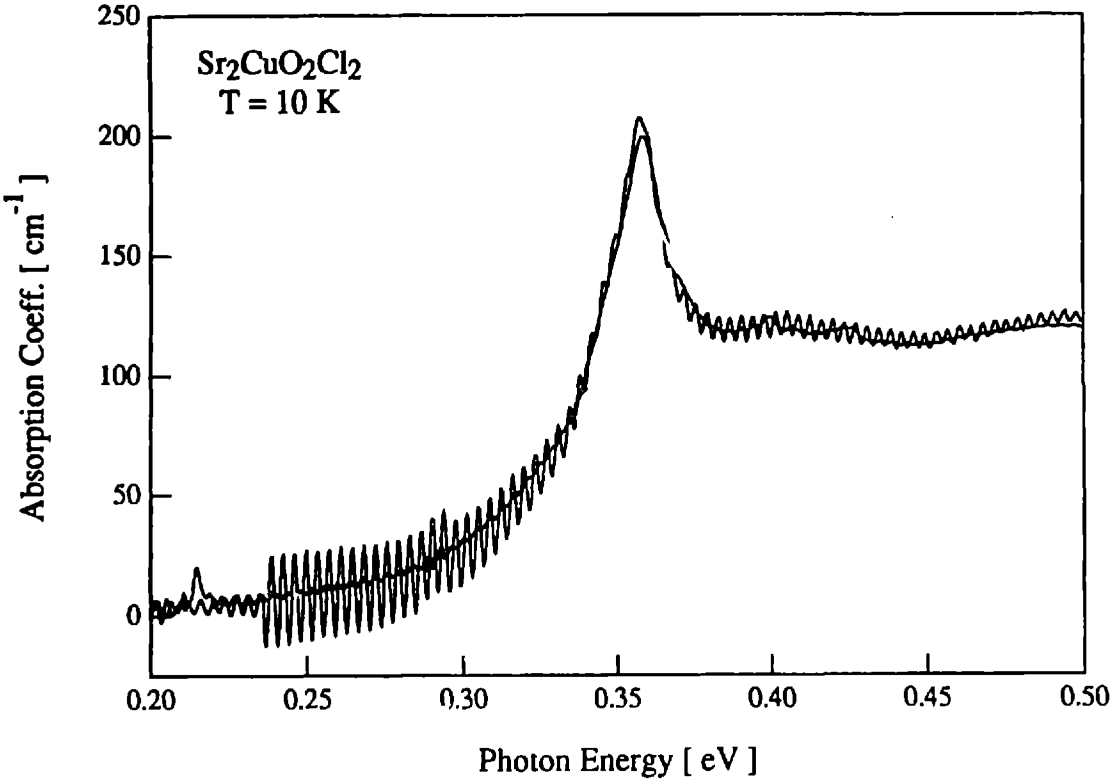

Figure 3.12: Absorption coefficient vs. photon energy at T = 10K for two $Sr_2CuO_2Cl_2$ crystals. This is an expanded view of the same data shown in Figure 3.11.

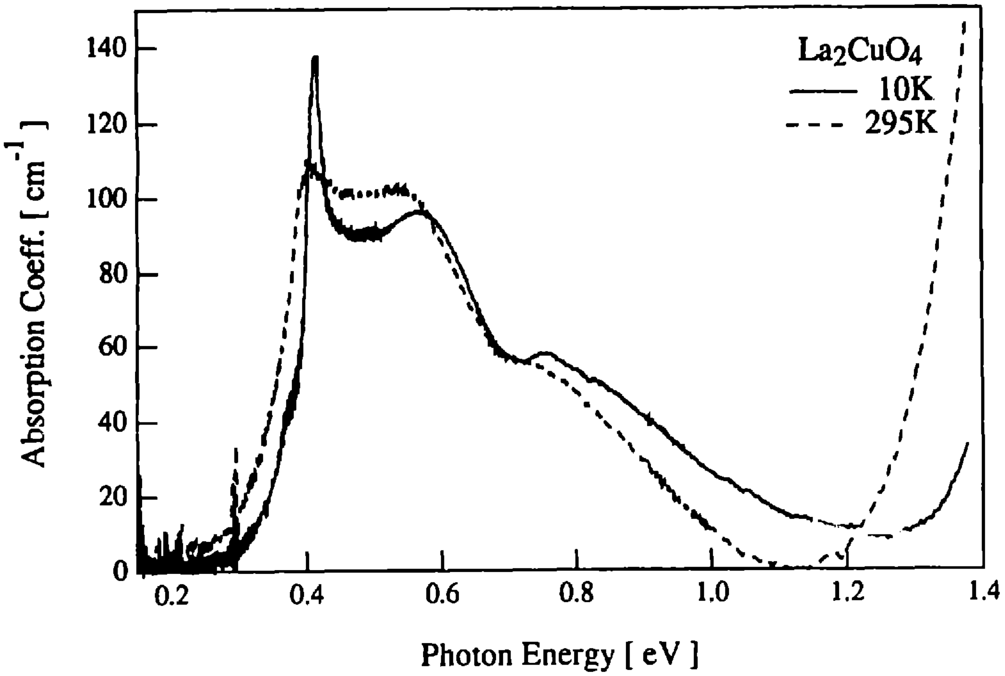

Figure 3.13: La_2CuO_4 absorption coefficient vs. photon energy in σ-polarization at T = 10K and T = 295K. The π-polarized spectra were used as the energy dependent background. An additional DC component was subtracted to set the flat low-energy absorption at ~ 0.2 eV equal to zero.

Temperature Dependence of Absorption Spectra

The temperature dependence of the absorption spectra was studied in La_2CuO_4 and $Sr_2CuO_2Cl_2$ from 10K to 300K. One sample of La_2CuO_4 was also measured in the α-polarization at 400K. No dramatic change in the absorption was seen above the Neel temperature of T_N ~ 325K. Figure 3.13 shows the σ-polarized absorption spectra for La_2CuO_4 at 10K and 300K. An additional full spectrum taken at 90K is essentially identical to the 10K spectra. The low energy peak broadens and shifts to lower energy with increasing temperature. Above the low energy peak the spectra show little temperature dependence except for some filling in just above the peak.

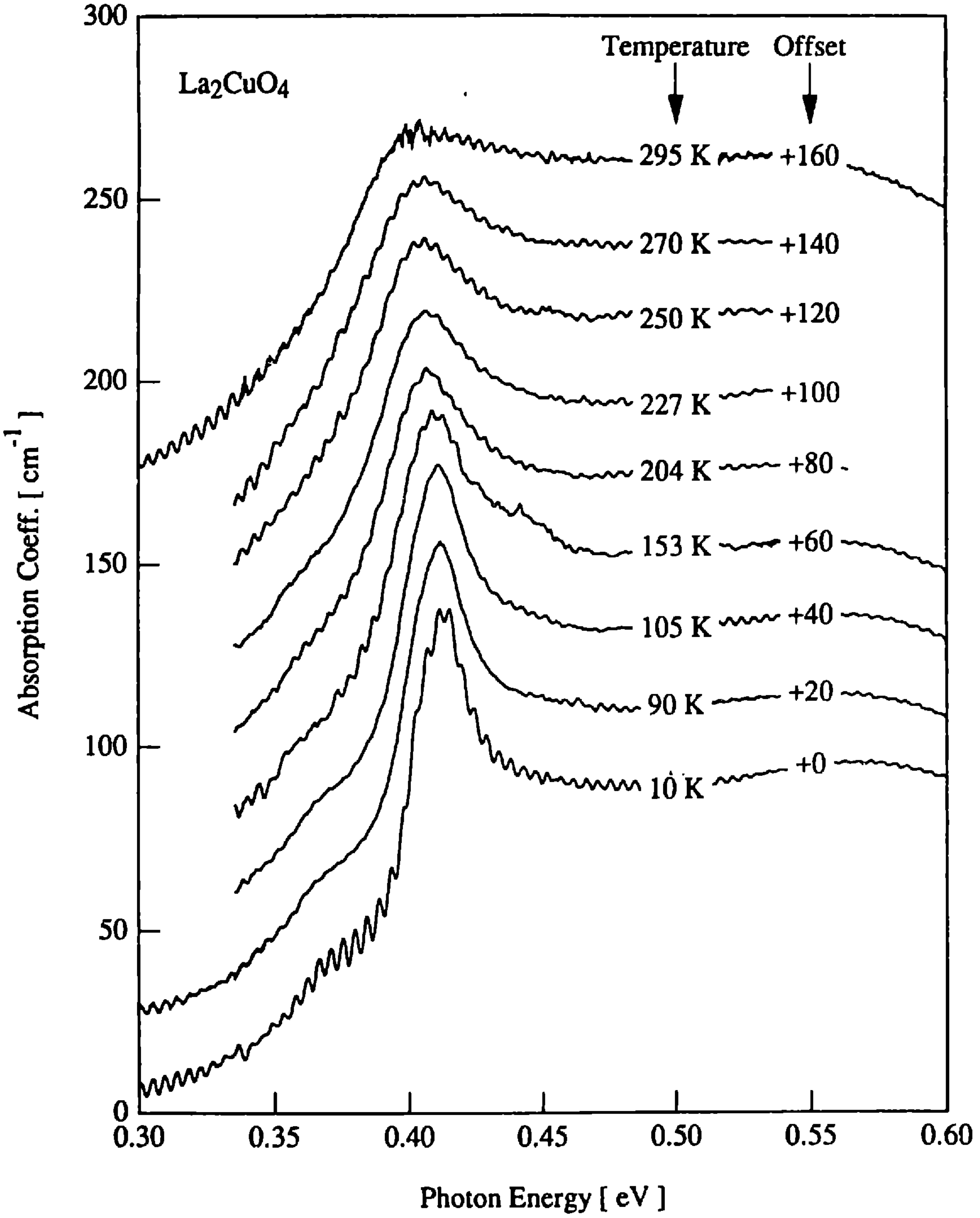

Figure 3.14: La_2CuO_4 absorption coefficient vs. photon energy in σ-polarization at several temperatures. Note the indicated offsets.

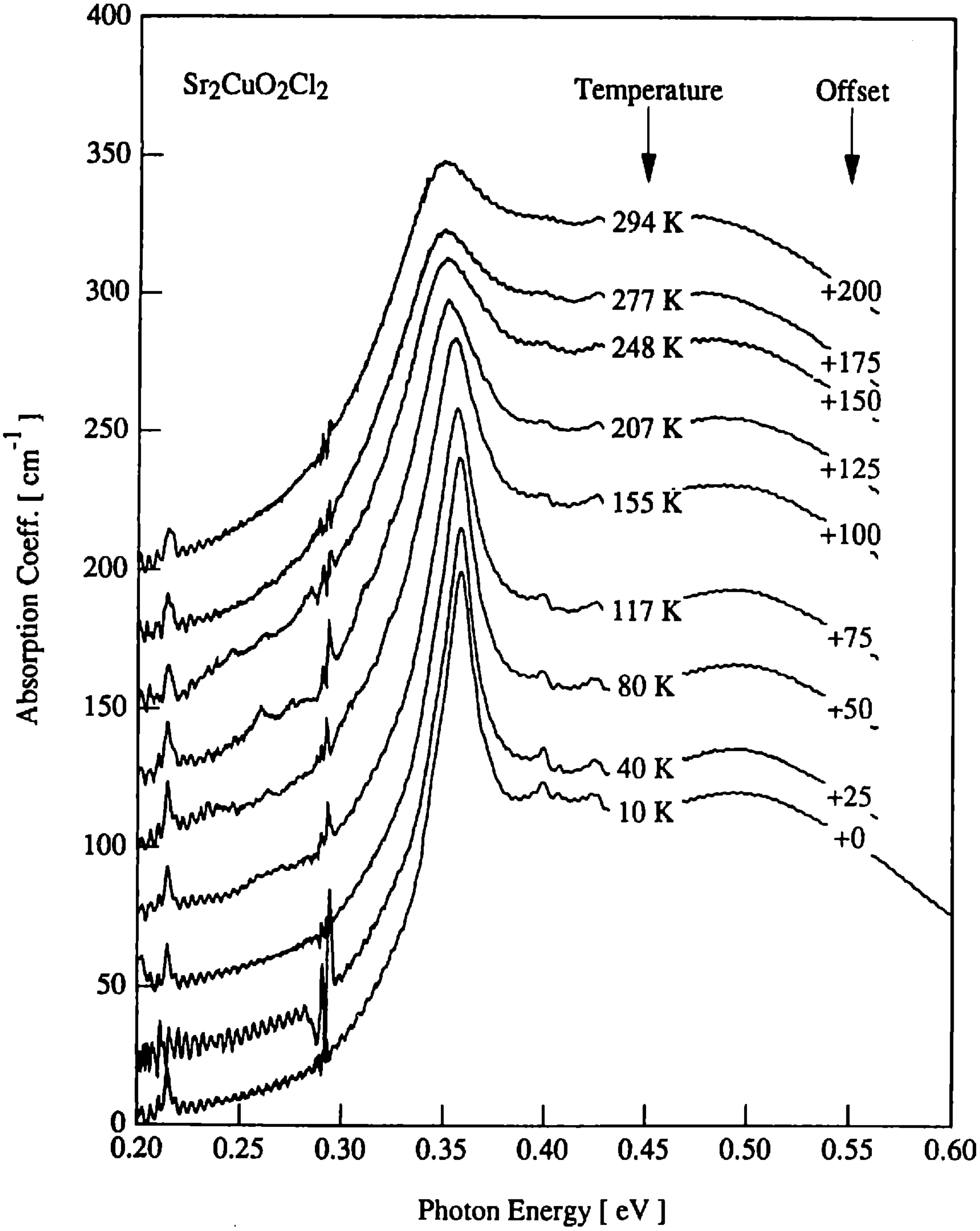

Figure 3.15: $Sr_2CuO_2Cl_2$ absorption coefficient vs. photon energy in α-polarization at several temperatures. Note the indicated offsets.

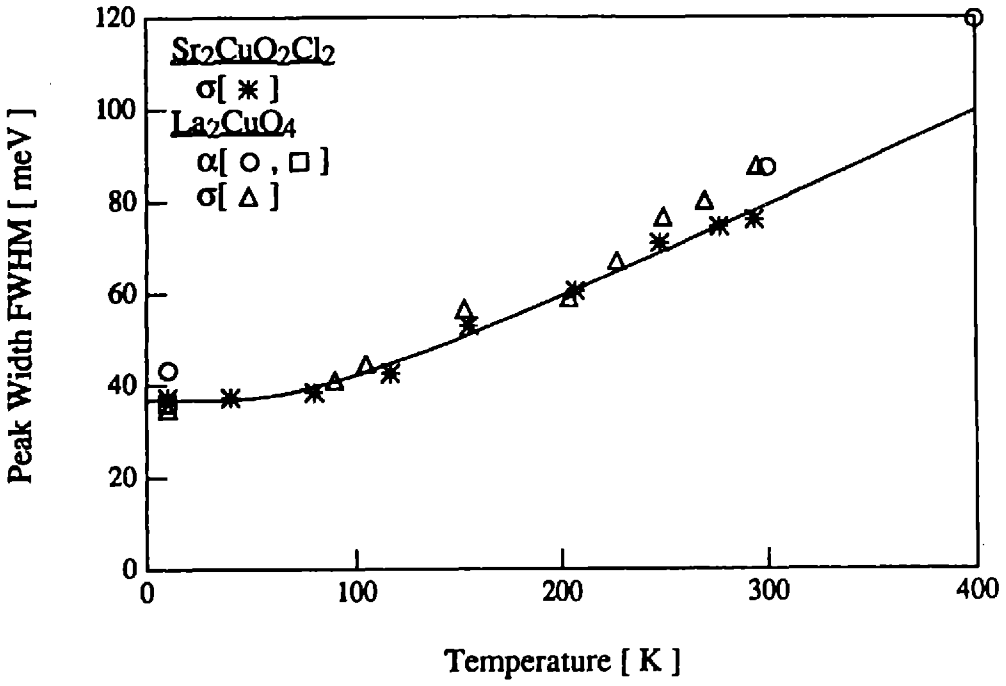

Figure 3.16: FWHM of vs. temperature for ~ 0.4 eV peak in La_2CuO_4 and ~ 0.36 eV peak in $Sr_2CuO_2Cl_2$ The solid line fit is described in the text.

Figure 3.14 shows a series of σ-spectra for La_2CuO_4 from 10K to 295K. Note the offsets used to more clearly display the data. Only the spectra at 10K, 90K, and 295K extend to low enough energy for the π-spectra plus DC background subtraction method to be applicable as previously described. For the other spectra, after subtracting the π-spectra, the DC component is set by matching the spectra to the 10K data at 0.56 eV as suggested by figure 3.13. The evolution with temperature of α-polarized spectra in $Sr_2CuO_2Cl_2$ is shown in figure 3.15. A linear background was subtracted from each spectrum using the slope determined from the 10K spectra. Again the data has been offset for clarity. The weak temperature dependence observed shows that the absorption mechanism does not require thermally generated excitations.

The peak width of the low energy peak was determined by measuring the half-width to the low energy side. This was done by simply taking the energy difference between the location of the peak maximum and the point at which it falls to half of the maximum on the low energy side. Attempts to fit the peak gave inconsistent results which depended strongly on the assumed background.

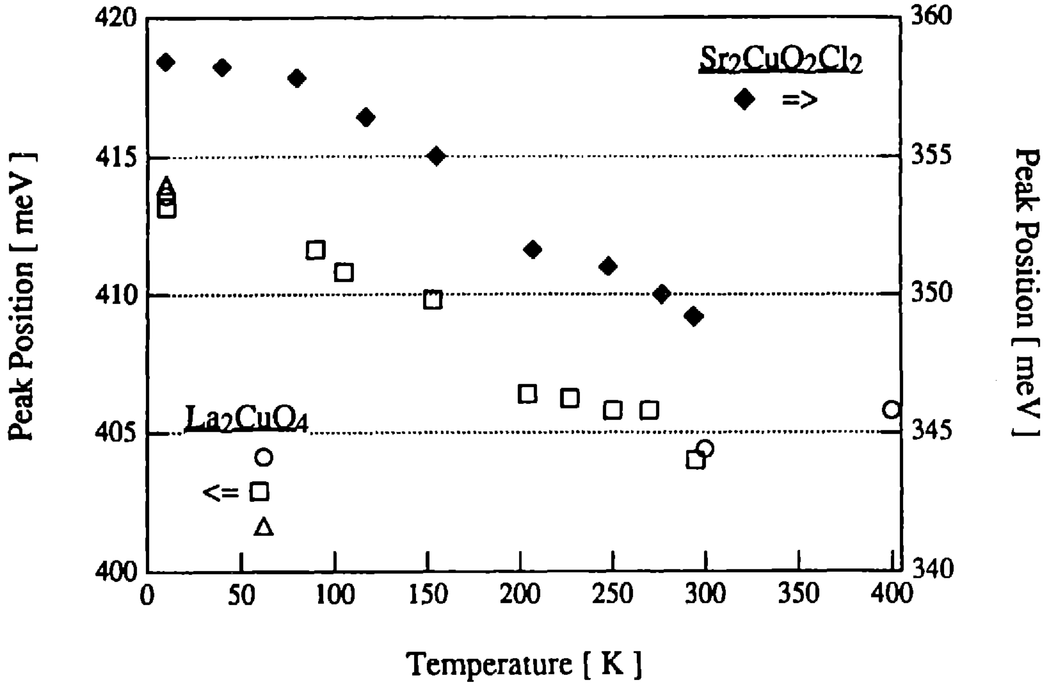

Figure 3.17: Peak position vs. temperature in La_2CuO_4 (left axis) and $Sr_2CuO_2Cl_2$ (right axis).

The empirical peak width is shown for both La_2CuO_4 (open symbols) and $Sr_2CuO_2Cl_2$ (*) in figure 3.16. The peak width and its temperature dependence is the same for both materials. The peak position of the low energy peak is shown in figure 3.17, with the La_2CuO_4 data plotted on the left axis and the $Sr_2CuO_2Cl_2$ on the right. The peak position is roughly 50 meV lower in $Sr_2CuO_2Cl_2$ than La_2CuO_4, but the shift with increasing temperature is about the same.

At the present time the temperature dependence of the low energy peak width is not understood. In Chapter 4, the broad bands above the sharp peak are explained in terms of magnon sidebands riding on a Cu d-d exciton which must be at nearly the same energy as the observed sharp peak. This suggests associating the sharp peak with the bare Cu d-d exciton. However, due to the inversion symmetry of the Cu-site, such transitions are electric dipole forbidden in the absence of symmetry breaking defects. The lack of sample to sample variations in the strength of the peak as shown in figure 3.12 suggests that the absorption is intrinsic and not defect related. Therefore, the electric dipole nature of the sharp absorption peak and hence the associated excitation are not understood. This makes analyzing the temperature dependence difficult. If the excitation is assumed to be a Cu d-d exciton then odd parity phonons, which break the inversion symmetry of the Cu site, can induce decay via the electric dipole emission of a photon accompanied by the creation or annihilation of a phonon. The resulting decay rate and hence the peak width is proportional to (2n+1), where n is the number of thermally excited optical phonons. The solid line shown in figure 3.16 shows the temperature dependence of such a decay fit to the $Sr_2CuO_2Cl_2$ data. The phonon energy from the fit is ~ 20 meV. Appropriate symmetry optical phonons exist at ~ 20 meV in $Sr_2CuO_2Cl_2$ and La_2CuO_4 [14]. Photoluminescence experiments might be able to examine this. The low temperature peak width of ~ 40 meV corresponds to a lifetime of $\tau \leq 10^{-13}$ seconds. Further experiments and analysis are clearly needed to understand temperature dependence of the absorption spectra.

Chapter 4: Magnons, Excitons, and Joint Exciton-Magnon Absorption

---

In chapter 3 the absorption spectra characterizing the mid-infrared absorption in undoped single crystals of lamellar copper oxides were presented. The absorption bands were shown to be weakly allowed, electric dipole excitations of the CuO_2 layers. This chapter begins the explanation of the absorption process. We will see that most features of the spectra can be understood as strong multimagnon sidebands to a dipole forbidden excitation. In particular, the possibility that the dipole forbidden excitation is a Cu d-d exciton will be explored in detail. The results of this analysis will suggest that the actual excitation may be more complex. Joint exciton-magnon absorption was well studied in the 1960's in materials such as MnF_2 [41]. An examination of previous work on exciton-magnon absorption will show magnon side bands to be a common feature of antiferromagnetic insulators. The understanding of the exciton-magnon absorption process gained in this review will then be applied towards explaining the measured absorption in the copper oxide materials under investigation.

Previous Work on Joint Exciton-Magnon Absorption.

Electric dipole exciton-magnon absorption was first seen in MnF_2 by Greene *et al* [41] in 1965. This launched a furor of work, both experimental and theoretical. A review of magnon-sideband

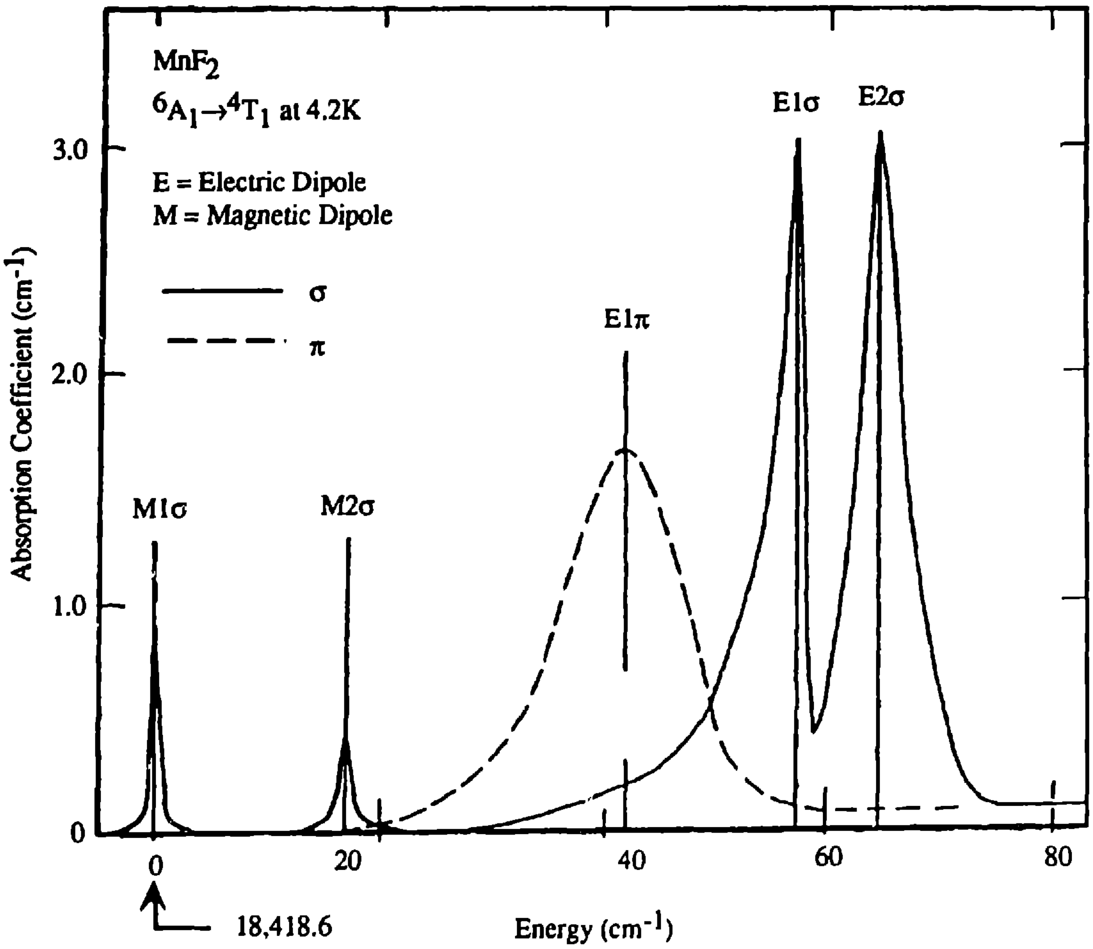

Figure 4.1: Exciton and joint exciton-magnon absorption for ${}^6A_1 \rightarrow {}^4T_1(I)$ excitons in MnF_2 at 4.2 K. From Meltzer et al [13]. The M lines are magnetic dipole exciton transitions and the E lines electric dipole magnon sidebands.

experiments published in 1968 by Sell [42] lists eleven materials in which magnon-sidebands had been identified at that time. They are MnF_2, $KMnF_3$, $RbMnF_3$, $CsMnF_3$, FeF_2, $FeCO_3$, NiF_2, $KNiF_3$, Cr_2O_3, CoF_2, and Rb_2MnF_4. Of these, MnF_2, and Cr_2O_3 have been studied in the greatest detail. A model developed for Rb_2MnF_4, which has the same crystal structure as La_2CuO_4, will be compared to our data in a later section. Several good reviews of exciton-magnon absorption exist, including those by Allen

[38], Tanabe [43,44], McClure [45], and Greene [46]. Of these, the work by Allen, "Optical properties of magnetic oxides" provides the broadest overview.

Figure 4.1 shows exciton and magnon sideband absorption in MnF_2 taken from Meltzer et *al* [13]. The sharp lines labeled M1 and M2 are the excitons seen as magnetic dipole excitations. The broader bands labeled E1π, E1σ, and E2σ are magnon sidebands associated with the excitons M1 and M2. In magnon sideband absorption a single photon is absorbed, simultaneously creating an exciton and a magnon. The mechanism for this will be discussed later. The bare excitons M1 and M2 are at about 18,400 cm^{-1}, or roughly 2.3 eV (1ev $\approx$ 8065 cm^{-1}). Excitons associated with intra d-shell excitations of transition metal ions are frequently in the visible. They are responsible for the vivid color of many materials, such as Ruby, which is Al_2O_3 doped with Cr. Consideration of the sidebands in the copper oxide materials being studied will put the exciton energy at about 0.4 eV. This would be surprisingly low for a Cu d-d exciton. Chapter 5 explores whether the Cu d-d exciton could really be at such a low energy. The magnon sidebands in MnF_2 are roughly 50 cm^{-1}, or 6 meV, above the excitons. In MnF_2 the Heisenberg exchange coupling (J) is ~ 1.2 cm^{-1} or ~ 0.15 meV [42] with a maximum magnon energy of roughly 50 cm^{-1} or ~ 6 meV. In MnF_2, each Mn ion has spin S = 5/2 and eight antiferromagnetically aligned neighbors. In La_2CuO_4 where the S = 1/2 Cu ions have four nearest neighbors and J $\approx$ 130 meV, the maximum magnon energy is 2J or 260 meV [12]. As we shall see, this large value of J and the spin 1/2 nature of the CuO_2 layers result in magnon sidebands which are orders of magnitude stronger and have orders of magnitude larger energy shifts than previously studied materials. Before considering the magnon sidebands themselves, a discussion of excitons in magnetic insulators will be useful.

Excitons in Magnetic Insulators

In the simplest view of an undoped semiconductor, the lowest energy electronic excitation is to promote an electron from the valence band to the conduction band, leaving a hole behind. A lower energy electronic excitation consists of an electron and hole bound together by their coulomb attraction to form an exciton. There are basically two types of excitons. Excitons where the average electron-hole orbits span many lattice sites are called Mott-Wannier excitons. They can be viewed as a conduction band electron and a valence band hole bound together. The binding energy, typically ~ 10 meV, is measured with respect to the creation of a separated conduction band electron and valence band hole. In La_2CuO_4, the creation of a free electron and hole is a charge transfer excitation involving the transfer of an electron from a O 2p orbital to Cu 3d state. As discussed in Chapter 1, the copper is nominally in the +2 charge state, Cu^{++}. This leaves 9 electrons or one hole in the d-shell. Figure 1.2 shows the d-state wavefunctions and their level splitting in cubic and tetragonal symmetries. In the ground state the hole is in the $d_{x^2-y^2}$ state. The excitation of the hole to any of the four other d-states can be viewed as an electron-hole pair located on the same ion. Such tightly bound excitons are called Frenkel excitons. Many of the properties of Frenkel excitons can be understood by thinking about ionic excitations. However, the true exciton states are well described by forming tight binding Bloch waves of localized ionic excitations. In conventional semiconductors, such as GaAs, a conduction band electron and a valence band hole can bind together to form a hydrogenic exciton which spans many lattice sites. The coulomb interaction binding such excitons is screened by the dielectric constant and hence they typically have small binding energies and are called Wannier excitons. In GaAs the exciton binding energy is 4.2 meV. The excitons considered in this work are the tightly bound, ionic excitation like, Frenkel excitons.

Exciton Dispersion

In an antiferromagnet the optical activity and the exciton dispersion depends strongly on whether the exciton is spin-allowed or spin-forbidden. Spin-allowed transitions involve no change in the spin state and hence are not spin blocked as optical transitions. Spin-forbidden transitions involve a change in the spin state and are only optically allowed via the mixing of spin states by the spin-orbit interaction. This is discussed at greater length in Appendix A. The effects of spin on exciton transfer can be understood by studying an ion pair. Consider two ion sites, labeled a and b. Lowercase letters denote the ground state orbital and uppercase letters an excited state for each site. For spin-allowed excitons in a ferromagnetically aligned pair, the ground state, and excitons on sites A and B are given respectively as:

$$\begin{aligned}|gs\rangle &= \left(|a\uparrow(1)b\uparrow(2)\rangle - |a\uparrow(2)b\uparrow(1)\rangle\right)/\sqrt{2}\\ |A\rangle &= \left(|A\uparrow(1)b\uparrow(2)\rangle - |A\uparrow(2)b\uparrow(1)\rangle\right)/\sqrt{2}\\ |B\rangle &= \left(|a\uparrow(1)B\uparrow(2)\rangle - |a\uparrow(2)B\uparrow(1)\rangle\right)/\sqrt{2}\end{aligned} \tag{4.1}$$

The letters denote wavefunctions centered at each ion site, the arrows show the spin orientation and the numbers show the electron number. The coulomb interaction allows hopping of excitons between ion sites with matrix elements given by:

$$\langle B|\frac{e^2}{r_{12}}|A\rangle = \underbrace{\langle a\uparrow(1)B\uparrow(2)|\frac{e^2}{r_{12}}|A\uparrow(1)b\uparrow(2)\rangle}_{\text{Direct or Coulomb}} - \underbrace{\langle B\uparrow(1)a\uparrow(2)|\frac{e^2}{r_{12}}|A\uparrow(1)b\uparrow(2)\rangle}_{\text{Exchange}} \tag{4.2}$$

The first term is the direct term which is often referred to as the coulomb or multipole-multipole term. The second term is an exchange type term. For spin-allowed excitons with ferromagnetically aligned spins neither term is spin blocked. Now consider spin-allowed excitons for an antiferromagnetic pair.

$$\begin{aligned}|gs\rangle &= \left(|a\uparrow(1)b\downarrow(2)\rangle - |a\uparrow(2)b\downarrow(1)\rangle\right)/\sqrt{2}\\ |A\rangle &= \left(|A\uparrow(1)b\downarrow(2)\rangle - |A\uparrow(2)b\downarrow(1)\rangle\right)/\sqrt{2}\\ |B\rangle &= \left(|a\uparrow(1)B\downarrow(2)\rangle - |a\uparrow(2)B\downarrow(1)\rangle\right)/\sqrt{2}\end{aligned} \tag{4.3}$$

$$\langle B|\frac{e^2}{r_{12}}|A\rangle = \underbrace{\langle a\uparrow(1)B\downarrow(2)|\frac{e^2}{r_{12}}|A\uparrow(1)b\downarrow(2)\rangle}_{\text{Coulomb}} - \underbrace{\langle B\downarrow(1)a\uparrow(2)|\frac{e^2}{r_{12}}|A\uparrow(1)b\downarrow(2)\rangle}_{\text{Exchange}} \tag{4.4}$$

The exchange term is spin blocked, that is the spin space overlap integral for both electrons one and two is zero. So, spin-allowed excitons can only hop to antiferromatically aligned neighbors via the direct coulomb

Exciton Type	Spin Alignment Prior to Excitation	
	Ferromagnetic	Antiferromagnetic
Spin Allowed	Coulomb + Exchange	Coulomb Only
Spin Forbidden	Exchange Only	None

Table 4.1: Dependence of exciton dispersion mechanism on exciton type and ion pair spin alignment.

term. These results plus those for spin-forbidden excitons are summarized in Table 4.1 Spin-forbidden excitons can hop to a ferromagnetically aligned neighbor via the exchange interaction. Both the direct term and the exchange term are spin blocked for spin-forbidden transitions in a antiferromagnetic pair. The spin orbit interaction mixes various spin states and will weaken these rules, but this effect will be small.

When discussing exciton-magnon sidebands and possible exciton-magnon bound states it will be important to know if the exciton dispersion is appreciable on the scale of the magnon energies. A simple tight binding model of exciton dispersion will be useful. For a 2D antiferromagnet on a square lattice, such as the spin lattice in La_2CuO_4 the exciton dispersion is governed by the following Hamiltonian:

$$H = \sum_i n_i \varepsilon + \tfrac{1}{4} T_{\alpha\alpha} \left[\sum_{\alpha\alpha'} |\alpha\rangle\langle\alpha'| + \sum_{\beta\beta'} |\beta\rangle\langle\beta'| \right] + \tfrac{1}{2} T_{\alpha\beta} \left[\sum_{\alpha\beta} |\alpha\rangle\langle\beta| + |\beta\rangle\langle\alpha| \right]. \qquad (4.5)$$

The states α and β represent localized ionic excitations on the up and down spin sublattices respectively Here $T_{\alpha\alpha}$, the nearest neighbor intra-sublattice coupling, and $T_{\alpha\beta}$, the nearest neighbor inter-sublattice coupling, allow the ionic excitations to hop from one lattice site to another.

$$\begin{aligned} T_{\alpha\alpha} &= 4\langle \alpha(R) | H | \alpha(R') \rangle \\ T_{\alpha\beta} &= 2\langle \alpha(R) | H | \beta(\tilde{R}) \rangle \end{aligned} \qquad (4.6)$$

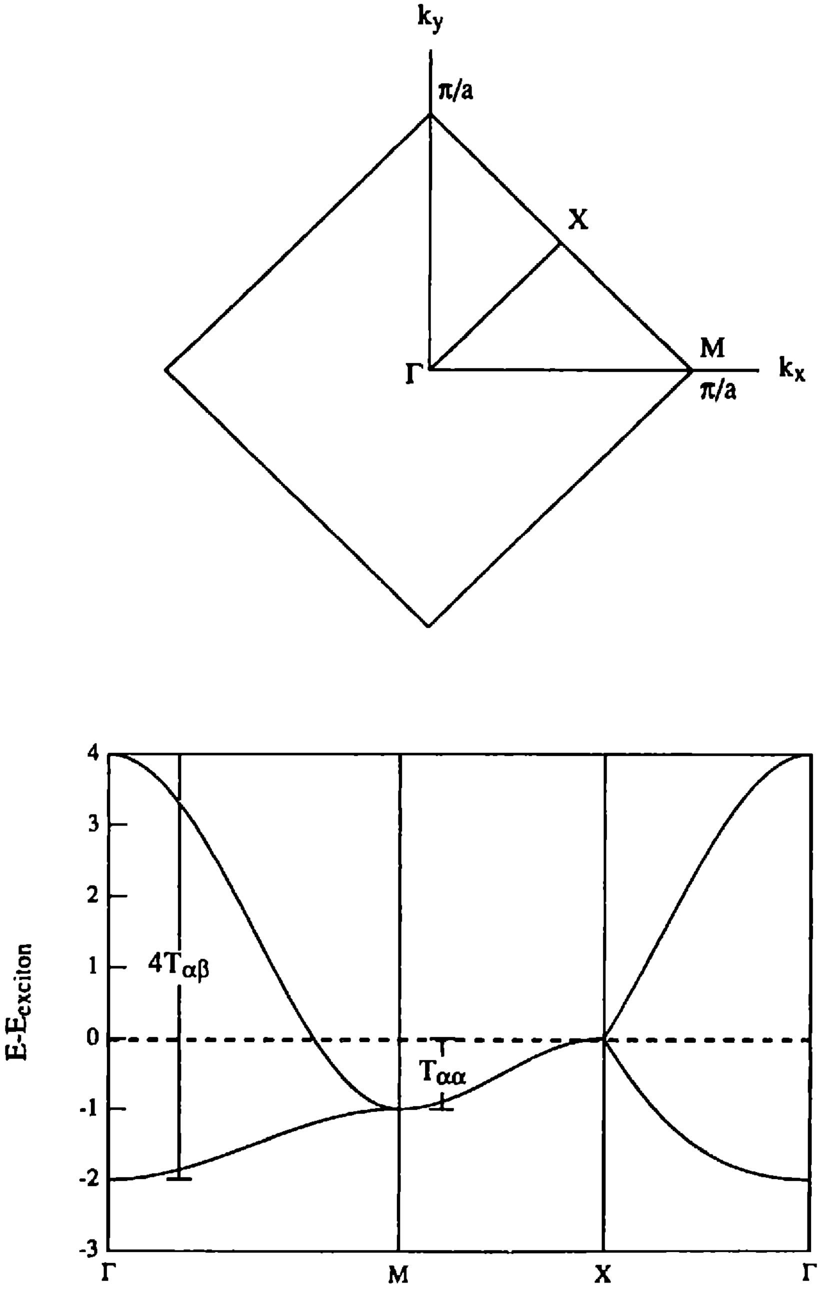

Figure 4.2: Top: Magnetic Brillouin zone for 2D antiferromagnetic copper oxide layers. Bottom: Exciton dispersion for copper site excitons including intra- and inter-sublattice coupling.

The lattice sites R and R' are nearest neighbors on the same sublattice and $\tilde{R}$ a nearest neighbor site on the opposite sublattice. Keeping only nearest neighbor intra- and inter-sublattice couplings yields a conventional tight binding solution.

$$E = \varepsilon + T_{\alpha\alpha} \cos(k_x a)\cos(k_y a) \pm T_{\alpha\beta}\left[\cos(k_x a) + \cos(k_y a)\right] \tag{4.7}$$

This is shown in figure 4.2 The mechanism for single magnon sideband absorption involves the creation of an exciton with a spin flip at one site and a spin flip at a neighboring site. This will be explained in greater detail later. Since the exciton involved includes a spin flip, it is spin-forbidden in the sense of the preceding discussion on exciton dispersion. In La_2CuO_4 the nearest neighbor intersublattice spins are antiferromagnetically aligned and hence $T_{\alpha\beta}$ should be zero. The intra-lattice coupling is expected to be very weak relative to the magnon energies since the diagonal, same spin, Cu sites are not coupled by an intermediate oxygen. Recall that it is the superexchange through the intermediate oxygen which results in the large exchange interaction in the undoped lamellar copper oxides and hence high magnon energies. Hence, for the one magnon sidebands ignoring the exciton dispersion should be a reasonable approximation. For spin-allowed excitons, which may play a role in multimagnon sidebands both intra- and inter-sublattice coupling exists and the existence of direct coulomb coupling may yield appreciable dispersion.

In Cr_2O_3, which is antiferromagnetic, there are four Cr ions per unit cell. This yields four sublattices and hence two pairs of sublattices which are ferromagnetically aligned. As shown in table 4.1 this allows inter-sublattice coupling for spin-forbidden excitons. As seen in figure 4.2 this yields level splitting at the zone center. Such splitting are called Davydov splittings and have indeed been seen in Cr_2O_3 as shown in figure 4.3 In La_2CuO_4 and related materials, no such splitting is expected.

Magnon Sideband Matrix Elements

In 1965 Tanabe *et al*[47] proposed an off-diagonal exchange mechanism for the experimentally observed electric dipole exciton-magnon sidebands. Off diagonal exchange is simply the exchange

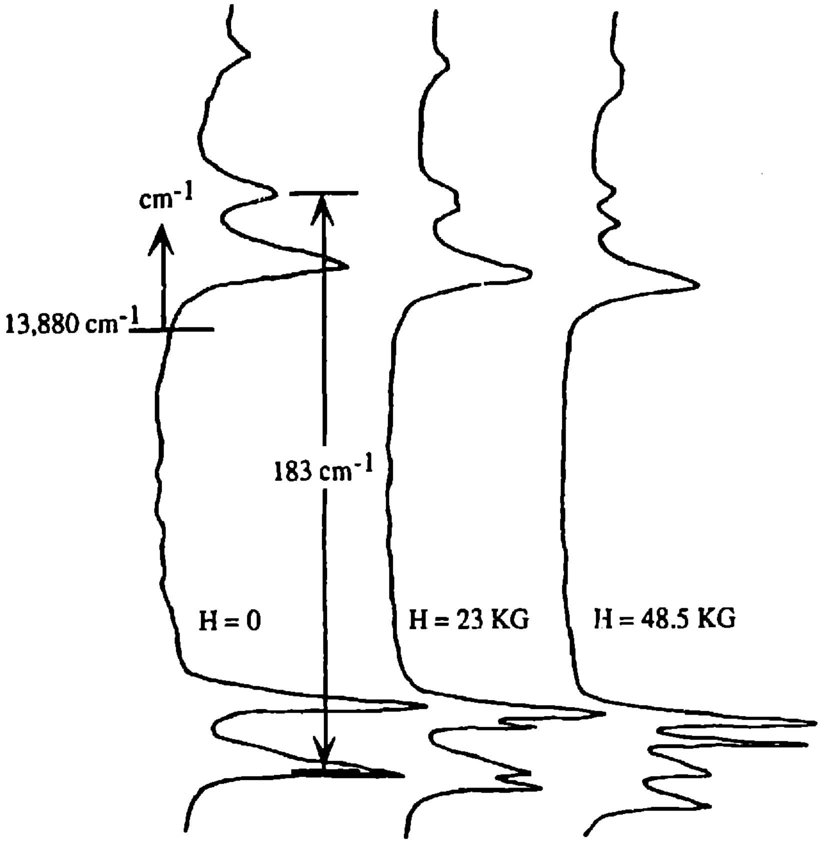

Figure 4.3: Zeeman splitting of Davydov split $^4A_2 \rightarrow {}^2E$ excitons in Cr_2O_3. From Allen et al [48].

interaction between different states. Again consider an ion pair at sites a and b with a definite spin at each site. This is essentially a Heitler-London model. The ground state is given by:

$$|gs\rangle = |\uparrow\downarrow\rangle = \left(|a\uparrow(1)b\downarrow(2)\rangle - |a\uparrow(2)b\downarrow(1)\rangle\right)/\sqrt{2} \tag{4.8}$$

In the visual short hand $|\uparrow\downarrow\rangle$ arrows indicate the ion site spin direction with site A first then B. Double arrows $\Uparrow$ represent an excited state. Odd parity ionic states have a tilde over the arrow such as $\tilde{\Downarrow}$. Now consider an excited state given by:

$$|\tilde{e}\rangle = \left|\tilde{\Downarrow}\uparrow\right\rangle = \left(\left|\tilde{A}\downarrow(1)b\uparrow(2)\right\rangle - \left|\tilde{A}\downarrow(2)b\uparrow(1)\right\rangle\right)\Big/\sqrt{2} \tag{4.9}$$

where $\tilde{A}\downarrow(1)$ denotes an odd parity spin down excited state occupied by electron one. Note, that unlike the spin-forbidden excitons states discussed with respect to exciton dispersion this excited state also includes a spin flip at site b. The direct coulomb term between these two states is spin blocked, but the exchange term is non zero.

$$\left\langle\tilde{\Downarrow}\uparrow\left|\frac{e^2}{r_{12}}\right|\uparrow\downarrow\right\rangle = \left\langle\tilde{e}\left|\frac{e^2}{r_{12}}\right|gs\right\rangle = \left\langle\tilde{A}\downarrow(1)b\uparrow(2)\left|\frac{e^2}{r_{12}}\right|a\uparrow(2)b\downarrow(1)\right\rangle \tag{4.10}$$

Note that the spins at sites a and b are flipped in excited state $|\tilde{e}\rangle$ relative to the ground state $|gs\rangle$. Therefore the addition of off-diagonal exchange will mix the spin flipped state $|\tilde{e}\rangle$ into the ground state.

$$|gs\rangle = |\uparrow\downarrow\rangle = |\uparrow\downarrow\rangle_0 + \sum\left|\tilde{\Downarrow}\uparrow\right\rangle\frac{\left\langle\tilde{\Downarrow}\uparrow\left|\frac{e^2}{r_{12}}\right|\uparrow\downarrow\right\rangle_0}{\Delta E} \tag{4.11}$$

Since state $|\tilde{e}\rangle$ has an odd parity state at site a, it is electric dipole coupled to the state with an even parity excited state at site a with spin flips at both sites a and b relative to the ground state. This state, call it $|A\rangle$, represents a spin-forbidden exciton at site a and a spin flip at site b.

$$|A\rangle = |\Downarrow\uparrow\rangle = |A\downarrow(1)b\uparrow(2)\rangle - |A\downarrow(2)b\uparrow(1)\rangle \tag{4.12}$$

So through off diagonal exchange the ground state is electric dipole connected to excited state $|A\rangle$ allowing weak electric dipole absorption.

$$\left\langle\Downarrow\uparrow\left|\bar{P}\right|\uparrow\downarrow\right\rangle \approx \left\langle\Downarrow\uparrow\left|\bar{P}\right|\tilde{\Downarrow}\uparrow\right\rangle\frac{\left\langle\tilde{\Downarrow}\uparrow\left|\frac{e^2}{r_{12}}\right|\uparrow\downarrow\right\rangle}{\Delta E} \tag{4.13}$$

This is the basic matrix element which allows magnon sideband absorption. Since the off-diagonal exchange term will be strongest for nearest neighbors, zone boundary magnons which look like nearest neighbor spin flips will dominate the magnon sideband absorption.

The magnon sideband matrix element can be recast in a spin operator formalism. This is given by Tanabe as [47]:

$$\vec{P}_{eff}(\varphi'_a \leftarrow \varphi_a) = \vec{\Pi}_{a'a,b}(\vec{s}_{a'a} \cdot \vec{s}_b) \tag{4.14}$$

where the operator $\vec{s}_{a'a}$ creates an exciton at site a with a possible change of spin.

$$\vec{s}_{a'a} = \sum_{m,m'} c_{a'm'}{}^{*}c_{am} \langle m' | \vec{s} | m \rangle \tag{4.15}$$

The details of $\vec{\Pi}_{a'a,b}$ are provided in several longer papers and reviews [43,44,49]. Of course there will be terms involving excitations of site b and mixing of intermediate states into the exciton state as well. However, for an ion pair with a center of symmetry there will still be a finite dipole moment given by [47]:

$$\vec{P}_{eff}(\varphi'_a \leftarrow \varphi_a) = \vec{\Pi}_{a'a,b}(\vec{s}_{a'a} \cdot \vec{s}_b - \vec{s}_a \cdot \vec{s}_{b'b}) \tag{4.16}$$

Later when discussing which exciton the sidebands are associated with some simple selection rules will be derived from equation 4.13. The origin of the multimagnon sidebands will be discussed beginning from equation 4.14.

From this brief review we have seen that joint exciton-magnon absorption in the form of magnon sidebands is a common feature of antiferromagnetic insulators. Off-diagonal exchange mixes in odd parity spin flipped states which are electric dipole coupled to the ground and exciton-magnon states. The excitons associated with the one magnon sidebands are spin-forbidden. For spin-forbidden excitons in a two sublattice planar antiferromagnet such as La_2CuO_4 the exciton dispersion should be very small with respect to the magnon energies. There should also be no Davydov splitting of the exciton band.

Application to Lamellar Copper Oxides

The undoped insulating High-T_c host materials are planar, spin 1/2, antiferromagnetic insulators. There is one hole per copper site and these are well localized on the copper sites. The large superexchange between holes on nearest neighbor Cu ions results in zone boundary magnon energies of ~ 250 meV. From the preceding discussion on joint exciton-magnon absorption it is clear that such absorption should exist in the undoped lamellar copper oxides. An examination of the energy scales for magnon sidebands, the polarization selection rules for magnon sidebands and bare excitons, the rough scaling of the absorption strength with J^2, and the results of some other symmetry sensitive experiments will provide strong evidence that the absorption band around ~ 0.5 eV in the undoped lamellar copper oxides is due to magnon sidebands associated with the $d_{x^2-y^2} \rightarrow d_{3z^2-r^2}$ Frenkel exciton located at roughly ~0.4 eV. Additional absorption measured in ~ 10 µm thick samples of $Sr_2CuO_2Cl_2$ is attributed to absorption associated with the $d_{x^2-y^2} \rightarrow d_{xz}$ exciton.

Ising Model for Magnon Sideband Energy Scales

As discussed in the preceding discussion of magnon sideband matrix elements, the strongest absorption will be associated with zone boundary magnons, which resemble nearest neighbor spin flips. Furthermore the exciton dispersion associated spin-forbidden excitons is expected to be negligible. In the absence of exciton-magnon interactions the absorption spectrum should resemble the magnon density of states and hence be peaked 2J above the exciton energy. A simple Ising model of the exciton-magnon interaction appropriate for the lamellar cuprates will show that excitons and magnons interact strongly yielding a peak ~ 3/2 J above the exciton energy.

Figure 4.4 depicts the model being discussed. For simplicity only the Cu ion sites are shown. At each site the spin is either up or down. The ground state is antiferromagnetically aligned. The energy of the spin system can be represented by bonds between nearest neighbors. The ground state bonds are represented by straight dashed lines. A simple spin flip results in nearest neighbor ion pairs with parallel

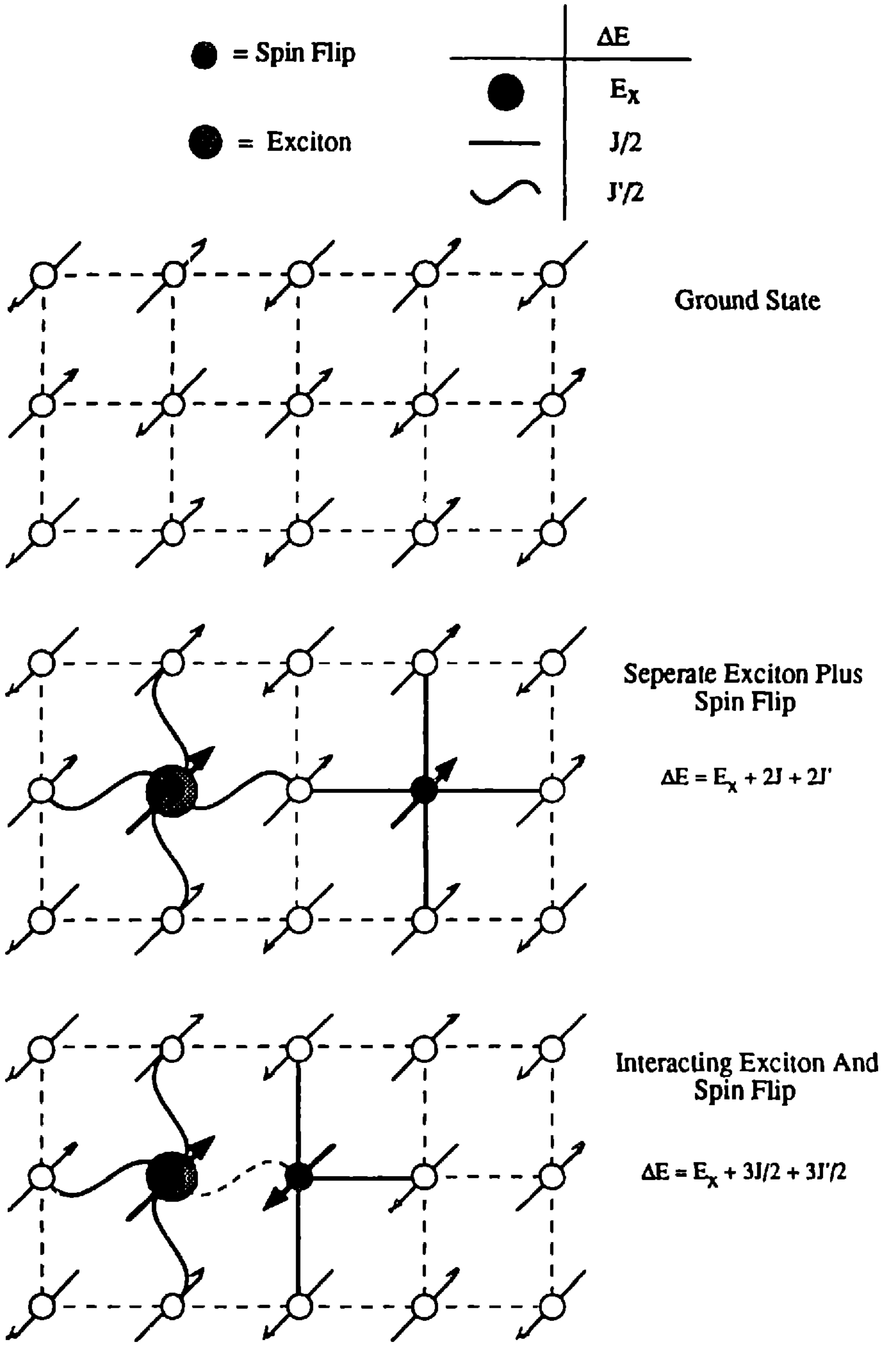

Figure 4.4: Ising model for exciton-magnon interaction. An exciton and magnon on non-nearest neighbor sites have an energy (J+J')/2 higher than a nearest neighbor pair.

spins but all the holes still in the ground state orbital, $d_{x^2-y^2}$. Such pairs of parallel spins are joined by straight solid lines which have an energy cost of J/2 per bond relative to the antiferromagnetically aligned ground state. If the hole on one ion is excited to a higher energy orbital the exchange coupling changes and will be denoted as J'. Antiparallel spin pairs involving an exciton are represented by dashed wavy lines and parallel spin pairs with an exciton by solid wavy lines with an energy cost of J'/2 per bond above the bare exciton energy. Figure 4.4 panel A shows the ground state. Panel B shows a spin-forbidden exciton and a spin flip which are not nearest neighbors. By naive bond counting, the energy of this configuration is

$$\Delta E = E_x + 2J + 2J', \tag{4.17}$$

with E_x being the spin-allowed exciton energy. The energy cost for these excitations formed on nearest neighbor sites as shown in panel C is:

$$\Delta E_{nn} = E_x + \tfrac{3}{2}J + \tfrac{3}{2}J'. \tag{4.18}$$

The exchange coupling, J, is large in these materials due in part to the large overlap of the Cu site $d_{x^2-y^2}$ orbital and the O p_σ orbitals. For an excited state involving the $d_{3z^2-r^2}$ hole a simple overlap argument suggests J'/J = 1/6. For excitons involving d_{xy}, d_{yz}, or d_{xz} the exchange J' via p_σ orbitals is zero by symmetry. For simplicity let J' = 0. In this approximation there is no energy difference between a spin-allowed and a spin-forbidden exciton. Comparing equations 4.17 and 4.18 shows that the excitation energy is reduced by J/2 for nearest neighbor spin flips and excitons due to exciton-magnon interaction. Therefore, the peak in the one magnon sideband absorption is expected to be lower than the zone boundary magnon energy. Also, the energy cost per extra spin flip in multimagnon sidebands is 3J/2.

Figure 4.5 shows the α-polarized absorption spectra for La_2CuO_4 and $Sr_2CuO_2Cl_2$ measured at T = 10K. A linear background has been subtracted as discussed in Chapter 3. Initially, take the sharp peak to represent the bare exciton transition energy. The simple Ising model predicts that the 1-magnon peak

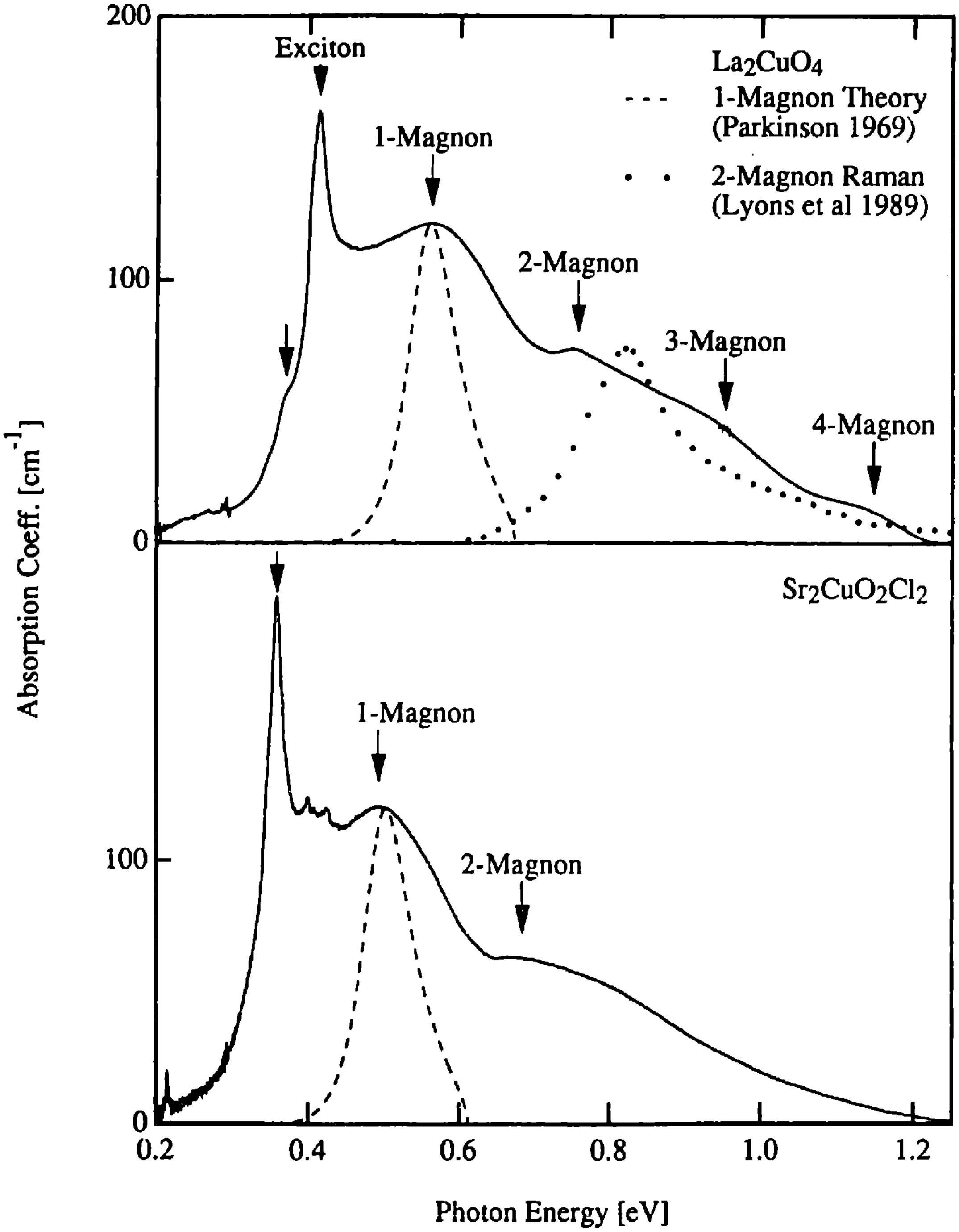

Figure 4.5: La_2CuO_4 and $Sr_2CuO_2Cl_2$ absorption coefficients in α-polarization. Characteristic energies for magnon sidebands are noted (see text). The predicted functional form [50] for a 1-magnon sideband (dashed line), and the measured 2-magnon Raman data of Lyons *et al.* [51] (dotted line) are also shown.

should occur ~ 0.19 eV above the exciton line. In La_2CuO_4 the measured offset from the peak at 0.41 eV is 0.15 eV. For $Sr_2CuO_2Cl_2$ the peak is at 0.36 eV and the offset is 0.14 eV. The predicted positions for the 2-, 3- and 4-magnon peaks relative to the 1-magnon peak are shown assuming a constant energy difference of $3J/2$ ~ 0.19 eV for each additional magnon. Alternatively, subtracting $3J/2$ from the magnon sideband peak would put the pure exciton at 0.37 eV and the sharp peak 0.04 eV above it. In $Sr_2CuO_2Cl_2$ the position for the 2-magnon peak is indicated. Clearly, the predicted 2-magnon position agrees well with the observed second peak in both La_2CuO_4 and $Sr_2CuO_2Cl_2$. In La_2CuO_4 there are also pronounced shoulders at the 3- and 4-magnon positions. Although there is absorption in $Sr_2CuO_2Cl_2$ at these energies, there are no pronounced shoulders. Furthermore in La_2CuO_4 there is a shoulder at 0.370 eV on the low energy side of the sharp 0.41 eV peak. Due to the slight orthorhombic buckling of the Cu-O plane in the low temperature phase of La_2CuO_4 it is possible this is direct two magnon absorption. For the strictly planar materials $Sr_2CuO_2Cl_2$, Nd_2CuO_4, and Pr_2CuO_4 this should not be visible and no shoulder is seen in the data. In $Sr_2CuO_2Cl_2$ there are two small peaks between the sharp 0.36 eV peak and the one magnon sideband peak. The energy shifts relative to the sharp peak are close to known optic phonons in $Sr_2CuO_2Cl_2$ which have the proper E_u symmetry for exciton-phonon sidebands [14]. However, the presence of strong water lines at precisely this energy make such an interpretation unlikely. No such potential phonon sidebands are seen in the other materials.

Classical Spin Model for 1-Magnon Sideband

To explain the full spectra, a proper calculation for the exciton-multimagnon absorption in quantum spin systems must be carried out. At this time, no such calculation exists. A classical spin model was developed by Parkinson [50] to explain the exciton-1-magnon absorption in Rb_2MnF_4 which has K_2NiF_4 crystal structure like La_2CuO_4 and $Sr_2CuO_2Cl_2$. It assumes a flat exciton dispersion and uses a Green's function technique to calculate the effect of the exciton-magnon interaction on the line shape which is proportional to $\mathrm{Im}\left\{G_p(\mathrm{E})\right\}$. The details of the Green's function and the line shape calculation are

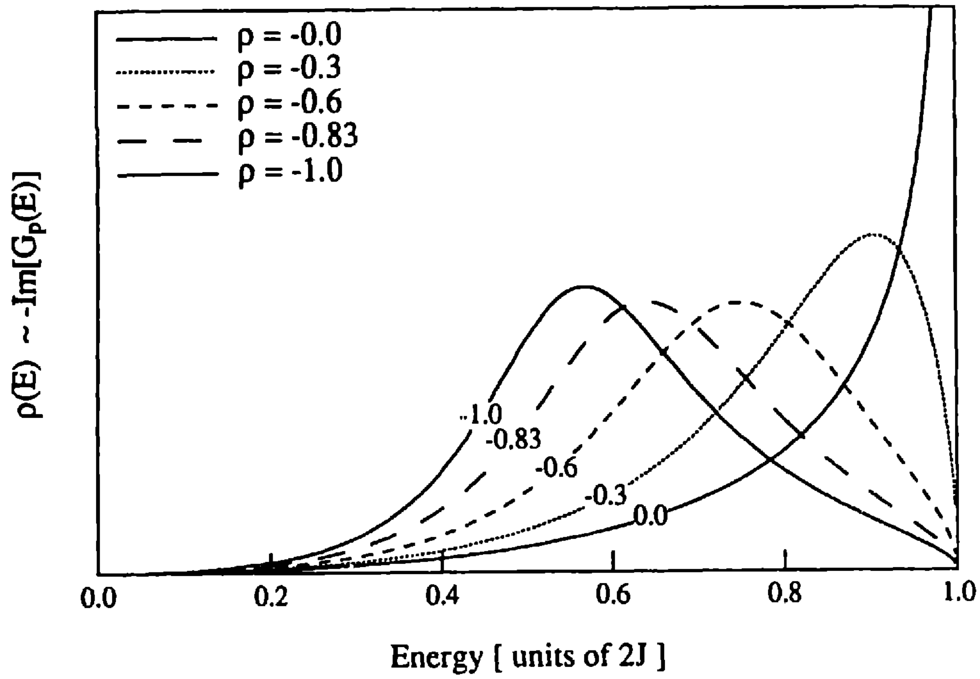

Figure 4.6: Effect of exciton-magnon interaction on magnon sideband line shape in the Parkinson [50] classical spin model, with parameters appropriate for La_2CuO_4. The interaction is given by $\rho = J'/J - 1$.

included in Appendix B. The exciton-magnon interaction is included via a coupling parameter $\rho = (J'S'/JS) - 1$.

$$G_p(\mathrm{E}) = \frac{G_p^o(\mathrm{E})}{1 - (\rho/z) G_p^o(\mathrm{E})} \tag{4.19}$$

$G_p^0(\mathrm{E})$ is the non-interacting Green's function and z the number of nearest neighbors.

The Mn ions in Rb_2MnF_4 have spin S = 5/2 and hence quantum fluctuations were not considered important. The exciton transition in Rb_2MnF_4 is $^6A_1 \rightarrow ^4T_1$. The total spin changes from 5/2 to 3/2 and hence this is a spin-forbidden transition. The spin of the excited ion is still anti-ferromagnetically aligned with its nearest neighbors. In contrast, for a spin-forbidden exciton in a spin-1/2 system such as La_2CuO_4, the total spin doesn't change but the spin becomes ferromagnetically aligned with respect to its nearest neighbors. With this in mind the coupling parameter can be expressed in the following way. The product

JS or J'S' measures extremal energies for nearest neighbor spin configurations. In terms of energy per bond we have:

$$\rho = \frac{E'_{bond} - E_{bond}}{E_{bond}} \tag{4.20}$$

where E_{bond} is the energy per bond for the spin configuration involved in the exciton. In Rb_2MnF_4 this is the same as the given expression for ρ. For La_2CuO_4, E'_{bond} represents ferromagnetically aligned spins and hence has the opposite sign. Therefore for spin-forbidden excitons in La_2CuO_4 the coupling parameter is given by:

$$\rho = -\left(J'/J \right) - 1 \tag{4.21}$$

For J'/J = 0 this has no effect. For finite J' it effects the direction the peak shifts relative to the J'=0 result. The effect of exciton-magnon interactions on the magnon sideband line shape in the Parkinson classical spin model is shown for La_2CuO_4 parameters in figure 4.6. Note that this model assumes dispersionless excitons. For J'/J << 1 the peak is at roughly 55% of the zone boundary magnon energy. The simple Ising model presented above predicted the peak at 75% of the zone boundary magnon energy.

The line shape for the Parkinson model applied to La_2CuO_4 is shown in figure 4.5. The inputs to the model are the exciton energy, the ground state exchange coupling, J, and the excited state exchange coupling, J'. The exciton energy we take to be the sharp peak. The ground state exchange coupling is known from 2-magnon Raman scattering [12] and neutron scattering experiments [52] and as discussed above we take J'=0. The magnitude of the absorption is scaled to match the measured absorption at the 1-magnon peak. As shown in figure 4.6, this classical theory predicts the peak position well but underestimates the peak width.

Currently no theory exists for the 2-, 3-, and 4-magnon sidebands. The 2-magnon sideband should be similar, albeit not identical, to the spectrum observed with 2-magnon Raman scattering. The Raman spectra for La_2CuO_4 from Lyons *et al* [51] with the zero of energy taken at the 0.41 eV peak is shown in figure 4.5. The intensity has been scaled to match the 2-magnon peak. As expected, there is a discrepancy in the 2-magnon peak position since the Raman spectrum does not include exciton-magnon interactions. Nevertheless, the overall shapes and ranges of the 2-magnon Raman scattering and the multimagnon sideband absorption are similar.

Oscillator Strength Scaling

To help determine if the measured absorption is a purely intrinsic process it will be helpful to understand how the magnitude of the exciton-magnon absorption scales from one material to another. As previously discussed and shown in equation 4.13 the effective dipole matrix elements scale with the off-diagonal exchange coupling. The magnon energies are determined by the ground state diagonal exchange energies which is well known. The following argument will show that the off diagonal exchange scales roughly with diagonal exchange, J. Hence, the dipole cross section scales roughly with J^2. Since the number of magnon states doesn't vary much between materials, the integrated absorption should scale roughly as J^2.

To understand this scaling the exchange process for an ion pair will be considered in the context of the Hubbard model. The Hamiltonian is given by:

$$H = \varepsilon\sum_{i\sigma} n_{i\sigma} + t\sum_{ik\sigma} c^{\dagger}_{i\sigma} c_{k\sigma} + U\sum_{i} n_{i\sigma} n_{i-\sigma} \tag{4.22}$$

Each ion site has only one orbital, making this a one band model. It has either zero, one, or two particles in it. The site can only be double occupied if the particles have opposite spin. Sums on i are over lattice sites, and σ over the two spin states. The sum on i and k is for nearest neighbor sites only. The first term is simply the sum of the single particle energies and will not contribute to the exchange. The second term allows hopping of particles from one site to the next. The third term gives the coulomb repulsion when a site is doubly occupied. For strong coulomb repulsion the unperturbed ground state has one particle localized on each ion and the energy is simply 2ε for both ferromagnetic and antiferromagnetic pairs. For an antiferromagnetic pair an excited state exists with two particles on a single ion. The energy of this state is $2\varepsilon + U$ and the matrix element coupling it to the ground state is t. Therefore,

$$E_{\uparrow\uparrow} - E_{\uparrow\downarrow} = \sum_{\alpha} \frac{\langle gs|V|\alpha\rangle\langle\alpha|V|gs\rangle}{\Delta E} = \frac{2t^2}{U} \tag{4.23}$$

yielding $J \propto t^2/U$. In La_2CuO_4 the exchange process is really a superexchange process that occurs in fourth order perturbation theory by hopping via the intermediate oxygen ion. In the extended Hubbard model of Emery and Reiter [53] they give J as:

$$J = \frac{4t^4}{(\varepsilon+V)^2}\left[\frac{1}{U_d} + \frac{2}{U_p + 2\varepsilon}\right] \tag{4.24}$$

Here, V is the coulomb repulsion between two holes on nearest neighbor Cu and O-sites. For two holes on the same site the coulomb repulsion is U_d or U_p for Cu d-states ore O p-states respectively. This can be viewed as the ground state being connected to the ground state via four hops through three intermediate states. Each hop between nearest neighbor Cu and O-sites contributes a power of t and each intermediate state an energy factor in the denominator. The sum in square brackets is from different hopping paths. A particle can hop all the way to a neighboring Cu ion and then interact, or particles from neighboring Cu sites can both hop to the central oxygen ion. For off-diagonal exchange one of the end point ground states is simply an excited state. This changes one factor of t and one energy denominator. So roughly the off-diagonal exchange should go as:

$$J_{off-diag} \propto \left(\frac{\tilde{t}}{t}\right)\left(\frac{\Delta\varepsilon}{\Delta\tilde{\varepsilon}}\right)J. \tag{4.25}$$

If the odd parity excited state is a transition metal ion p-state then the change in the ratio of the hopping parameters and energy factors should be roughly the same between different materials. Therefore, the material dependence of the off-diagonal exchange should be dominated by the diagonal exchange which is well known for different materials.

Material	fwhm[cm^{-1}]	α_{max}[cm^{-1}]	osc. str.[cm^{-2}] α_{max}*fwhm	J [cm^{-1}]	eff. str.[cm^{-2}] $\left(\frac{J_{LCO}}{J}\right)^2 osc.str.$
MnF_2	1.7	12.0	20	1.2	1.5*10^7
MnF_2	30.	3.2	9.6	1.2	7.3*10^7
MnF_2	3.3	5.0	16.5	1.2	1.2*10^7
Cr_2O_3	93	2150	2*10^5	66	5*10^7
$RbMnF_3$	10	100	1000	4.7	5*10^7
La_2CuO_4			4*10^5	1050	4*10^5

Table 4.2: Magnon sideband absorption strength and exchange coupling, J, for several materials. The oscillator strength for La_2CuO_4 is the total integrated strength from ~ 0.4 to 1.2 eV. References: MnF_2([13,42,54]), Cr_2O_3([55,56], $RbMnF_3$([54,57])

Table 4.2 shows the magnon sideband integrated absorption strength and nearest neighbor exchange coupling for MnF_2, $RbMnF_3$, Cr_2O_3, and La_2CuO_4. The last column shows the predicted absorption in La_2CuO_4, assuming the scaling goes as $\left(J_{LCO}/J\right)^2$. This is shown in figure 4.7. The measured absorption in La_2CuO_4 is roughly two orders of magnitude less than expected but there is great uncertainty in this comparison given the differences in crystal structures and the states involved in the exciton. Furthermore, the ground state ion spins in MnF_2, $RbMnF_3$, and Cr_2O_3 are 5/2, 5/2, and 3/2 respectively with nearest neighbor pairs coupled in three dimensions. The integrated absorption strength in La_2CuO_4 is much larger than in MnF_2 and $RbMnF_3$ and about equal to that seen in Cr_2O_3. Although, the integrated absorption strength in La_2CuO_4 is much larger than that due to magnon sidebands in most previously studied materials, the scaling discussed here indicates that is actually less than one might have expected.

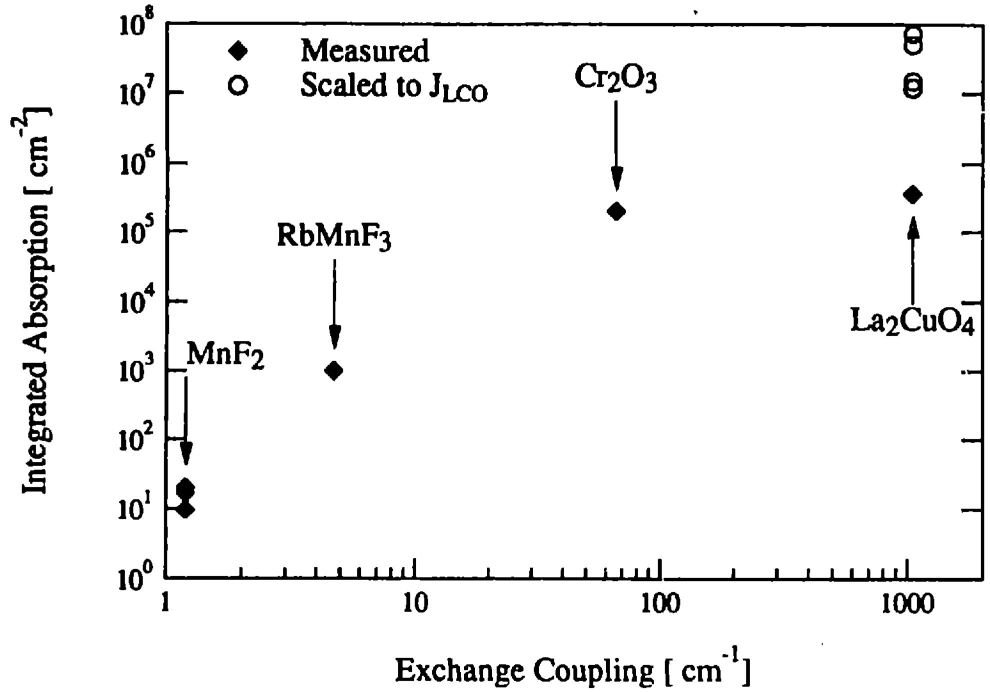

Figure 4.7: Scaling of magnon sideband absorption with the exchange coupling. The open circles show the results for MnF_2, $RbMnF_3$ and Cr_2O_3 scaled by J^2 with respect to La_2CuO_4. Note that the measured value for La_2CuO_4 is roughly two orders of magnitude lower than predicted.

Selection Rules

In the previous sections we have seen that magnon sidebands on excitons are a common feature in antiferromagnetic insulators. Furthermore, the position and strength of the broad bands seen above the sharp peak in both La_2CuO_4 and $Sr_2CuO_2Cl_2$ are well explained on the basis of magnon sideband absorption. To address the question of which exciton the magnon sidebands are associated with it will be useful to examine the selection rules for both the magnon sidebands and the bare exciton transition itself. These selection rules in conjunction with the measured polarization dependence, the electroreflectance experiments of Falck *et al*, and high energy shift Raman scattering experiments of Liu *et al* will show that the exciton associated with the observed magnon sidebands is most likely the copper ion $d_{x^2-y^2} \to d_{3z^2-r^2}$ transition at ~0.4 eV with the $d_{x^2-y^2} \to d_{xy}$ at ~1.5 eV.

Magnon Sideband Selection Rules

Equation 4.13 shows that the dipole moment for joint exciton-magnon absorption arises from off diagonal exchange mixing in odd parity ionic wavefunctions. To determine the polarization selection rules for the magnon sidebands it is necessary to determine which odd parity excited states are mixed in by the off diagonal exchange. For concreteness of language consider an ion pair consisting of nearest neighbor ions separated in the $\hat{x}$ direction and restrict the odd parity excited states to copper ion p-orbitals. The off-diagonal exchange for mixing into the ground state wavefunction is given by:

$$\left\langle p_{\alpha}^{A}(2)d_{x^2-y^2}^{B}(1)\right|\frac{e^2}{r_{12}}\left|d_{x^2-y^2}^{A}(1)d_{x^2-y^2}^{B}(2)\right\rangle \tag{4.26}$$

The superscript A or B denotes the ion the wave function is centered on and the number 1 or 2 is the particle number. The subscript α can be either x, y, or z. This can be viewed as the overlap of two charge clouds with charge densities given by:

$$\begin{aligned} \rho(2) &= p_{\alpha}^{A}(2)\bullet d_{x^2-y^2}^{B}(2) \\ \rho(1) &= d_{x^2-y^2}^{A}(1)\bullet d_{x^2-y^2}^{B}(1) \end{aligned} \tag{4.27}$$

For an ion pair separated along the $\hat{x}$ direction if the excited state at ion A is either p_y or p_z the odd parity in either y or z will cause the integral to vanish. For an excited state of p_x the integral will be finite and hence some ionic p_x will be mixed into the ground state. The mixing of odd parity ionic states into the final exciton states can be determined in a similar fashion. These results are summarized in table 4.3. Table 4.4 shows the polarization selection rules for p-state to d-state electric dipole transitions. The information in Tables 4.3 and 4.4 can be combined to determine the polarization selection rules for magnon sidebands involving d-d excitons. The results are shown in Table 4.5. Recall that magnon sidebands observed are seen in both α– and σ-polarization, but not in π–polarization. Therefore the exciton involved must be either the $d_{x^2-y^2}\to d_{3z^2-r^2}$ or the $d_{x^2-y^2}\to d_{xy}$ exciton.

Unperturbed State	Odd Parity State Mixed In
$d^A_{x^2-y^2}d^B_{x^2-y^2}$	$p^A_x d^B_{x^2-y^2}\left(p^A_y d^B_{x^2-y^2}\right)$
$d^A_{3z^2-r^2}d^B_{x^2-y^2}$	$p^A_x d^B_{x^2-y^2}\left(p^A_y d^B_{x^2-y^2}\right)$
$d^A_{xy}d^B_{x^2-y^2}$	$p^A_y d^B_{x^2-y^2}\left(p^A_x d^B_{x^2-y^2}\right)$
$d^A_{xz}d^B_{x^2-y^2}$	$p^A_z d^B_{x^2-y^2}$
$d^A_{yz}d^B_{x^2-y^2}$	$\left(p^A_z d^B_{x^2-y^2}\right)$

Table 4.3: Off-diagonal exchange mixing of single ion states with odd parity into ion pair state composed of even parity single ion states. Sites A and B are nearest neighbors separated in the $\hat{x}$ $(\hat{y})$ direction.

	p_x	p_y	p_z
$d_{x^2-y^2}$	$\hat{x}$	$\hat{y}$	
$d_{3z^2-r^2}$	$\hat{x}$	$\hat{y}$	$\hat{z}$
d_{xz}	$\hat{y}$	$\hat{x}$	
d_{xz}	$\hat{z}$		$\hat{x}$
d_{yz}		$\hat{z}$	$\hat{y}$

Table 4.4: Polarization necessary for electric dipole transitions between p-states and d-states.

Exciton Transition	Polarization
$d_{x^2-y^2} \rightarrow d_{3z^2-r^2}$	α, σ
$d_{x^2-y^2} \rightarrow d_{xy}$	α, σ
$d_{x^2-y^2} \rightarrow d_{xz}$	π
$d_{x^2-y^2} \rightarrow d_{yz}$	π

Table 4.5: Polarization selection rules for magnon sidebands to a d-d exciton.

Most calculations for exciton energies put the $d_{x^2-y^2} \rightarrow d_{3z^2-r^2}$ exciton at a lower energy than the $d_{x^2-y^2} \rightarrow d_{xy}$. However, these same calculations yield exciton energies for the $d_{x^2-y^2} \rightarrow d_{3z^2-r^2}$ transition of greater than 1 eV. This discrepancy will be discussed in chapter 5. To determine which of the two possible excitons the observed magnon sidebands are associated with, it will be necessary to consider more selection rules and additional experiments.

Electric Field-Induced Dipole Transitions

In chapter 3, the polarization selection rules for electric dipole, magnetic dipole and electric quadruple transitions were determined. These, in conjunction with the measured polarization dependence of the spectra (see figure 3.10) show that the absorption process is an electric dipole transition. Due to the inversion symmetry of the copper ion sites in these crystals the bare d-d exciton transition are electric dipole forbidden by parity conservation. However, if an odd parity perturbation exists at an ion site, then some odd parity wave function will be mixed into the even parity d-states and electric dipole transitions can occur. Such a mechanism might make the exciton observable as an electric dipole process. Group theory allows one to determine the selection rules for such transitions. Using the Wigner-Eckart theorem it is possible to work out not just the selection rules but the relative intensities for different d-d transitions for arbitrary linear polarization and perturbation direction.

Before developing the magnon sideband explanation for the spectra, the possibility that the structure observed represented the different copper ion d-d excitons was considered. This model, which I called the Random Perturbation Model, assumed that impurities result in a net randomly oriented vector perturbation at each copper ion. To understand the polarization dependence, the crystal is approximated as a collection of non-interacting ions with a randomly oriented vector perturbation at each site. The absorption intensity is calculated for a fixed polarization , with arbitrary perturbation orientation, and then averaged over the perturbation direction. The resulting selection rules indicate that if the sharp low energy (~ 0.4 eV) peak observed were such a transition, it would be either the $d_{x^2-y^2} \rightarrow d_{3z^2-r^2}$ or the $d_{x^2-y^2} \rightarrow d_{xy}$ exciton. At one point, this was believed to be the case. However, in such a picture the oscillator strength of the exciton line would be expected to vary significantly between samples due to variations in the impurity concentration. As shown in figure 3.11 which compares several crystals of La_2CuO_4 and $Sr_2CuO_2Cl_2$ this is not the case. In particular, for La_2CuO_4, there is no measurable difference in the oscillator strength of the sharp line for samples grown by the top seeded solution method or the floating zone method. This, combined with the oscillator strength scaling discussed above, indicates that the measured absorption is a purely intrinsic process of the undoped copper oxygen planes. The nature of the sharp peak will be discussed later in this chapter.

However, an external electric field may be intentionally applied to the sample to break the copper site inversion symmetry. The orientation of both the perturbing electric field and the polarization of the incident light may be controlled with respect to the crystalline axis, thus allowing only certain d-d transitions to be enhanced akin to Raman scattering but without the complexity of coupling to the magnon excitations. Such an electroreflectance experiment has been carried out by *Falck et al.* [58]on La_2CuO_4. To understand the results of this experiment and the potential for future electroreflectance and electrotransmission experiments, the selection rules for electric field induced electric dipole transitions will be discussed.

For the excitons under consideration, the electron and hole reside on the same copper ion site. Therefore, the selection rules for the transition will simply be the selection rules for the individual ionic transitions. The odd parity states most likely to be mixed into the copper d-states are p-like states. These could be the copper p-states or p-symmetry states made from the nearest neighbor oxygen p-orbitals. All that matters in the following discussion is the symmetry properties of the states, so only generic d- and p-states will be discussed. In Appendix A the symmetry of all the possible states made of a central copper ion d-states and nearest neighbor oxygen p-states are given for tetragonal (D_{4h}) symmetry.

An electric field applied to a copper ion mixes p-states into the d-states by first order perturbation theory,

$$\begin{aligned} \left|\bar{D}\right\rangle &= \left|D^0\right\rangle + \sum_{\{|p\rangle\}} \left|p\right\rangle \frac{\left\langle p\middle|V\middle|D^0\right\rangle}{E_d - E_p} \\ V &= V(r)\,\hat{V}\cdot\hat{r} \\ V_R &\equiv \left\langle \Psi_p(r)\middle|V(r)\middle|\Psi_D(r)\right\rangle \end{aligned} \tag{4.28}$$

where $V(r)\,\hat{V}$ denotes a generic vector perturbation, and V_R the result of the radial integrals. The copper ion p-states and those constructed from the neighboring oxygens will simply have different radial integrals. Electric dipole transitions occur between the copper d-states and the mixed in p-states. To determine the selection rules, first the mixing in of p-states will be calculated and then the selection rules evaluated. To determine the mixing it is necessary to work out matrix elements such as $\left\langle p_x\middle|x\middle|D\right\rangle$. There are five d-states, three perturbation components, and three p-states, giving 45 possible matrix elements. Group theory can be used to determine which are non-zero. Appendix A provides a tutorial on the use of group theory to evaluate selection rules. Table 4.6 lists the relevant states, their corresponding irreducible

Ionic states	D4h Irreducible Rep.	Spherical Harmonic Expansion
$d_{x^2-y^2}$	B1g	$\frac{1}{\sqrt{2}}\left(Y_{2,2}+Y_{2,-2}\right)$
d_{xy}	B2g	$\frac{-i}{\sqrt{2}}\left(Y_{2,2}-Y_{2,-2}\right)$
d_{yz}	Eg	$\frac{i}{\sqrt{2}}\left(Y_{2,1}+Y_{2,-1}\right)$
d_{xz}	Eg	$\frac{-1}{\sqrt{2}}\left(Y_{2,1}-Y_{2,-1}\right)$
$d_{3z^2-r^2}$	A1g	Y_{20}
p_x	Eu	$\frac{-1}{\sqrt{2}}\left(Y_{1,1}-Y_{1,-1}\right)$
p_y	Eu	$\frac{i}{\sqrt{2}}\left(Y_{1,1}+Y_{1,-1}\right)$
p_z	A2u	$Y_{1,0}$

Table 4.6: Tetragonal (D_{4h}) symmetry classification and spherical harmonic expansion for ion states important in electric field induced electric dipole transitions for copper ion d-d excitons.

representation in D_{4h}, and their spherical harmonic expansion. The terms x, y, and z transform as vectors in the same way as p_x, p_y, and p_z respectively, namely E_u, E_u, and A_{2u}. The subscripts indicate the parity of the state with g (gerade) for even and u (ungerade) for odd parity. A matrix element is non-zero if the joint product contains some spherical, A_{1g}, component. For example,

$$\begin{gathered}\left\langle p_x \middle| \left(\tfrac{x}{r}\right) \middle| D_{x^2-y^2}\right\rangle \approx E_u \otimes E_u \otimes B_{1g} \approx \left(A_{1g}+A_{2g}+B_{1g}+B_{2g}\right)\otimes B_{1g} \\ B_{1g}\otimes B_{1g} \approx A_{1g}\end{gathered} \tag{4.29}$$

The direct product multiplication table for the D_{4h} group is given in Table 4.7. It shows that $E \otimes E \approx A_1 + A_2 + B_1 + B_2$. Parity must be kept track of separately with $g \otimes g \approx g$, $g \otimes u \approx u$ and $u \otimes u \approx g$. The $B_{1g} \otimes B_{1g}$ term yields A_{1g} and hence this matrix element is non-zero. Note that A_1 only

D4,C4v	A1	A2	B1	B2	E
A1	A1	A2	B1	B2	E
A2	A2	A1	B2	B1	E
B1	B1	B2	A1	A2	E
B2	B2	B1	A2	A1	E
E	E	E	E	E	A1+A2+B1+B2

Table 4.7: Direct product multiplication table for irreducible representations in D_{4h} or C_{4v} symmetries.

occurs on the diagonal of the direct product multiplication table. This method shows that of the 45 possible matrix elements only 11 are non-zero. These can be further grouped into three classes as listed below. The operators x, y, and z can be written in terms of spherical harmonics.

$$\begin{aligned} \left(\tfrac{x}{r}\right) &= -\sqrt{\tfrac{2\pi}{3}}\left(Y_{1,1} - Y_{1,-1}\right) \\ \left(\tfrac{y}{r}\right) &= i\sqrt{\tfrac{2\pi}{3}}\left(Y_{1,1} + Y_{1,-1}\right) \\ \left(\tfrac{z}{r}\right) &= \sqrt{\tfrac{4\pi}{3}}Y_{1,0} \end{aligned} \tag{4.30}$$

Therefore the three matrix elements which must be determined can be evaluated using the rule for integrals over triple products of spherical harmonics,[40]

$$\int d\Omega\, Y_{lm}^{*} Y_{l_1 m_1} Y_{l_2 m_2} = \sqrt{\frac{(2l_1+1)(2l_2+1)}{4\pi(2l+1)}}\langle l_1 0; l_2 0 | l 0\rangle\langle l_1 m_1; l_2 m_2 | l m\rangle \tag{4.31}$$

with $\langle l_1 m_1; l_2 m_2 | l m\rangle$ just being a Clebsch-Gordan coefficient. The non-zero matrix elements are then:

$\frac{\lvert D\rangle - \lvert D^0\rangle}{\vec{V}}$	$\frac{\langle p_x \lvert(\hat{V}\cdot\hat{r})\rvert D^0\rangle}{E_D - E_{p_x}}$	$\frac{\langle p_y \lvert(\hat{V}\cdot\hat{r})\rvert D^0\rangle}{E_D - E_{p_y}}$	$\frac{\langle p_z \lvert(\hat{V}\cdot\hat{r})\rvert D^0\rangle}{E_D - E_{p_z}}$
$D_{x^2-y^2}$	$\frac{\sqrt{\frac{1}{5}}\left(\hat{V}\cdot\hat{x}\right)}{\Delta\left(d_{x^2-y^2}\to p_x\right)}$	$\frac{-\sqrt{\frac{1}{5}}\left(\hat{V}\cdot\hat{y}\right)}{\Delta\left(d_{x^2-y^2}\to p_y\right)}$	
$D_{3z^2-r^2}$	$\frac{-\sqrt{\frac{1}{15}}\left(\hat{V}\cdot\hat{x}\right)}{\Delta\left(d_{3z^2-r^2}\to p_x\right)}$	$\frac{-\sqrt{\frac{1}{15}}\left(\hat{V}\cdot\hat{y}\right)}{\Delta\left(d_{3z^2-r^2}\to p_y\right)}$	$\frac{\sqrt{\frac{4}{15}}\left(\hat{V}\cdot\hat{z}\right)}{\Delta\left(d_{3z^2-r^2}\to p_z\right)}$
D_{xy}	$\frac{\sqrt{\frac{1}{5}}\left(\hat{V}\cdot\hat{y}\right)}{\Delta\left(d_{xy}\to p_x\right)}$	$\frac{\sqrt{\frac{1}{5}}\left(\hat{V}\cdot\hat{x}\right)}{\Delta\left(d_{xy}\to p_y\right)}$	
D_{xz}	$\frac{\sqrt{\frac{1}{5}}\left(\hat{V}\cdot\hat{z}\right)}{\Delta\left(d_{xz}\to p_x\right)}$		$\frac{\sqrt{\frac{1}{5}}\left(\hat{V}\cdot\hat{x}\right)}{\Delta\left(d_{xz}\to p_z\right)}$
D_{yz}		$\frac{\sqrt{\frac{1}{5}}\left(\hat{V}\cdot\hat{z}\right)}{\Delta\left(d_{yz}\to p_y\right)}$	$\frac{\sqrt{\frac{1}{5}}\left(\hat{V}\cdot\hat{y}\right)}{\Delta\left(d_{yz}\to p_z\right)}$

Table 4.8: Matrix elements for mixing of p-states into d-states due to a vector perturbation such as an applied electric field.

$$\begin{aligned}
I)\quad & \left\langle p_x \middle|\left(\tfrac{x}{r}\right)\middle| D_{x^2-y^2}\right\rangle = -\left\langle p_y \middle|\left(\tfrac{y}{r}\right)\middle| D_{x^2-y^2}\right\rangle = \sqrt{\tfrac{1}{5}} \\
II)\quad & \left\langle p_x \middle|\left(\tfrac{y}{r}\right)\middle| D_{xy}\right\rangle = \left\langle p_y \middle|\left(\tfrac{x}{r}\right)\middle| D_{xy}\right\rangle = \left\langle p_x \middle|\left(\tfrac{z}{r}\right)\middle| D_{xz}\right\rangle = \left\langle p_z \middle|\left(\tfrac{x}{r}\right)\middle| D_{xz}\right\rangle = \left\langle p_y \middle|\left(\tfrac{z}{r}\right)\middle| D_{yz}\right\rangle = \\
& = \left\langle p_z \middle|\left(\tfrac{y}{r}\right)\middle| D_{yz}\right\rangle = \sqrt{\tfrac{1}{5}} \\
III)\quad & \left\langle p_z \middle|\left(\tfrac{z}{r}\right)\middle| D_{z^2}\right\rangle = -2\left\langle p_y \middle|\left(\tfrac{y}{r}\right)\middle| D_{z^2}\right\rangle = -2\left\langle p_x \middle|\left(\tfrac{x}{r}\right)\middle| D_{z^2}\right\rangle = 2\sqrt{\tfrac{1}{15}}
\end{aligned} \tag{4.32}$$

From these matrix elements the mixing of p-states into the copper ion d-states can be determined and is given in table 4.8. The effective electric dipole matrix elements for transitions between these states

Vector Perturbation Induced Electric Dipole Transition Matrix Elements

$$\left\langle \tilde{D}_{z^2} \middle| \hat{\varepsilon}\cdot\hat{r} \middle| \tilde{D}_{x^2-y^2} \right\rangle = \frac{V_R}{5\sqrt{3}}\left(\frac{1}{\Delta_x^{x^2-y^2}} + \frac{1}{\Delta_x^{z^2}}\right)\left\{-(\hat{\varepsilon}\cdot\hat{x})(\hat{V}\cdot\hat{x}) + (\hat{\varepsilon}\cdot\hat{y})(\hat{V}\cdot\hat{y})\right\}$$

$$\left\langle \tilde{D}_{xy} \middle| \hat{\varepsilon}\cdot\hat{r} \middle| \tilde{D}_{x^2-y^2} \right\rangle = \frac{V_R}{5}\left(\frac{1}{\Delta_x^{x^2-y^2}} - \frac{1}{\Delta_y^{xy}}\right)\left\{-(\hat{\varepsilon}\cdot\hat{x})(\hat{V}\cdot\hat{y}) + (\hat{\varepsilon}\cdot\hat{y})(\hat{V}\cdot\hat{x})\right\}$$

$$\left\langle \tilde{D}_{xz} \middle| \hat{\varepsilon}\cdot\hat{r} \middle| \tilde{D}_{x^2-y^2} \right\rangle = \frac{V_R}{5}\left\{\frac{(\hat{\varepsilon}\cdot\hat{x})(\hat{V}\cdot\hat{z})}{\Delta_x^{xz}} + \frac{(\hat{\varepsilon}\cdot\hat{z})(\hat{V}\cdot\hat{x})}{\Delta_x^{x^2-y^2}}\right\}$$

$$\left\langle \tilde{D}_{yz} \middle| \hat{\varepsilon}\cdot\hat{r} \middle| \tilde{D}_{x^2-y^2} \right\rangle = \frac{V_R}{5}\left\{\frac{-(\hat{\varepsilon}\cdot\hat{y})(\hat{V}\cdot\hat{z})}{\Delta_y^{yz}} - \frac{(\hat{\varepsilon}\cdot\hat{z})(\hat{V}\cdot\hat{y})}{\Delta_y^{x^2-y^2}}\right\}$$

$$\left|\tilde{D}\right\rangle = |D\rangle + \sum |p\rangle \frac{\langle p|V|D\rangle}{E_D - E_p} \qquad V = V(r)\,\hat{V}\cdot\hat{r}$$

$$\Delta_x^{x^2-y^2} \equiv E_{d_{x^2-y^2}} - E_{p_x} \qquad V_R = \left\langle \Psi_p(r) \middle| V(r) \middle| \Psi_D(r) \right\rangle$$

Table 4.9: Electric dipole transition matrix elements for applied electric field induced d-d transitions.

are given in table 4.9, with $\hat{\varepsilon}$ being the incident light polarization. If both the perturbing electric field and the polarization lie in the copper oxygen plane, then only the $d_{x^2-y^2} \to d_{3z^2-r^2}$ or $d_{x^2-y^2} \to d_{xy}$ are observed. If either the polarization vector of the perturbing electric field is perpendicular to the Cu-O plane, then the $d_{x^2-y^2} \to d_{xz}$ or $d_{x^2-y^2} \to d_{yz}$ may be seen. For the former case with the perturbing electric field and the incident polarization constrained to lie in the Cu-O plane, and measuring their angular orientation with respect to the x-axis then:

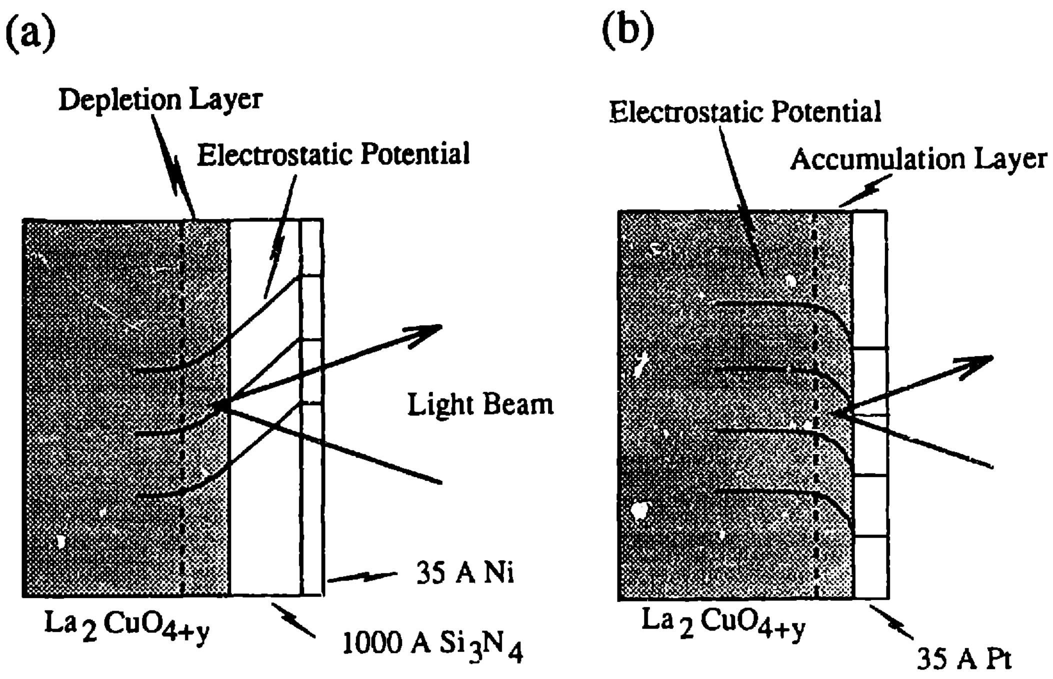

Figure 4.8: (a) The metal-insulator-semiconductor configuration used to modulate the electric field in a natural depletion layer. (b) The metal-semiconductor configuration used to modulate the hole concentration in a natural accumulation layer. The displayed ideal electrostatic potential equals the hole potential. (Taken from Falck *et al.*. [58])

$$\begin{aligned} \left\langle \tilde{D}_{z^2} \middle| (\hat{\varepsilon}\cdot\hat{r}) \middle| \tilde{D}_{x^2-y^2} \right\rangle &\approx \cos\left(\theta_{\hat{\varepsilon}} + \theta_{\hat{V}}\right) \\ \left\langle \tilde{D}_{xy} \middle| (\hat{\varepsilon}\cdot\hat{r}) \middle| \tilde{D}_{x^2-y^2} \right\rangle &\approx \sin\left(\theta_{\hat{\varepsilon}} - \theta_{\hat{V}}\right) \end{aligned} \qquad (4.33)$$

The purpose in presenting the above is to help determine whether the exciton associated with the magnon sidebands observed in the range ~0.4 - 1.2 eV is the $d_{x^2-y^2} \to d_{3z^2-r^2}$ or $d_{x^2-y^2} \to d_{xy}$ transition. The sample configuration for the electroreflectance experiments of Falck *et al* [58] is shown in figure 4.8 (a). An insulating layer and then a thin transparent metal layer are deposited on the sample. This forms a natural depletion layer at the sample-insulator interface, and hence a perturbing electric field. The electrode allows the strength of the electric field in the depletion region to be modulated which simplifies determining what absorption structure is due to the perturbing field. The sample is oriented such that the perturbing electric field always lies in the Cu-O plane and the incident polarization can be rotated to be either parallel or perpendicular to the plane. The perturbing electric field and polarization are always mutually perpendicular. Figure 4.9 shows some spectra from this experiment. Panels (b) and (c) show the change in the imaginary part of the dielectric constant, Δe_2. By choice of sign convention, negative peaks in Δe_2 correspond to transitions enhanced by a perturbing electric field. The positive peaks in panel (b) probably correspond to a doping effect. This is discussed in detail by Falck *et al* [58]/ The important result is that the strong negative peak in shown in panel (b) corresponds to a transition of $d_{x^2-y^2} \rightarrow d_{xy}$ symmetry at ~1.5 eV. As shown in figure 3.7 for thin samples of $Sr_2CuO_2Cl_2$ a second absorption band is observed at ~1.5 eV. Furthermore, recent high energy shift Raman scattering experiments of Liu *et al.* [59] shown in figure 4.10 show an excitation of A_{2g} symmetry at ~1.5 eV in several undoped copper oxide materials. Recall that the magnon sideband selection rules for sidebands observed in α and σ but not π require that the exciton be either $d_{x^2-y^2} \rightarrow d_{3z^2-r^2}$ or $d_{x^2-y^2} \rightarrow d_{xy}$. The electroreflectance and Raman scattering experiments strongly suggest that the $d_{x^2-y^2} \rightarrow d_{3z^2-r^2}$ exciton is at ~0.4 eV and the $d_{x^2-y^2} \rightarrow d_{xy}$ at ~1.5 eV in the undoped layered copper oxides. This is in accord with the predicted energy level ordering of several calculations, but the ~0.4 eV energy for the $d_{x^2-y^2} \rightarrow d_{3z^2-r^2}$ exciton is significantly lower than the ~1-1.5 eV predicted calculationally. This discrepancy is the subject of Chapter 5.

Now consider the possibility for observing the $d_{x^2-y^2} \rightarrow d_{3z^2-r^2}$ transition in an electroreflectance or electrotransmission experiment. Equation 4.33 a shows the matrix element goes like $\cos\left(\theta_{\hat{\varepsilon}} + \theta_{\hat{V}}\right)$. For the perturbing electric field and the incident polarization both in the Cu-O plane and parallel to each other this transition will be observable. This is perhaps more evident in equation 4.32. This configuration is difficult to achieve experimentally. However, this transition will also be observable for perturbing electric field and the incident polarization mutually perpendicular and oriented in the Cu-O plane but at 45° with respect to the Cu-O bond direction. For a sample cut and polished perpendicular to the <110> (<001> ⊥ Cu-O plane) direction this will be easily achieved.

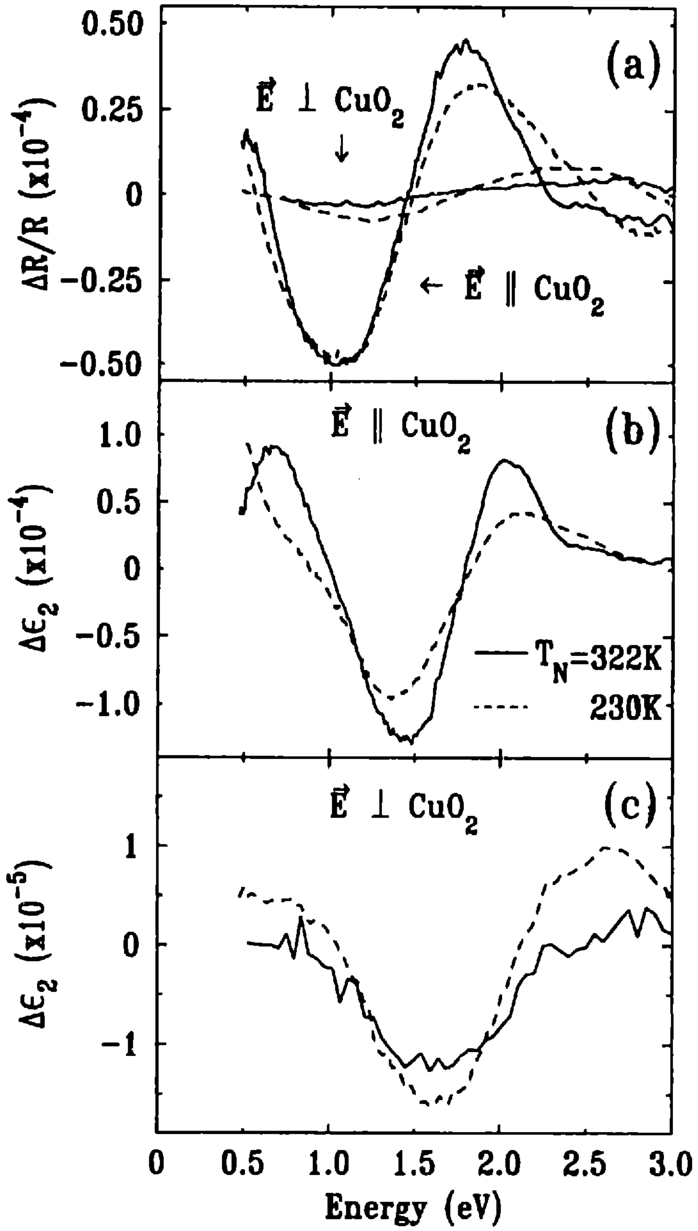

Figure 4.9: (a) Modulation reflectivity spectra of La_2CuO_{4+y} with T_N = 322 K (y=0) and T_N = 230 K (y = 0.016) at 295 K for the metal-insulator-semiconductor configuration. The in-plane $\Delta\varepsilon_2(\omega)$ (b) and the out-of-plane $\Delta\varepsilon_2(\omega)$ (c) corresponding to the ΔR/R spectra in panel (a). From Falck *et al* [58].

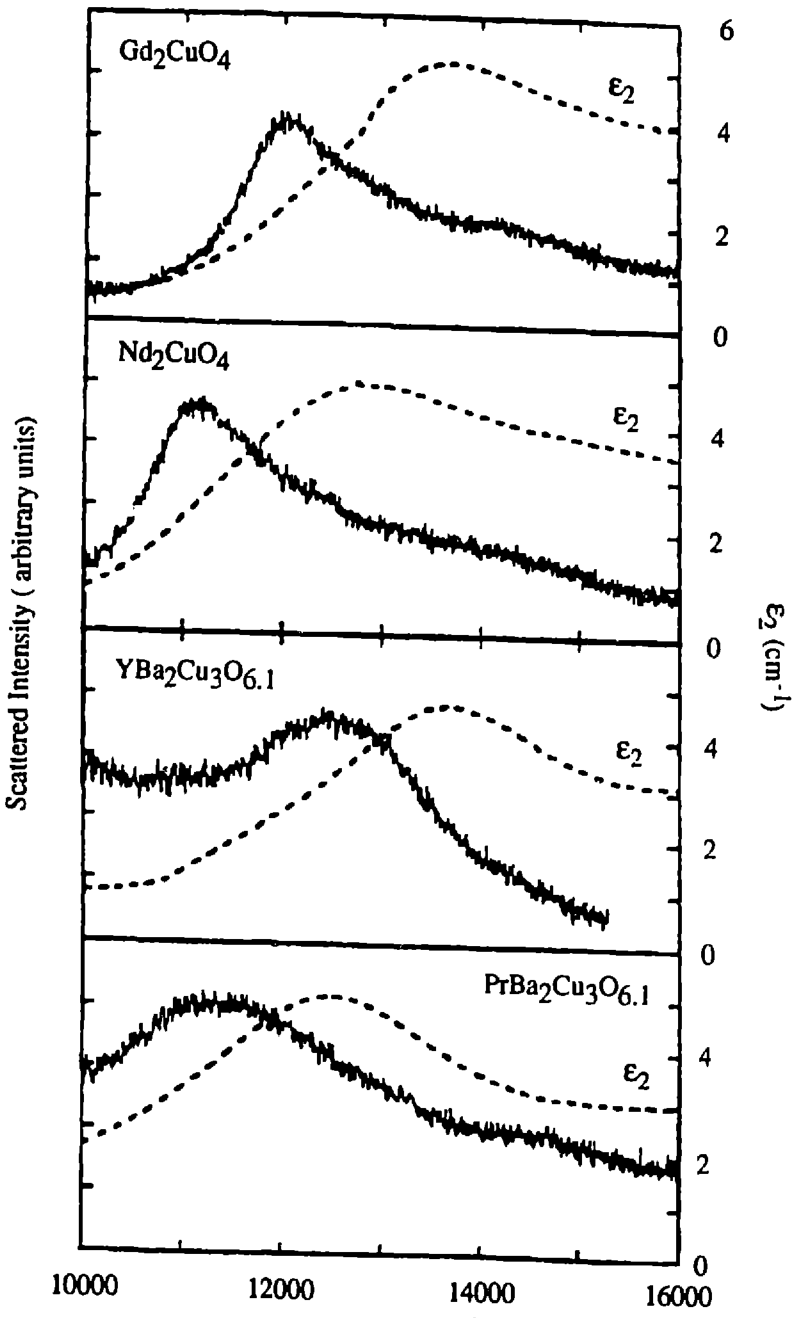

Figure 4.10: Raman spectra (in relative cm^{-1} shift) and ε_2 (in absolute cm^{-1}) for four different insulating cuprates. The Raman spectra were taken in the A_{2g} geometry with 3.81 eV excitation. From Liu *et al* [59].

The $d_{x^2-y^2} \rightarrow d_{xy}$ transition will also be observed in this configuration but comparison with samples cut perpendicular to the <100> direction should allow positive identification of the $d_{x^2-y^2} \rightarrow d_{3z^2-r^2}$ transition. This is discussed in more detail in Chapter 7 on potential future work.

Direct Exciton Selection Rules and Oscillator Strength

The bare d-d excitons are not electric dipole allowed due to the inversion symmetry of the copper ion sites. However, these transitions are possible as magnetic dipole and electric quadrupole processes. This section determines the selection rules and approximate oscillator strength for these transitions. The results show that the $d_{x^2-y^2} \rightarrow d_{3z^2-r^2}$ exciton is observable as a σ-polarized electric quadrupole process and the $d_{x^2-y^2} \rightarrow d_{xy}$ as a σ-polarized magnetic dipole transition. The estimated oscillator strength shows that the $d_{x^2-y^2} \rightarrow d_{3z^2-r^2}$ would be unobservable in our data where as the $d_{x^2-y^2} \rightarrow d_{xy}$ line strength would be 20% of the entire magnon sideband spectrum. Therefore if the $d_{x^2-y^2} \rightarrow d_{xy}$ exciton were at ~0.4 eV it would be very evident in the σ-polarized spectra. However, the σ- and α-polarized spectra are identical. Hence assigning the ~ 0.4 eV exciton to the $d_{x^2-y^2} \rightarrow d_{3z^2-r^2}$ transition is consistent with the lack of an observed bare exciton line.

The absorption cross section for single photon processes is given by:[40]

$$\sigma = \frac{4\pi^2\hbar}{m_e^2\omega}\frac{e^2}{\hbar c}\left|\langle f|e^{i\vec{k}\cdot\vec{r}}\,\vec{\varepsilon}\cdot\vec{p}|i\rangle\right|^2 \delta(E_f - E_i - \hbar\omega). \tag{4.34}$$

The magnetic dipole and electric quadrupole matrix elements are:

$$\langle f|(\vec{k}\cdot\vec{r})(\vec{\varepsilon}\cdot\vec{p})|i\rangle = \frac{|k|}{2}\underbrace{\langle f|\hat{B}\cdot\vec{L}|i\rangle}_{\substack{\text{Magnetic}\\ \text{Dipole}}} + \underbrace{\frac{im\omega_{fi}}{2}\langle f|(\vec{\varepsilon}\cdot\vec{x})(\vec{k}\cdot\vec{x})|i\rangle}_{\substack{\text{Electric}\\ \text{Quadrapole}}}. \tag{4.35}$$

To determine the selection rules one must understand the symmetry of the transition matrix elements. For example, consider the σ-polarized magnetic dipole, σ(MD), element. As shown in figure 3.1 for σ-

Magnetic Dipole and Electric Quadrupole Transition Symmetries in D_{4h}

Polarization	Magnetic Dipole	Electric Quadrupole
α	E_g	E_g
σ	A_{2g}	$B_{1g} + B_{2g}$
π	E_g	E_g

Table 4.10: Transition symmetries in D_{4h} for magnetic dipole and electric quadrupole transitions for α, σ, and π-polarizations.

polarization the magnetic field points in the z-direction and hence the matrix element transforms as L_z. The D_{4h} character table (table A.2) shows that the z-component of polar vectors, denoted R_z, transforms as A_{2g}.

$$\sigma(MD) \sim \hat{B} \cdot \vec{L} \sim L_z \sim A_{2g} \tag{4.36}$$

In this manner the transition symmetries for the matrix elements can be determined. The only tricky one is the σ-polarized electric quadrupole transition. It is given by:

$$\sigma(EQ) \sim (\hat{\varepsilon} \cdot \vec{x})(\vec{k} \cdot \vec{x}) \sim E_u \otimes E_u \sim A_{1g} + A_{2g} + B_{1g} + B_{2g} \tag{4.37}$$

The E_u representation for $(\hat{\varepsilon} \cdot \vec{x})$ and $(\vec{k} \cdot \vec{x})$ only constrains the polarization and wave vectors to lie in the Cu-O plane. The additional constraint that they be mutually orthogonal reduces the possible transition symmetries, giving:

$$\sigma(EQ) \sim B_{1g} + B_{2g}. \tag{4.38}$$

The symmetries for magnetic dipole and electric quadrupole transitions in the three polarizations, α, σ and π are given in table 4.10. The transition symmetries for the excitons are as follows:

Selection Rules for Cu d-d Transitions

Transition	α	σ	π
$d_{x^2-y^2} \rightarrow d_{3z^2-r^2}$		EQ	
$d_{x^2-y^2} \rightarrow d_{xy}$		MD	
$d_{x^2-y^2} \rightarrow d_{xz,yz}$	MD, EQ		MD, EQ

Table 4.11: Polarization selection rules for d-d excitons as magnetic dipole and electric quadrupole transitions.

$$\begin{aligned} d_{x^2-y^2} &\rightarrow d_{z^2} \sim B_{1g} \otimes A_{1g} \sim B_{1g} \sim \sigma(EQ) \\ d_{x^2-y^2} &\rightarrow d_{xy} \sim B_{1g} \otimes B_{2g} \sim A_{2g} \sim \sigma(MD) \end{aligned} \tag{4.39}$$

For the matrix elements to be non-zero the symmetry of the exciton transition, and the multipole matrix element must have a common component. Therefore the $d_{x^2-y^2} \rightarrow d_{3z^2-r^2}$ is observed as a σ-polarized electric quadrupole process and the $d_{x^2-y^2} \rightarrow d_{xy}$ as a σ-polarized magnetic dipole process. The selection rules for the four possible d-d excitations of a Cu^{+2} ion with a $d_{x^2-y^2}$ ground state hole are summarized in table 4.11.

The d-d selection rules show that the bare exciton might be observable in the σ-polarization. Experimentally there is no discernible difference between the α and σ-polarized spectra. A simple estimate of the expected absorption strength is needed to understand if the line should be visible in the measurements made so far. The absorption coefficient is simply the cross section times the ion density.

$$\alpha(\omega) = \rho_{Cu}\sigma(\omega) \tag{4.40}$$

Using the absorption cross section from equation 4.34 the integrated absorption for the $d_{x^2-y^2} \rightarrow d_{3z^2-r^2}$ is given by

$$\int \alpha(E)dE = \tfrac{\pi^2}{4}\alpha\,\varepsilon\,\rho\frac{(\hbar\omega)^3}{(\hbar c)^2}\left(\langle r^2\rangle\right)^2\left|\left\langle d_{z^2}\right|\frac{x^2-y^2}{r^2}\left|d_{x^2-y^2}\right\rangle\right|^2 \tag{4.41}$$

where α is the fine structure constant, ε the dielectric constant, and ρ the Cu ion density. This is evaluated using the following values:

$$\begin{aligned}\alpha &= \tfrac{1}{137}\\ \varepsilon &= 5\\ \rho_{Cu} &\approx 10^{22}cm^{-3}\\ \hbar\omega &\approx 0.4\,eV\\ mc^2 &\approx 0.5\,MeV\\ \langle r^2\rangle &= 0.3\,\mathring{A}^2\end{aligned} \tag{4.42}$$

The value for $<r^2>$ is from an Hartree-Fock calculation for d-electrons on a Cu^{+2} ion [60]. The resulting absorption strength is $\int\alpha(E)dE \approx 1.4\times10^{-5}\,cm^{-1}eV$. The intensity for the $d_{x^2-y^2} \rightarrow d_{xy}$ magnetic dipole transition is given by:

$$\int \alpha(E)dE = \pi^2\alpha\,\varepsilon\,\rho\frac{(\hbar c)^2(\hbar\omega)}{\left(mc^2\right)^2}\left|\left\langle d_{z^2}\right|\frac{L_z}{\hbar}\left|d_{x^2-y^2}\right\rangle\right|^2. \tag{4.43}$$

The integrated absorption is 10 cm^{-1}-eV. The total integrated absorption for the exciton-magnon sideband structure from ~ 0.4 to 1.25 eV, measured experimentally, is about 46 cm^{-1}-eV. These results are summarized in table 4.12.

If the $d_{x^2-y^2} \rightarrow d_{xy}$ exciton were at ~ 0.4 eV then the bare exciton line should appear in only the σ-polarization and would represent ~1/5 of the entire absorption strength. However, the α- and σ-polarized spectra are the same. If the $d_{x^2-y^2} \rightarrow d_{3z^2-r^2}$ exciton were at ~ 0.4 eV, it would be unobservable in our data given its weak absorption strength. Furthermore, it would only be observable when the polarization

Transition	$\int \alpha(E)dE\left[cm^{-1}-eV\right]$
$d_{x^2-y^2} \rightarrow d_{3z^2-r^2}$ σ(EQ)	$1.4 * 10^{-5}$
$d_{x^2-y^2} \rightarrow d_{xy}$ σ(MD)	10
Measured Spectra [~ 0.4 - 1.2 eV] α,σ(ED)	46

Table 4.12: Calculated integrated absorption for the Cu^{+2} ion $d_{x^2-y^2} \rightarrow d_{3z^2-r^2}$ and $d_{x^2-y^2} \rightarrow d_{xy}$ transitions in an ionic approximation. The measured experimental absorption for the entire exciton-magnon sideband complex is given as well.

vector and wave vector are at 45° with respect to the Cu-O bond directions. No experiments have been done in this configuration. In thin samples of $Sr_2CuO_2Cl_2$, as shown in figure 3.7, an additional band is seen at ~ 1.5 eV. As discussed earlier in this chapter, electroreflectance and Raman scattering experiments suggest that this band is associated with the $d_{x^2-y^2} \rightarrow d_{xy}$ exciton. The measured integrated absorption strength is ~ 250 cm^{-1}-eV. Thus, it might be possible to observe the $d_{x^2-y^2} \rightarrow d_{xy}$ as a σ-polarized magnetic dipole transition with an absorption strength of 10 cm^{-1}-eV if a <100> oriented sample of La_2CuO_4 can be polished thin enough. The micaceous nature of $Sr_2CuO_2Cl_2$ allows only <001> oriented samples and hence only α-polarized measurements. Again, the only exciton assignment consistent with all the selection rules and the observed spectra is for magnon sidebands to be riding on the $d_{x^2-y^2} \rightarrow d_{3z^2-r^2}$ transition.

Discussion of Other Experiments

Two Magnon Raman Scattering

Raman scattering experiments are a powerful tool for studying electronic transitions in solids. The symmetry of the transition probed is determined by the polarization of the incident and detected scattered light. The scattering rate is given by third order perturbation theory as:

$$W_{f\leftarrow i} \sim \left| \sum_{\alpha\beta} \frac{\langle f|e^{-i\bar{k}_2\cdot\bar{x}}(\hat{\varepsilon}_2\cdot\bar{x})|\beta\rangle\langle\beta|V_p^{\dagger}e^{-i\bar{k}_p\cdot\bar{x}}|\alpha\rangle\langle\alpha|e^{+i\bar{k}_1\cdot\bar{x}}(\hat{\varepsilon}_1\cdot\bar{x})|i\rangle}{\left[\left(E_\beta - E_f\right) - \hbar\omega_2\right]\left[\left(E_\alpha - E_i\right) - \hbar\omega_1\right]} \right|^2 \tag{4.44}$$

where $\hat{\varepsilon}_1$ and $\hat{\varepsilon}_2$ are respectively the incident and scattered light polarization. The operator $V_p^{\dagger}$ creates what ever type of excitation is being scattered off. If the electronic configuration and hence the symmetry of the initial and final states is the same, then for finite matrix elements the symmetry of the scattering creation operator $V_p^{\dagger}$ must be the direct product of the dipole operators $\left(\hat{\varepsilon}_2\cdot\bar{x}\right)\otimes\left(\hat{\varepsilon}_1\cdot\bar{x}\right)$. Let the x and y axis point along the Cu-O bond directions. Then for the incident and scattered polarizations in the Cu-O plane, at 45 degrees from the x and y axis and mutually orthogonal, the transition symmetry is B_{1g}.

$$\left(\hat{\varepsilon}_2\cdot\bar{x}\right)\left(\hat{\varepsilon}_1\cdot\bar{x}\right) \sim (-x+y)(x+y) \sim x^2 - y^2 \sim B_{1g} \tag{4.45}$$

The spectra for two magnon Raman scattering in La_2CuO_4 from Sugai *et al*[61] is shown in Figure 4.11. In the B_{1g} symmetry spectra the strong peak at ~ 3300 cm^{-1} (0.41 eV) has been interpreted as scattering from two magnon excitations. Figure 4.12 compares the electric dipole exciton-magnon absorption presented in this thesis with the B_{1g} Raman spectra taken at an incident laser wavelength of 5145 Å (2.41 eV). The correlation in energy of the features is quite striking and very puzzling.

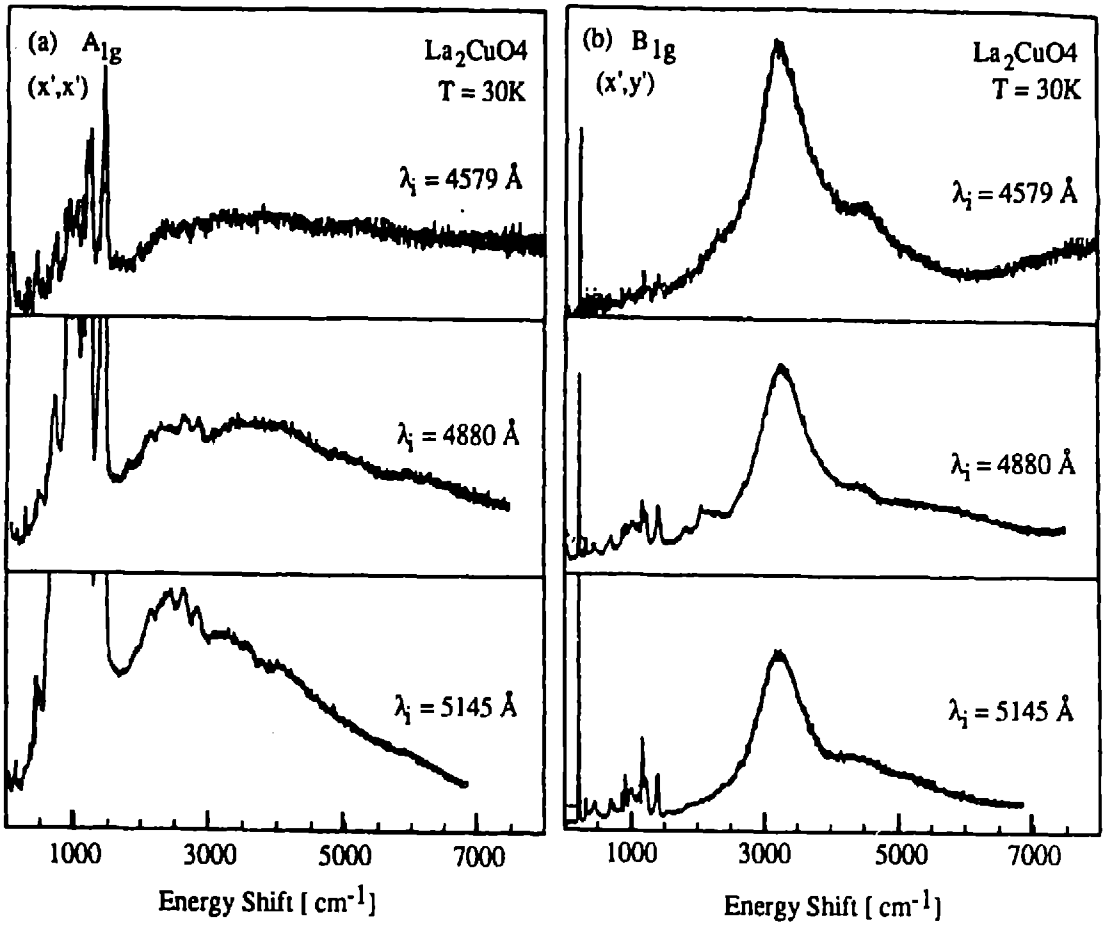

Figure 4.11: Raman spectra for La_2CuO_4 at T = 30K, in A_{1g} and B_{1g} geometry at various incident wavelengths. All spectra are plotted in the same scale. From Sugai [61]

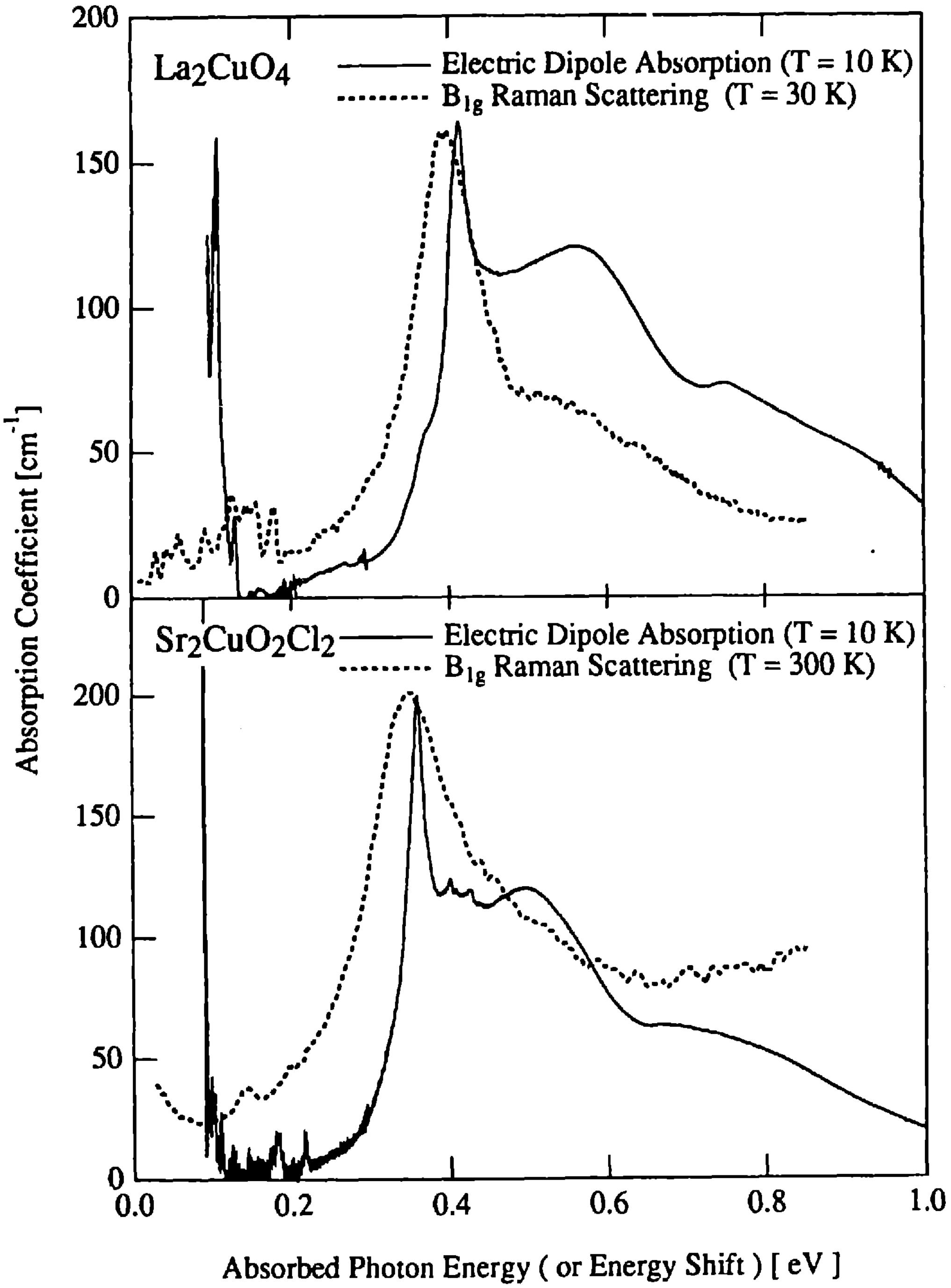

Figure 4.12: Comparison of electric dipole exciton-magnon absorption (solid line) and B_{1g} Raman spectra (dashed line). Top: La_2CuO_4. Raman measured at T = 30 K (Sugai [61]). Bottom: $Sr_2CuO_2Cl_2$. Raman measured at T = 300 K (Tokura *et al.* [12]). Absorption measured at T = 10 K in both.

The polarization experiments presented in Chapter 3 show the exciton-magnon absorption to be electric dipole. The Raman spectra in figure 4.12 arise from even parity B_{1g} symmetry excitations, such as the two magnon excitations in a two dimensional Heisenberg antiferromagnet with classical spins. The $d_{x^2-y^2} \rightarrow d_{3z^2-r^2}$ exciton which we have argued must be at ~ 0.4 eV in La_2CuO_4 is also of B_{1g} symmetry and hence may contribute to the Raman spectra. Using an Ising model it was shown that excitons and magnons interact strongly in undoped Cu-O layer. Therefore the B_{1g} symmetry excitons and two magnon excitations will mix and not exist as distinct excitations. In addition, Raman scattering experiments would probe the spin-allowed exciton which, as discussed earlier in this chapter, should have greater dispersion than the spin-forbidden exciton associated with the 1-magnon sideband. If there really are both 2-magnon and exciton excitations at ~ 0.4 eV, these effects may explain the absence of a sharp exciton peak in the Raman spectra. Further experiments are needed to clarify the nature of the excitation on which the magnon sidebands riding. Several possible experiments are described in chapter 7.

The peak in the measured two magnon Raman scattering spectra is much broader than that predicted by a classical spin model similar to the magnon sideband model of Parkinson discussed earlier. Singh *et al* [62] explain this additional width along with the A_{1g} and B_{2g} spectra (figure 4.11) which are classically forbidden as a consequence of the strong quantum fluctuations in a S =1/2 antiferromagnet. Canali *et al* [63] and Sugai *et al* [61,64] conclude that the width of the two magnon peak and the high energy shoulder can not be explained by quantum fluctuations and hence this provides evidence for a four spin cyclical exchange term in the spin Hamiltonian.

$$H_{4-Spin} = K \sum_{\langle ijkl \rangle} \left\{ (\vec{S}_i \cdot \vec{S}_j)(\vec{S}_k \cdot \vec{S}_l) + (\vec{S}_i \cdot \vec{S}_l)(\vec{S}_j \cdot \vec{S}_k) - (\vec{S}_i \cdot \vec{S}_k)(\vec{S}_j \cdot \vec{S}_l) \right\} \qquad (4.46)$$

Where the four sites i, j, k, and l form a square with a copper ion at each corner.

None of these explanations of the Raman scattering spectra consider the possibility of an additional B_{1g} excitation of electronic origin such as the $d_{x^2-y^2} \rightarrow d_{3z^2-r^2}$ exciton. The recent high energy shift (~1-2 eV) Raman scattering of Liu *et al* [59] show A_{2g} symmetry ($d_{x^2-y^2} \rightarrow d_{xy}$) excitations at ~1.5 eV in several layered copper oxides. It is clear that further experimental and theoretical work is needed to clearly identify the basic excitations and their mutual interactions.

Van Vleck Susceptibility

As discussed previously, the magnon sideband polarization selection rules indicate that the low energy exciton must be either the $d_{x^2-y^2} \rightarrow d_{3z^2-r^2}$ or $d_{x^2-y^2} \rightarrow d_{xy}$ transition. Electroreflectance and high energy-shift Raman scattering experiments indicate the $d_{x^2-y^2} \rightarrow d_{xy}$ transition is at ~1.5 eV and hence it must be the $d_{x^2-y^2} \rightarrow d_{3z^2-r^2}$ transition at ~0.4 eV. This section continues this argument by showing that several magnetic properties are consistent with our exciton assignment and inconsistent with the reverse assignment.

The interaction of a magnetic moment with an applied magnetic field is given by the Hamiltonian $H = -\vec{\mu} \cdot \vec{B}$, with $\vec{\mu} = \mu_B\left(\vec{L} + 2\vec{S}\right)$ where μ_B is the Bohr magneton and $\hbar = 1$. Van Vleck susceptibility is an induced orbital contribution to the magnetic response. In the following discussion the spin contribution will be ignored, hence $\mu = \mu_B \vec{L}$. For the copper d-states involved in the crystal field excitons all components of the angular momentum vanish even though the total angular momentum of the state is L=2.

$$\begin{aligned} \langle x^2 - y^2 | L_z | x^2 - y^2 \rangle &= \tfrac{1}{2}\left(\langle 2,2| + \langle 2,-2|\right) L_z \left(|2,2\rangle + |2,-2\rangle\right) = 0 \\ \langle x^2 - y^2 | L^2 | x^2 - y^2 \rangle &= \tfrac{1}{2}\left(\langle 2,2| + \langle 2,-2|\right) L^2 \left(|2,2\rangle + |2,-2\rangle\right) = L(L+1) = 6 \end{aligned} \tag{4.47}$$

This effect is called angular momentum quenching. Now consider the effect of a magnetic field on a particle with a $d_{x^2-y^2}$ ground state. Since the unperturbed ground state has no orbital magnetic moment there is no interaction at the zeroeth order. For the sake of discussion let the magnetic field point in the z-direction, hence $H = -\mu_B L_z B$. Since the d_{xy} state is simply the $d_{x^2-y^2}$ rotated by 45 degrees about the z-axis, these states will be coupled by the L_Z operator and mixed in first order perturbation theory by the magnetic interaction,

$$\left|x^2-y^2\right\rangle^{(1)}=\left|x^2-y^2\right\rangle+\frac{\mu_B B}{\Delta_{xy}}\left|xy\right\rangle\left\langle xy\right|L_z\left|x^2-y^2\right\rangle \tag{4.48}$$

where $\Delta_{xy}=E(xy)-E\left(x^2-y^2\right)$. The first order perturbed ground state has an orbital magnetic moment in the z-direction given by:

$$\frac{\langle\mu_z\rangle}{\mu_B}=2\,\frac{\mu_B B}{\Delta_{xy}}\left|\left\langle xy\right|L_z\left|x^2-y^2\right\rangle\right|^2. \tag{4.49}$$

This paramagnetic response is known as Van Vleck paramagnetism. The pertinent matrix elements for magnetic fields both parallel and perpendicular to the Cu-O layers are:

$$\begin{gathered}\left\langle xy\right|L_z\left|x^2-y^2\right\rangle=2i\\ \left\langle xz\right|L_y\left|x^2-y^2\right\rangle=\left\langle yz\right|L_x\left|x^2-y^2\right\rangle=-i\end{gathered} \tag{4.50}$$

The factor of two arises from the fact that when the $d_{x^2-y^2}$ orbital is rotated around the x-axis it will not fully overlap the d_{yz} orbital. The result of this is a factor of 4 in the Van Vleck magnetic moment for in plane versus out of plane magnetic fields, assuming equal energy denominators.

$$\begin{aligned}B\,//\,\hat{z}:&\quad \frac{\langle\mu_z\rangle}{\mu_B}=8\frac{\mu_B B}{\Delta_{xy}}\\ B\perp\hat{z}:&\quad \frac{\langle\mu_{x(y)}\rangle}{\mu_B}=2\frac{\mu_B B}{\Delta_{yz(xz)}}\end{aligned} \tag{4.51}$$

As long as $\frac{\Delta}{kT}>>1$ the Van Vleck paramagnetism will be temperature independent. For exciton energies of ~0.4 eV or higher this holds for room temperature and below.

In a real material like La_2CuO_4 there will also be a diamagnetic response from the ion cores as well as a spin response. In 3D antiferromagnets, such as MnF_2, the spin susceptibility is very anisotropic [65]. However, in a perfect 2D Heisenberg antiferromagnet there is no long range order except at T=0. The peak at the Neel temperature in La_2CuO_4 is a consequence of the weak ferromagnetic moment of each layer

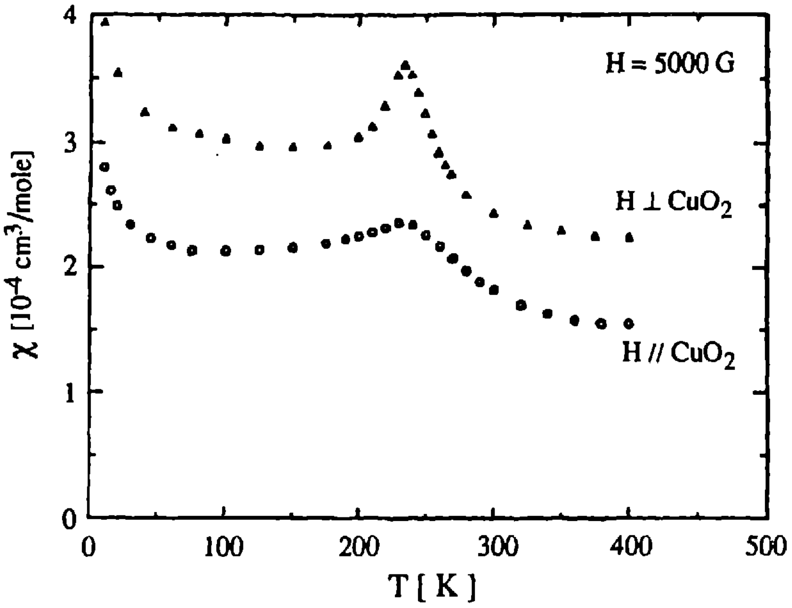

Figure 4.13: Magnetic susceptibility in La_2CuO_4 as a function of temperature with a core susceptibility of -9.9 x 10^{-5} cm^3/mole subtracted. Data is shown for both the magnetic field parallel and perpendicular to the Cu-O layers. From Ph.D. thesis of T. Thio [35].

due to canting of the CuO_6 octahera [33]. For this discussion the important result is that the spin response should be isotropic. All of this makes estimating the absolute magnetic response difficult. However, the difference between the in-plane and out-of-plane response due to the Van Vleck paramagnetism is easy to estimate from equation 4.51. Using the copper ion density for La_2CuO_4 of $N = 1.05 \cdot 10^{22}\ cm^{-3}$ and changing units to the molar susceptibility we find:

$$\Delta\chi = \chi_{\perp} - \chi_{//} = 2.6 \cdot 10^{-4}\left(\frac{1}{\Delta_{xy}[eV]} - \frac{1}{4\Delta_{xz}[eV]}\right) cm^3/mole. \tag{4.52}$$

Using Δ_{xy} = 1.4 eV and Δ_{xz} = 1.6 eV from the electroreflectance experiments of Falck *et al* [58] gives $\Delta\chi$ = 1.4 cm^3/mole. Figure 4.13 shows the magnetic susceptibility data of T. Thio [35] for La_2CuO_4 with the magnetic field parallel and perpendicular to the Cu-O layers. As can be seen from the sharp peak the Neel temperature for this sample is roughly T_N = 240 K. The difference between the in-plane and out-of-plane response is reasonably temperature independent and roughly 1 cm^3/mole at T = 100 K. Given the simplicity of the calculation for the Van Vleck susceptibility this agreement is very good. Note for Δ_{xy} = 0.4 eV the calculated anisotropy is roughly four times larger and in poor agreement with the data. This provides more evidence that the ~0.4 eV exciton is not $d_{x^2-y^2} \to d_{xy}$.

Spin Orbit Coupling

In a similar fashion to the case of Van Vleck paramagnetism, if the $d_{x^2-y^2} \to d_{xy}$ were at ~ 0.4 eV, the electron spin g-factor would be highly anisotropic due to spin orbit coupling. This would result in large anisotropies for the spin susceptibility and the anisotropic exchange, neither of which is seen experimentally[66]. To estimate the magnitude of the g-factor anisotropy consider an ion with a single unpaired spin in an orbital $d_{x^2-y^2}$ state. The g-factor is determined from the energy difference of the electron spin being parallel or antiparallel to the applied magnetic field $\Delta E = g\mu_B H$, hence $g_i = 2\langle L_i + 2S_i\rangle = 2 + 2\langle L_i\rangle$. The spin orbit interaction, $H = \lambda\, \vec{L}\cdot\vec{S}$, mixes different orbital states into the unperturbed ground state depending on the orientation of the spin, which is along the magnetic field direction. As this calculation is almost identical to the one for Van Vleck paramagnetism just the results will be given.

$$\begin{aligned} B \,//\, \hat{z}:&\quad g_z = 2 - \frac{8\lambda}{\Delta_{xy}}\cdot(Cov) \\ B \perp \hat{z}:&\quad g_{x(y)} = 2 - \frac{2\lambda}{\Delta_{yz(xz)}}\cdot(Cov) \end{aligned} \tag{4.53}$$

The term (Cov) is a correction from the ionic approximation due to covalency. Using values of $(Cov) \approx 0.7$, $\lambda \approx -0.1\,eV$ [67], Δ_{xy} = 1.4 eV and Δ_{yz} = 1.6 eV yields g_z = 2.4 and g_x = 2.1. In contrast, if Δ_{xy} = 0.4 eV then g_z = 3.4 which would result in large anisotropies. Again, although both the $d_{x^2-y^2} \to d_{3z^2-r^2}$ and $d_{x^2-y^2} \to d_{xy}$ exciton transition are consistent with the magnon sideband selection rules, the lack of a highly anisotropic g-factor shows that the $d_{x^2-y^2} \to d_{xy}$ transition is not at ~ 0.4 eV.

Polarized X-Ray Absorption Spectra

Polarized x-ray absorption experiments are simply high energy electric-dipole absorption experiments. Core state electrons can be excited to the empty valence states. For this discussion it will suffice to consider a simple CuO_6 cluster as shown if figure A.1. For the undoped case, the orbitals involved in the ground state can be written as:

$$|gs\rangle = Cud^9 + Cud^{10}\underline{O2p}. \qquad (4.54)$$

In this notation only the partially filled shells are noted. Furthermore, the Cu-states are given in terms of electrons and the oxygen states in terms of holes, as indicated by the underbar. This is the notation typically used to discuss this type of experiment. Equation 4.54 says that ground state is an admixture of states with the one hole either on the Cu-site (Cu d^9) or the O-site (Cu d^{10} $\underline{O2p}$). An x-ray can be absorbed by exciting an O1s electron to the empty 02p orbital of the second term in equation 4.54. This is known as an O K-line. Of course other transitions are possible, but this is the one of interest. The final state is given by:

$$|f\rangle = \underline{O1s}\,Cud^{10}. \qquad (4.55)$$

Since there is only one possible final state associated with the O1s→O2p transition, there will only be one line. This is not very interesting. Now consider the doped case with two holes in a cluster. The initial and final states relevant to O K-line absorption are:

$$\begin{aligned} |i\rangle &= Cud^8 + Cud^9_{z^2}\underline{O2p} + Cud^9_{x^2-y^2}\underline{O2p} \\ |f\rangle &= \underline{O1s}\,Cud^9_{z^2} + \underline{O1s}\,Cud^9_{x^2-y^2} \end{aligned}. \qquad (4.56)$$

An additional subscript has been added to the Cu states to indicate the empty state. The final state is now composed of two possible final states and hence there should be two lines associated with the O1s→O2p transition. As both final states have a Cu d^9 configuration, this experiment probes the energy difference between having the hole in the $d_{x^2-y^2}$ or $d_{3z^2-r^2}$ orbital. Except for the presence of the O1s core hole, this is the energy difference for the $d_{x^2-y^2} \to d_{3z^2-r^2}$ exciton which the magnon sideband absorption spectra suggest might be at ~0.4 eV. X-ray absorption experiments of this type have been done by Li *et al* [68] on La_2CuO_4. They do not resolve two lines but instead get one broad line. Based on the instrumental resolution, they put a ceiling of ~ 0.5 eV on the energy difference between the two final states. It is important to note that this is not a positive identification of the energy difference and that the exciton of interest to the magnon sidebands does not have a core hole. However, this negative result is consistent with a Cu $d_{x^2-y^2} \to d_{3z^2-r^2}$ exciton as low as ~ 0.4 eV.

Multimagnon Sidebands

One of the striking features of the magnon sideband absorption spectra of the undoped copper oxides is the strong multimagnon sidebands. The Tanabe mechanism discussed earlier is a first order perturbation effect incorporating off-diagonal exchange. Multimagnon sidebands in a classical spin theory can be generated by higher order perturbation terms. As shown in equation 4.11 the small expansion parameter is the off-diagonal exchange divided by the energy to the first on site odd parity state. To estimate the effect of higher order terms assume the off-diagonal exchange is as strong as the nearest neighbor diagonal exchange, J ~ .1 eV and that ΔE ~ 2 eV which is the charge transfer energy. Since the absorption depends on the square of the matrix element this would give a two magnon absorption strength relative to the one magnon sideband of roughly $(0.1/2)^2 = 0.003$ or less than one percent. This is clearly not the case. Another explanation is needed.

In antiferromagnets multimagnon sidebands can also occur due to quantum fluctuations. A variant of this effect was discussed by Cowley *et al*. [69] for analogous processes in neutron scattering. The purpose of this section is to show how this effect arises in quantum antiferromagnets and show that it will be particularly strong in spin 1/2 systems such as the undoped copper oxides. The following discussion is based on the presentation of magnons in Kittel's *Quantum Theory of Solids* [70] (QTS). We will accept the results derived in Kittel and try to apply them to understanding the origin of the multimagnon sidebands. As previously discussed the off diagonal exchange mechanism of Tanabe can be recast in a spin operator formalism. Equation 4.14, repeated here gives the effective dipole moment due to off-diagonal exchange as.

$$\vec{P}_{eff}\left(\varphi_a' \leftarrow \varphi_a\right) = \vec{\Pi}_{a'a,b}\left(\vec{s}_{a'a} \cdot \vec{s}_b\right) \tag{4.57}$$

where the operator $\bar{S}_{a'a}$ creates an exciton at site a with a possible change of spin.

$$\vec{s}_{a'a} = \sum_{m,m'} c_{a'm'}{}^{*}c_{am}\langle m'|\vec{s}|m\rangle \tag{4.58}$$

Since we are interested in the creation of multimagnon sidebands we can ignore the exciton creation and concentrate on the spin operators. However, without the exciton creation the term involving $\bar{S}_{a'a} \cdot \bar{S}_b$ and $\bar{S}_a \cdot \bar{S}_{b'b}$ would exactly cancel for an ion pair with a center of symmetry.[47]. That is, there is no electric dipole absorption due to only two magnon absorption. Classically, the spin flip term involving $\left(S_{a'a}^{+}S_b^{-} + S_{a'a}^{-}S_b^{+}\right)$ creates an exciton-magnon pair. As will be shown, quantum effects also make the exciton-3-magnon processes allowed via this term as well as the exciton-2-magnon and exciton-4-magnon absorption via the diagonal term $S_{a'a}^{z}S_b^{z}$.

The spin Hamiltonian for the Heisenberg antiferromagnet is given by.

$$H = J\sum_{<jl>} \vec{S}_j \cdot \vec{S}_l \tag{4.59}$$

with J positive for an antiferromagnet. At each site there are three components of spin S_x, S_y, and S_z which are not independent but coupled by the constraint $|S|^2 = S(S+1)$. In order to work with only two on-site operators, Holstein and Primakoff introduced the following transformation which carries their names.

$$
\begin{aligned}
S_{aj}^{+} &= \sqrt{2S}\left(1-\frac{a_j^{+}a_j}{2S}\right)^{1/2} a_j \\
S_{aj}^{-} &= \sqrt{2S}\,a_j^{+}\left(1-\frac{a_j^{+}a_j}{2S}\right)^{1/2} \\
S_{bl}^{+} &= \sqrt{2S}\,b_l^{+}\left(1-\frac{b_j^{+}b_j}{2S}\right)^{1/2} \\
S_{bl}^{-} &= \sqrt{2S}\left(1-\frac{b_j^{+}b_j}{2S}\right)^{1/2} b_l \\
S_{aj}^{z} &= S-a_j^{+}a_j \\
-S_{bl}^{z} &= S-b_l^{+}b_l
\end{aligned}
\tag{4.60}
$$

In the ground state the a sublattice spins point up and the b down. A Zeeman term representing the crystal anisotropy can be added to provide a preferred spin orientation and therefore a well defined ground state. We will just assume an oriented ground state. The indices j and l indicate the ion site on sublattices a and b respectively. The operators a_j^{+} and a_j create and destroy spin deviations at the a-sublattice site j. Note that in creating a spin deviation on the up sublattice, the operator a_j^{+} flips an up spin to a down spin. In the high spin limit the square roots are well approximated by one. The simple spin wave theory dispersion relations derived from this approximation agree with more sophisticated calculations[71] and experiments [72] to with in about 10% in the lamellar copper oxides. Hence we will take the simple spin wave solution presented by Kittel as basically valid and expand upon it in an iterative manner.

As a first step towards diagonalizing the Hamiltonian spin wave operators for the separate sublattices are introduced according to:

$$
\begin{aligned}
c_k &= \tfrac{1}{\sqrt{N}}\sum_j e^{+i\vec{k}\cdot\vec{x}_j} a_j & \qquad c_k^{+} &= \tfrac{1}{\sqrt{N}}\sum_j e^{-i\vec{k}\cdot\vec{x}_j} a_j^{+} \\
d_k &= \tfrac{1}{\sqrt{N}}\sum_l e^{-i\vec{k}\cdot\vec{x}_l} b_l & \qquad d_k^{+} &= \tfrac{1}{\sqrt{N}}\sum_l e^{+i\vec{k}\cdot\vec{x}} b_l^{+}
\end{aligned}
\quad . \tag{4.61}
$$

These spin wave operators create and destroy spin deviation waves on their respective sublattices. The Hamiltonian is now written as,

$$\begin{gathered} H = 2JSz\sum_k \left[\gamma_k\left(c_k^+ d_k^+ + c_k d_k\right) + \left(c_k^+ c_j + d_k^+ d_k\right)\right] \\ \gamma_k = z^{-1}\sum_\delta e^{+i\vec{k}\cdot\vec{\delta}} \end{gathered} \tag{4.62}$$

with z being the number of nearest neighbors and γ_k a sum over nearest neighbor vectors, δ. Fourier transforming to the spin wave variables has simplified the Hamiltonian but it is not diagonalized yet. To achieve this the following Bogoliubov transformation is made:

$$\begin{aligned} \alpha_k &= u_k c_k - v_k d_k^+ \\ \alpha_k^+ &= u_k c_k^+ - v_k d_k \\ \beta_k &= u_k d_k - v_k c_k^+ , \\ \beta_k^+ &= u_k d_k^+ - v_k c_k \end{aligned} \tag{4.63}$$

These operators couple the two sublattices and the resulting Hamiltonian is given by:

$$H = \sum_k \omega_k\left(\alpha_k^+\alpha_k + \beta_k^+\beta_k + 1\right). \tag{4.64}$$

The Hamiltonian is now diagonal and the resulting excitations are magnons. There are two degenerate magnons at each wave vector. In the simple spin wave theory these excitations are non-interacting. Note that each magnon creation operator α^+ and β^+ create spin deviations on both the up and down sublattices. To obtain the proper commutation relations for the α and β operators there is a constraint on the parameters v and u:

$$u_k^2 - v_k^2 = 1. \tag{4.65}$$

To see the origin of the multimagnon sidebands consider the S_z operator, $S_a^z = S - a_j^+ a_j$. Plugging in the spin wave operators for the a operators yields:

$$S^z_{aj} = S - \tfrac{1}{N}\sum_{kk'} e^{+i(\vec{k}-\vec{k}')\cdot\vec{x}_j} c_k^+ c_{k'}. \tag{4.66}$$

Expanding the up-sublattice spin wave operators c_k^+ and c_k via the Bogoliubov transformation gives:

$$c_k^+ c_{k'} = u_k u_{k'} \alpha_k^+ \alpha_{k'} + v_k v_{k'} \beta_k \beta_{k'}^+ + v_k u_{k'} \beta_k \alpha_{k'} + \underbrace{u_k v_{k'} \alpha_k^+ \beta_{k'}^+}_{\substack{\text{2-magnon}\\ \text{creation}}}. \tag{4.67}$$

As noted, the last term generates two magnons. Hence the site operator S^Z_{aj} can generate a pair of α and β magnons. From equation 4.63 we see that α magnons change the total z component by -1 and β magnons by +1, leaving the total S_Z unchanged. As will be shown, the magnitude of the coefficient $u_k v_{k'}$ depends on the deviation of the ground state staggered magnetization from the saturated value of $\langle S^z_{aj} \rangle = S$. In other words, the generation of α,β magnon pairs by the S^Z_{aj} operator scales with the magnitude of the quantum fluctuations and hence is a much larger effect in the spin 1/2 copper oxides than the higher spin materials previously studied. The triple product terms such as $a_j^+ a_j a_j$ obtained by expanding the square roots in equation 4.60 for the on site spin raising and lowering operators will generate 3-magnon excitations in a similar fashion.

As shown by Kittel, u_k and $v_{k'}$ are real and related by the constraint of equation 4.65. Therefore u_k is always non-zero with $|u_k| \geq 1$. The generation of 2-magnon pairs will basically depend on the magnitude of v_k, which as will now be shown is a measure of the quantum fluctuations. The following calculation of the zero-point sublattice magnetization is taken directly for Kittel's book. The total z-component of spin for the up sublattice is given by:

$$\begin{aligned} \langle S^a_z \rangle = \left\langle \sum_j S^z_{aj} \right\rangle &= NS - \sum_k \langle c_k^+ c_k \rangle \\ &= NS - \sum_k \left\langle u_k^2 \alpha_k^+ \alpha_k + v_k^2 \beta_k \beta_k^+ + \text{cross - terms} \right\rangle \end{aligned} \tag{4.68}$$

At zero temperature there are no thermal magnons and hence the magnon number operators and off diagonal terms yield zero. Using the commutation relation $\left[\beta_k, \beta_k^+\right] = 1$ to evaluate $\beta_k \beta_k^+$ yields the following result:

$$\sum_k v_k^2 = NS - \left\langle S_a^z \right\rangle. \tag{4.69}$$

Since $v_k^2 \geq 0$ the average magnitude of v_k is a measure of the quantum fluctuations. For the 2D, S=1/2, Heisenberg antiferromagnet on a square lattice the deviation has been calculated [73] as $\left|\left\langle S_z \right\rangle\right| \cong 0.31$ for each spin site.

For the optical absorption the pertinent matrix element coupling as given by equation 4.67 $u_k v_{k'}$. To estimate the magnitude of the coupling we can use the Brillouin zone averaged values given by:

$$\begin{aligned} (\bar{v})^2 &= \tfrac{1}{N} \sum_k v_k^2 = S - \langle S_z \rangle \cong 0.2 \\ (\bar{u})^2 &= 1 + (\bar{v})^2 = 1.2 \\ (\bar{u}\bar{v})^2 &\cong 0.24 \end{aligned} \quad . \tag{4.70}$$

This crude estimate which ignores the variation of the coupling across the Brillouin zone indicates that the strength of the 2-magnon sideband should be roughly one quarter of the 1-magnon sideband. This is much more in accord with the measured spectra than the less than one percent estimate based on higher order classical spin processes. Therefore we conclude that the strong multimagnon sidebands observed are a direct consequence of the large quantum fluctuations of spin 1/2 systems.

The variation of the coupling across the Brillouin zone will be largely determined by v_k. Kittel gives an expression for v_k as:

$$v_k^2 = \frac{1}{2}\left[\frac{1}{\sqrt{1-\gamma_k^2}} - 1\right]. \tag{4.71}$$

For a 2D square lattice this yields:

$$v_k^2 = \tfrac{1}{2}\left[\frac{1}{\sqrt{1-\left(\dfrac{\cos(k_x a)+\cos(k_y a)}{2}\right)^2}} - 1\right]. \qquad (4.72)$$

This vanishes on the zone boundary and hence zone boundary magnons do not generate multimagnon sidebands. This is in agreement with similar remarks by Cowley with regards to two magnon scattering of neutrons.[69]. Furthermore the coupling diverges at the zone center. This raises the intriguing question of whether the sharp peak seen at roughly the exciton energy is a consequence of this divergence. To study this, a more careful investigation is needed.

In this section we have seen that the strong multimagnon sidebands observed in the undoped copper oxides are a consequence of the large quantum fluctuations of spin 1/2 systems. The one and three magnon sidebands are generated by the off diagonal spin terms $\left(S^{+}_{a'a}S^{z}_{b} + S^{-}_{a'a}S^{+}_{b}\right)$ and the two and four magnon sidebands by the diagonal term $S^{z}_{a'a}S^{z}_{b}$. Furthermore, the divergence of the exciton-2-magnon matrix elements at the zone center raises intriguing questions about the origin of the sharp low energy peak seen at the exciton energies. Clearly, a proper calculation of the magnon sideband absorption spectra including both quantum spins and exciton-magnon interactions is needed.

Exciton-Magnon Bound States

The electric dipole nature of the sharp line at ~ 0.4 eV is as of yet unexplained. One possible explanation previously mentioned is the divergence at the Brillouin zone center of matrix elements for exciton-2-magnon absorption. Another possibility is a true exciton-magnon bound state. It has already been shown that the excitons and magnons interact quite strongly, with an interaction energy of ~$J/2$. Exciton-magnon bound states have been observed in MnF_2[54] and $YbCrO_3$[74]. Figure 4.14 shows

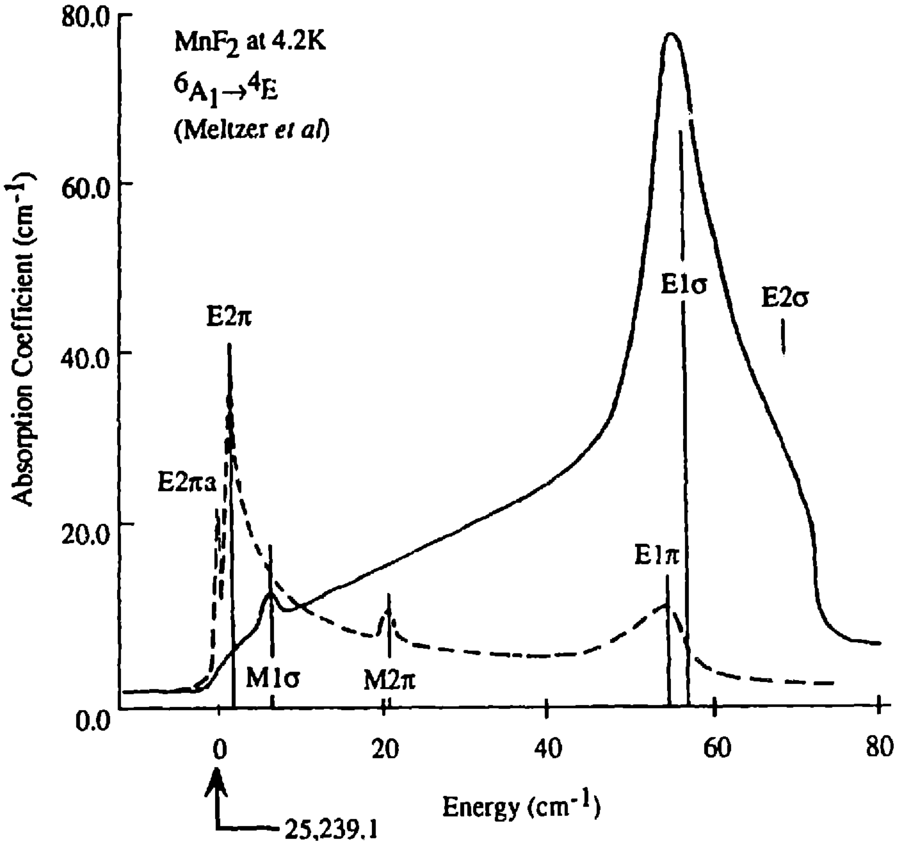

Figure 4.14: Exciton-magnon absorption in MnF$_2$ associated with the $^6A_1 \to ^4E$ exciton. The peak denoted E2πa is attributed to an exciton-magnon bound state. From Meltzer *et. al.* [13].

magnon sideband absorption spectra in MnF$_2$ of Meltzer *et. al.* [54]. The peak labeled E2πa is attributed to an exciton-magnon bound state associated with the magnon sideband E2π. In order for the sharp peak observed in the copper oxides to be an exciton-magnon bound state, the binding would have to be much stronger than in materials such as MnF$_2$. In addition to J being much larger in the copper oxides, the spin systems are well modeled as two dimensional Heisenberg antiferromagnets and binding is generally stronger in lower dimensions.

There is also an inter-sublattice exciton-spin flip resonance [43,75]. This may be quite strong in the lamellar copper oxides being studied. In the same manner as the discussion of exciton dispersion earlier in this chapter we will consider excitons and spin flips on an ion pair. In order to have electric dipole absorption, the total z-component of spin for the excited state and the ground state must be conserved. Hence, the exciton must be a spin-forbidden exciton. For spin-forbidden excitons with neighboring spin flips, the ground state and excitons on sites A and B are given as:

$$\begin{aligned} |gs\rangle &= \left(|a\uparrow(1)b\downarrow(2)\rangle - |a\uparrow(2)b\downarrow(1)\rangle\right)/\sqrt{2} \\ |A\rangle &= \left(|A\downarrow(1)b\uparrow(2)\rangle - |A\downarrow(2)b\uparrow(1)\rangle\right)/\sqrt{2}. \\ |B\rangle &= \left(|a\downarrow(1)B\uparrow(2)\rangle - |a\downarrow(2)B\uparrow(1)\rangle\right)/\sqrt{2} \end{aligned} \tag{4.73}$$

The notation is the same as in the section on exciton dispersion. Capital A and B denote excitons at sites a and b respectively. The arrows indicate the site spin direction and the numbers the electron number. The coupling of states $|A\rangle$ and $|B\rangle$ by the coulomb interaction will have both a direct and an exchange term. The exchange term will be spin blocked and the direct term cast as interacting charge clouds is given by:

$$\langle B|\frac{e^2}{r_{12}^2}|A\rangle = \int d1d2\ a^*(1)A(1)\frac{e^2}{r_{12}^2}B^*(2)b(2). \tag{4.74}$$

This will result in states $|A\rangle$ and $|B\rangle$ mixing into a bonding and antibonding state. The energy of the bonding state will be lowered with respect to the non-interacting states by the coupling matrix element $\langle A|e^2/r_{12}|B\rangle$. Two unit charges four angstroms apart have an unscreened coulomb interaction of nearly 1 eV. This will be reduced by screening via $\varepsilon(q,\omega)$ at $q \approx \pi/a$. Recall that the optical dielectric constant, $\varepsilon(0,\omega)$, is ~ 5 in La_2CuO_4. The effects of the different states at each ion for the exciton and ground state as well as the distributed nature of the electron wave functions is hard to estimate. However, the strength of the unscreened coulomb interaction suggests this may be pertinent on the energy scale of the magnons.

Presently we can not make a strong case for or against the sharp low energy peak being an exciton-magnon bound state. We only point out that such states have been seen in other materials, would be electric dipole coupled to the ground state and should be enhanced by the two dimensionality of the lamellar copper oxides. However, it seems unlikely that the bound state would be at exactly the same energy as the origin of the magnon sidebands. Hence, this is probably not the correct explanation for the sharp peak.

Summary of Joint Exciton-Magnon Absorption

As presented in Chapter 3, weak electric dipole allowed absorption occurs in the lamellar copper oxides La_2CuO_4, $Sr_2CuO_2Cl_2$, Pr_2CuO_4 and Nd_2CuO_4 in the energy range from ~ 0.4 to 1.2 eV. In addition measurements on thin samples of $Sr_2CuO_2Cl_2$ show an additional band of absorption at ~1.5 eV. This chapter has shown that this absorption is associated with joint exciton-magnon excitations often referred to as magnon sidebands.

A review of previous work, mostly from the 1960's, showed that magnon sideband absorption is a common feature in antiferromagnetic insulators. As proposed by Tanabe *et al.* [47] electric dipole magnon sideband absorption is allowed by off-diagonal mixing of odd parity excited states into the exciton and ground states. As shown by a simple Ising model and the classical spin model of Parkinson[50] the exciton-magnon interaction reduces the energy shift of the magnon sideband peak from the zone boundary magnon energy of 2J to roughly 3J/2. The structure seen in the sideband absorption in La_2CuO_4 and $Sr_2CuO_2Cl_2$ suggest an exciton energy very close to the sharp peak with one, two, three, and four magnon sideband absorption. The polarization selection rules for the magnon sidebands indicate the exciton at ~ 0.4 eV must be either the $d_{x^2-y^2} \rightarrow d_{3z^2-r^2}$ or the $d_{x^2-y^2} \rightarrow d_{xy}$ transition if it is a Cu d-d exciton.

Recent electroreflectance and Raman scattering experiments show that an excitation with the same symmetry as $d_{x^2-y^2} \rightarrow d_{xy}$ exists at ~ 1.5 eV in the copper oxide materials. In $Sr_2CuO_2Cl_2$ our measurements show a second absorption band at this energy, suggesting that the $d_{x^2-y^2} \rightarrow d_{xy}$ exciton is at ~ 1.5 eV. The selection rules and estimated oscillator strengths for the bare d-d excitons as magnetic dipole or electric quadrupole processes were calculated. These show that if the $d_{x^2-y^2} \rightarrow d_{xy}$ transition were at ~ 0.4 eV, then the bare exciton would be observable as a σ-polarized magnetic dipole transition with an integrated strength of 1/4 of the entire magnon sideband absorption. Furthermore, it would not be observable in the α-polarization. The measured α and σ-polarized spectra are identical. This shows that the $d_{x^2-y^2} \rightarrow d_{xy}$ exciton is not at ~ 0.4 eV. The same analysis shows that if the $d_{x^2-y^2} \rightarrow d_{3z^2-r^2}$ were at ~ 0.4 eV, its integrated strength would be about six orders of magnitude smaller and hence unobservable. Hence a $d_{x^2-y^2} \rightarrow d_{3z^2-r^2}$ at ~ 0.4 eV is consistent with the lack of an observed direct d-d line. Two magnon Raman scattering experiments in the B_{1g} ($d_{x^2-y^2} \rightarrow d_{3z^2-r^2}$) symmetry show a strong but broad peak at ~ 0.4 eV. This has been previously interpreted as due entirely to 2-magnon excitations, but to date the line shape has not been fully explained. It is possible that the measured Raman scattering has an excitonic component as well. In fact, due to the strong magnon-exciton interaction and near degeneracy these excitations will mix.

Due to the coupling of the $d_{x^2-y^2}$ and d_{xy} states by the L_z operator, if the $d_{x^2-y^2} \rightarrow d_{xy}$ exciton were at ~ 0.4 eV there would be large anisotropies in the g-factor and thereby the spin susceptibility and the anisotropic exchange, as well as a large and anisotropic Van Vleck susceptibility. None of these are seen. In fact, the measured anisotropy of the Van Vleck susceptibility is in good agreement with a $d_{x^2-y^2} \rightarrow d_{xy}$ exciton energy of ~1.5 eV.

Estimates of the multimagnon sideband strength due to higher order classical processes or quantum fluctuations in the first order process indicate that the strong multimagnon absorption observed is a direct consequence of the strong quantum fluctuations in a spin 1/2 system. Furthermore, the divergence of the two magnon sideband matrix element at the Brillouin zone center raises the interesting question of whether the observed sharp peak is simply part of the two magnon sideband. Another possibility is that the sharp peak is an exciton-magnon bound state.

In summary, the absorption in the undoped lamellar copper oxides in the energy range of ~ 0.4-1.2 eV is ascribed to strong multimagnon sidebands to an electric-dipole forbidden excitation at ~ 0.4 eV.

If the later excitation is a Cu d-d exciton, then it must be the $d_{x^2-y^2} \rightarrow d_{3z^2-r^2}$ exciton. However, if this is correct then the low energy of the exciton and the absorption mechanism for the sharp line are not understood. The similarity in energy of the sharp line and the peak in the 2-magnon Raman spectra as seen in figure 4.12 suggests that the excitation may be more complex. In either case, the mechanism of the sharp line is not yet understood. Chapter 5 discusses the exciton energy.

Chapter 5: Calculations of Exciton Energies

Although, the magnon sideband absorption process discussed in Chapter 4 does an excellent job of explaining the measured absorption spectra, this explanation is not without controversy. If the sidebands are associated with a Cu d-d exciton, then the energy ascribed to the copper ion $d_{x^2-y^2} \rightarrow d_{3z^2-r^2}$ exciton is ~ 0.4 eV. While cluster calculations predict that the $d_{x^2-y^2} \rightarrow d_{3z^2-r^2}$ exciton is the lowest energy exciton, the energies are in the range of 0.9 - 1.6 eV [76-79]. The point-ion calculations presented in this chapter predict that the $d_{x^2-y^2} \rightarrow d_{xy}$ transition is the lowest in energy. As discussed at length in Chapter 4, an energy of ~ 0.4 eV for the $d_{x^2-y^2} \rightarrow d_{xy}$ exciton is not consistent with a variety of experimental results. For point ion calculations, the crystal-field Hamiltonian can be written in terms of operators that are second and fourth order in the orbital angular momentum operators. To explain the low energy of the $d_{3z^2-r^2}$ state relative to the d_{xy} we must assume that the second order terms are more effectively screened than the fourth order ones. Furthermore the similar energy for the $d_{x^2-y^2} \rightarrow d_{3z^2-r^2}$ exciton in the four materials initially appears surprising because of their differing out-of-plane structure. However, point ion calculations give very similar level spacings for these materials because the primary energy scale is set by the four nearest oxygen ions. The screening is expected to be similar as well.

This chapter presents two simple calculations to address these issues. First a point ion calculation is presented. Then a simple cluster calculation examines the effect of screening by the neighboring copper holes on the exciton energy. Although too simple to give realistic absolute energies, the model suggests screening is important and reduces the exciton energy. Such effects have not been considered in the existing cluster calculations.

Point Ion Calculations

The holes in the undoped lamellar copper oxides are highly localized on the copper ions. Therefore, a point ion calculation may be useful in examining the effect of the different crystal structures. The four materials share two-dimensional approximately square-planar CuO_2 layers, with comparable nearest-neighbor exchange interactions. However, as discussed in Chapter 1 and summarized here, the out-of-plane structures have important differences. At high temperatures, La_2CuO_4 and $Sr_2CuO_2Cl_2$ are tetragonal with octahedrally coordinated Cu-sites. Below ~ 530 K, La_2CuO_4 acquires a slight orthorhombic distortion. In tetragonal $Sr_2CuO_2Cl_2$, the La is replaced by Sr and the apical O by Cl. Both Nd_2CuO_4 and Pr_2CuO_4 are tetragonal with square-planar coordinated Cu-sites and no apical ions. To examine the importance of the out-of-plane ions, point ion calculations for La_2CuO_4 and Nd_2CuO_4 have been done. As these point ion calculations do not allow any hybridization, they are certainly not the best method for calculating the exciton transition energies in the undoped copper oxides. However, their simplicity and the insights gained make them worth examining.

In this point ion calculation La_2CuO_4 will be considered to be tetragonal. All ions except the central copper site are considered to be point charges. The La and Nd ions have charge +3, the O, -2 and the Cu, +2. The anisotropic potential generated by these point charges breaks the degeneracy of the five central Cu-site d-states. Due to the crystal symmetry, only a few terms in the multipole expansion will have to be considered. All results will be given in terms of hole energies.

In terms of spherical harmonics, the Coulomb multipole expansion is given by [80].

$$\frac{1}{\bar{x}-\bar{x}'} = 4\pi \sum_{lm} \frac{1}{2l+1} \frac{r_<^l}{r_>^{l+1}} Y_{lm}^*(\theta',\phi') Y_{lm}(\theta,\phi) \tag{5.1}$$

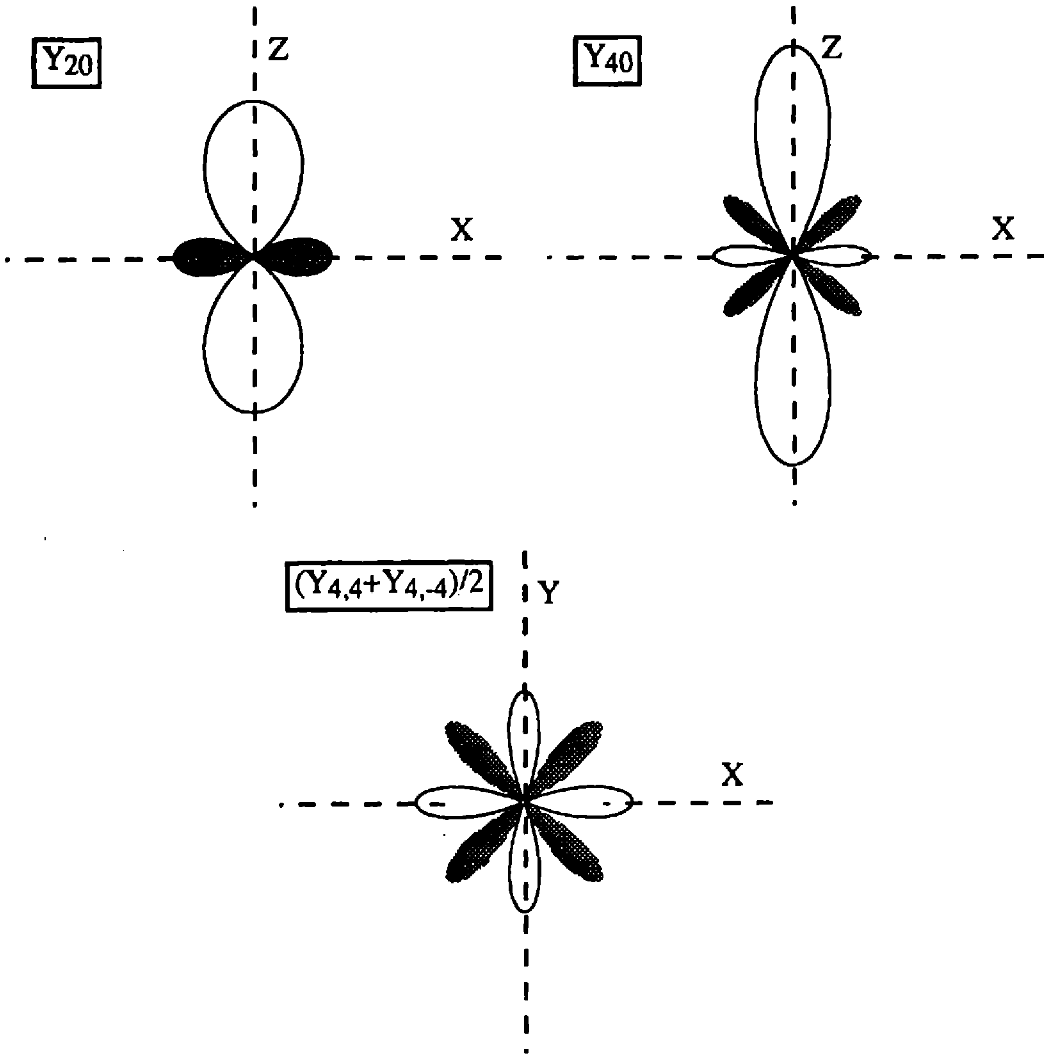

Figure 5.1: Polar plots of spherical harmonics relevant to point ion calculations for d-states in a tetragonal environment. Negative lobes are shaded.

D-State	Hole Energy [e^2/a]
x^2-y^2	$\frac{1}{7}B_{20}\left\langle\left(\frac{r}{a}\right)^2\right\rangle-\frac{1}{168}B_{40}\left\langle\left(\frac{r}{a}\right)^4\right\rangle-\frac{5}{24}B_{4+}\left\langle\left(\frac{r}{a}\right)^4\right\rangle$
$3z^2$-r^2	$-\frac{1}{7}B_{20}\left\langle\left(\frac{r}{a}\right)^2\right\rangle-\frac{1}{28}B_{40}\left\langle\left(\frac{r}{a}\right)^4\right\rangle$
xy	$\frac{1}{7}B_{20}\left\langle\left(\frac{r}{a}\right)^2\right\rangle-\frac{1}{168}B_{40}\left\langle\left(\frac{r}{a}\right)^4\right\rangle+\frac{5}{24}B_{4+}\left\langle\left(\frac{r}{a}\right)^4\right\rangle$
xz, yz	$-\frac{1}{14}B_{20}\left\langle\left(\frac{r}{a}\right)^2\right\rangle+\frac{1}{42}B_{40}\left\langle\left(\frac{r}{a}\right)^4\right\rangle$

$$B_{20}=\sum_i\frac{-Z_i}{\left(\frac{r_i}{a}\right)^3}\left[3\left(\frac{z_i}{r_i}\right)^2-1\right]$$

$$B_{40}=\sum_i\frac{-Z_i}{\left(\frac{r_i}{a}\right)^5}\left[35\left(\frac{z_i}{r_i}\right)^4-30\left(\frac{z_i}{r_i}\right)^2+3\right]$$

$$B_{4+}=\sum_i\frac{-Z_i}{\left(\frac{r_i}{a}\right)^5}\left[\left(\frac{x_i}{r_i}\right)^4-6\left(\frac{x_i}{r_i}\right)^2\left(\frac{y_i}{r_i}\right)^2+\left(\frac{y_i}{r_i}\right)^4\right]$$

Table 5.1: Point ion splitting of d-states in tetragonal crystal in hole energies.

For r < r', the potential inside the charge distribution is:

$$\tilde{V}=\frac{V}{\left(\frac{e^2}{a}\right)}=\sum_{lm}A_{lm}\left(\frac{r}{a}\right)^l Y_{lm}(\theta,\phi) \tag{5.2}$$

$$A_{lm}=\sum_i\frac{4\pi}{2l+1}\frac{Z_i}{\left(\frac{r_i}{a}\right)^{l+1}}Y^*_{lm}(\theta_i,\phi_i) \tag{5.3}$$

The sum on i is over the ion sites of the crystal. Since the d-states are composed of l = 2 spherical harmonics, the matrix elements will be of the form $\langle 2m|Y_{lm}|2m'\rangle$ and only terms in the potential of order l = {0,2,4} will couple to the d-states. The Y_{00} term may be ignored when calculating energy differences. Furthermore, because the potential must be real and have four-fold rotational symmetry about the z-axis, there are only three terms to evaluate. They are Y_{20}, Y_{40}, and $(Y_{4,4} + Y_{4,-4})$. Polar plots of these functions are shown in figure 5.1. The shaded lobes denote a negative value.

After evaluating the angular matrix elements, the energies are determined by the three point ion parameters B_{20}, B_{40}, and B_{4+} and the two radial expectation values $\langle r^2 \rangle$ and $\langle r^4 \rangle$. These results are summarized in table 5.1. For simplicity in evaluating the point ion sums, all distances are expressed in units of a, the nearest neighbor Cu-Cu bond length which is ~ 3.8 Å in La_2CuO_4 and ~ 3.9 Å in Nd_2CuO_4[81]. The radial expectation values, $<r^2> = 1.03$ Å^2 and $<r^4> = 2.50$ Å^4, are based on Hartree-Fock calculations for a free Cu^{+2} ion [60].

Figure 5.2 shows the d-state point ion energies for La_2CuO_4 and Nd_2CuO_4 as a function of the radius within which all ions are included. At the right hand edge of the graph, where all ions within two Cu-Cu bond lengths have been included, the transition energies are remarkably similar. The only difference is the interchange of the $d_{3z^2-r^2}$ and d_{xz} levels. Figure 5.3 compares the transition energies in La_2CuO_4 and Nd_2CuO_4 including all ions within two Cu-Cu bond lengths. In this point ion approximation the lowest energy transition is the $d_{x^2-y^2} \rightarrow d_{xy}$ exciton. As was discussed at great length in Chapter 4, the $d_{x^2-y^2} \rightarrow d_{xy}$ transition is believed to be at ~ 1.5 eV in these materials. Furthermore, cluster calculations [76] predict that the $d_{3z^2-r^2}$ is the lowest energy excited state, but with an energy in the range of 0.9-1.6 eV. The important point of figure 5.2 is the similarity of the energy splittings in spite of the differing crystal structures. Figure 5.4 shows the effect of varying the apical oxygen ion position within the La_2CuO_4 crystal structure. In the real crystal, the ratio of the distance to the apical oxygen with respect to the in-plane oxygen is 1.25. As seen in figure 5.4 the oxygen octahedron in La_2CuO_4 is very elongated. Together, these figures show that the primary energy scale is set by the four nearest neighbor in-plane oxygen ions. However, the point ion calculation is insufficient to understand the low energy of the $d_{x^2-y^2} \rightarrow d_{3z^2-r^2}$ exciton.

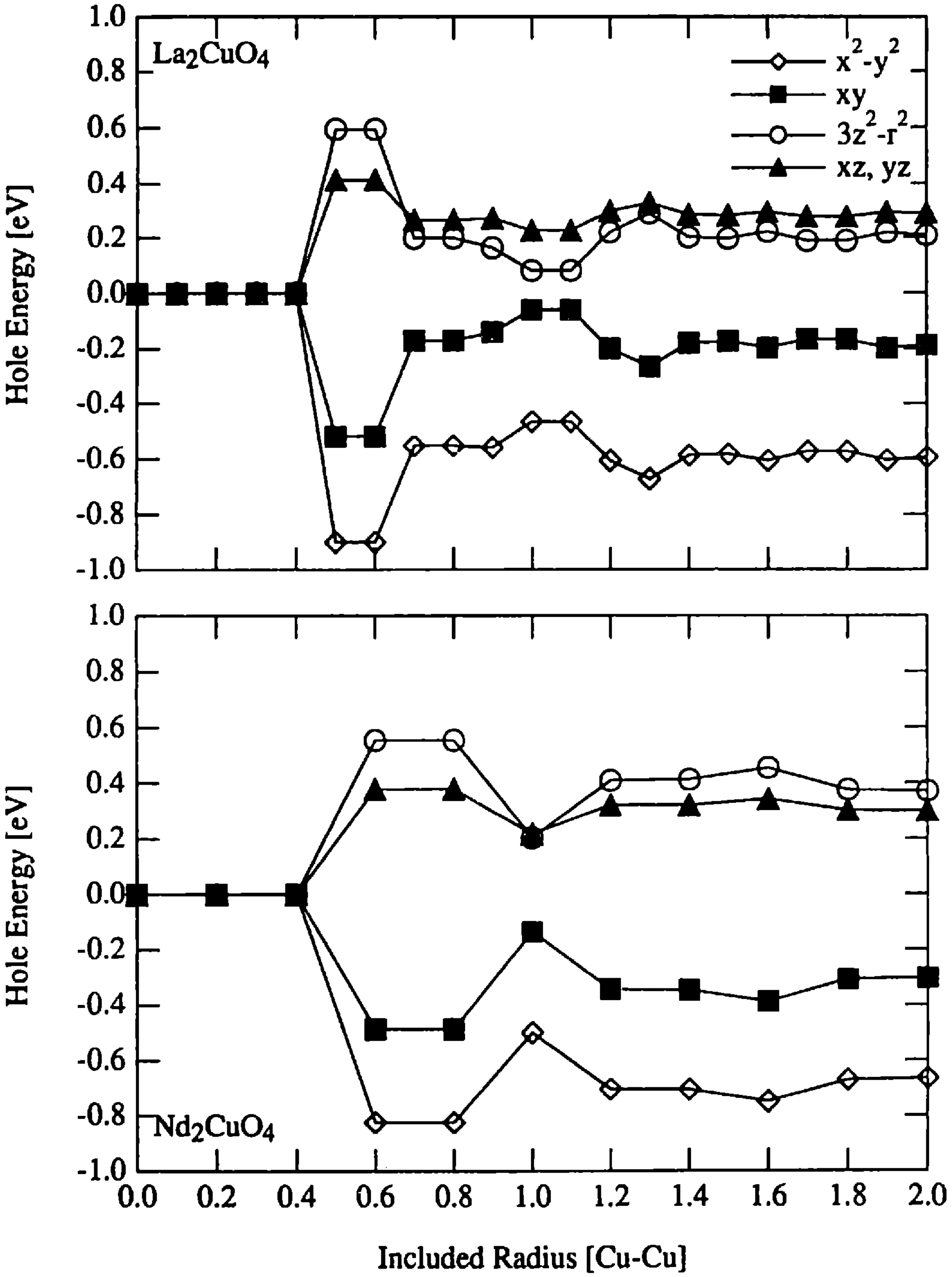

Figure 5.2: Crystal field levels for copper d-states in a point ion approximation for La_2CuO_4 (top) and Nd_2CuO_4 (bottom) versus radius of sphere for which all ions are included. The radius is measured in units of the material dependent Cu-Cu bond length.

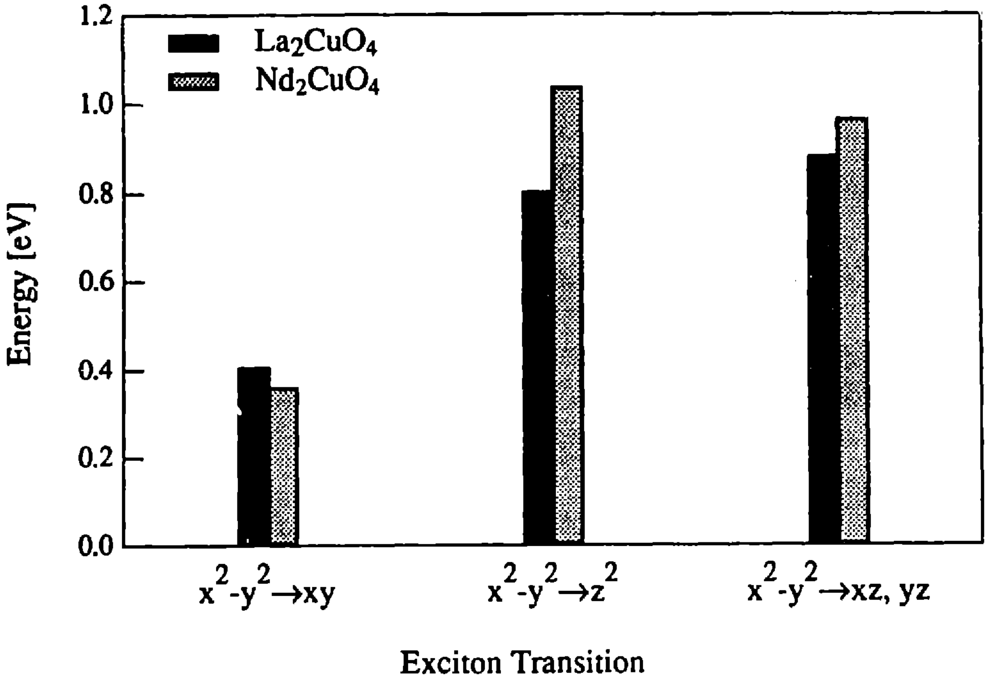

Figure 5.3: Exciton transition energies in a point ion approximation for La_2CuO_4 and Nd_2CuO_4 including all ions with in two Cu-Cu bond lengths.

From this work and the electroreflectance experiments of Falck *et al.* [58] the experimentally determined exciton energies in La_2CuO_4 are about 0.4, 1.4 and 1.6 eV for the final states $d_{3z^2-r^2}$, d_{xy} and d_{xz} or d_{yz} respectively. From these energies the crystal field parameters BR_{lm} may be determined.

$$BR_{lm} = \left(\frac{e^2}{a}\right) B_{lm} \left\langle \left(\frac{r}{a}\right)^l \right\rangle \tag{5.4}$$

The experimentally determined crystal field parameters for La_2CuO_4 are compared with point ion values in table 5.2. The values of BR_{20} and BR_{4+} differ by about a factor of 2 and the value for BR_{40} changes by about a factor of 5. In the real solid the copper and oxygen orbitals hybridize. This might be incorporated into a point ion model with the use of non-integer ion charges. Because the in-plane oxygen ions are closer to the copper ion than the apical oxygen ions, the effective charge of the in-plane ions due to orbital hybridization would be smaller than that for the apical ions. Such a difference in the charge between the in-

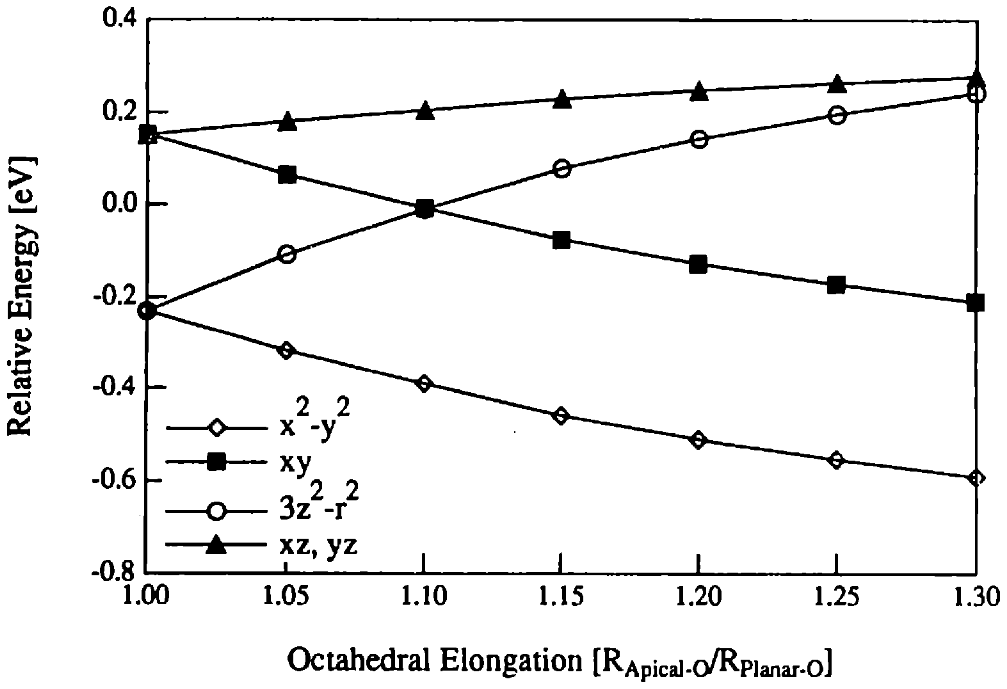

Figure 5.4: Point ion approximation crystal field levels for Cu ion in La_2CuO_4 as a function of the central ion oxygen octahedral elongation. Real La_2CuO_4 has an elongation of 1.25

plane and apical oxygen ions would offset the effect of the elongation of the oxygen octahedra in La_2CuO_4 and reduce the $d_{x^2-y^2} \rightarrow d_{3z^2-r^2}$ splitting. However, cluster calculations for a single copper ion and the surrounding oxygen ions show that the lowering of the Cu $d_{x^2-y^2}$ orbital energy due to hybridization is the dominant effect and that the transition energy actually increases when hybridization is included for an isolated CuO_6 cluster [76,82]. The next section discusses the potential importance of screening by the neighboring Cu site holes which are not included in such small clusters.

Within the point ion approximation the d-d exciton energies for La_2CuO_4 and Nd_2CuO_4 are very similar. Due to the large elongation of the oxygen octahedron in La_2CuO_4 the primary energy scale for d-d excitons in these materials is set by the four nearest neighbor in-plane oxygens. However, in the point ion calculation the lowest energy exciton is the $d_{x^2-y^2} \rightarrow d_{xy}$ transition. This is in disagreement with both cluster calculations and pertinent experimental observations.

Crystal Field Parameter	Fit to Data [eV]	Point Ion [eV]
BR_{20}	-1.2	-2.43
BR_{40}	21.5	4.16
BR_{4+}	3.36	1.84

Table 5.2: Crystal field parameters for copper ion d-states as determined by fitting to La_2CuO_4 data and by point ion calculations.

Cluster Calculations

Cluster calculations are an obvious way to calculate the copper ion d-d exciton energies. Cluster calculations are done in the following way. First choose what ion sites and ionic orbitals at each site are to be include. Figure 5.5 shows an example with nine ion sites and a total of ten orbitals. Then, for a given number of particles in the cluster, list all the states presumed to be important. Next, use a model Hamiltonian to evaluate the matrix elements between all the states and then solve for the eigen energies. In practice these problems are usually solved numerically.

Existing cluster calculations predict that the $d_{x^2-y^2} \rightarrow d_{3z^2-r^2}$ exciton is the lowest energy exciton, but with an energy in the range of 0.9 - 1.6 eV [76-79]. These models include a large number of orbitals at each site and hence might be expected to yield reasonable results. However, the exciton energies are based on one hole in a cluster including only a central Cu ion and the nearest neighbor oxygen ions. This ignores the interaction of the hole with its nearest neighbor holes. In the undoped lamellar copper oxides where the hole-hole interaction yields an exchange coupling of ~ 130 meV, this may not be a reasonable approximation. Calculations on larger clusters have been performed to study the behavior of doped holes, but not the exciton energies in the undoped materials[82-84].

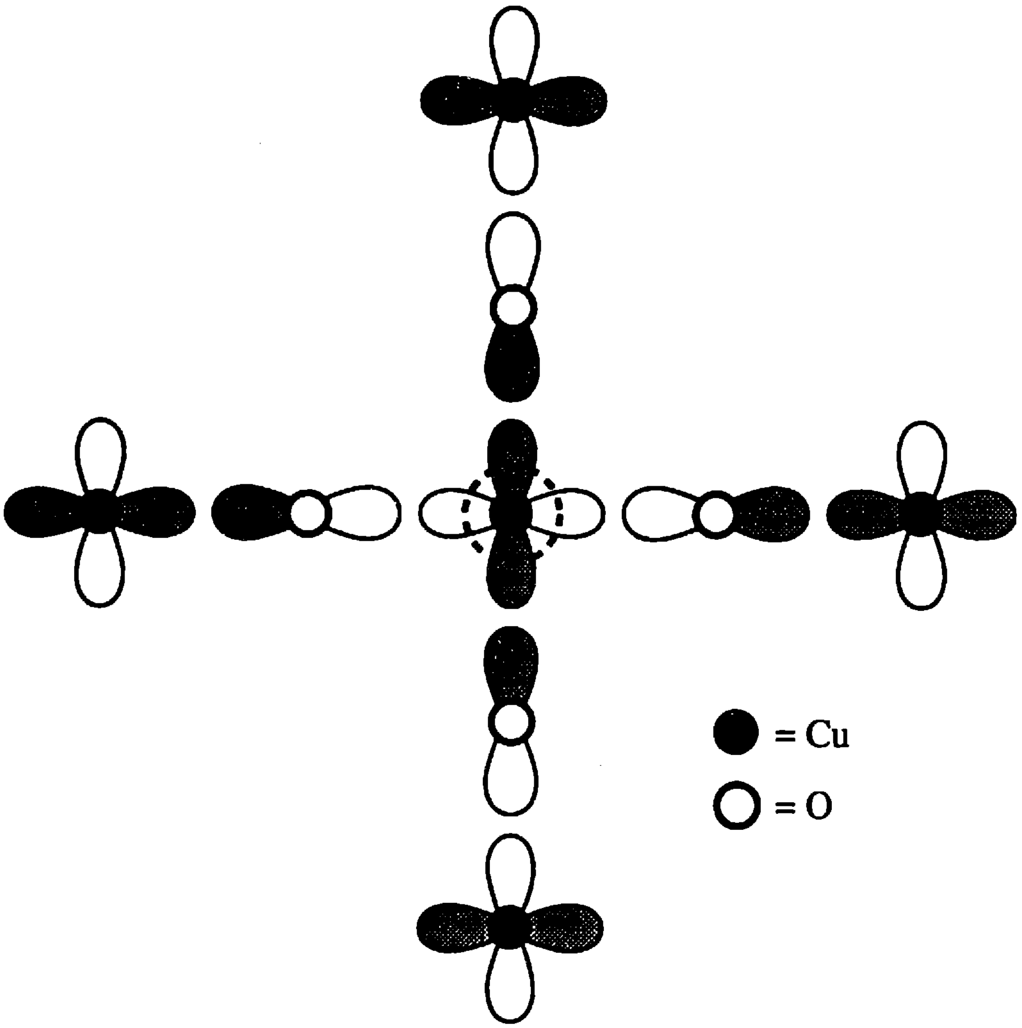

Figure 5.5: Model for cluster calculation. Negative lobes are shaded. Each Cu site has a $d_{x^2-y^2}$ state. Each O site a p_σ state. The central Cu site also has a $d_{3z^2-r^2}$ state denoted by the dashed circle.

A few calculations report exciton energies on larger clusters, but make some sort of single particle approximation which eliminates the possibility of the nearest neighbor holes screening the exciton[85]. A calculation including the nearest neighbor copper sites and many orbitals per site would be onerous. In this section I present a simple calculation including the nearest neighbor copper sites, but only one orbital per site. The central copper site has two orbitals in order to make excitons possible.

The cluster used in these calculations is shown in figure 5.5. The central copper site has both a $d_{x^2-y^2}$ and a $d_{3z^2-r^2}$ orbital. The four in-plane, nearest neighbor, oxygen sites each have one p_σ orbital. The four nearest neighbor copper sites each have a single $d_{x^2-y^2}$ orbital. In figure 5.5 the negative lobes are shaded. The orientation of the orbitals is chosen such that all the hopping matrix elements are positive except for hopping between the central Cu-site $d_{3z^2-r^2}$ state and lateral nearest neighbor oxygen sites. A Hubbard type Hamiltonian is used to study this cluster.

$$H = \sum_i \varepsilon_i n_i + \sum_{ik} t_{ik} c_i^\dagger c_k + \sum_{ik} V_{ik} n_i n_k \tag{5.5}$$

Because the holes are fermions, no states where a single ionic orbital is occupied by two or more holes with the same spin are allowed. The sums are over ion sites. The first term is simply the sum of the single particle energies. The single particle energies are denoted ε_d, $\varepsilon_d^{z^2}$, and ε_p for the Cu-site $d_{x^2-y^2}$, the Cu-site $d_{3z^2-r^2}$ and the O-site p_σ respectively. The second term allows hopping between nearest neighbor sites. The matrix elements for hopping between the O-site p_σ and the Cu-site $d_{x^2-y^2}$ or $d_{3z^2-r^2}$ are t and t_z respectively. The third term includes the Coulomb repulsion between the holes. Holes two or more lattice sites apart are assumed not to interact. The Coulomb repulsion between nearest neighbor holes will be denoted V. The repulsion between two holes on the same site is about 5-10 eV [82]. However, this simple model will only include states which are coupled to the unperturbed ground or exciton states by a single hop of one hole. Hence no site will ever be doubly occupied. This restriction could be removed if desired. The parameter values used are from the *ab initio* calculations of Grant *et al* [82] but are similar to those used in other cluster calculations[79]. The values in eV are:

$$\begin{aligned} \varepsilon_d &= 0 \\ \varepsilon_d^{z^2} &= 0.64 \\ \varepsilon_p &= 3.51 \\ t &= 1.47 \\ t_z &= 0.50 \\ V &= 0.52 \end{aligned} \tag{5.6}$$

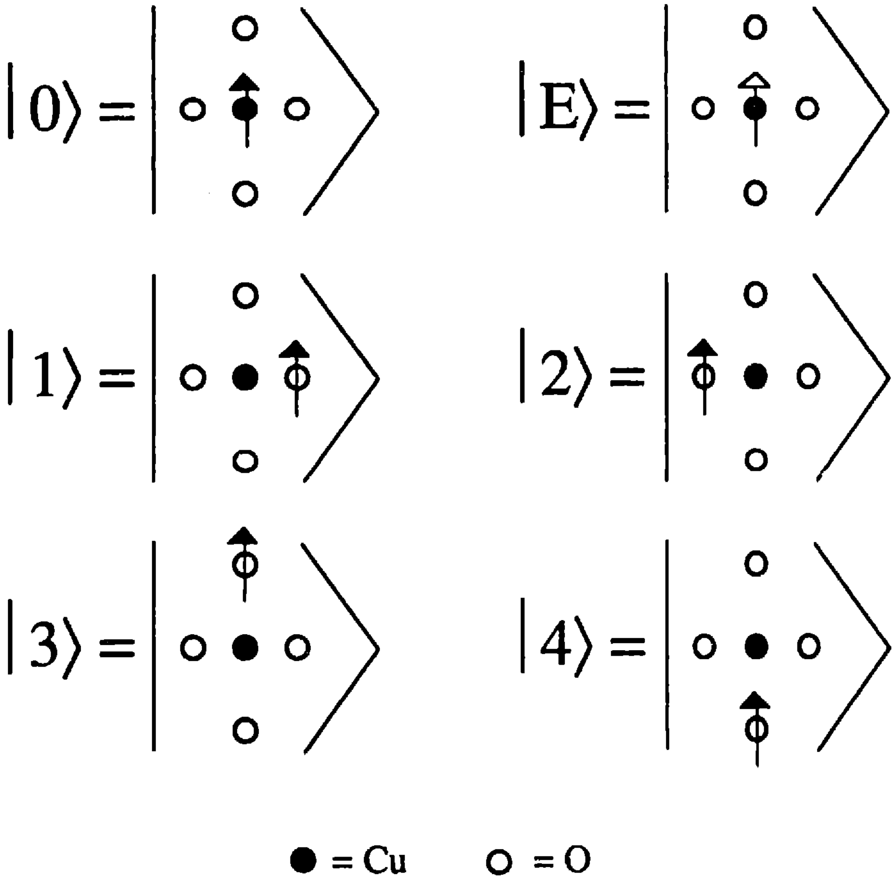

Figure 5.6: States used in the 1-hole problem which ignores the nearest neighbor Cu sites.

To see if including the nearest neighbor copper site holes influences the exciton energy, it is first necessary to calculate the exciton energy excluding the nearest neighbor holes. The cluster for this is the same as that shown in figure 5.5 except that the four outer copper sites are considered to be fixed point charges. Figure 5.6 shows the six states which will be considered. In the unperturbed ground state, labeled 0, the hole is in the Cu-site $d_{x^2-y^2}$ orbital. The unperturbed exciton state, E, has the hole in the $d_{3z^2-r^2}$ orbital as indicated by the open arrow head. In states 1-4, the hole resides on one of the oxygen sites.

The non-zero matrix elements are:

$$\left[\begin{array}{c|cccccc} H & 0 & E & 1 & 2 & 3 & 4 \\ \hline 0 & \varepsilon_d & & t & t & t & t \\ E & & \varepsilon_d^{z^2} & -t_z & -t_z & t_z & t_z \\ 1 & t & -t_z & \varepsilon_p + V & & & \\ 2 & t & -t_z & & \varepsilon_p + V & & \\ 3 & t & t_z & & & \varepsilon_p + V & \\ 4 & t & t_z & & & & \varepsilon_p + V \end{array}\right] \tag{5.7}$$

This may be block diagonalized by forming the following two states.

$$\begin{aligned} |\mathrm{I}\rangle &= \tfrac{1}{2}\{|1\rangle + |2\rangle + |3\rangle + |4\rangle\} \\ |\mathrm{II}\rangle &= \tfrac{1}{2}\{-|1\rangle - |2\rangle + |3\rangle + |4\rangle\} \end{aligned} \tag{5.8}$$

The Hamiltonian matrix is now reduced to two 2x2 problems.

$$\begin{array}{c|cc:cc} H & 0 & \mathrm{I} & \mathrm{E} & \mathrm{II} \\ \hline 0 & \varepsilon_d & 2t & & \\ \mathrm{I} & 2t & \varepsilon_p + V & & \\ \hdashline \mathrm{E} & & & \varepsilon_d^{z^2} & 2t_z \\ \mathrm{II} & & & 2t_z & \varepsilon_p + V \end{array} \tag{5.9}$$

The resulting eigenvalues are

$$\lambda = \frac{\left(\varepsilon_p + V + \tilde{\varepsilon}_d\right) \pm \sqrt{\left(\varepsilon_p + V + \tilde{\varepsilon}_d\right)^2 - 4\tilde{\varepsilon}_d\left(\varepsilon_p + V\right) + 16\tilde{t}^2}}{2} \tag{5.10}$$

where the parameters $\left(\tilde{\varepsilon}_d, \tilde{t}\right)$ are $\left(\varepsilon_d, t\right)$ for the ground state block and $\left(\varepsilon_d^{z^2}, t_z\right)$ for the exciton. Using the values listed in equation 5.6 the ground and first excited state energies are -1.55 eV and +0.37 eV, giving an exciton transition energy of +1.92 eV. Before hybridization the exciton energy was +0.64 eV. The

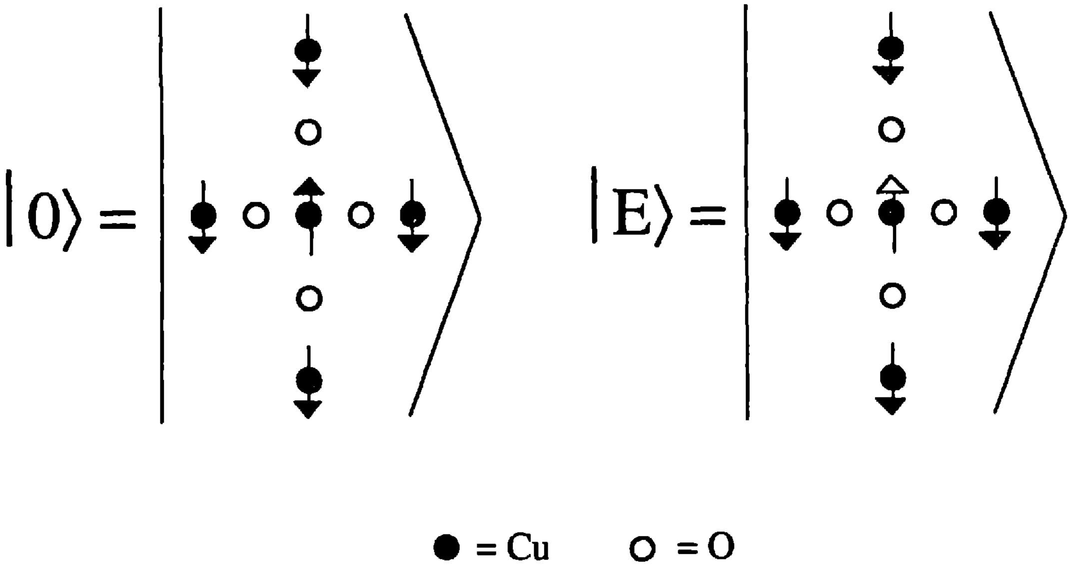

Figure 5.7: Unperturbed states for the ground state and exciton in the 5-hole problem. An hole in the $d_{3z^2-r^2}$ is denoted with an open arrow head.

stronger interaction of the $d_{x^2-y^2}$ hole with the oxygen states causes a larger splitting of the levels, thereby increasing the exciton energy. Remember that this calculation does not have enough orbitals to realistically determine the exciton energy. The purpose here is to explore the possible influence of the nearest neighbor Cu-site holes.

The unperturbed ground and exciton states for the 5-hole problem are shown in figure 5.7. For simplicity no spin flips will be allowed. The four states involving the central Cu-site hole hopping to an O-site are shown in figure 5.8. These four states are analogous to those in the 1-hole problem, having the same energies and matrix elements. In the 5-hole problem, the four outer Cu-site holes may also hop into an O-site. The four such states with the central Cu-site hole in the $d_{x^2-y^2}$ orbital are shown in figure 5.9.and are denoted with a leading X. The four analogous states with the central Cu-site hole in the $d_{3z^2-r^2}$ orbital are labeled with a leading Z.

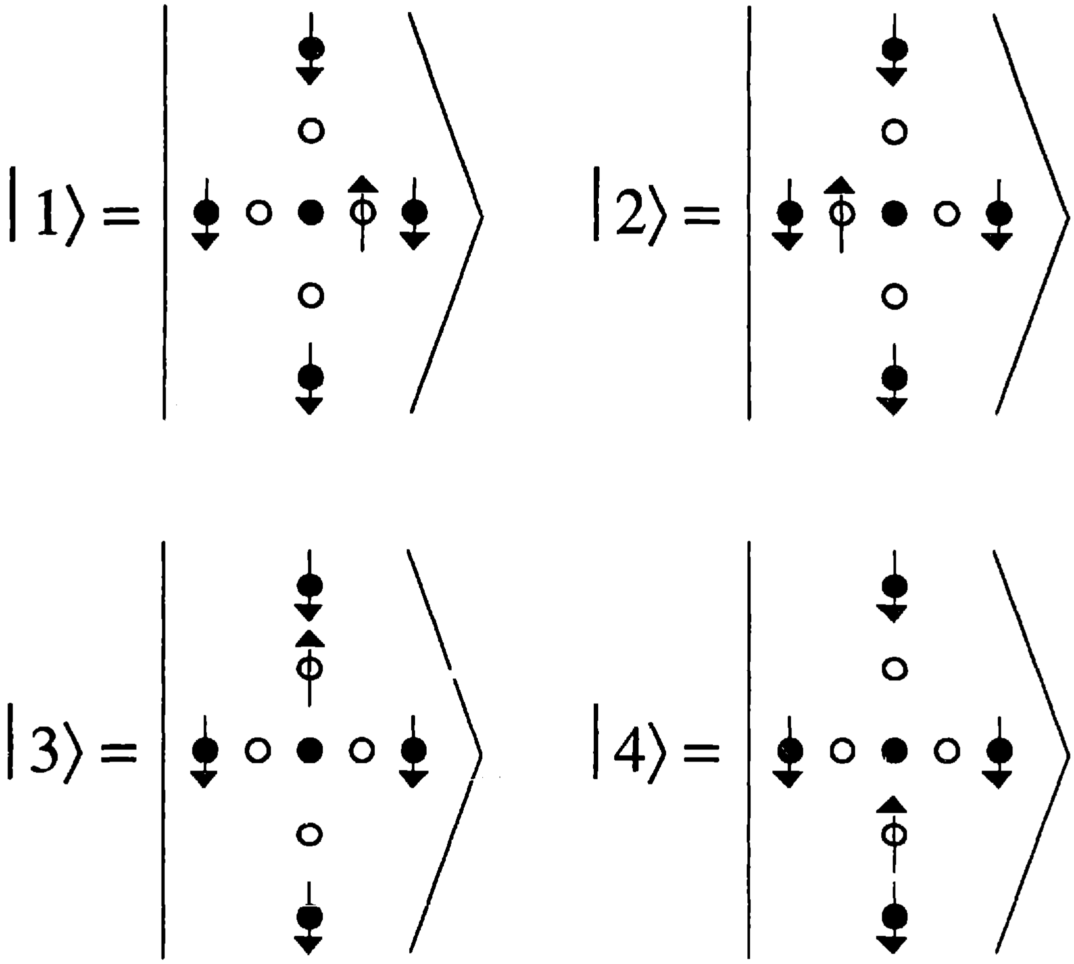

Figure 5.8: States in the 5-hole problem with one hop of the central Cu site hole.

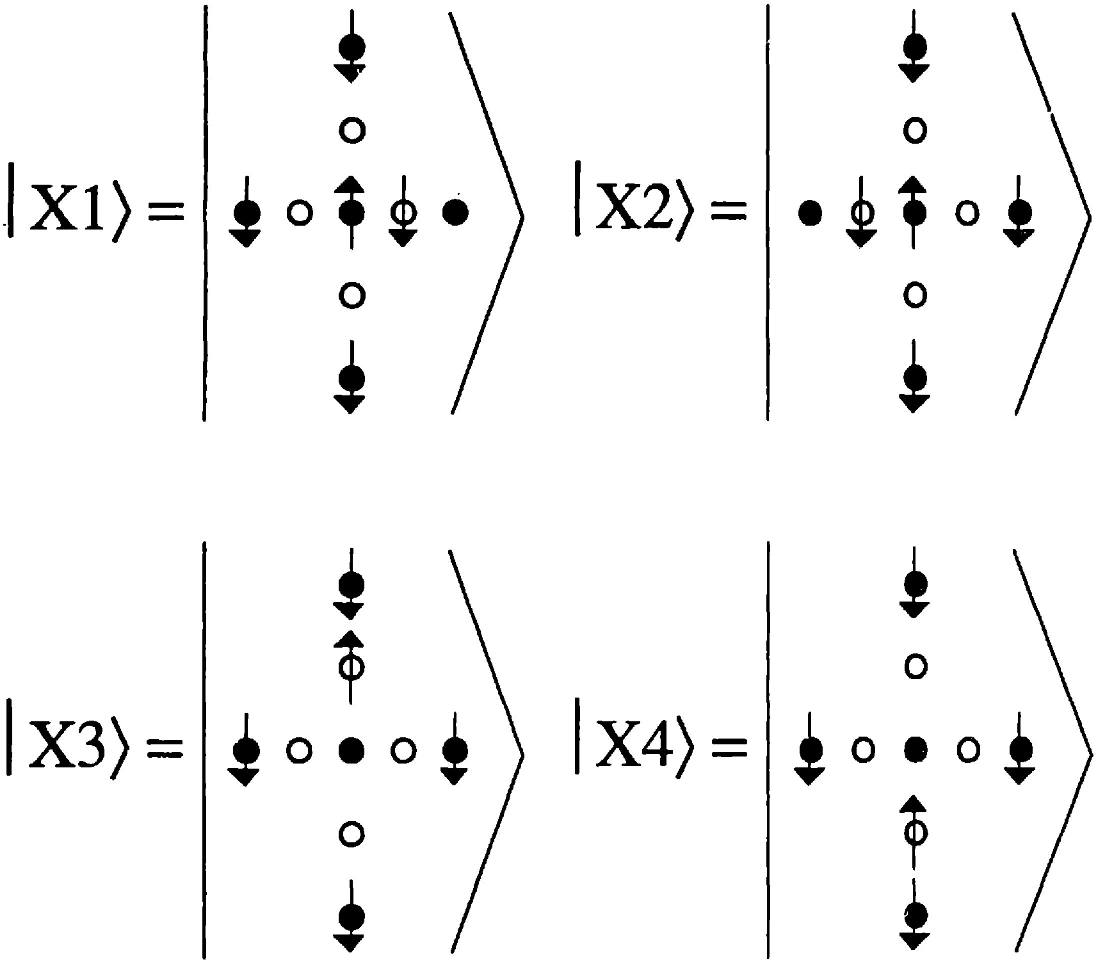

Figure 5.9: States in the 5-hole problem with the central Cu site hole in the $d_{x^2-y^2}$ state and one hop of another Cu hole. The four similar states with the central Cu site hole in the $d_{3z^2-r^2}$ state are labeled with a Z instead of an X.

The 14 x 14 Hamiltonian matrix for these states can be block diagonalized by forming the following states.

$$\begin{aligned} |\mathrm{I}\rangle &= \tfrac{1}{2}\{|1\rangle + |2\rangle + |3\rangle + |4\rangle\} \\ |\mathrm{II}\rangle &= \tfrac{1}{2}\{-|1\rangle - |2\rangle + |3\rangle + |4\rangle\} \\ |X\rangle &= \tfrac{1}{2}\{|X1\rangle + |X2\rangle + |X3\rangle + |X4\rangle\} \\ |Z\rangle &= \tfrac{1}{2}\{|Z1\rangle + |Z2\rangle + |Z3\rangle + |Z4\rangle\} \end{aligned} \tag{5.11}$$

The resulting matrix is.

$$\begin{array}{c|ccc:ccc} H & 0 & \mathrm{I} & \mathrm{X} & \mathrm{E} & \mathrm{II} & Z \\ \hline 0 & 5\varepsilon_d & 2t & 2t & & & \\ \mathrm{I} & 2t & 4\varepsilon_d + \varepsilon_p + V & 0 & & & \\ \mathrm{X} & 2t & 0 & 4\varepsilon_d + \varepsilon_p + V & & & \\ \hdashline \mathrm{E} & & & & 4\varepsilon_d + \varepsilon_d^{z^2} & 2t_z & 2t \\ \mathrm{II} & & & & 2t_z & 4\varepsilon_d + \varepsilon_p + V & 0 \\ Z & & & & 2t & 0 & 3\varepsilon_d + \varepsilon_d^{z^2} + \varepsilon_p + V \end{array} \tag{5.12}$$

The upper left hand block contains the ground state and the lower right hand block the exciton. Each 3x3 block can be reduced to a 2x2 by forming the following states.

$$\begin{aligned} |X0\rangle &= \frac{|\mathrm{I}\rangle - |X\rangle}{\sqrt{2}} \\ |X1\rangle &= \frac{|\mathrm{I}\rangle + |X\rangle}{\sqrt{2}} \\ |Z0\rangle &= \frac{t|\mathrm{II}\rangle - t_z|Z\rangle}{\sqrt{t^2 + t_z^2}} \\ |Z1\rangle &= \frac{t_z|\mathrm{II}\rangle + t|Z\rangle}{\sqrt{t^2 + t_z^2}} \end{aligned} \tag{5.13}$$

The states X0 and Z0 don't couple to the states 0 or E. The resulting matrix is now.

$$\begin{array}{c|cc:cc} H & 0 & X1 & E & Z1 \\ \hline 0 & 5\varepsilon_d & 2\sqrt{t^2+t^2} & & \\ X1 & 2\sqrt{t^2+t^2} & 4\varepsilon_d+\varepsilon_p+V & & \\ \hdashline E & & & 4\varepsilon_d+\varepsilon_d^{z^2} & 2\sqrt{t_z^2+t^2} \\ Z1 & & & 2\sqrt{t_z^2+t^2} & 4\varepsilon_d+\varepsilon_p+V+\left(\frac{t^2}{t_z^2+t^2}\right)\left(\varepsilon_d^{z^2}-\varepsilon_d\right) \end{array} \tag{5.14}$$

For both the ground state block and the exciton block the effective hopping parameter comes from adding the previous two hopping parameters in quadrature.

$$\begin{aligned} t_{eff} &= \sqrt{t^2+t^2} \\ t_{eff}^{z} &= \sqrt{t_z^2+t^2} \end{aligned} \tag{5.15}$$

With $\varepsilon_d = 0$ and letting the superscript α denote the z-labels for exciton block and x-label for the ground state block, the matrix for either block is:

$$\begin{array}{c|cc} H & & \\ \hline & \varepsilon_d^{\alpha} & 2t_{eff}^{\alpha} \\ & 2t_{eff}^{\alpha} & \underbrace{\varepsilon_p+V+\frac{t^2}{\left(t_{eff}^{\alpha}\right)^2}\varepsilon_d^{\alpha}}_{\tilde{\varepsilon}_{eff}} \end{array} \tag{5.16}$$

The resulting eigenvalues are:

$$\lambda = \frac{\left(\varepsilon_d^{\alpha}+\tilde{\varepsilon}_{eff}\right) \pm \sqrt{\left(\varepsilon_d^{\alpha}+\tilde{\varepsilon}_{eff}\right)^2 - 4\left(\varepsilon_d^{\alpha}\tilde{\varepsilon}_{eff}\right) + 16\left(t_{eff}^{\alpha}\right)^2}}{2} \tag{5.17}$$

Using the values from equation 5.6, the ground state and excited state energies are -2.61 and -1.06 eV respectively. The resulting exciton energy is now 1.55 eV compared to 1.92 eV without the nearest neighbor holes. Examining the eigenvectors shows that the probability for one outer Cu-site hole to be on an O-site is 14% in the ground state and 21% in the exciton state. Due to the weaker interaction between the exciton hole and its neighbors, the surrounding holes relax in towards the central Cu-site. This is simply a screening of the exciton. Such a process can not occur in the 1-hole problem. To understand how much this screening can lower the exciton energy a more detailed study is required. It should include those states which are two hops from the unperturbed ground and excited states so that the exchange process will be included. Furthermore, it should systematically examine how the screening changes as the cluster size is increased to include more holes. The question of how big a cluster is needed may be examined with a minimal number of orbitals per site. To really get a good calculation of the energy, one must then include more orbitals per site on the appropriate size cluster.

Summary

This chapter has examined the Cu-site exciton transitions through two very simple calculations. Neither calculation is adequate to correctly calculate the energy, but each has provided some insight into understanding the exciton transitions in the undoped lamellar copper oxides. The point ion calculation shows that overall energy scale of the excitons is similar for materials with and without apical ions. This is because the oxygen octahedra in La_2CuO_4 are very elongated and in Nd_2CuO_4 and Pr_2CuO_4, the missing apical oxygen exist in a layer only slightly farther away. Hence, the four nearest neighbor oxygen ions set the primary energy scale. The cluster calculation shows that screening of the exciton by the neighboring holes may play an important role in reducing the exciton energy. A proper calculation of the exciton energy has yet to be done.

Chapter 6: Photo-induced Absorption

Photo-induced absorption experiments are conceptually quite simple. In a semiconducting material, such as La_2CuO_4, electron-hole pairs are created by illuminating the sample with photons of an energy greater than the band gap. Typically a laser is used. The presence of the photo-excited electrons and holes alters the absorption spectrum of the material. The probe beam spectral dependence of the induced absorption shows the effect of the additional electrons and holes on the absorption processes in the sample. The time evolution of the induced absorption at a fixed probe energy can yield information about the decay processes for photo-excited electrons and holes.

This chapter, which discusses photo-induced absorption in the undoped lamellar copper oxides, consists of two essentially separate parts. The first section treats photo-induced absorption as a simple means to study the doping dependence of the measured absorption spectrum. It shows that the magnon sideband absorption spectrum can be expected to grow with doping and hence is probably responsible for the doping enhanced mid-infrared absorption in the lamellar copper oxides.

The second section presents preliminary time-resolved photo-induced absorption data. The decay of the photo-induced absorption is extremely slow, with effects lasting to time scales of a second or longer. Some experiments report persistent photo-induced conductivity at low temperatures in the High-T_c related materials[86-88]. At the present time this behavior is not understood. The main purpose of this section is to document the current experimental picture. The potential for further work is discussed in Chapter 7. This section is not central to the ongoing explanation of the mid-infrared absorption process. However, the results presented show that the time decay of the photo-induced absorption in the lamellar copper oxides is unusual and worthy of further study.

Growth of Mid-infrared Absorption with Photo-induced Doping

As discussed in Chapter 1, doping the High-T_c host materials increases the absorption in the infrared below the charge-transfer gap of ~ 2 eV. The data presented in Chapter 3 shows that a weak electric dipole absorption process exists below the gap in the undoped materials. Chapters 4 and 5 show that the absorption is intrinsic and due to an exciton at ~ 0.4 eV with multimagnon sidebands. It is natural to wonder whether this process is responsible for mid-infrared absorption in the doped materials. The addition of holes, which strongly modify the antiferromagnetic ground state, may introduce new matrix elements for dipole allowed exciton-magnon excitations. This section provides empirical evidence that the strength of the exciton-magnon absorption does grow with doping.

Figure 6.1 shows the optical conductivity as measured in reflectivity by Thomas *et al* [28] for undoped and lightly oxygen doped $YBa_2Cu_3O_{6+y}$, Nd_2CuO_4 and La_2CuO_4 single crystals. For weak absorption, the optical conductivity is related to the absorption coefficient by:

$$\alpha(\omega) = \frac{4\pi}{c\sqrt{\varepsilon_1}}\sigma(\omega) \qquad \left|\frac{\varepsilon_2}{\varepsilon_1}\right| << 1. \tag{6.1}$$

For La_2CuO_4, with $\varepsilon_1 = 5$, $\alpha[cm^{-1}] \approx 200\,\sigma[\Omega^{-1}cm^{-1}]$. At ~ 0.6 eV, the absorption of the doped La_2CuO_{4+y} sample of figure 6.1 is roughly two orders of magnitude stronger than that we observe in the undoped samples. Our transmission measurements are not good for measuring such strong absorption processes and the reflection experiments of Thomas *et al* are not good for measuring those as weak as in

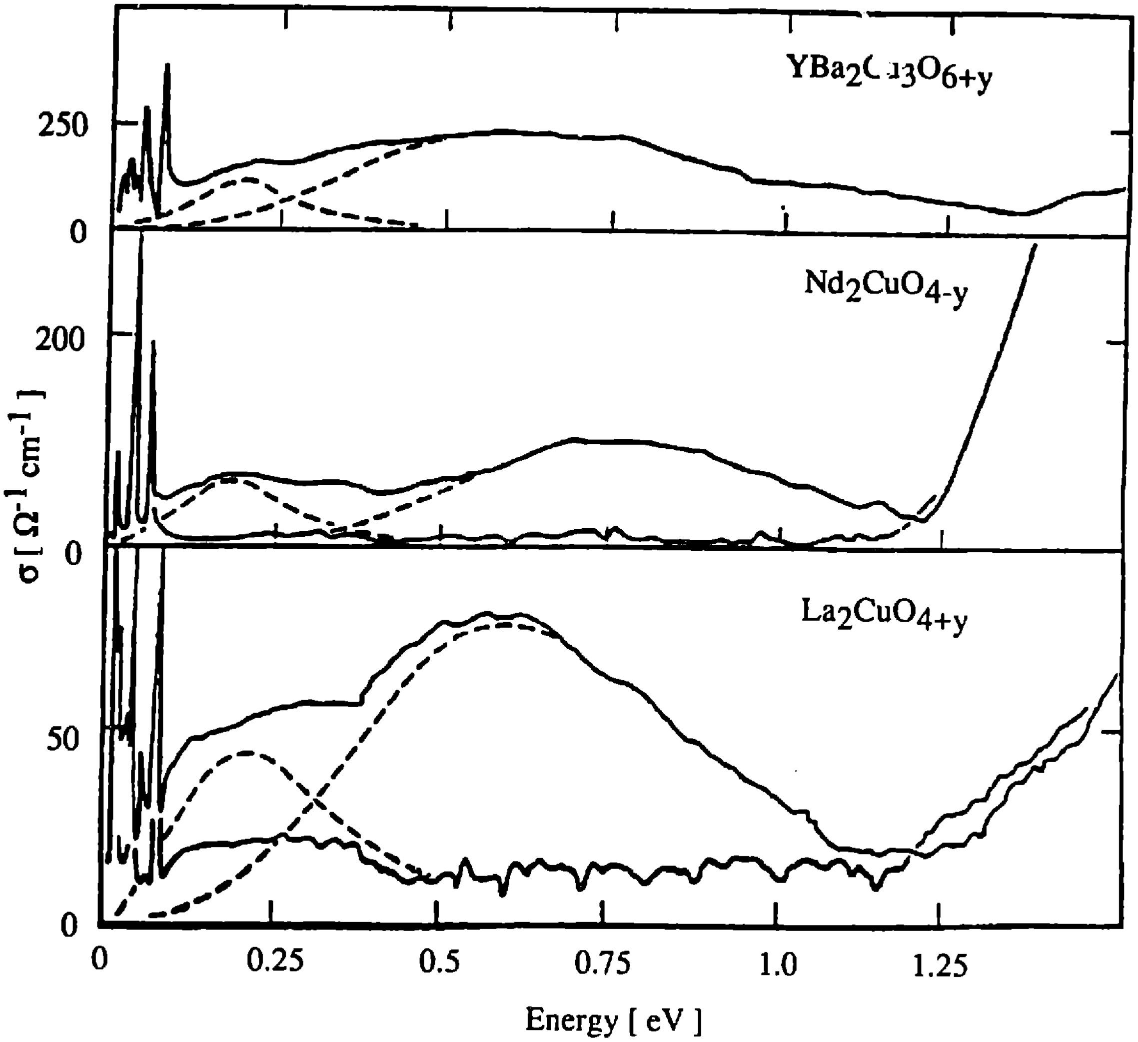

Figure 6.1: Comparison of the optical conductivity, σ, for several different materials. The YBCO is measured at 300 K, the rest at 10 K. The lower curves for Nd_2CuO_4 and La_2CuO_4 are undoped. From Thomas *et al* [28].

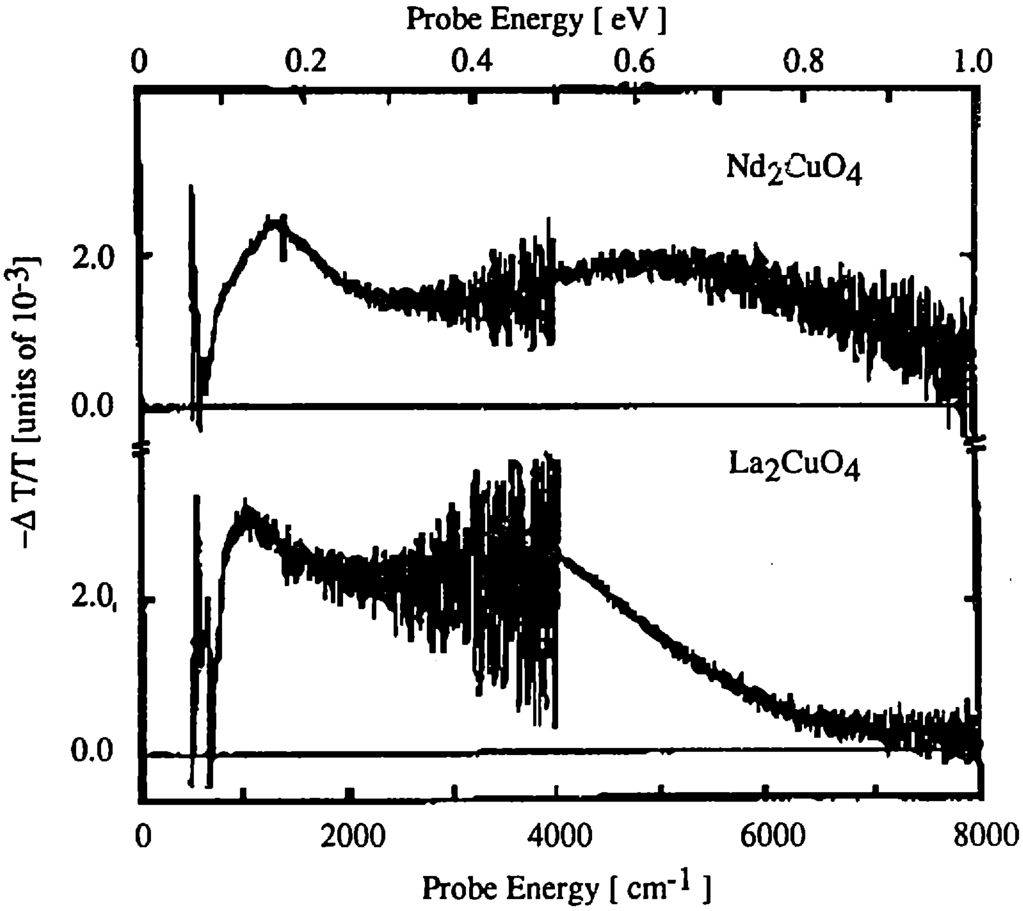

Figure 6.2: Photoinduced absorption spectra in Nd_2CuO_4 and La_2CuO_4 pressed pellets. Pumped at 2.7 eV. T = 4.2 K. From Kim *et al* [89].

the undoped crystals. However, the overall shape of the absorption from ~ 0.4 to 1.25 eV in the lightly oxygen doped La_2CuO_{4+y} is similar to that in the undoped material.

The photo-induced absorption as measured by Kim *et al* [89] for Nd_2CuO_4 and La_2CuO_4 pressed pellets is shown in figure 6.2. The similarity of the spectra in figures 6.1 and 6.2 suggest that the effect of photoexcited carriers is similar to that of chemical doping.

The relative change in the transmission is related to the change in the absorption coefficient by:

$$\Delta\alpha = \frac{-1}{d_{pump}}\frac{\Delta T}{T} \,, \tag{6.2}$$

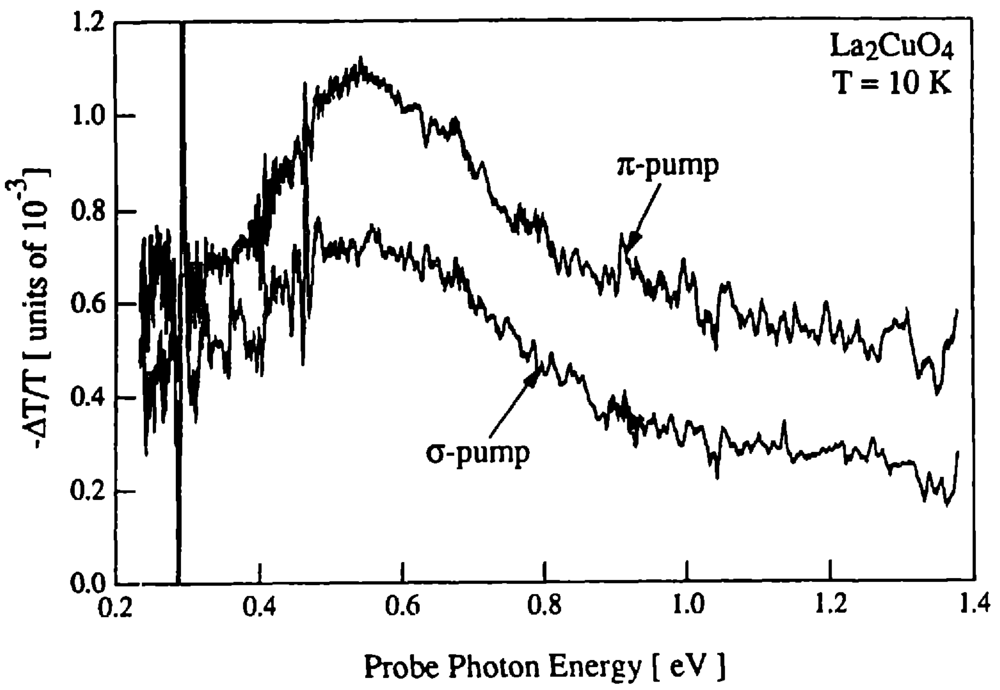

Figure 6.3: Photoinduced absorption vs. probe photon energy in La_2CuO_4 single crystal. Pumped at 1.96 eV (632.8 nm). Pump laser chopped at 5 Hz. Pump beam polarized either parallel (σ) or perpendicular (π) to the CuO_2 plane. T = 10 K. Probe beam is σ-polarized.

where d_{pump} is the effective thickness pumped. Figure 6.3 shows the photo-induced absorption in La_2CuO_4 single crystals at T = 10 K. The sample was pumped at 5 Hz. with a He-Ne laser at 1.96 eV (632.8 nm) with the electric field of the laser polarized either parallel (σ) or perpendicular (π) to the CuO_2 layers. This non-time-resolved measurement was done with two lock-in amplifiers in series as described in Chapter 2. Reflectivity experiments [15,16,19] show that the charge transfer excitation only absorbs light polarized parallel to the Cu-O layers. It is believed that scattering processes randomize the polarization and hence allow the π-polarized pump beam to be absorbed. For the sample measured, which was ~ 70 μm thick, the transmission for π-polarized light at 2 eV is ~ 3% at T = 90 K. This suggests that carriers are being created through out the entire thickness of the sample.

To facilitate comparison of the measured photo-induced absorption spectra with that measured in the undoped crystals a nearly flat linear background is subtracted from the photo-induced spectra as shown in

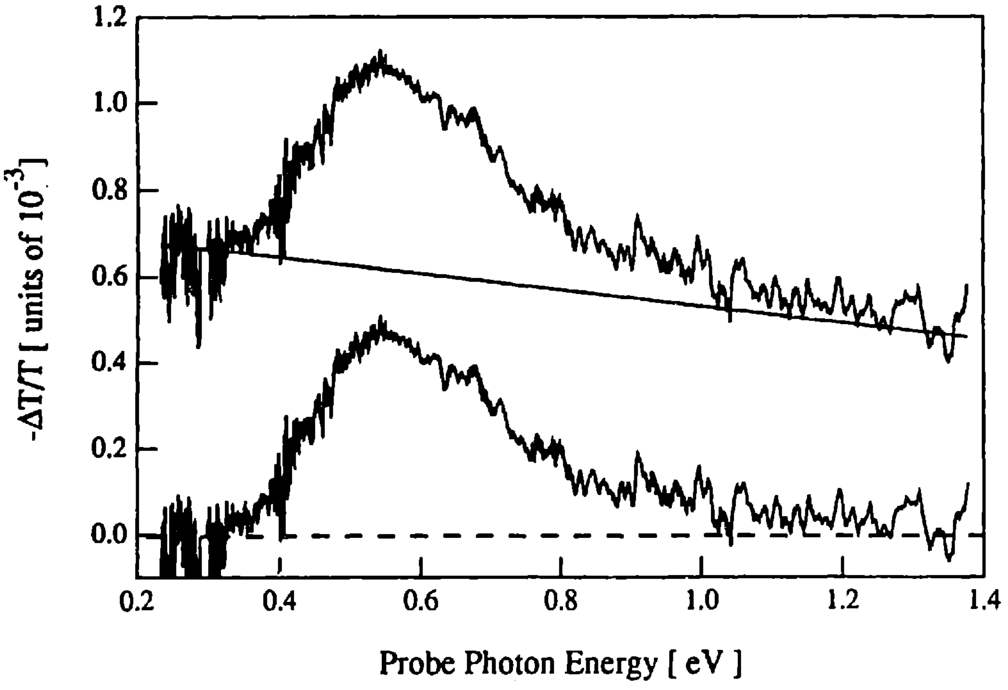

Figure 6.4: Subtraction of linear background from π-pumped photoinduced absorption in La_2CuO_4 single crystal. Data from figure 6.3.

figure 6.4. At the present time, the origin of this nearly energy independent contribution is not understood. The top panel of figure 6.5 compares the π-pumped photo-induced absorption with the intrinsic absorption in undoped La_2CuO_4 single crystals. Note that the vertical axis have different scales.

The high degree of similarity between the two spectra strongly suggests that the magnon sidebands are enhanced by adding carriers. If the entire thickness of the crystal is pumped, the peak in the photo-induced absorption corresponds to $\Delta\alpha \approx 3.5\ cm^{-1}$. Falck *et al* [27] have measured the mid-infrared reflectivity in lightly doped La_2CuO_{4+y}. For $y = 0.014$ the absorption at ~ 0.55 eV is ~ $1.7\times10^4\ cm^{-1}$. Assuming a linear scaling and uniform pumping, the induced absorption in figure 6.5 corresponds to a doping level of $y \cong 4\times10^{-6}$. To determine the quantum efficiency from these non-time-resolved measurements the functional form of the decay must be known, which it isn't. However, similar experiments on a Nd_2CuO_4 thin film sample, using the same pump laser, produce roughly the same amount of photo-induced absorption as shown in figure 6.8.

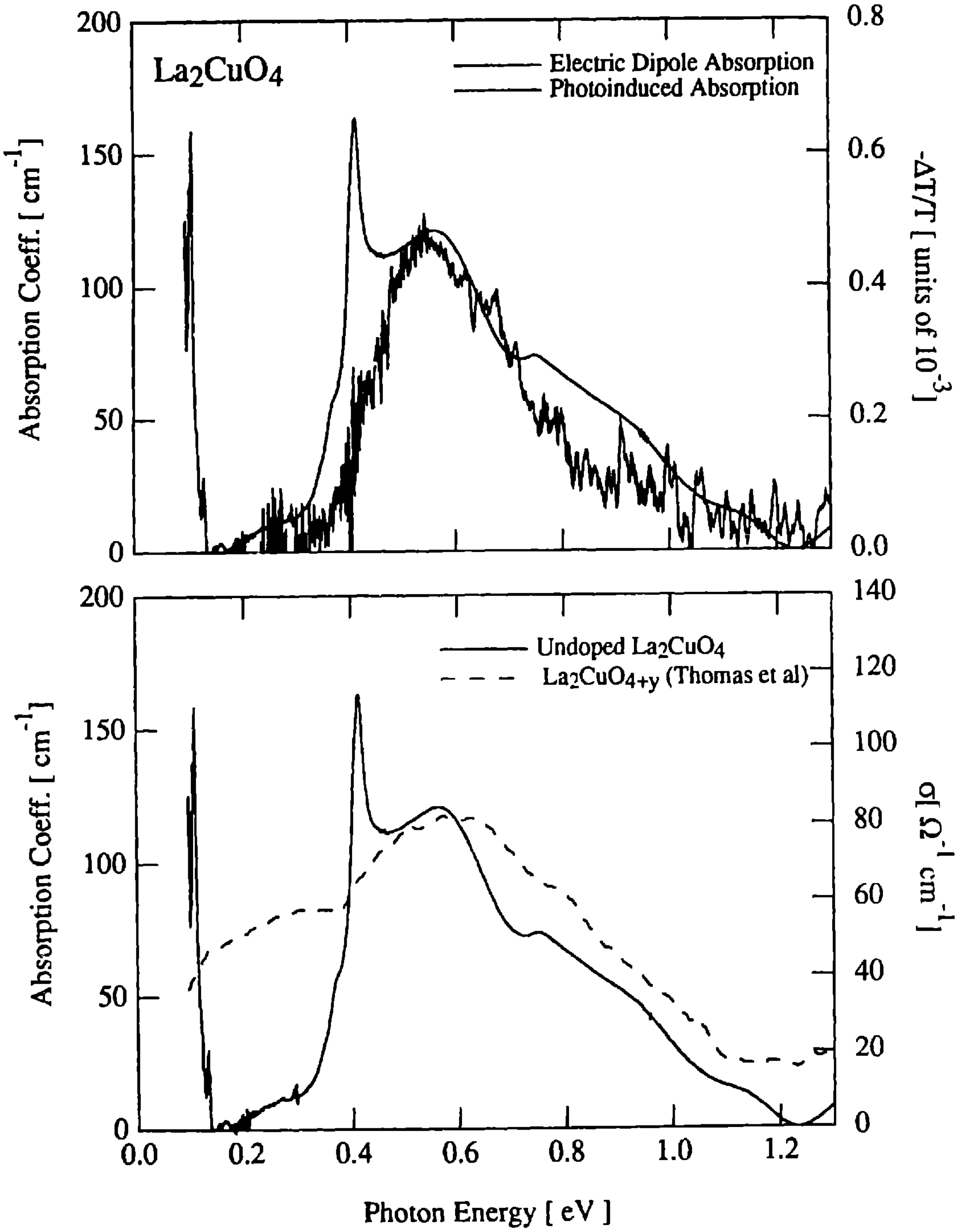

Figure 6.5: Comparison of intrinsic absorption in undoped La_2CuO_4 with photoinduced absorption (top) and optical conductivity in lightly oxygen doped La_2CuO_{4+y} (bottom, Thomas *et al* [28])

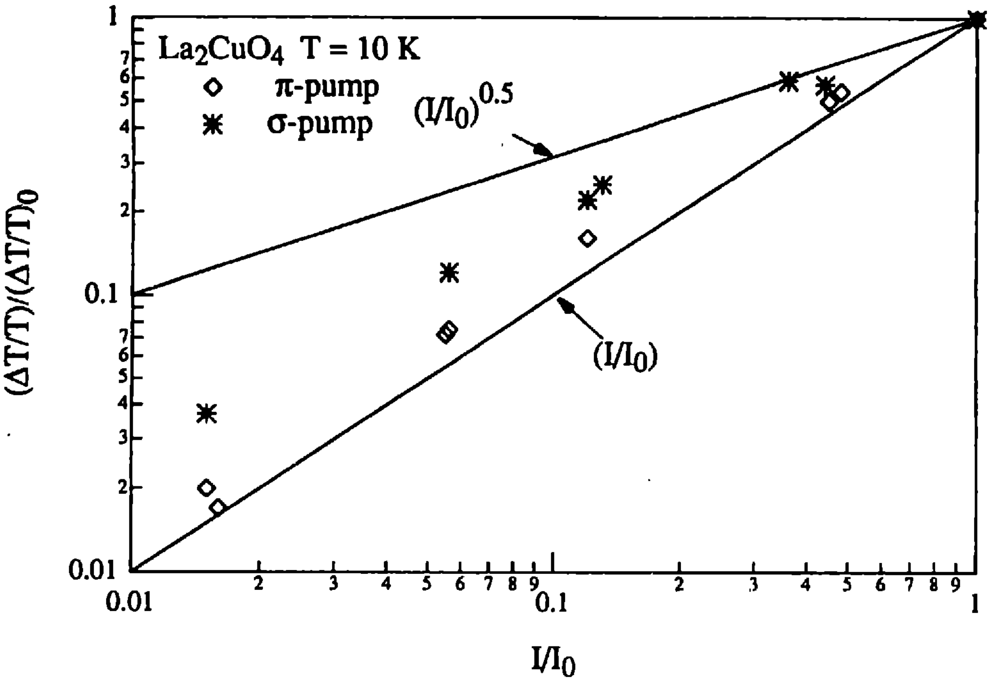

Figure 6.6: Pump intensity dependence of photoinduced absorption in La_2CuO_4 single crystal at T = 10K for both σ and π-pumping. Pump at 1.96 eV (632.8 nm). Pump laser chopped at 5 Hz Probe beam at 0.55 eV, corresponding to the peak in the induced absorption.

Time-resolved photo-induced absorption experiments done with a pulsed laser on the Nd_2CuO_4 thin film sample indicate a quantum efficiency of ~ 2×10^{-2}. The bottom panel of figure 6.5 compares the intrinsic absorption in undoped La_2CuO_4 with optical conductivity in lightly oxygen doped La_2CuO_{4+y} as measured by Thomas *et al* [28]. Again there is a strong similarity between the two spectra.

The peak of the photo-induced absorption for a Nd_2CuO_4 thin film shown in figure 6.8 does not appear to line up as well with the 1-magnon peak of the Nd_2CuO_4 single crystal data from figure 3.2 as the La_2CuO_4 comparison shown in figure 6.5. However, the Nd_2CuO_4 single crystal measured was not thin enough to measure the full magnon sideband structure and the Nd_2CuO_4 thin film may well have a significant defect level. The La_2CuO_4 spectra compared in figure 6.5 were measured on the same single crystal sample.

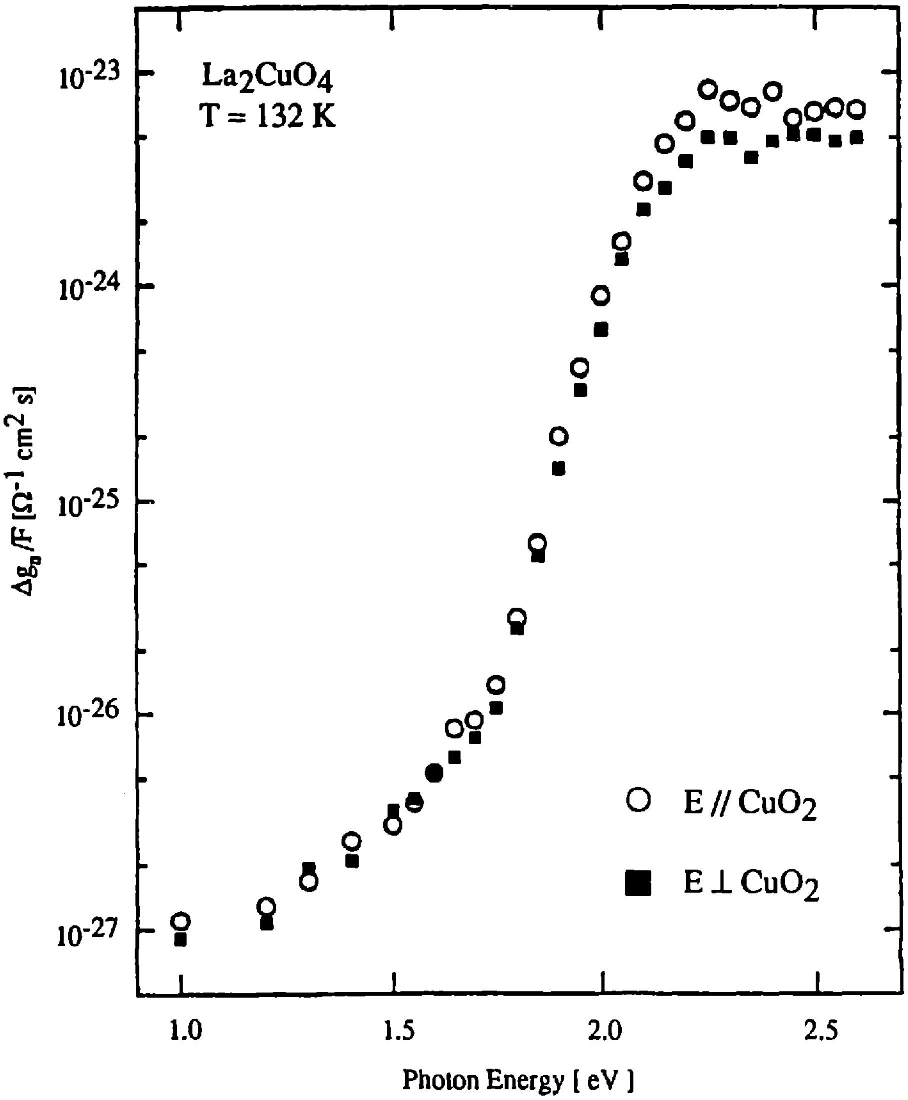

Figure 6.7: The photoconductance per square, Δg, normalized to the incident photon flux, F, as a function of photon energy for light polarized parallel (open circles) and perpendicular (filled squares) to the CuO_2 plane in La_2CuO_4 single crystals.. From Thio *et al* [90]

Figure 6.6 shows the pump intensity dependence of the induced absorption in La_2CuO_4 for both σ and π-pumping. The nearly linear dependence on pump intensity for both polarizations of pumping suggests that even the σ-pumped case can be considered in the weak pumping limit. Figure 6.7 shows the pump photon energy dependence of the photo-induced conductivity from Thio *et al* [90]. Note that the left axis is logarithmic. The pump photon energy for the photo-induced absorption experiments presented above was 1.96 eV. As seen in figure 6.7, the photoconductance per unit photon flux drops rapidly below a photon energy of about 2.2 eV and is down by an order of magnitude at 1.96 eV. For future photo-induced absorption experiments it may be better to use a higher photon energy source for pumping.

In summary, the similarity in shape of the intrinsic absorption spectra in undoped La_2CuO_4 with that in lightly oxygen doped La_2CuO_{4+y} and the photo-induced absorption spectra in undoped La_2CuO_4 strongly suggests that the magnon sidebands grow with doping and hence provide the mechanism for the doping enhanced mid-infrared absorption observed in the High-T_c related materials.

Time-resolved Photo-induced Absorption

This section presents time-resolved photo-induced absorption data. As mentioned before, this section is not important to the explanation of the mechanism of the mid-infrared absorption in the undoped lamellar copper oxides. The photo-induced absorption is used as a probe of the decay of the photo injected carriers. The decay of the photo-induced absorption is extremely slow, with effects lasting a second or longer. The majority of the data presented is taken on an epitaxial Nd_2CuO_4 thin film sample. From a selection of about ten candidate samples, the particular sample studied was chosen because it had the sharpest charge transfer edge and hence, presumably the lowest carrier concentration. Similar results are also obtained in Pr_2CuO_4 single crystals.

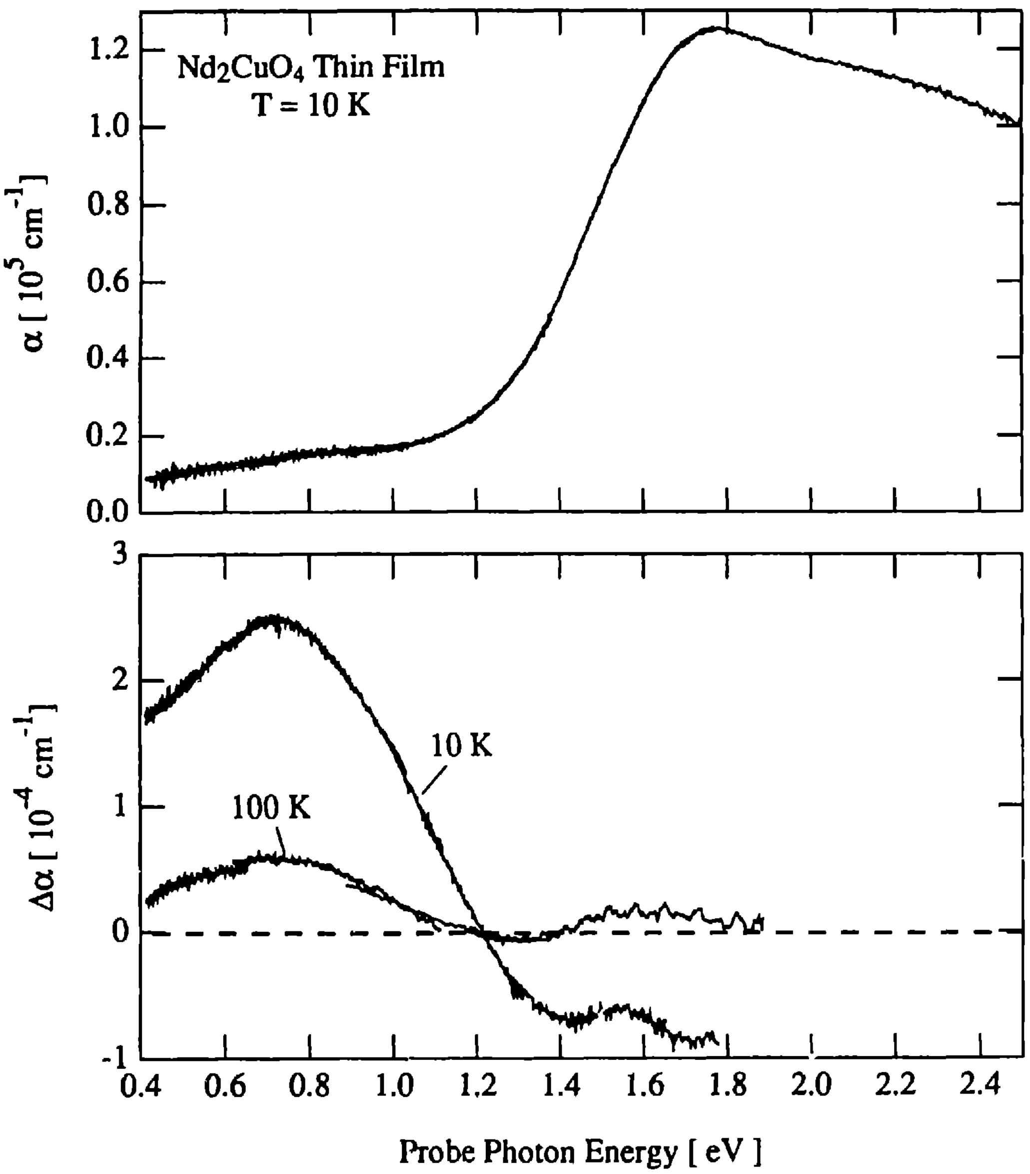

Figure 6.8: Top: Absorption coefficient vs. photon energy for a Nd_2CuO_4 thin film at T = 10K. Bottom: Photoinduced absorption vs. probe photon energy for the same film. Pumped at 1.96 eV (632.8 nm). Pump laser chopped at 5 Hz.

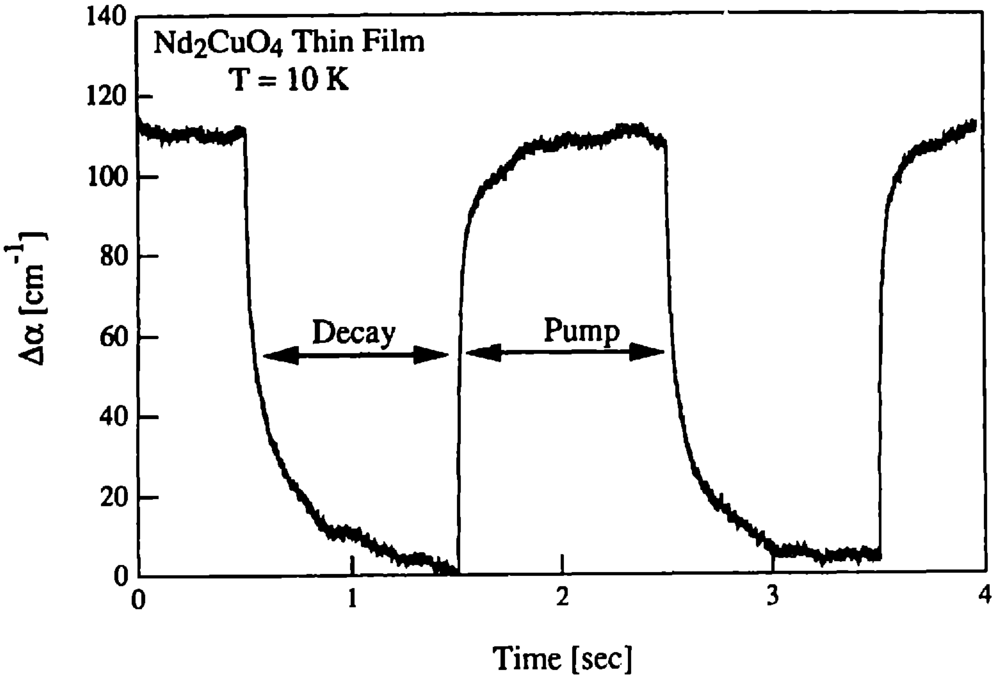

Figure 6.9: Photoinduced absorption vs. time for a Nd_2CuO_4 thin film at T = 10K. Pumped at 1.96 eV (632.8 nm). Pump laser chopped at 0.5 Hz. Probe beam at 0.7 eV (1750 nm).

Steady State Pumping

Pumping the sample with a laser above the charge transfer gap creates electron and hole carriers as has been demonstrated by photoconductivity experiments [90]. If the decay of the carriers is dominated by single particle effects, then the time dependence will be exponential. If a free electron and hole must find each other, then the rate of decay will be proportional to the joint density of electrons and holes:

$$\frac{dn_e}{dt} \propto -n_e n_h = -n_e^2. \tag{6.3}$$

For photo-injected carriers the density of electrons and holes are equal. Integrating this equation gives:

$$n_e \propto \frac{1}{t}. \tag{6.4}$$

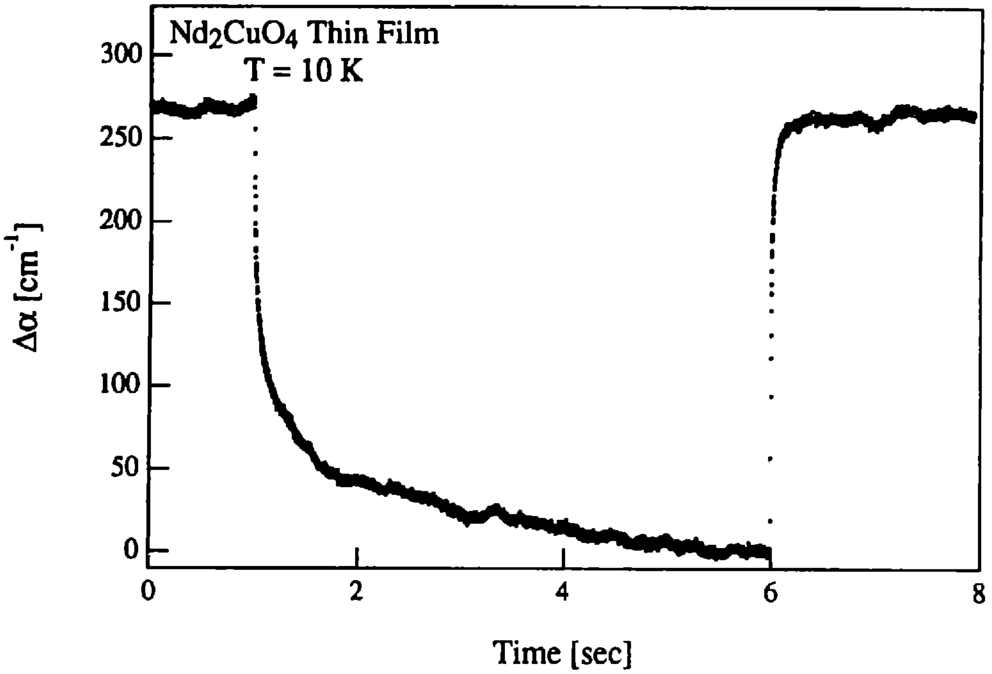

Figure 6.10: Photoinduced absorption vs. time for a Nd_2CuO_4 thin film at T = 10K. Pumped at 1.96 eV (632.8nm). Pump laser chopped at 0.1 Hz. Probe beam at 0.7 eV (1750 nm).

This type of decay is called bimolecular decay since it originates from two objects searching for each other. As will be shown, neither of these two simple mechanisms describes the decay of the photo-induced absorption in the lamellar copper oxides.

The top panel of figure 6.8 shows the absorption coefficient vs. photon energy for the Nd_2CuO_4 thin film used in these experiments. In the photo-induced absorption experiments pump photon energies of 1.96, 2.21, and 2.33 eV were used. All of these are well above the charge transfer gap in Nd_2CuO_4. The bottom panel of figure 6.8 shows the probe photon energy dependence of the non-time-resolved photo-induced absorption, which is peaked at about 0.7 eV. Therefore, all the time-resolved experiments were done with a probe photon energy of 0.7 eV (1750 nm). Figure 6.9 shows the time-resolved photo-induced absorption at T = 10 K obtained using a Helium-Neon laser at 1 96 eV and a simple mechanical shutter to chop the pump beam at 0.5 Hz. Figure 6.10, shows a similar experiment with the pump laser chopped at 0.1 Hz. The photo-induced absorption has not completely decayed five seconds after the end of the pumping

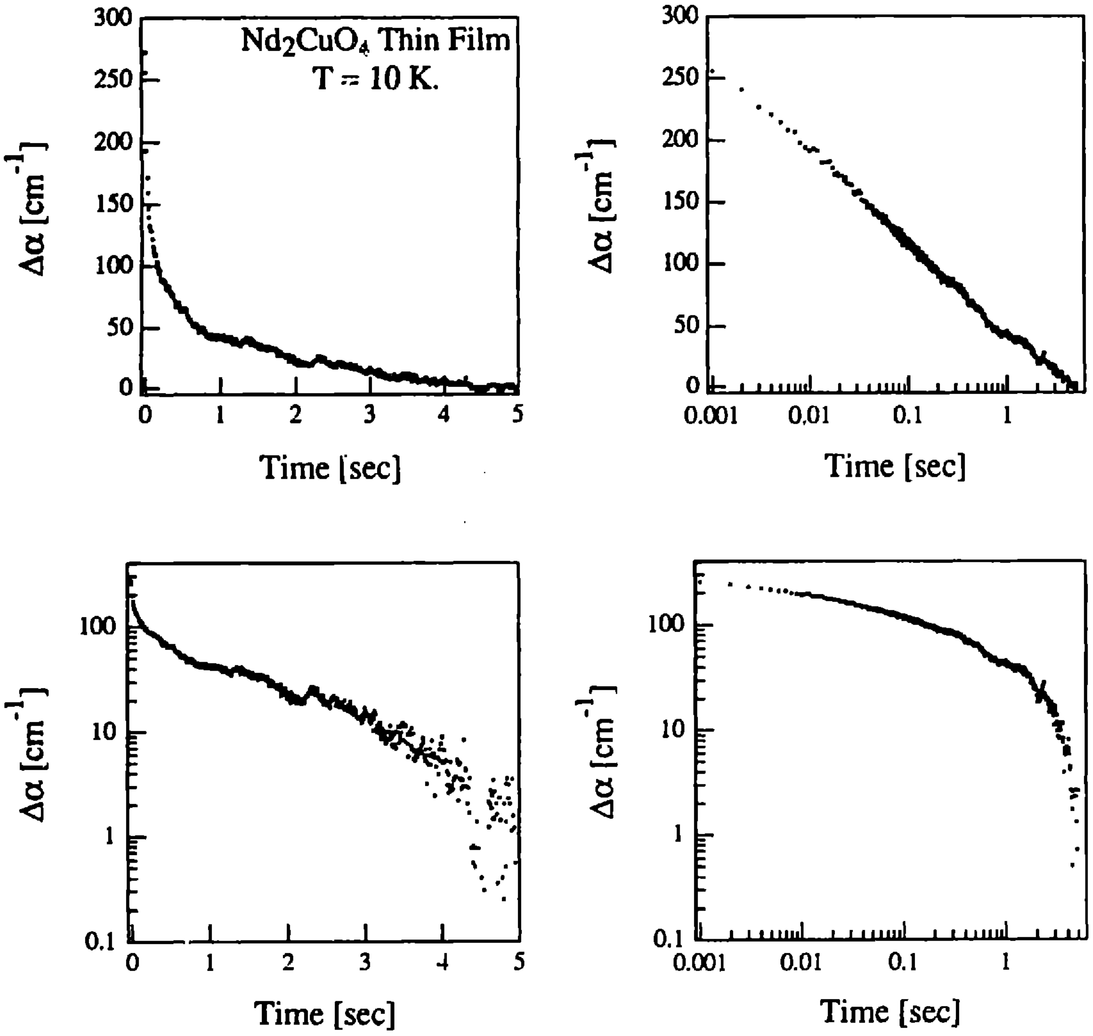

Figure 6.11: Decay of photoinduced absorption vs. time for a Nd_2CuO_4 thin film. Data from Figure 6.10. Pumped at 1.96 eV (632.8 nm). Pump laser chopped at 0.1 Hz. Probe beam at 0.7 eV (1750 nm). T = 10K.

period, when the pumping resumes. To analyze the decay, the last point before the decay begins is taken to define the zero of time and the last point at the end of the decay to define the zero of the induced absorption. Clearly this second assumption is not entirely correct because the induced absorption is still decaying at this point. The time decay is shown plotted in the four combinations of linear and logarithmic axis in figure 6.11. The decay forms a nearly straight line when plotted on linear y axis and a logarithmic time axis. Since the y-axis is linear, the shape of the line is not effected by any error in choosing the zero of the

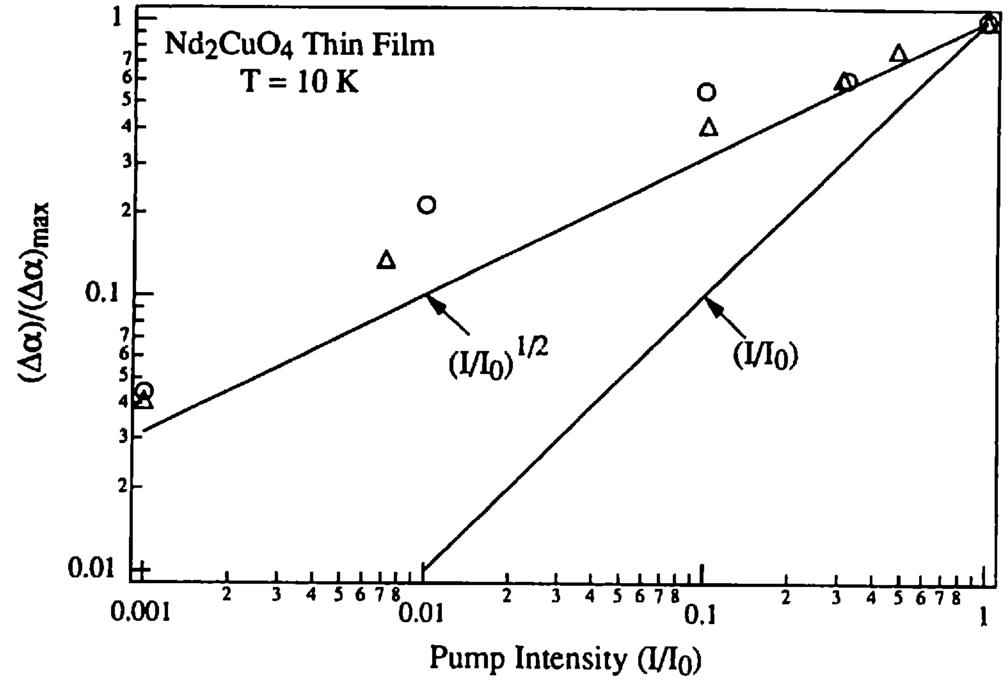

Figure 6.12: Pump intensity dependence of photoinduced absorption in Nd_2CuO_4 thin film at T = 10 K. Pump at 1.96 eV (632.8 nm). Pump laser chopped at 5 Hz. Probe beam at 0.7 eV (1750 nm). The open circles and triangles represent two separate measurements of the pump intensity dependence.

induced absorption and the zero of time is well defined on the time scale shown. In GaP lightly doped with sulfur donors and silicon acceptors, the total photo-induced fluorescence decays as 1/t [91]. The fluorescence measures the rate of decay. Therefore, the decay of the total number of excited carriers in the doped GaP is logarithmic. A logarithmic decay can be understood in terms of a distribution of decay rates. However, as will be shown by the rest of this section, the empirical nature of the decay is not yet well enough defined by experiments to warrant further analysis of the mechanism.

It is hard to believe that the decay would not continue at times greater than five seconds, if the pump laser where chopped at a lower frequency. This indicates that the photo-injected carriers do not completely decay between laser pumping periods and that a steady state density of photo-injected carriers must be present. The photoconductivity experiments of Thio *et al* [90] observed carrier lifetimes of 10 seconds or more in La_2CuO_4 single crystals. In thin films of $YBa_2Cu_3O_{6+\delta}$, persistent photoconductivity has been seen at T = 4K[86,87]. This was reproduced by Ady Levy at MIT [88]. In a Nd_2CuO_4 thin film immersed in liquid nitrogen, the conductivity increased continuously for two hours under illumination by a 25 mW, 2eV laser [88]. The total change in the conductivity was about 2%. When the illumination by the laser was stopped the conductivity decayed over several hours back to the initial value. This suggests that the interpretation of repetitively pulsed experiments may be complicated by the presence of a steady state background. However, if a steady state background does increase continuously under laser illumination, this may provide a simple method to study the doping dependence of the mid-infrared absorption.

Figure 6.12 shows the pump intensity dependence for the above steady state pumping experiments. On the time scale of a single laser pump period, figure 6.9 shows that the induced absorption is in quasi-equilibrium with the pumping laser. If this is true, then the pumping intensity dependence of the induced absorption would be linear for exponential decays and square root for bimolecular decay. As can be seen in 6.12, the intensity dependence is clearly not linear and is probably weaker than square root. However, given the strange nature of the decay, this is not surprising.

Pulsed Pumping

In order to look at faster time scales than allowed with the simple mechanical chopper used above, a Nd:YAG laser with 10 nS output pulses was used to pump the sample. The frequency doubled output produced photons of energy 2.33 eV (532 nm). For some experiments, the Nd:YAG was used to pump a dye laser, resulting in photons of energy 2.21 eV (560 nm). At the present time, no significance is placed on this energy difference. The output of the dye laser simply results in a more uniform beam spot for pumping the sample than the Nd:YAG laser, which produces a donut shaped spot. The fastest time scales examined in these experiments is of order 10 μS. Hence, the 10 nS laser pulse, can be considered to instantaneously inject a number of electrons and holes proportional to the number of photons in the pulse. For pumping intensities weak enough for this assumption to be valid, the pump intensity dependence of the induced absorption should be linear, independent of the decay mechanism.

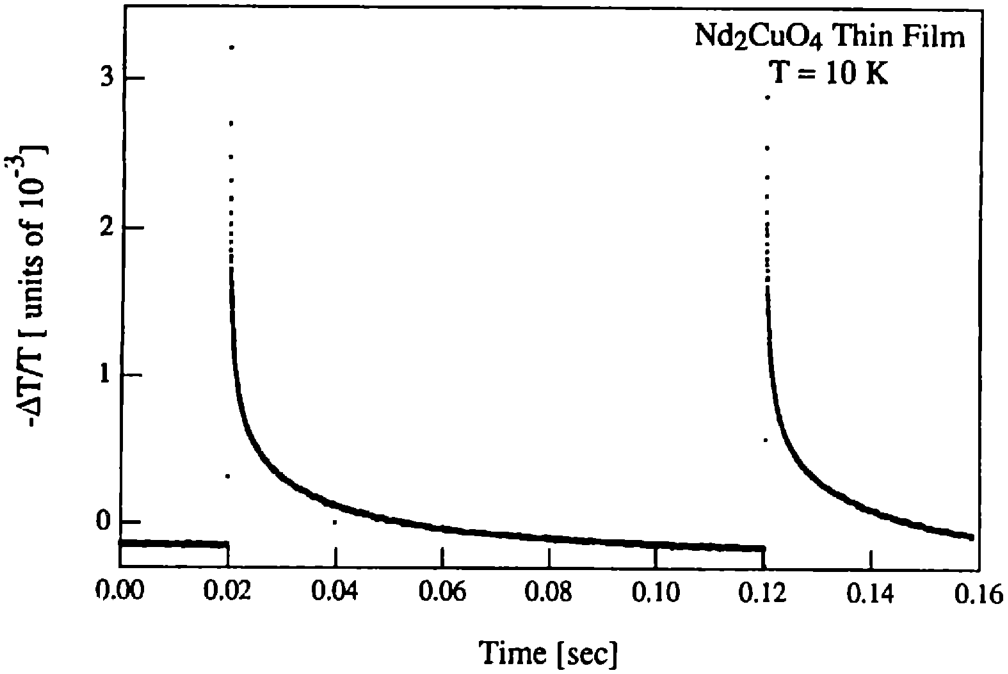

Figure 6.13: Photoinduced absorption vs. time for a Nd_2CuO_4 thin film. Pumped at 2.21 eV (560 nm) with 10 nS pulses at 10 Hz. Probe at 0.7 eV (1750 nm). T = 10K.

Figure 6.13 shows the induced absorption in a Nd_2CuO_4 thin film at T = 10 K, due to pulsed pumping at 10 Hz. To analyze the decay, the last point prior to the jump in the induced absorption is taken as the zero of both time and the induced absorption. All of the data is shown in terms of the relative change in transmission. The induced change in the absorption coefficient can be determined from equation 6.2 using the film thickness of 700 Å. The decay of the data from figure 6.13 is shown in figure 6.14. The linear y, logarithmic x plot now shows a slight, but continuous, curvature. In the log-log plot, the decay is straight at short time scales. This suggests that the decay may be described as a weak power law. The abrupt down turn of the decay in the log-log plot at times greater than 10 milliseconds may be due to an incorrect determination of the zero of the induced decay. Figure 6.15 shows a power law fit to the decay. Although the data is taken at points equally spaced in time, the fit is to an interpolated array with an equal number of points per decade in time. This causes the fit to treat all decades of time equally.

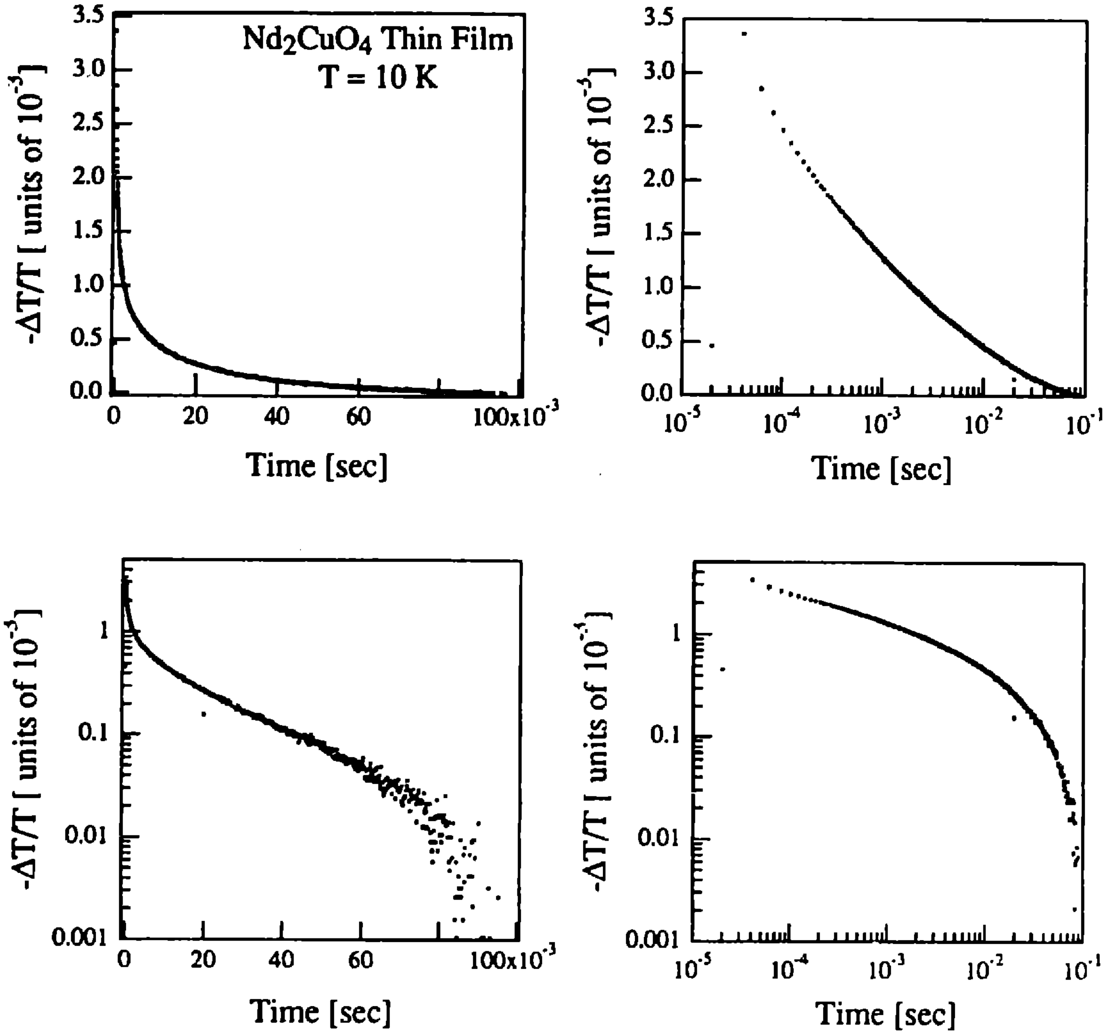

Figure 6.14: Decay of photoinduced absorption vs. time for a Nd_2CuO_4 thin film. Data from Figure 6.13. Pumped at 2.21 eV (560 nm) with 10 nS pulses at 10 Hz. Probe at 0.7 eV (1750 nm). T = 10K.

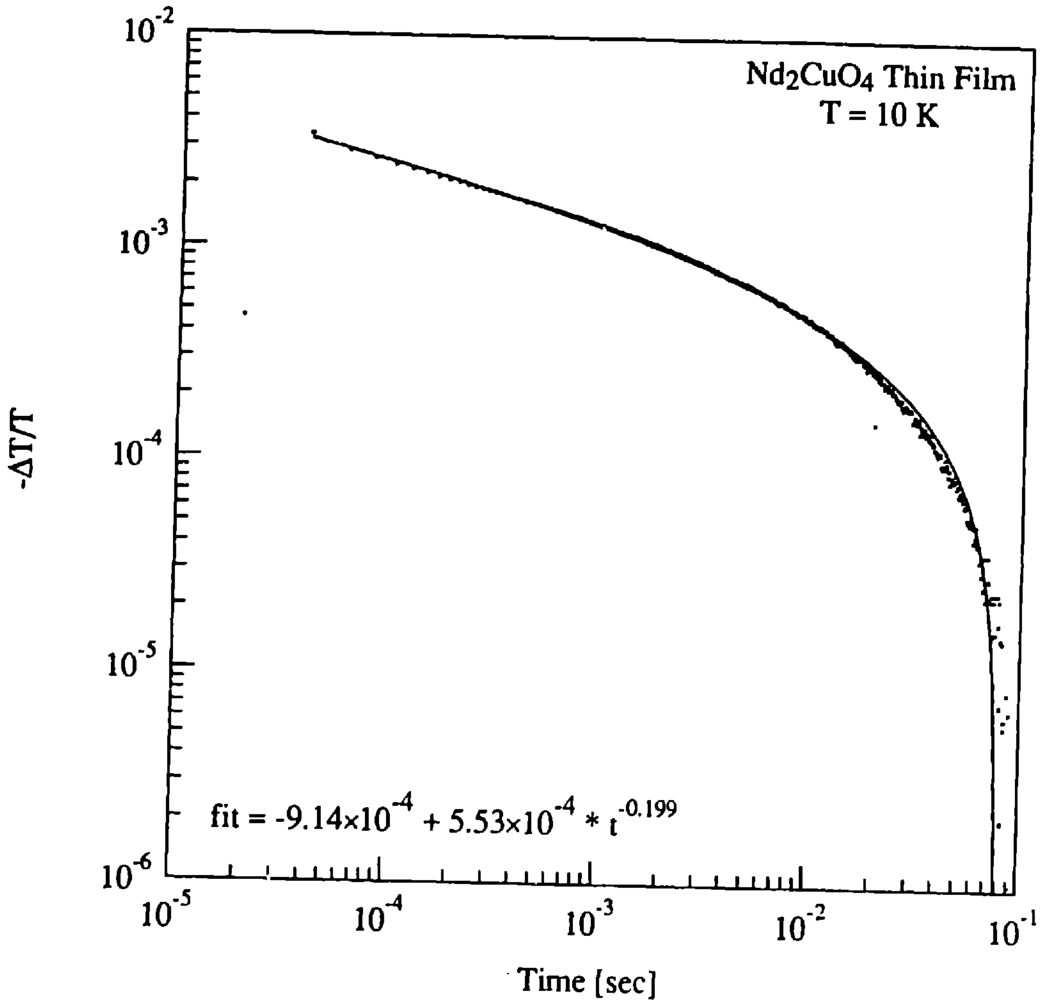

Figure 6.15: Decay of photoinduced absorption vs. time for a Nd_2CuO_4 thin film. The solid line is a power law fit to the data. Data from Figure 6.13. Pumped at 2.21 eV (560 nm) with 10 nS pulses at 10 Hz. Probe at 0.7 eV (1750 nm). T = 10 K.

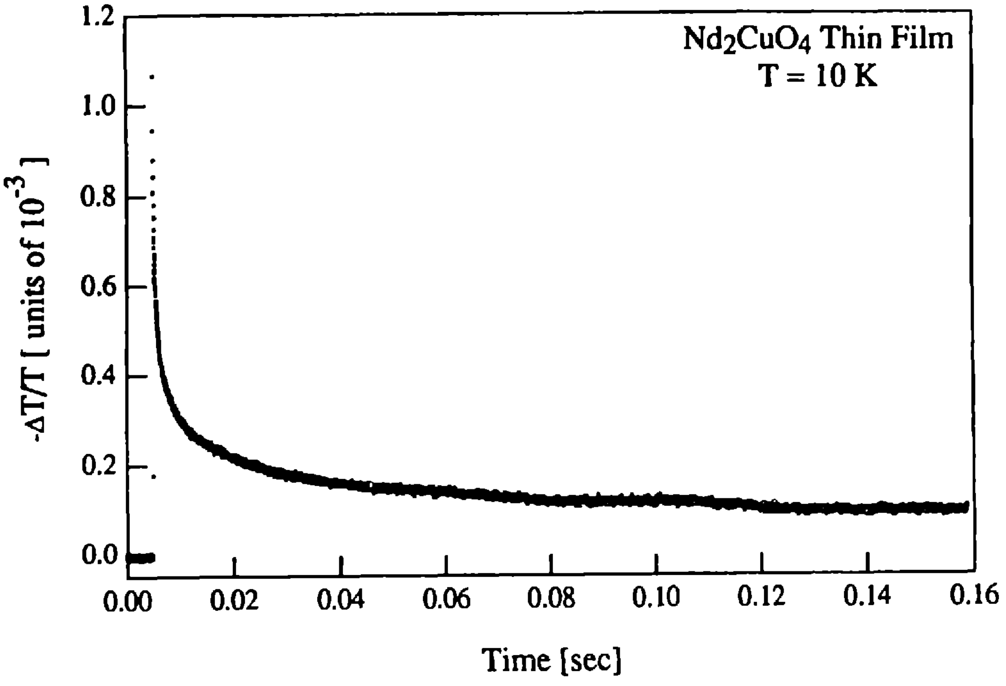

Figure 6.16: Photoinduced absorption vs. time for a Nd_2CuO_4 thin film. Pumped at 2.21 eV (560 nm) with 10 nS pulses at 0.1 Hz. Probe at 0.7 eV (1750 nm). T = 10 K.

The fit is reasonably good. The exponent of the decay is ~ 0.2 and the offset is about 10^{-3}. This implies that the accumulated steady state background induced absorption is as large as the change induced by a single pulse.

Figure 6.16 shows the induced absorption taken at the same temporal resolution, but with a pumping frequency of 0.1 Hz. Now the induced absorption decays for ten seconds between each pulse instead of only 100 milliseconds. The difference in pre-pulse value and that 100 milliseconds later clearly shows that the induced absorption had not fully decayed in the previous experiments. Again the last point prior to the jump in the induced absorption is taken as the zero of both time and the induced absorption. The resulting decay is shown in figure 6.17. The decay, plotted on a log-log plot now looks straighter than before. In addition the late time down turn is noticeably decreased. This is consistent with the decay being a weak power law, with an as of yet undetermined zero. A power law fit to the decay is shown in figure 6.18. The exponent of the decay is ~ 0.25, and the offset is now about 5×10^{-5}.

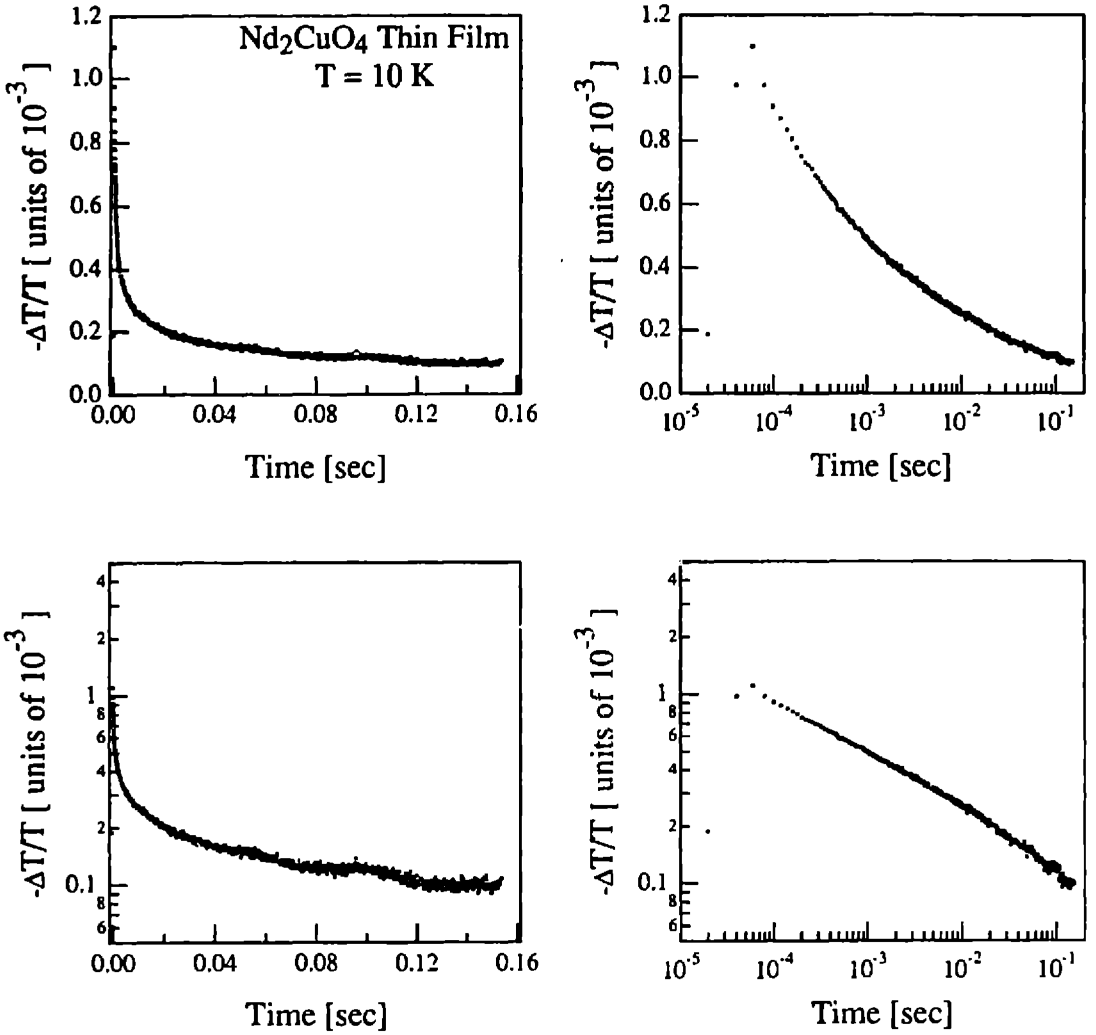

Figure 6.17: Decay of photoinduced absorption vs. time for a Nd_2CuO_4 thin film. Data from Figure 6.16. Pumped at 2.21 eV (560 nm) with 10 nS pulses at 0.1 Hz. Probe at 0.7 eV (1750 nm). T = 10 K.

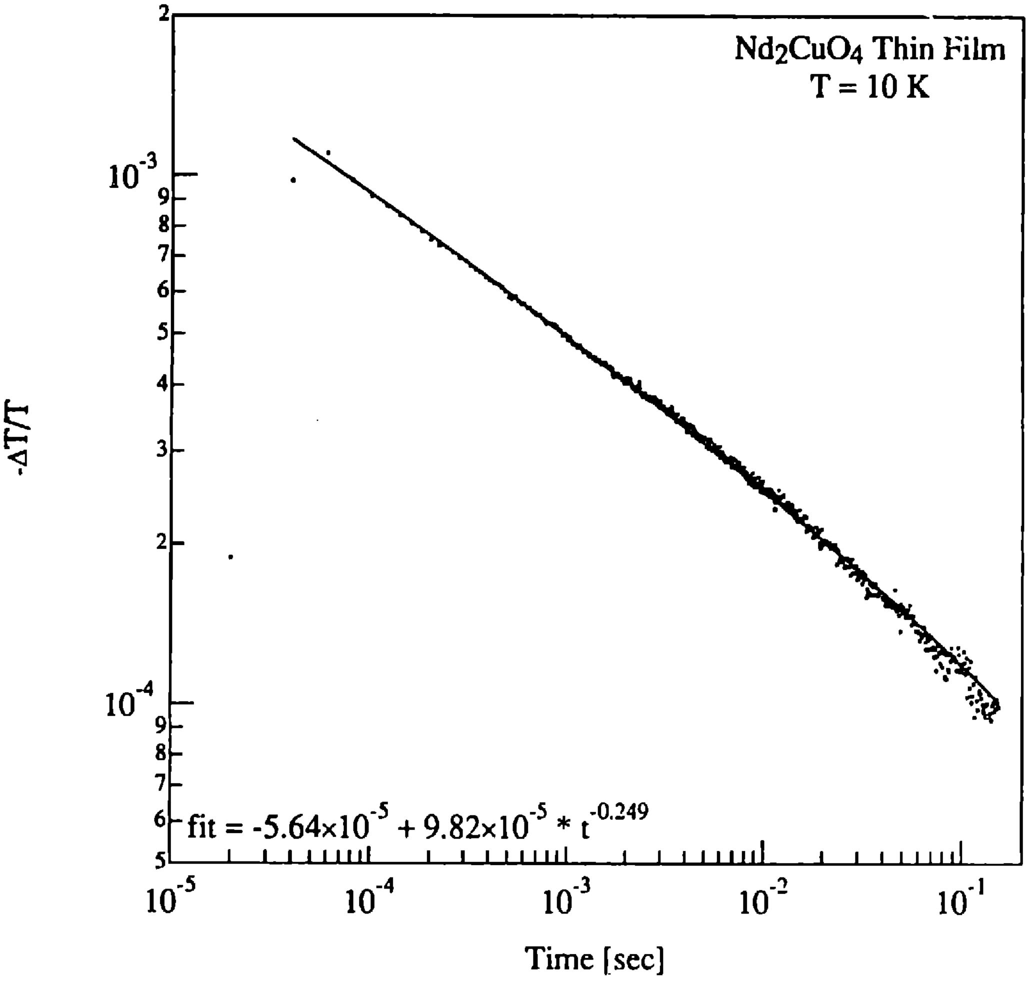

Figure 6.18: Decay of photoinduced absorption vs. time for a Nd_2CuO_4 thin film. The solid line is a power law fit to the data. Data from Figure 6.16. Pumped at 2.21 eV (560 nm) with 10 nS pulses at 0.1 Hz. Probe at 0.7 eV (1750 nm). T = 10 K.

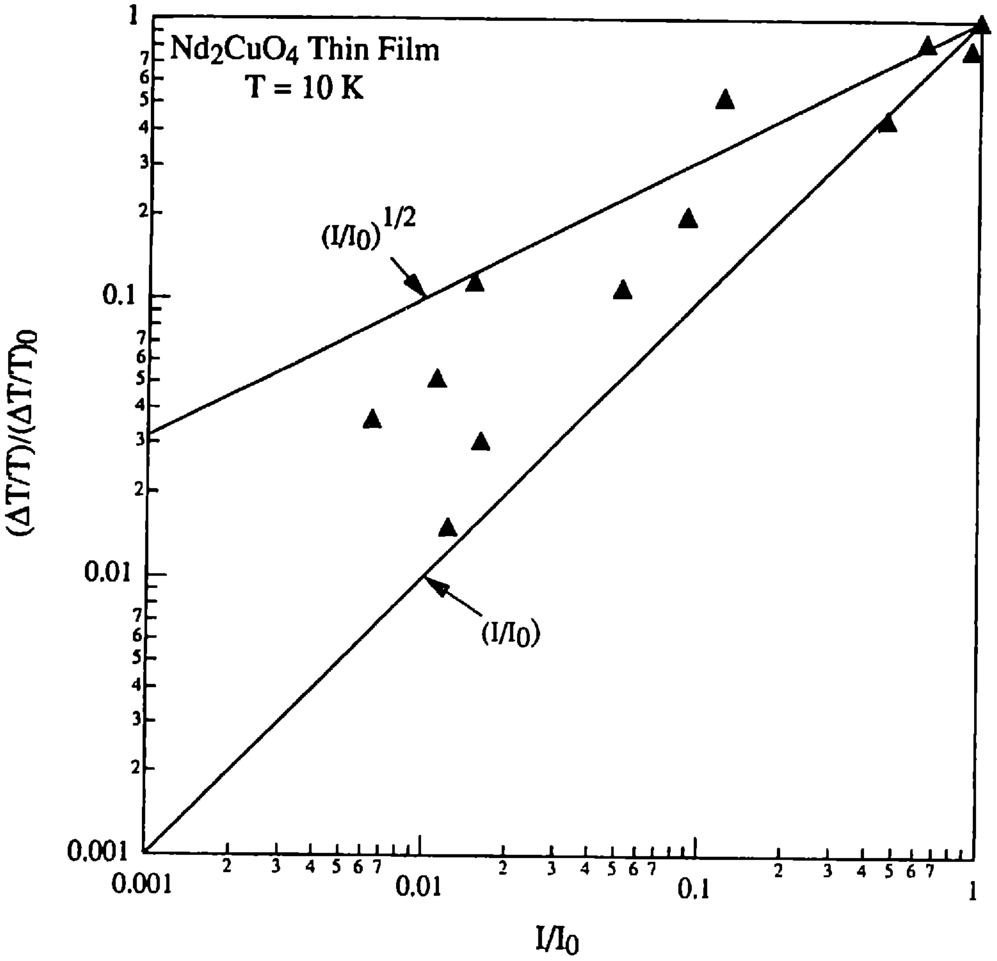

Figure 6.19: Pump intensity dependence of photoinduced absorption in Nd_2CuO_4 thin film at T = 10 K. Pump at 2.21 eV (560 nm) with 10 nS pulses at 10 Hz. Probe beam at 0.7 eV (1750 nm) T = 10 K.

To really see if the decay is well described by a power law, more data needs to be taken. Figure 6.19 shows the pump intensity dependence of the induced absorption with pulsed pumping at 10 Hz. The dependence is closer to linear than in the steady state pumping experiments, but the large scatter in the data makes it difficult to extract a well defined dependence. The scatter may well be due to small changes in the relative position of the sample and the pump beam. Because these photo-induced absorption measurements are sensitive to vibration, the optics table is floated. The Nd:YAG laser is located on a different table and hence, the sample is not rigidly positioned with respect to the pump beam. Potential solutions to this problem are discussed in Chapter 7.

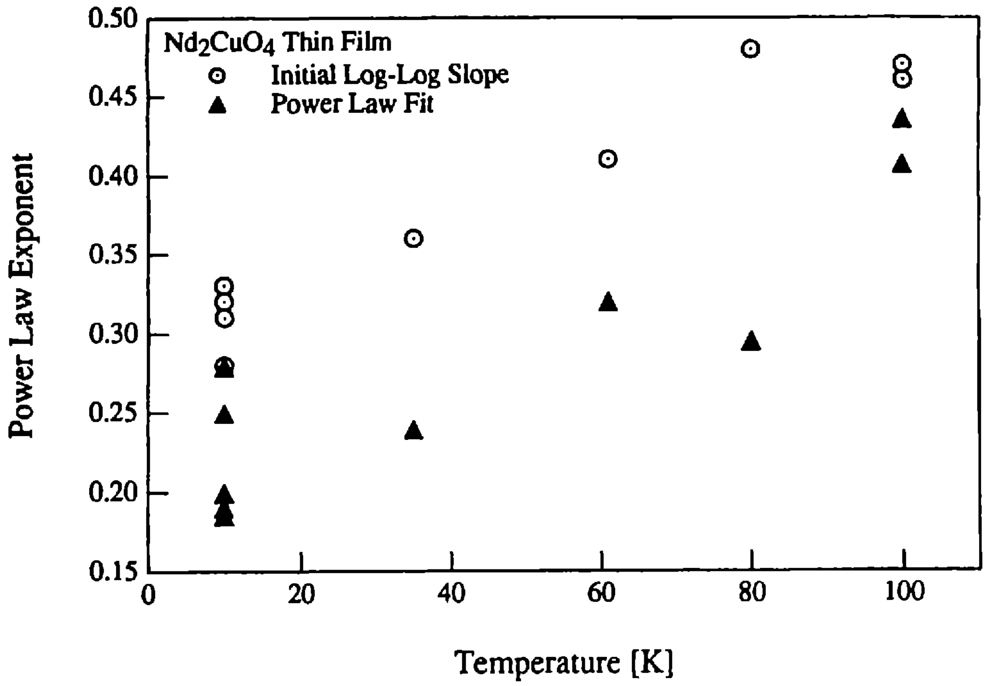

Figure 6.20: Exponent in power law decays for photoinduced absorption in Nd_2CuO_4 thin films at T = 10 K. Pumped at 2.21 eV (560 nm) with 10 nS pulses at 10 Hz. Probe beam at 0.7 eV (1750 nm). The open circles give the initial slope in a log-log plot using the last pretrigger point as the zero point. The filled triangles represent a fit with the y offset allowed to float.

In addition to the power law fitting described above, an exponent for the power law decay may be extracted by assuming the zero point is defined correctly and measuring the initial slope of the decay. Figure 6.20 shows power law decay exponent for both methods of analysis as a function of temperature. The initial slope method consistently yields a higher value for the exponent. In the analysis of the initial-slope method, the last pretrigger point is taken to be the zero of induced absorption. As discussed above, there is almost certainly a steady state build up of induced absorption. If a steady state term is added to the induced absorption, the initial slope in a log-log plot will decrease. Hence, the larger exponent derived by the initial-slope method is consistent with the buildup of a steady state background. Both methods of analysis show that the decay quickens with increasing temperature. Temperature dependent power law decays have been seen in the photoconductivity of amorphous semiconductors and are explained in terms of a multiple trapping model[92-94]. Figure 6.21 shows the dependence of the difference in the power law

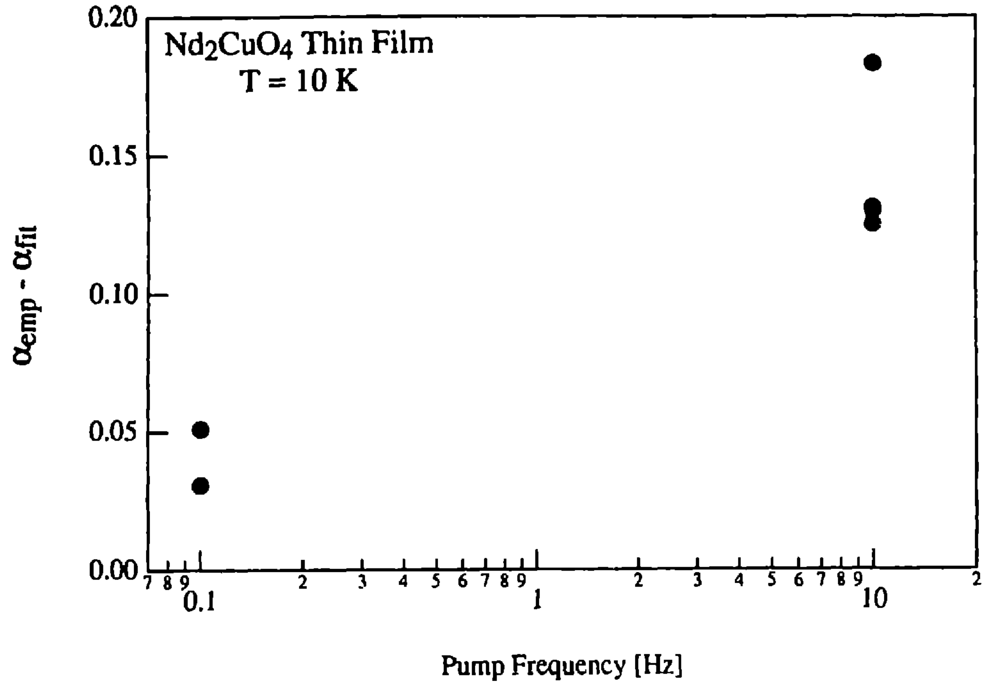

Figure 6.21: Difference in derived power law decay as a function of laser pumping rep rate for photoinduced absorption in Nd_2CuO_4 thin film at T = 10 K.

exponent derived by the initial slope method and the fitting method as a function of the repetition rate of the pumping laser pulses. The two methods are converging as the pump frequency is lowered.

To see if this peculiar decay is a general property of the High-Tc host materials or particular to the Nd_2CuO_4 film studied, the time-resolved photo-induced absorption was measured for a Pr_2CuO_4 single crystal. The data is shown in figure 6.22. Clearly, long time scales still exist in the decay. The jump in the induced absorption at ~ 0.12 seconds is noticeably smaller than the first jump. The signal averaging scope is triggered on the first pulse so the averaged pulses always add coherently. Due to jitter in the laser pump rep rate, the second pulse does not always begin at the same time after the scope trigger. Approximately 1500 traces were averaged for the data shown in figure 6.22. This accounts for the decrease in the size of the second jump in the induced absorption. Figure 6.23 shows the photo-induced absorption in Pr_2CuO_4 with a pump frequency of 0.8 Hz. Figure 6.24 shows a power law fit to both decays.

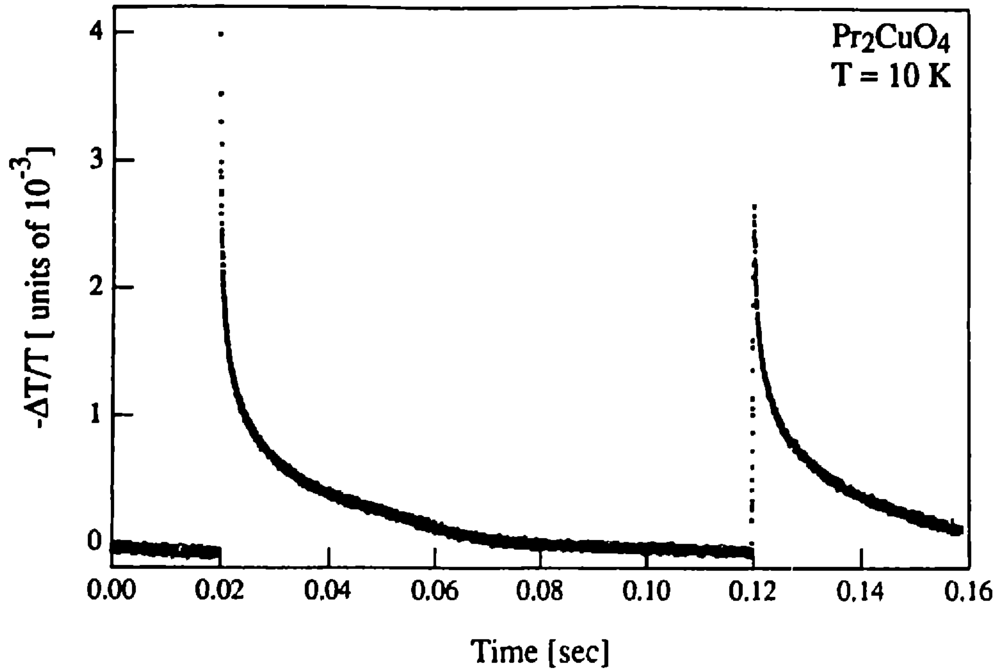

Figure 6.22: Photoinduced absorption vs. time for a Pr_2CuO_4 single crystal. Pumped at 2.33 eV (532 nm) with 10 nS pulses at 10 Hz. Probe at 0.7 eV (1750 nm). T = 10K.

A steady state offset is added to the 10 Hz pump rep rate decay data to match the 0.8 Hz decay data at about 1 millisecond. The agreement between the two data sets after this offset is made suggests that this is a reasonable way to match the data. The data from 4×10^{-5} to 1 second is well fit by a power law decay. Figure 6.25 shows the same data plotted lin-log so that a logarithmic decay would yield a straight line.

Summary of Photo-induced Absorption Measurements

The first section of this chapter compared the spectral shape of the intrinsic absorption in La_2CuO_4 single crystals with that of lightly oxygen doped La_2CuO_{4+y} and the non-time-resolved, steady state pumped, photo-induced absorption. The similarity of the spectral shapes from ~ 0.4 to 1.2 eV strongly suggests that the magnon sidebands grow with doping. The addition of holes, which strongly modify the antiferromagnetic ground state, may introduce new matrix elements for dipole allowed exciton-

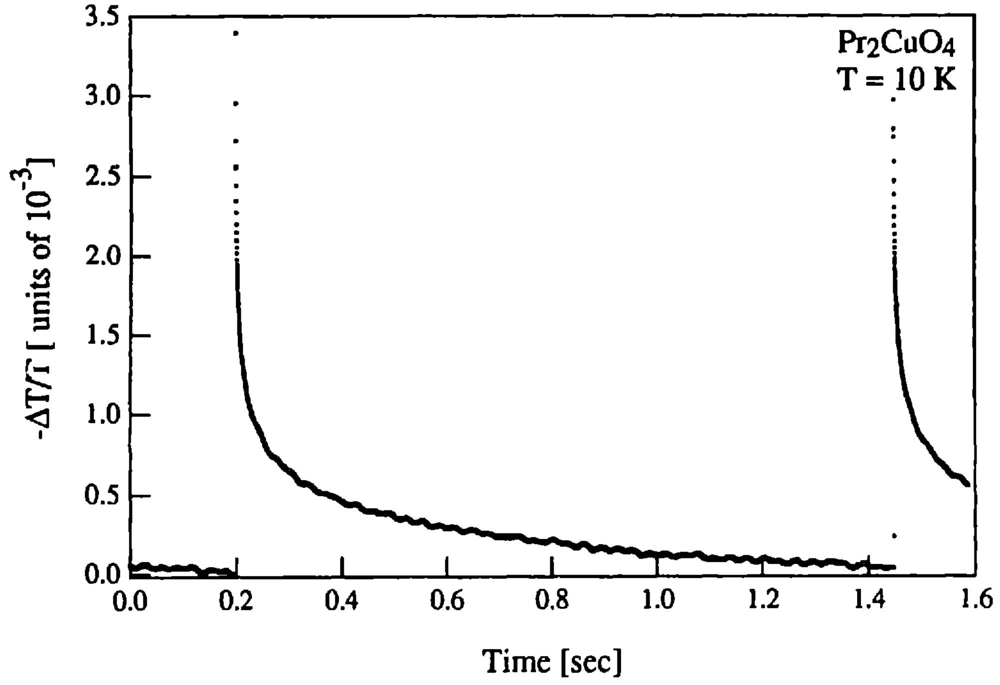

Figure 6.23: Photoinduced absorption vs. time for a Pr_2CuO_4 single crystal. Pumped at 2.33 eV (532 nm) with 10 nS pulses at 0.8 Hz. Probe at 0.7 eV (1750 nm). T = 10K.

magnon excitations. Further experiments to study the evolution of the mid-infrared absorption in very lightly oxygen doped La_2CuO_4 single crystals are presently under way.

The time-resolved photo-induced absorption measurements of Nd_2CuO_4 thin films and Pr_2CuO_4 single crystals show that the decay of photo-induced carriers is very slow. The decay from tens of microseconds to seconds can be described as a weak power law decay with an exponent of roughly 0.2 at T = 10K. The exponent increases with increasing temperature. However, all these conclusions are tentative. To really understand the time decay of the photo-induced absorption further experiments are needed. At the time of these experiments it was not known that the mid-infrared absorption in the La_2CuO_4 and $Sr_2CuO_2Cl_2$ crystals was much cleaner than that in the Nd_2CuO_4 and Pr_2CuO_4 samples studied. Presumably, among the presently available samples, the La_2CuO_4 and $Sr_2CuO_2Cl_2$ single crystals are better for studying the intrinsic behavior of photo-injected carriers. Assuming that similar decays are seen

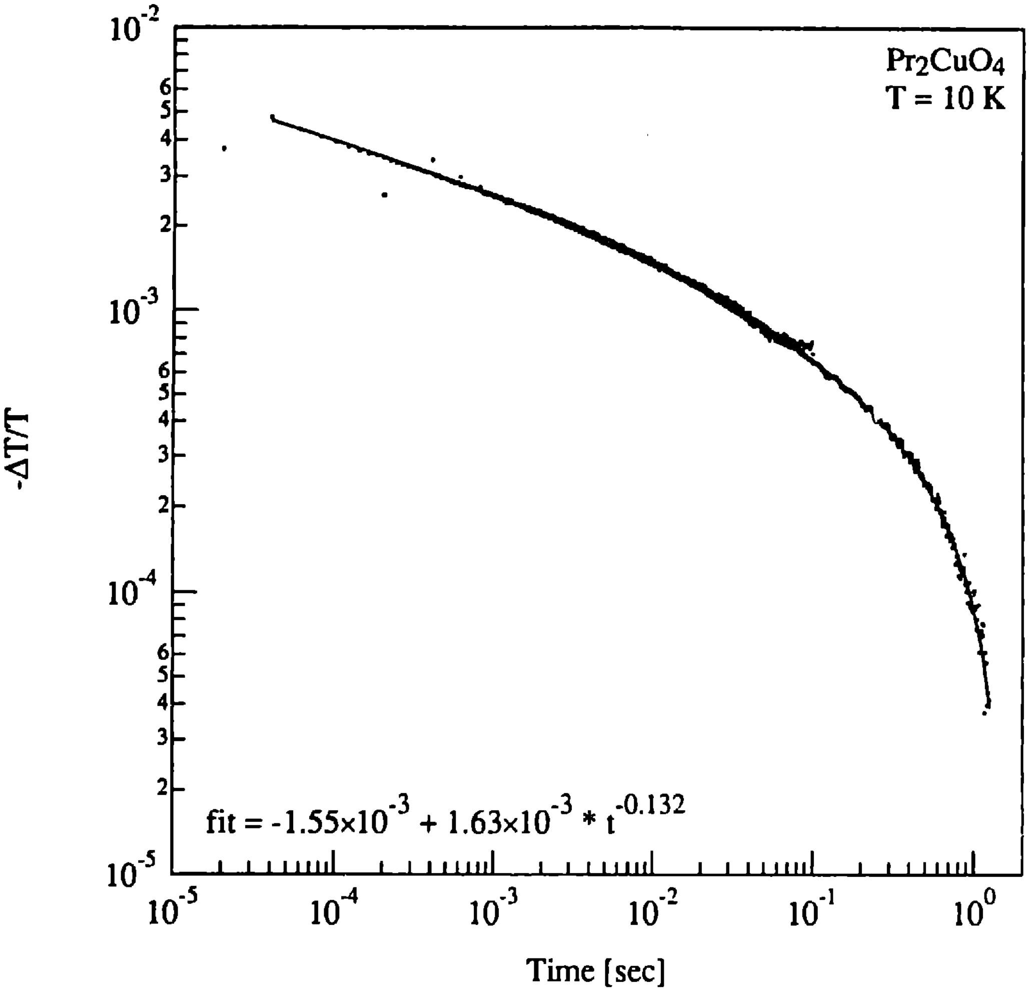

Figure 6.24: Decay of photoinduced absorption vs. time for a Pr_2CuO_4 single crystal. The solid line is a power law fit to the data. Data from Figure 6.22 and 6.23 is matched at ~ 1 msec by additive offset. Pumped at 2.21 eV (560 nm) with 10 nS pulses. Probe at 0.7 eV (1750 nm). T = 10 K.

in these materials, the measurements will need to span more decades in time to accurately determine the functional dependence of the time decay.

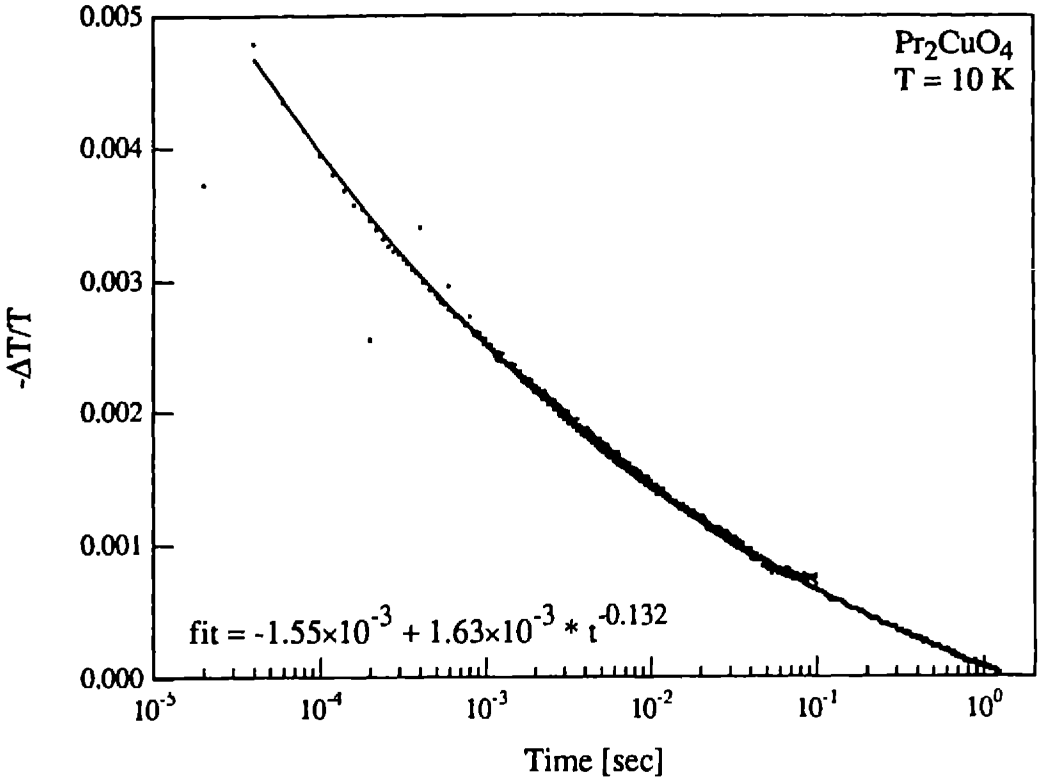

Figure 6.25: Decay of photoinduced absorption vs. time for a Pr_2CuO_4 single crystal. The solid line is a power law fit to the data. Data from Figure 6.22 and 6.23 is matched at ~ 1 msec by additive offset. Pumped at 2.21 eV (560 nm) with 10 nS pulses. Probe at 0.7 eV (1750 nm). T = 10 K. This is the same data as in figure 6.24.

Chapter 7: Summary and Potential for Future Work

Summary of Mid-infrared Absorption

The mid-infrared optical properties of the doped lamellar copper oxides have been the subject of intense interest[15-17] since the discovery of high temperature superconductivity. A broad absorption band peaked at ~ 0.5 eV is observed together with additional absorption in the vicinity of 1.5 eV. While much speculation has appeared, the absence of sharp spectral features has made a definitive interpretation of these excitations very difficult. Surprisingly, less attention has been paid to the mid-infrared spectra in the undoped materials.

Optical transmission experiments on ~ 100 μm thick high quality single crystals of antiferromagnetic La_2CuO_4, $Sr_2CuO_2Cl_2$, Nd_2CuO_4 and Pr_2CuO_4 show similar absorption spectra in the energy range of ~ 0.4 to 1.3 eV. For all four compounds, the spectra display a sharp low-energy line centered near 0.4 eV and a set of broader bands which extend to higher energies. The absorption coefficient is weak, roughly 10^3 times smaller than in the heavily doped materials. Polarization experiments on La_2CuO_4 samples show that the absorption is due to an electric dipole process occurring only when the electric field is polarized in the Cu-O plane. Identical results are obtained for La_2CuO_4 crystals grown by both the floating-zone and top-seeded-solution growth methods as well as for $Sr_2CuO_2Cl_2$ crystals grown from different starting materials. The lack of sample to sample variation indicates that the absorption is not due to impurities and hence, is intrinsic. The only common structural element of the four materials studied is the Cu-O layer. Therefore, the observed absorption is attributed to intrinsic electric dipole excitations of the undoped Cu-O layer.

Weak electric dipole absorption due to joint exciton-magnon excitation in antiferromagnets was first observed in MnF_2 by Greene *et al* [41]. A large amount of work in the 1960's showed that magnon sidebands of excitons are a common feature in antiferromagnetic insulators. As proposed by Tanabe *et al* [47], the electric dipole magnon sideband absorption is allowed by off-diagonal exchange mixing of odd parity excited states into the exciton and ground states. The structure seen in the sideband absorption in La_2CuO_4 and $Sr_2CuO_2Cl_2$ puts the exciton energy very close to the sharp low energy peak with one, two, three and four magnon sideband absorption extending to higher energies. The strong multimagnon absorption is due to the large quantum fluctuations of a spin 1/2 system.

The polarization selection rules for the magnon sidebands show that if the exciton at ~ 0.4 eV is a Cu d-d exciton then it must be either the $d_{x^2-y^2} \rightarrow d_{3z^2-r^2}$ or the $d_{x^2-y^2} \rightarrow d_{xy}$ transition. Recent electroreflectance [58] and Raman scattering [59] experiments show that an excitation with the same symmetry as $d_{x^2-y^2} \rightarrow d_{xy}$ exists at ~ 1.5 eV in the copper oxide materials. In $Sr_2CuO_2Cl_2$ a second absorption band is seen at this energy, hence it is natural to assign the ~ 1.5 eV exciton to the $d_{x^2-y^2} \rightarrow d_{xy}$ transition. This assignment of the ~ 1.5 eV exciton to the $d_{x^2-y^2} \rightarrow d_{xy}$ transition and the $d_{x^2-y^2} \rightarrow d_{3z^2-r^2}$ to the ~ 0.4 eV transition, but not the reverse, is also consistent with the lack of an observed bare exciton line in σ-polarization at ~ 0.4 eV and the lack of large anisotropies in the g-factor and thereby the spin susceptibility and anisotropic exchange, as well as the lack of a large and anisotropic Van Vleck susceptibility. However, the similarity in energy of the sharp line with the peak in the 2-magnon Raman spectra suggests that the excitation at ~ 0.4 eV may be more complex.

The absorption in the undoped lamellar copper oxides in the energy range of ~ 0.4 to 1.2 eV is ascribed to strong multimagnon sidebands to an electric dipole forbidden excitation at ~ 0.4 eV. Preliminary photo-induced absorption experiments show that the magnon sideband absorption increases with doping and hence probably provides the mechanism of the doping enhanced mid-infrared absorption in the High-T_c compounds. However, there are several important unresolved questions regarding the interpretation of the mid-infrared absorption in terms of joint exciton-magnon absorption. First, if the magnon sidebands are really associated with the Cu $d_{x^2-y^2} \to d_{3z^2-r^2}$ exciton, the exciton energy is significantly lower than expected. As suggested in Chapter 5, this may be due to screening of the excitation by the neighboring holes. Closely related to this is the empirical observation that the peak in the two-magnon Raman scattering is nearly degenerate with the proposed exciton energy. The $d_{x^2-y^2} \to d_{3z^2-r^2}$ exciton has the same B_{1g} transition symmetry as the two-magnon excitation. Hence if the $d_{x^2-y^2} \to d_{3z^2-r^2}$ exciton is really at ~ 0.4 eV, these excitations would mix and the peak in the Raman scattering may have an excitonic component. Hence, the observed spectra may indicate the presence of a Cu d-d exciton at ~ 0.4 eV. The central unresolved question is the mechanism for the sharp electric-dipole line at nearly the exciton energy. The answer to this question will almost certainly answer the question of exactly what excitation the magnon sidebands are riding on.

The possibility of low energy Cu d-d excitons in $YBa_2Cu_3O_{7-y}$ was first proposed by Geserich *et al* [95] in 1988. At that time, a mechanism for pairing based on Cu d-d excitations was developed by Weber[96]. Since then, the potential role of such excitations in the superconducting pairing mechanism has received little attention. This is probably due to the lack of compelling experimental evidence that such excitons really have an energy as low as roughly 0.4 eV. This is not a suggestion that the pairing excitation has been found, only that the role of low energy excitons has not received much attention. If further experiments confirm the picture presented in this thesis, then the low energy excitations of the undoped High-T_c host materials will include phonons, magnons, excitons, and various combinations of these excitations. It amazes me that seven years after the discovery of the copper oxide based High-T_c

materials by Bednorz and Muller[1], research into the electronic structure of the simplest, single layer, undoped host materials still yields new and interesting discoveries. As indicated by the potential for future work described below, there is no reason to believe this period of discoveries has ended.

Potential for Future Work

In this thesis I have tried to present a comprehensive explanation of the mid-infrared absorption in the undoped lamellar copper oxides. The spectra are well explained in terms of joint exciton-magnon absorption. Such excitations are common in antiferromagnetic insulators, but usually occur at energies in the visible. The unusual aspects of the exciton-magnon absorption in the High-T_c host materials stem from the low energy of the $d_{x^2-y^2} \to d_{3z^2-r^2}$ exciton and the large value of the exchange coupling J ~ 130 meV. The spectra presented in Chapter 3 represent the first observation of structured mid-infrared absorption in undoped single crystals. Similar spectra are seen in four different materials and in every piece of these materials that has been measured. To date, this includes about a dozen different samples. Hence, I feel that the experimental spectra are robust. It is still possible that the explanation in terms of joint-exciton magnon sidebands is incorrect. However, given the strong correlation of the features in the absorption with multimagnon energy shifts, I will be shocked if magnons are not involved at all. This section discusses the potential for further experiments and calculations to confirm or refute the explanation of the mid-infrared absorption in terms of a joint exciton-magnon mechanism as well as other interesting extensions of this work.

Electrotransmission Experiments

The magnon sideband polarization selection rules derived in Chapter 4 show that the observed magnon sideband absorption must be associated with either the $d_{x^2-y^2} \to d_{3z^2-r^2}$ or $d_{x^2-y^2} \to d_{xy}$ exciton. Direct experimental evidence exists for a $d_{x^2-y^2} \to d_{xy}$ symmetry excitation at ~ 1.5 eV. A $d_{x^2-y^2} \to d_{xy}$ exciton at ~ 0.4 eV is also inconsistent with other experimental results. Hence the exciton at ~ 0.4 eV is assigned to the $d_{x^2-y^2} \rightarrow d_{3z^2-r^2}$ transition. It would be very nice to directly confirm the $d_{x^2-y^2} \rightarrow d_{3z^2-r^2}$ excitation. This should be possible in an electrotransmission experiment, which is a simple variation on the electroreflectance experiment described in Chapter 4.

Because of the inversion symmetry of the Cu ion sites, the Cu d-d excitations are electric dipole forbidden. An estimate of the electric quadrupole oscillator strength for the $d_{x^2-y^2} \rightarrow d_{3z^2-r^2}$ transition in Chapter 4 indicates it would be essentially impossible to see the bare exciton absorption given the strength of the electric dipole absorption observed. However, the application of an electric field to the sample will break the inversion symmetry of the copper site. This mixes odd parity excited states into the ground and exciton states, making an electric dipole transition possible. By carefully choosing the orientation of the perturbing electric field and the polarization of the light, it should be possible to see the $d_{x^2-y^2} \rightarrow d_{3z^2-r^2}$ transition in an electrotransmission experiment. The geometry necessary for this is discussed in Chapter 4. Here, the strength of the absorption is estimated.

From Sakurai[40] the cross section for electric dipole absorption is given by:

$$\sigma_{abs} = 4\pi^2 \Delta E_{fi} \left(\frac{e^2}{\hbar c} \right) \left| \langle f | \hat{\varepsilon} \cdot \vec{r} | i \rangle \right|^2 \delta\left(E_f - E_i - \hbar\omega \right). \qquad (7.1)$$

Using the matrix elements summarized in table 4.9, the transition matrix element in the presence of an externally applied electric field is:

$$\left\langle \tilde{D}_{z^2} \middle| \hat{\varepsilon} \cdot \vec{r} \middle| \tilde{D}_{x^2-y^2} \right\rangle = \left| \langle \Psi_D(r) | r | \Psi_P(r) \rangle \right|^2 \left(\frac{eV}{d} \right) \frac{1}{5\sqrt{3}} \left(\frac{1}{\Delta_x^{x^2-y^2}} + \frac{1}{\Delta_x^{z^2}} \right) \cos\left(\theta_{\hat{v}} + \theta_{\hat{\varepsilon}} \right). \qquad (7.2)$$

The applied electric field and the polarization lie in the Cu-O plane, making angles θ_V and θ_ε with a Cu-O bond direction. If the externally applied electric field and the incident polarization are mutually perpendicular and oriented in the Cu-O plane but at 45° with respect to the Cu-O bond direction, then the cosine term has unit magnitude. The energy differences, Δ, are the energy differences between the copper ion d-states and the odd parity excited state which gets mixed in. For the purposes of estimating the absorption strength let $\Delta = 2$ eV, which is roughly the charge transfer excitation. The applied external field is given by the applied voltage, V, and the sample thickness, d. For simplicity, the odd parity excited state is taken to be a Cu 3P state. The radial wavefunctions, Ψ_D and Ψ_P, are approximated by hydrogenic wavefunctions. An effective nuclear charge of Z = 11 is chosen so that $\langle \Psi_D | r^2 | \Psi_D \rangle = 1.028 a_o^2$, which is the value for a Cu^{+2} ion as determined by Hartree-Fock calculations[60]. The integrated oscillator strength is given by:

$$\int \alpha(E) dE = \frac{16\pi^2}{75} \left(\left| \langle \Psi_D | r | \Psi_P \rangle \right|^2 \right)^2 \frac{\rho_{Cu}}{d^2} \left(\frac{e^2}{\hbar c} \right) \Delta E \left(\frac{eV}{\Delta} \right)^2 . \tag{7.3}$$

This is evaluated using the following values:

$$\begin{aligned} \rho_{Cu} &= 10^{22}\, cm^{-3} \\ \Delta E &= 0.5 eV \\ \Delta &= 2 eV \\ \langle \Psi_D | r | \Psi_P \rangle &= 6 \times 10^{-8}\, cm \end{aligned} \tag{7.4}$$

The resulting integrated oscillator strength is given by:

$$\int \alpha(E) dE \approx \left(2.5 \times 10^{-2} \right) \left(\frac{V[volts]}{d[\mu m]} \right)^2 \quad eV - cm^{-1} . \tag{7.5}$$

For d = 20 μm and V = 500 volts, which are both reasonable values, the integrated oscillator strength would be about 15 eV-cm^{-1}. The integrated strength of the entire absorption spectrum from ~ 0.4 - 1.2 eV is about 46 eV-cm^{-1}. This suggests that the induced absorption would be detectable with out even using a lock-in amplifier to extract the signal proportional to the applied voltage. Hence, an electrotransmission experiment on a sample polished perpendicular to the <110> direction (<001> ⊥ Cu-O plane) should be able to detect an excitation of $d_{x^2-y^2} \rightarrow d_{3z^2-r^2}$ symmetry. The copper ion d-d exciton is one such excitation.

Other Materials

It is interesting to note that at the level of the first order perturbation theory used above, the lack of inversion symmetry due to the single apical oxygen ion in $YBa_2Cu_3O_6$ will not make the $d_{x^2-y^2} \rightarrow d_{3z^2-r^2}$ visible. However, the large electric fields associated with a nearest neighbor ion may make higher order processes important. It would be very interesting to repeat these experiments on insulating $YBa_2Cu_3O_6$ samples.

Another material it would be interesting to study is CuO. Like the High-T_c host materials, it is a charge transfer insulator but with a charge transfer gap of ~ 1.4 eV [24]. Furthermore, the spins order antiferromagnetically below ~ 225 K with an ordered moment of $0.58\ \mu_B$ [97] and an exchange constant of J ~ 80 meV [98]. The similarities with the High-T_c host materials studied in this thesis suggest that joint exciton-magnon excitations should exist. Thus, a study of CuO would provide a strong test of the universality of the mid-infrared absorption and possibly further insights into the absorption mechanism.

Raman Scattering Experiments

The proposed low-energy $d_{x^2-y^2} \rightarrow d_{3z^2-r^2}$ exciton is nearly degenerate with the peak in the B_{1g} symmetry two magnon Raman scattering and also has B_{1g} transition symmetry. This raises the possibility that there may be an excitonic component to the Raman scattering. Raman scattering experiments performed several years ago [61] show that an high energy shoulder starts to become resolved in undoped samples at low temperatures. Since then progress in the preparation of undoped La_2CuO_4 single crystals and the growth of high quality $Sr_2CuO_2Cl_2$ crystals should allow higher quality measurements to be done. Due to the unusual line shape of the two magnon Raman scattering, this would be an interesting experiment even without the possibility that another excitation is involved. If it is actually shown that two excitations of B_{1g} symmetry exist, then the question simply becomes why are they nearly degenerate in energy. A new set of Raman scattering experiments are currently being conducted in collaboration with Ken Lyons at Bell Labs.

Another set of interesting Raman scattering experiments are being conducted by Liu *et al* [59] at the University of Illinois. These experiments are looking at energy shifts of ~ 1.2 to 2 eV. If the $d_{x^2-y^2} \rightarrow d_{xy}$ and $d_{x^2-y^2} \rightarrow d_{xz}, d_{yz}$ transitions are at ~ 1.4 and 1.6 eV as suggested by the electroreflectance experiments of Falck *et al* [58] at MIT, then these should be detectable by the high energy shift Raman experiments.

Measurements on Thinner La_2CuO_4 samples

The electroreflectance experiments of Falck *et al* on La_2CuO_4 and the α-polarized measurements on $Sr_2CuO_2Cl_2$ show absorption around 1.5 eV. It is suggested that both the $d_{x^2-y^2} \rightarrow d_{xy}$ and $d_{x^2-y^2} \rightarrow d_{xz}, d_{yz}$ excitons lie in this energy range. Magnon sidebands of the $d_{x^2-y^2} \rightarrow d_{xy}$ exciton may account for the observed absorption in $Sr_2CuO_2Cl_2$. However, the micaceous nature of $Sr_2CuO_2Cl_2$ prevents preparing any samples for σ and π-polarized experiments. Experiments on a 70 μm thick La_2CuO_4 sample show a sharp absorption edge at ~ 1.4 eV in σ-polarization and at peak in the π-polarized spectra at ~ 1.7 eV. However, the σ-polarized absorption becomes too strong to measure above 1.5 eV. Hence it is impossible to tell whether or not the observed π-polarized peak is simply σ-polarized absorption seen due to a misalignment of the sample with respect to the beam. Samples of Pr_2CuO_4 have been polished as thin as 20 μm. If a thinner sample of La_2CuO_4 could be prepared, it might be possible to do polarization experiments of the spectra measured around 1.5 eV. It may also be possible to see the bare Cu $d_{x^2-y^2} \rightarrow d_{xy}$ exciton. The strength for the direct $d_{x^2-y^2} \rightarrow d_{xy}$ transition as a σ-polarized magnetic dipole process was estimated in Chapter 4. Comparing this to the observed strength of the α-polarized 1.5 eV band in $Sr_2CuO_2Cl_2$ suggests that direct exciton might comprise one eighth of the σ-polarized band. This would be a clearly visible difference in the α and σ-polarized spectra.

Doping Dependence

A comparison of the spectra in the undoped single crystals with the preliminary photo-induced absorption spectra of Chapter 6 and the spectra in lightly doped materials [28] suggest that the magnon sideband absorption grows with doping. To confirm and quantify this, a series of experiments on very lightly oxygen doped La_2CuO_4 is necessary. The maximum product of αd which is easily measured is roughly 6 due to the typically small lateral dimensions of the polished thin samples. Assuming a linear doping dependence based on the measured absorption in $La_2CuO_{4.014}$ [27], the maximum doping easily measured for a sample thickness of 60 µm is about 10^{-3} holes per copper site, corresponding to a Neel temperature of about 315 K [27]. Improved experimental techniques along with thinner, larger area, samples could make higher doping levels measurable by transmission experiments.

Photo-induced Absorption

The second section of Chapter 6 presented preliminary time resolved photo-induced absorption data. The decay of the photo-induced absorption and presumably the photo-injected electrons and holes is very slow, with effects lasting a second or more. It also appears that a steady state background develops due to repetitive pumping on a time scale faster than that required for complete decay. As an aside, it may be possible to use this steady state background as a means to study the evolution with doping of the mid-infrared absorption. Since the time of the experiments presented in Chapter 6, it has become clear that the presently available samples of La_2CuO_4 and $Sr_2CuO_2Cl_2$ have cleaner mid-infrared optical properties than the Nd_2CuO_4 thin films and Pr_2CuO_4 single crystals studied in the time-resolved photo-induced absorption experiments. An investigation of the time-resolved photo-induced absorption and the time-resolved photoconductivity in high quality samples of La_2CuO_4 and $Sr_2CuO_2Cl_2$ would be very interesting.

As a technical note, the photo-induced absorption measurements are very sensitive to mechanical vibrations. Hence it is necessary to float the optics table. Unfortunately the pulsed Nd:YAG laser is on another table. This means that the sample is not fixed with the respect to the probe beam. Although this is not a problem for measurement of any single decay, the long term drifting of the optics table, not to mention bumping it, makes reproducibility of pumping over the course of a day very difficult. In particular, this makes doing pump intensity dependent experiments very frustrating. The obvious solution is to use a wide band pass fiber optic cable to run the laser pulse from the laser table to the measuring table. This would also have the advantage of letting one align the pump beam and the sample with a low power Helium Neon laser.

Calculations

The mid-infrared absorption spectra and their interpretation as joint exciton-magnon absorption presented in this thesis point out the need for several new calculations. To address the proposed low energy of the $d_{x^2-y^2} \rightarrow d_{3z^2-r^2}$ exciton, cluster calculations need to be performed on increasingly large clusters until the energies converge. Richard Martin, at LANL, is presently working on some new calculations. Parkinson's classical spin model [50] gives the peak location of the 1-magnon sideband quite well. However, it fails to account for the width of the 1-magnon peak and does not include any multimagnon absorption. As discussed in Chapter 4, the multimagnon sidebands are allowed due to quantum fluctuations. Therefore, a proper quantum calculation of the magnon sideband line shape in a spin 1/2 system is needed. Finally, if the exciton-magnon picture presented in this thesis proves correct, the possible role of these excitations with regards to the superconducting paring mechanism needs to be investigated.

Appendix A: Group Theory and Exciton Nomenclature

The purpose of this appendix is to explain enough about group theory so that the reader may understand the notation used to describe the excitonic transitions and selection rules discussed in this thesis. The discussion will be very applied. For a basic treatment of group theory see the book by Tinkham, *Group Theory and Quantum Mechanics* [99]. The book by Ballhausen, *Introduction to Ligand Field Theory* [100], applies symmetry concepts to the physical properties of inorganic molecules and solids.

The MnF_2 excitons shown in figure 4.1 are designated as ${}^6A_1 \rightarrow {}^4T_1(I)$. Like atomic term notation the leading superscript gives the spin degeneracy (2S+1). The A_1 and T_1 are group theory notations. In a crystalline environment the five atomic d-states are no longer degenerate. Consider an ion with one d-electron surrounded by 6 negative ions located at the corners of regular octahedron as shown in figure A.1. This might be a Ti^{+3} ion surrounded by oxygen ions. Figure A.2 shows polar plots of the five d-states appropriate for use in tetragonal symmetry. These are linear combinations of the L = 2 spherical harmonics as shown in Table A.1. Both the $d_{x^2-y^2}$ and $d_{3z^2-r^2}$ states have lobes which point directly at the negative ions located on the x, y and z axis. This raises the energy level of these states. The lobes of the d_{xy}, d_{xz} and d_{yz} states point between the negative ions and hence these states are lower in energy. This is shown as the cubic case of the energy level diagram in figure A.2.

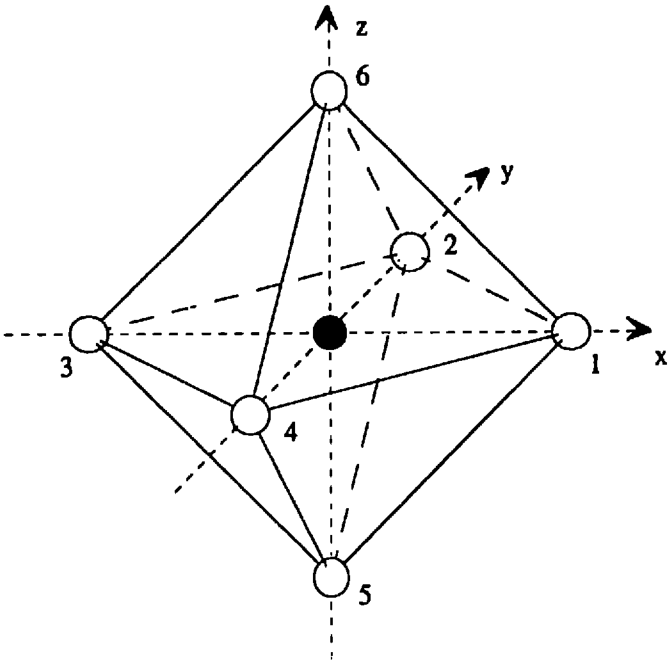

Figure A.1: Central ion surrounded by 6 ions in a regular octahedron. An example of O_h point group symmetry.

Cubic environments belong to the point group O. Table A.2 shows the character tables for the point groups O (cubic), D_4 (tetragonal), and C_{4v} (square pyramidal). The information to the right of the double bold line in each table shows how the states transform under the symmetry operations of the group listed in the top row. From this, most properties of the group can be derived. The present goal is to understand the nomenclature and learn how to derive selection rules. A complete set of character tables can be found in Tinkham's book [99]. Focus on the left half of the table for the point group O. Each row in the table, after the first, is for a different irreducible representation of the cubic group. These are designated by the symbols A_1, A_2, E, T_1, and T_2. The letter gives the degeneracy of the level, A and B are non degenerate, E is two fold degenerate, and T is three fold degenerate. If there is more than one irreducible representation of the same degeneracy subscripts are used to distinguish the representations.

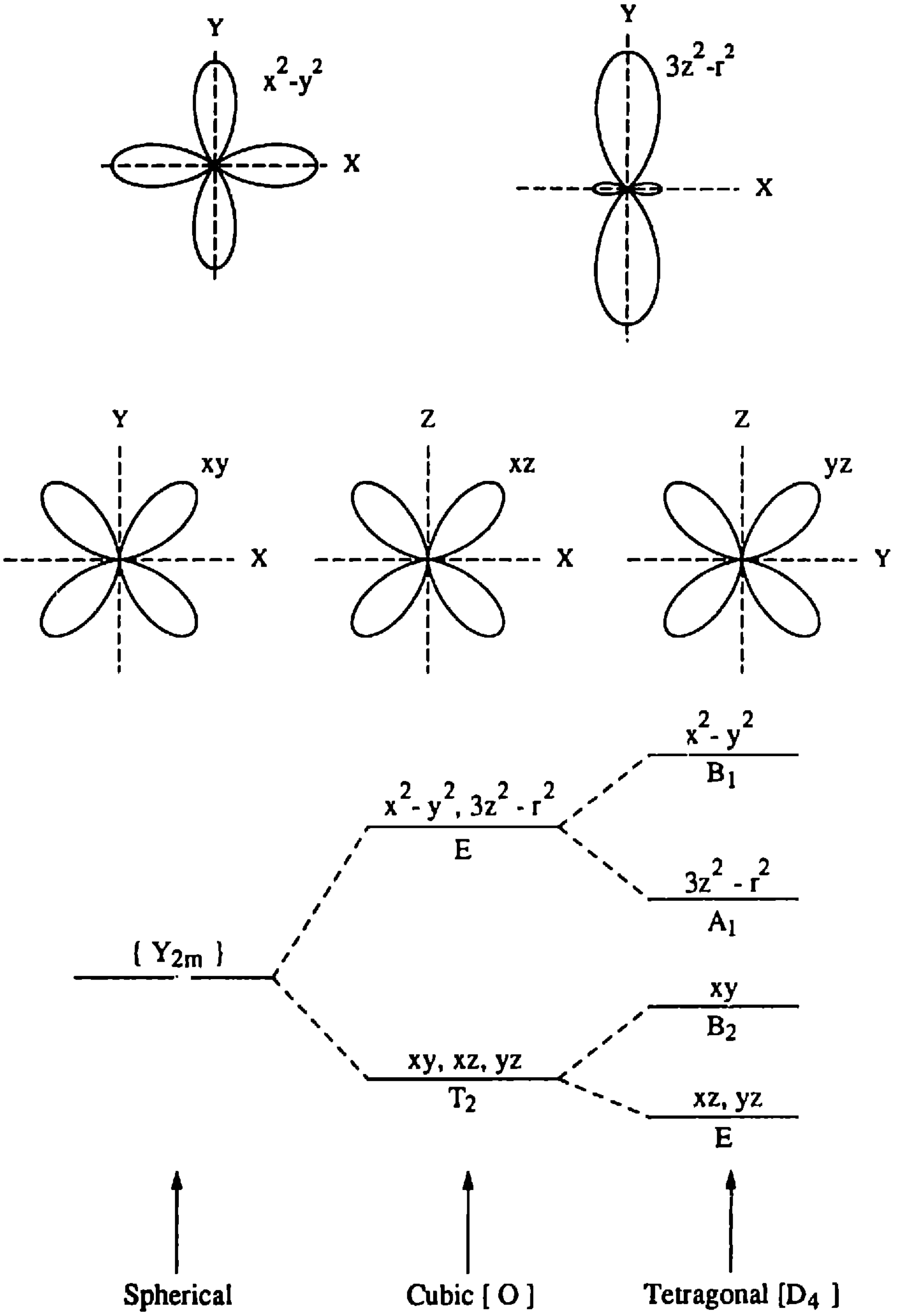

Figure A.2: Top: Polar plots of d-state electron density. Bottom: Splitting of d-states in non-spherical symmetry. In the tetragonal case, the regular octahedron of figure A.1 is slightly elongated along the z-axis. In the case of extreme elongation, the $d_{3z^2-r^2}$ and d_{xy} levels cross.

Ionic states	D4h Irreducible Rep.	Spherical Harmonic Expansion
$d_{x^2-y^2}$	B_{1g}	$\frac{1}{\sqrt{2}}\left(Y_{2,2}+Y_{2,-2}\right)$
d_{xy}	B_{2g}	$\frac{-i}{\sqrt{2}}\left(Y_{2,2}-Y_{2,-2}\right)$
d_{yz}	E_g	$\frac{i}{\sqrt{2}}\left(Y_{2,1}+Y_{2,-1}\right)$
d_{xz}	E_g	$\frac{-1}{\sqrt{2}}\left(Y_{2,1}-Y_{2,-1}\right)$
$d_{3z^2-r^2}$	A_{1g}	Y_{20}
p_x	E_u	$\frac{-1}{\sqrt{2}}\left(Y_{1,1}-Y_{1,-1}\right)$
p_y	E_u	$\frac{i}{\sqrt{2}}\left(Y_{1,1}+Y_{1,-1}\right)$
p_z	A_{2u}	$Y_{1,0}$

Table A.1: Ionic d and p-states in tetragonal (D_{4h}) symmetry expressed in terms of spherical harmonics.

For a given point group, the irreducible representations are mutually orthogonal. The first two columns of each row list a few functions which transform like that irreducible representation. In cubic symmetry (O), $d_{x^2-y^2}$ and $d_{3z^2-r^2}$ both belong to the E representation. States belonging to the same representation transform into each other under the symmetry operations of the group. Consider the vectors $\hat{x}, \hat{y}$, and $\hat{z}$, which belong to the T_1representation. Rotation of $\hat{x}$ by $\frac{\pi}{2}$ about the z-axis turns it into $\hat{y}$, about the y-axis turns it into $\hat{z}$. We see that a representation including $\hat{x}$ must be at least triply degenerate, as the T_1 group is. The A_1 representation is always the identity representation. An atomic S state is A_1 for all groups because no matter how one rotates or flips it, it always looks the same. Polar vectors, which are even parity, are designated R_x. When parity is a good quantum number an additional subscript is used to denote the parity, g is for even parity and e for odd parity. For example, in a cubic

O (432)			E	$8C_3$	$3C_2$	$6C_2$	$6C_4$
		A_1	1	1	1	1	1
		A_2	1	1	1	-1	-1
x^2-y^2 $3z^2-r^2$		E	2	-1	2	0	0
	(R_x,R_y,R_z) (x,y,z)	T_1	3	0	-1	-1	1
(xy,xz,yz)		T_2	3	0	-1	1	-1

D_4(422)			E	C_2	$2C_4$	$2C_2'$	$2C_2''$
x^2+y^2 z^2		A_1	1	1	1	1	1
	R_z,z	A_2	1	1	1	-1	-1
x^2-y^2		B_1	1	1	-1	1	-1
xy		B_2	1	1	-1	-1	1
(xz,yz)	(x,y) (R_x,R_y)	E	2	-2	0	0	0

C_{4v} (4mmm)			E	C_2	$2C_4$	$2\sigma_v$	$2\sigma_d$
x^2+y^2 z^2	z	A_1	1	1	1	1	1
	R_z	A_2	1	1	1	-1	-1
x^2-y^2		B_1	1	1	-1	1	-1
xy		B_2	1	1	-1	-1	1
(xz,yz)	(x,y) (R_x,R_y)	E	2	-2	0	0	0

Table A.2: Character Tables for point groups O (cubic), D_4 (tetragonal) and C_{4v} (square pyramidal).

D_4, C_{4v}	A_1	A_2	B_1	B_2	E
A_1	A_1	A_2	B_1	B_2	E
A_2	A_2	A_1	B_2	B_1	E
B_1	B_1	B_2	A_1	A_2	E
B_2	B_2	B_1	A_2	A_1	E
E	E	E	E	E	$A_1+A_2+B_1+B_2$

Table A.3: Direct product multiplication table for the D_4 point group.

crystal with inversion symmetry the orbital angular momentum operator L transforms as T_{1g} and linear momentum P as T_{1e}. Upon adding inversion symmetry, the point group O becomes O_h, and D_4 becomes D_{4h}. If one just keeps track of the parity separately, the character tables and direct product tables for the parent groups can be used.

In figure A.2, the group theory notation has been put below each level. In a cubic environment the five atomic d-states split into the doubly degenerate E level and the triply degenerate T_2 level. Now, if the apical ions located on the z- axis are pulled farther away from the central ion, the symmetry will change from cubic to tetragonal, D_{4h}. This introduces additional level splittings as shown in figure A.2. In point group O, $d_{x^2-y^2}$ and $d_{3z^2-r^2}$ transform as irreducible representation E, where as in D_{4h} it is d_{xz} and d_{yz} which transform as E. To understand the symmetry of the states being described one must know which point group the notation refers to. Frequently the states are labeled based on the cubic point group O, even if the real crystal structure is of lower symmetry. This facilitates comparing transitions between materials with different symmetries.

O'	A_1	A_2	E	T_1	T_2	E_2	E_3	G
A_1	A_1	A_2	E	T_1	T_2	E_2	E_3	G
A_2	A_2	A_1	E	T_2	T_1	E_3	E_2	G
E	E	E	A_1+A_2+E	T_1+T_2	T_1+T_2	G	G	E_2+E_3+G
T_1	T_1	T_2	T_1+T_2	$A_1+E+T_1+T_2$	$A_2+E+T_1+T_2$	E_2+G	E_3+G	E_2+E_3+2G
T_2	T_2	T_1	T_1+T_2	$A_2+E+T_1+T_2$	$A_1+E+T_1+T_2$	E_3+G	E_2+G	E_2+E_3+2G
E_2	E_2	E_3	G	E_2+G	E_3+G	A_1+T_1	A_2+T_2	$E+T_1+T_2$
E_3	E_3	E_2	G	E_3+G	E_2+G	A_2+T_2	A_1+T_1	$E+T_1+T_2$
G	G	G	E_2+E_3+G	E_2+E_3+2G	E_2+E_3+2G	$E+T_1+T_2$	$E+T_1+T_2$	$A_1+A_2+E+2T_1+2T_2$

Table A.4: Direct product multiplication table for the O' cubic double group. The sub-table defined by the double lines is the direct product table for the regular O group.

In spherical symmetry, states involving more than one electron can be described in a direct product format or as a sum of total angular momentum states. Similarly, in a crystalline environment, any direct product state transforms as a sum of irreducible representations. A simple example will make this clearer. Consider two d electrons in a tetragonal environment with inversion symmetry, point group D_{4h}. Single electron states will be denoted with lower case letters such as t_{2g} and the total wave function with capital letters such as T_{2g}. Table A.3 gives the direct product multiplication table for the D_4 point group. If the two electrons are each placed in the lowest level e_g, the direct product representation is $e_g \otimes e_g$. Direct products are in general reducible representations. That means they can be described as a sum of irreducible representations. Table A.3 shows that $e_g \otimes e_g = A_{1g} + A_{2g} + B_{1g} + B_{2g}$, in D_{4h} symmetry.

Direct product tables can also be used to determine if matrix elements are zero, and therefore evaluate selection rules. Consider the matrix element for magnetic dipole absorption $\langle f|\hat{B} \bullet \vec{L}|i\rangle$, which in σ polarization is $\langle f|L_z|i\rangle$. Let the initial state be $d_{x^2-y^2}$ and the final state be either $d_{3z^2-r^2}$ or d_{xy}. A matrix element is zero unless the corresponding direct product contains some A_1 component. In D_{4h} symmetry $\langle d_{xy}|L_z|d_{x^2-y^2}\rangle$ transforms as $B_{2g} \otimes A_{2g} \otimes B_{1g}$. For the parity subscripts $g \otimes g = e \otimes e = g$ and $g \otimes e = e$. Using this and the D_4 direct product table gives:

$$\Big\langle d_{xy} \Big| \Big(L_z \Big| d_{x^2-y^2} \Big\rangle \Big) = B_{2g} \otimes \left(A_{2g} \otimes B_{1g} \right) = B_{2g} \otimes B_{2g} = A_{1g} \tag{A.1}$$

Therefore the matrix element is non-zero. For the final state $d_{3z^2-r^2}$:

$$\Big\langle d_{3z^2-r^2} \Big| \Big(L_z \Big| d_{x^2-y^2} \Big\rangle \Big) = A_{1g} \otimes \left(A_{2g} \otimes B_{1g} \right) = A_{1g} \otimes B_{2g} = B_{2g} \tag{A.2}$$

In this case the matrix element contains no A_{1g} component and the transition does not occur. Group theory can be very useful in determining selection rules.

The exciton transition in MnF_2, ${}^6A_1 \rightarrow {}^4T_1(I)$, is described in terms of cubic (O) states, even though the crystal structure is not cubic. The ground state electronic configuration for the d electrons in Mn^{+2} is $(t_2)^3 \otimes (e)^2$. Table A.4 gives the direct product table for the O' double group, which includes spin. The top left 5x5 portion of the table is the table for the simple cubic group. Repeated use of this yields:

$$(t_2)^3 \otimes (e)^2 = 4A_1 + 4A_2 + 8E + 14T_1 + 14T_2 \tag{A.3}$$

The ground state is one of the A_1 representations. Hund's rules can be used to determine the ground state. The purpose here is to become comfortable with the group theory notation and concepts. The final state, T_1, would be triply degenerate in a cubic environment. In MnF_2 the T_1 level splits with $T_1(I)$, $T_2(II)$ and $T_3(III)$ denoting these three levels in order of increasing energy.

L, S	Term	Splitting
0	S	A_1
1	P	T_1
2	D	E_1+T_2
3	F	$A_2+T_1+T_2$
4	G	$A_1+E_1+T_1+T_2$
5	H	$E_1+2T_1+T_2$
6	I	$A_1+A_2+E_1+T_1+2T_2$
1/2		E_2
3/2		G
5/2		E_3+G
7/2		E_2+E_3+G
9/2		E_2+2G
11/2		E_2+E_3+2G

Table A.5: Splitting of spherical symmetry levels in the cubic double group. From Sugano [101] Tables 1.4 and 7.2.

The leading superscript is the spin degeneracy (2S+1). The $^6A_1 \rightarrow {}^4T_1(I)$ exciton includes a change in total spin from S=5/2 to S=3/2. Transitions involving a change in the spin state are said to be spin forbidden. In the absence of spin-orbit coupling such transitions would be forbidden as one photon processes due to blocking in spin space. Spin orbit coupling, $\bar{L} \bullet \bar{S}$, mixes in other spin states, allowing the transition to proceed. Half-integer spin states change sign upon rotation by 2π. To incorporate this into group theory an artificial distinction is made between rotations by 2π and 4π. The resulting groups are called double groups. Table A.5 shows how spherical symmetry orbital and spin states split into irreducible representations of the cubic double group O'. This and the direct product multiplication table for the O' group (table A.4) allow one to determine how spin orbit coupling mixes various spin states. Consider the matrix element $\left\langle {}^4T_1 \middle| \bar{L} \bullet \bar{S} \middle| {}^6A_1 \right\rangle$. The operators L and S are the generators for rotations in real and spin space. Therefore if the states $^6A_1$ and $^4T_1$ have components which transform in the same way under simultaneous rotation in spin and real space then the matrix element will be non-zero and spin orbit coupling will mix the two states. $^6A_1$ is a direct product representation of (S = 5/2)⊗(Spatial A_1). This can be written as a sum of irreducible representations of the cubic double group O'. From table A.5 we see that S=5/2 corresponds to E_3 + G. So, $^6A_1 = (E_3 + G)\otimes A_1$. The direct product table shows that:

$$\begin{aligned} {}^6A_1 &= (E_3 + G)\otimes A_1 = E_3 + G \\ {}^4T_2 &= G\otimes T_2 = E_2 + E_3 + 2G \end{aligned} \tag{A.4}$$

Both $^6A_1$ and $^4T_2$ have components that transform as G under simultaneous identical spin and space rotations. Therefore $^6A_1$ and $^4T_2$ will be coupled through their respective G components by spin-orbit coupling and the $^6A_1$ ground state will have some $^4T_2$ mixed in.

As a last step towards understanding the spin forbidden transition $^6A_1 \rightarrow {}^4T_1$(I), consider the σ-polarized magnetic dipole transition matrix element $\langle T_2|L_z|T_1\rangle$.

$$\langle T_2|L_z|T_1\rangle = T_2\otimes T_1\otimes T_1 = A_1 + A_2 + 2E + 4T_1 + 3T_2 \tag{A.5}$$

Since the matrix element has some A_1 component it will be non-zero. Therefore the $^6A_1 \rightarrow {}^4T_1$(I) spin forbidden transition occurs as a σ-polarized magnetic dipole transition due to the spin-orbit coupling mixing of some $^4T_2$ into the ground state which is then magnetic dipole coupled to the final state $^4T_1$.

In summary, this appendix has shown how to use character tables and direct product tables to understand the symmetry of an excitation and calculate selection rules. Selection rules will be very important in understanding the infrared absorption processes described in this thesis.

		Cu states	O states
A_{1g}	z^2, x^2+y^2	$d_{3z^2-r^2}$	$\frac{1}{2}\left(p_x^1+p_y^2-p_x^3-p_y^4\right)$, $\frac{1}{\sqrt{2}}\left(p_z^5-p_z^6\right)$
A_{2g}			$\frac{1}{2}\left(p_y^1-p_x^2-p_y^3+p_x^4\right)$
B_{1g}	x^2-y^2	$d_{x^2-y^2}$	$\frac{1}{2}\left(p_x^1-p_y^2-p_x^3+p_y^4\right)$
B_{2g}	xy	d_{xy}	$\frac{1}{2}\left(p_y^1+p_x^2-p_y^3-p_x^4\right)$
E_g	xz,yz	d_{xz}, d_{yz}	$\left\{\begin{array}{l}\frac{1}{\sqrt{2}}\left(p_z^1-p_z^3\right),\ \frac{1}{\sqrt{2}}\left(p_z^2-p_z^4\right)\\ \frac{1}{\sqrt{2}}\left(p_x^6-p_x^5\right),\ \frac{1}{\sqrt{2}}\left(p_y^6-p_y^5\right)\end{array}\right.$
A_{2u}	z		$\frac{1}{\sqrt{2}}\left(p_z^5+p_z^6\right)$, $\frac{1}{2}\left(p_z^1+p_z^2+p_z^3+p_z^4\right)$
B_{2u}			$\frac{1}{2}\left(p_z^1-p_z^2+p_z^3-p_z^4\right)$
E_u	x,y		$\left\{\begin{array}{l}\frac{1}{\sqrt{2}}\left(p_x^1+p_x^3\right),\ \frac{1}{\sqrt{2}}\left(p_x^2+p_x^4\right)\\ \frac{1}{\sqrt{2}}\left(p_y^1+p_y^3\right),\ \frac{1}{\sqrt{2}}\left(p_y^2+p_y^4\right)\\ \frac{1}{\sqrt{2}}\left(p_x^5+p_x^6\right),\ \frac{1}{\sqrt{2}}\left(p_y^5+p_y^6\right)\end{array}\right.$

Table A.6: Irreducible representations and basis functions for one hole in the CuO_6 cluster with D_{4h} symmetry. The numbering is defined in Figure A.1. Taken from Ph.D. thesis of J.P. Falck [27] and based on ref. [102].

Appendix B: Calculation of Magnon Sideband Line Shape

A classical spin model for the magnon sideband line shape in antiferromagnets with the K_2NiF_4 crystal structure was developed by Parkinson [50] in 1969. In Chapter 4, this model is compared to the measured spectra and accurately predicts the peak position of the 1-magnon sideband. This appendix simply outlines the evaluation of the line shape expressions given by Parkinson. So many of the equations in this appendix are directly from Parkinson's paper [50] that referencing them individually is unreasonable.

The Hamiltonian for a Heisenberg antiferromagnet with no anisotropy field is

$$H = J\sum_{n.n} \vec{S}_i \cdot \vec{S}_j . \tag{B.1}$$

For a two dimensional square lattice the resulting dispersion relation is

$$\begin{aligned} E^2(k) &= (JSz)^2\left(1-\gamma_k^2\right) \\ \gamma_k &= \tfrac{1}{2}\left(\cos(ak_x)+\cos(ak_y)\right) , \end{aligned} \tag{B.2}$$

where J is the exchange constant, S, the spin and z, the number of nearest neighbors. The Brillouin zone is that for the magnetic unit cell which is shown in figure 4.2. The magnon sideband line shape is proportional to $\operatorname{Im}\{G_p(E)\}$. The exciton-magnon interaction is included via a coupling parameter $p = (J'S'/JS) - 1$ where the primed variables refer to the excited state.

$$G_p(E) = \frac{G_p^0(E)}{1-\left(p/z\right)G_p^0(E)} \tag{B.3}$$

To evaluate this first a dimensionless energy is defined, $\varepsilon = E/E_0$ and $E_0 = JSz$. The non-interacting Green function is

$$G_p^0(\varepsilon) = \frac{\varepsilon+1}{N}\sum_k \frac{2\sin^2(k_x a)}{\varepsilon^2 - \varepsilon_k^2}. \tag{B.4}$$

This may be evaluated in terms of the functions L_{lm} defined by Parkinson, which may in turn be evaluated in terms of K() and E() which are respectively, the complete elliptical integrals of the first and second kind.

$$\beta^2 = 1 - \varepsilon^2 \tag{B.5}$$

$$G_p^0(\varepsilon) = -(\varepsilon+1)\frac{2}{\beta}\left\{2\beta + \left(2 - 4\beta^2\right)L_{00}(B) + 2L_{11}(\beta)\right\} \tag{B.6}$$

$$\begin{aligned} \operatorname{Im}\left[L_{oo}(\beta)\right] &= \frac{1}{\pi}K(\varepsilon) \\ \operatorname{Re}\left[L_{oo}(\beta)\right] &= \frac{1}{\pi}K(\beta) \end{aligned} \tag{B.7}$$

$$\begin{aligned} \operatorname{Im}\left[L_{11}(\beta)\right] &= \frac{-1}{\pi}\left[K(\varepsilon) - 2E(\varepsilon)\right] \\ \operatorname{Re}\left[L_{11}(\beta)\right] &= \frac{1}{\pi}\left[K(\beta) - 2E(\beta)\right] \end{aligned} \tag{B.8}$$

The elliptical integrals may be evaluated on the interval [0,1] using expressions from Abramowitz and Stegun (AS) [103]. Note that Parkinson and AS define the complete elliptical integral of the first kind slightly differently, so that

$$\begin{aligned} K_{Park}(x) &= \int_0^{\frac{\pi}{2}} \frac{d\phi}{\sqrt{1-x^2\sin^2(\phi)}} \\ K_{A\&S}(x) &= \int_0^{\frac{\pi}{2}} \frac{d\phi}{\sqrt{1-x\sin^2(\phi)}} \\ K_{Park}(x) &= K_{A\&S}(x^2) \end{aligned} \tag{B.9}$$

Through equation B.8 the notation of Parkinson has been used. The algebraic expressions given below are for the AS convention. The complete elliptical integral of the first kind is given by the following equations.

$$K(x) = a_0 + a_1(1-x) + a_2(1-x)^2 - \left[b_0 + b_1(1-x) + b_2(1-x)^2\right]\ln(1-x) \tag{B.10}$$

$$\begin{aligned} &0 < x \leq 1 \\ &|error| \leq 3 \bullet 10^{-5} \\ &a_0 = 1.3862944 \\ &a_1 = 0.1119723 \\ &a_2 = 0.0725296 \\ &b_0 = 0.5 \\ &b_1 = 0.1213478 \\ &b_2 = 0.0288729 \end{aligned} \tag{B.11}$$

The complete elliptical integral of the second kind is given by the following equations.

$$E(x) = 1 + a_1(1-x) + a_2(1-x)^2 - \left[b_1(1-x) + b_2(1-x)^2\right]\ln(1-x) \tag{B.12}$$

$$\begin{aligned} & 0 < x \leq 1 \\ & |error| \leq 4 \bullet 10^{-5} \\ & a_1 = 0.4630151 \\ & a_2 = 0.1077812 \\ & b_1 = 0.2452727 \\ & b_2 = 0.0412496 \end{aligned} \tag{B.13}$$

Figure 4.6 shows the magnon sideband line shape for several different values of the exciton magnon interaction parameter, ρ.

Bibliography

[1] J.G. Bednorz and K.A. Muller, *Zeitschrift fur Physik B* **64**, 189-193 (1986).

[2] M.K. Wu, J.R. Ashburn, C.J. Torny, P.H. Hor, R.L. Meng, L. Gao, Z.J. Huang, Y.Q. Wang and C.W. Chu, *Physical Review Letters* **58**, 908-910 (1987).

[3] S.S.P. Parkin, V.Y. Lee, E.M. Engler, A.I. Nazzel, T.C. Huang, G. Gorman, R. Savoy and R. Beyers, *Physical Review Letters* **60**, 2539-2542 (1988).

[4] Z.Z. Sheng and A.M. Hermann, *Nature* **332**, 55 (1988).

[5] Y. Tokura, H. Takagi and S. Uchida, *Nature* **337**, 345-347 (1989).

[6] S.N. Putilin, E.V. Antipov, O. Chmaissem and M. Marezio, *Nature* **362**, 226 (1993).

[7] A. Schilling, M. Cantoni, J.D. Guo and H.R. Ott, *Nature* **363**, 56 (1993).

[8] L. Gao, Y.Y. Xue, F. Chen, Q. Xiong, R.L. Meng, D. Ramirez, C.W. Chue, J.H. Eggert and H.K. Mao, *submitted to PRL* (1993).

[9] J. Bardeen, L.N. Cooper and J.R. Schreiffer, *Physical Review* **108**, 1175 (1957).

[10] C.E. Gough, M.S. Colclough, E.M. Forgan, R.G. Jordan, M. Keene, C.M. Muirhead, A.I.M. Rae, N. Thomas, J.S. Abell and S. Sutton, *Nature* **326**, 855 (1987).

[11] B.G. Levi, *Physics Today* **May**, 17-20 (1993).

[12] T. Tokura, S. Koshihara, T. Arima, H. Takagi, S. Ishibashi, T. Ido and S. Uchida, *Physical Review B* **41**, 11657 (1990).

[13] R.S. Meltzer, M. Lowe and D.S. McClure, *Physical Review* **180**, 561-578 (1969).

[14] S. Tajima, S. Uchida, S. Ishibashi, T. Ido and H. Takagi, *Physica C* **168**, 117-122 (1990).

[15] D.B. Tanner and T. Timusk in *Physical Properties of High-Temperature Superconductors III*, editted by D. Ginsberg (World Scientific, Singapore, 1992).

[16] G.A. Thomas in *High Temperature Superconductivity* , edited by D. P. Tunstall and W. Barford (Adam Hilger, Bristol, 1991).

[17] S. Uchida, T. Ido, H. Takagi, T. Arima, Y. Tokura and S. Tajima, *Physical Review B* **43**, 7942-7954 (1991).

[18] N.W. Preyer, R.J. Birgeneau, C.Y. Chen, D.R. Gabbe, H.P. Jenssen, M.A. Kastner, P.J. Picone and T. Thio, *Physical Review B* **39**, 11563-11569 (1989).

[19] J.P. Falck, A. Levy, M.A. Kastner and R.J. Birgeneau, *Physical Review Letters* **69**, 1109-1112 (1992).

[20] J. Hubbard, *Proc. Roy. Soc.* **A281**, 401 (1965).

[21] R.J. Birgeneau, *American Journal of Physics* **58**, 28-40 (1990).

[22] J. Zaanen, G.A. Sawatzky and J.W. Allen, *Physical Review Letters* **55**, 418-421 (1985).

[23] G.A. Sawatzky in *Studies in Inorganic Chemistry* , edited by H. J. M. Heijligers and J. Schoonman (Elsevier Scientific, Amsterdam, 1983).

[24] J. Ghijsen, L.H. Tjeng, J.v. Elp, H. Eskes, J. Westerink, G.A. Sawatzky and M.T. Czyzyk, *Physical Review B* **38**, 11322-11330 (1988).

[25] G. Shirane, R.J. Birgeneau, Y. Endoh and M.A. Kastner, *proceedings of LTXX, Physica B* (1993).

[26] M. Greven, R.J. Birgeneau, Y. Endoh, M.A. Kaster, B. Keimer, M. Matsuda and T.R. Thruston, *MIT Preprint* (1993).

[27] J.P. Falck Ph.D. Thesis, MIT, 1993.

[28] G.A. Thomas, D.H. Rapkine, S.L. Cooper, S-W. Cheong, A.S. Cooper, L.F. Schneemeyer and J.V. Waszczak, *Physical Review B* **45**, 2474-2479 (1992).

[29] P.J. Picone, H.P. Jenssen and D.R. Gabbe, *Journal of Crystal Growth* **85**, 576-580 (1987).

[30] Y. Hidaka, T. Enomoto, M. Suzuki, M. Oda and T. Murakami, *Journal of Crystal Growth* **85**, 581-584 (1987).

[31] L.L. Miller, X.L. Wang, S.X. Wang, C. Stassis, D.C. Johnston, J.F. Jr and C.K. Loong, *Physical Review B* **41**, 1921- (1990).

[32] D. Vaknin, S.K. Sinha, C. Stassis, L.L. Miller and D.C. Johnston, *Physical Review B* **41**, 1926-1933 (1990).

[33] T. Thio, T.R. Thurston, N.W. Preyer, P.J. Picone, M.A. Kastner, H.P. Jenssen, D.R. Gabbe, C.Y. Chen, R.J. Birgeneau and A. Aharony, *Physical Review B* **38**, 905-908 (1988).

[34] C.Y. Chen, R.J. Birgeneau, M.A. Kastner, N.W. Preyer and T. Thio, *Physical Review B* **43**, 392-401 (1991).

[35] T. Thio Ph.D. Thesis, MIT, 1988.

[36] J.T. Kucera, L.M. Rubin, K. Uwai, J.D. Perkins, J.M. Graybeal, T.P. Orlando, J.B. Vander Sande, A. Roshko and J. Moreland, *Physica C* **192**, 23-30 (1992).

[37] J.T. Kucera, J.D. Perkins, K. Uwai, J.M. Graybeal and T.P. Orlando, *Review of Scientific Instrumentation* **62**, 1630-1632 (1991).

[38] J.W. Allen in *Magnetic Oxides*, edited by D. J. Craik (Wiley, London, 1975).

[39] M.L. Jones, D.W. Shortt, B.W. Sterling, A.L. Schawlow and R.M. Macfarlane, *Physical Review B* **46**, 611-617 (1992).

[40] J.J. Sakurai *Modern Quantum Mechanics*, (Benjamin/Cummings, Menlo Park, CA, 1985), p. 474.

[41] R.L. Greene, D.D. Sell, W.M. Yen, A.L. Schawlow and R.M. White, *Physical Review Letters* **15**, 656-659 (1965).

[42] D.D. Sell, R.L. Greene and R.M. White, *Physical Review* **158**, 489-510 (1967).

[43] Y. Tanabe and K. Aoyagi in *Excitons*, edited by E. I. Rashba and M. D. Sturge (North-Holland, Amsterdam, 1982).

[44] Y. Tanabe and K. Gondaira in *Optical Properties of Ions in Crystals*, edited by H. H. Crosswhite and H. W. Moos (Wiley, New York, 1966).

[45] D.S. McClure, R. Meltzer, S.A. Reed, P. Russel and J.W. Stout in *Optical Properties of Ions in Crystals*, edited by H. M. Crosswhite and H. W. Moos, (Wiley, New York, 1966).

[46] R.L. Greene, D.D. Sell and R.M. White in *Optical Properties of Ions in Crystals*, edited by H. M. Crosswhite and H. W. Moos, (Wiley, New York, 1966).

[47] Y. Tanabe, T. Moriya and S. Sugano, *Physical Review Letters* **15**, 1023-1025 (1965).

[48] J.W. Allen, R.M. Macfarlane and R.L. White, *Physical Review* **179**, 523-541 (1969).

[49] K. Gondaira and Y. Tanabe, *Journal of the Physical Society of Japan* **21**, 1527-1548 (1966).

[50] J.B. Parkinson, *J. Phys. C. (Solid St. Phys.)* **2**, 2012-2021 (1968).

[51] K.B. Lyons, P.A. Sulewski, P.A. Fleury, H.L. Carter, A.S. Cooper and G.P. Espinosa, *Physical Review B* **39**, 9693-9696 (1989).

[52] G. Aeppli, S.M. Hayden, H.A. Mook, Z. Fisk, S.W. Cheong, D. Rytz, J.P. Remeika, G.P. Espinosa and A.S. Cooper, *Physical Review Letters* **62**, 2052 (1989).

[53] V.J. Emery and G. Reiter, *Physical Review B* **38**, 4547-4556 (1988).

[54] R.S. Meltzer, M.Y. Chen, D.S. McClure and M. Lowe-Pariseau, *Physical Review Letters* **21**, 913-916 (1968).

[55] R.M. Macfarlane and J.W. Allen, *Physical Review B* **4**, 3054-3067 (1971).

[56] E.J. Samuelsen, M.T. Hutchings and G. Shirane, *Solid State Communications* **7**, 1043-1045 (1969).

[57] J.B. Parkinson and R. Loudon, *J. Phys. C (Proc. Phys. Soc.)* **1**, 1568-1583 (1968).

[58] J.P. Falck, J.D. Perkins, A. Levy, M.A. Kastner, J.M. Graybeal and R.J. Birgeneau *Physical Review B* (in press 1993).

[59] R. Liu, D. Salamon, M.V. Klein, S.L. Cooper, W.C. Lee, S.W. Cheong and D.M. Ginsberg, *Physical Review Letters* **71**, 3709-3712 (1993).

[60] G. Burns, *Physical Review* **128**, 2121- (1962).

[61] S. Sugai, *Solid State Communications* **75**, 795-798 (1990).

[62] R.R.P. Singh, P.A. Fleury, K.B. Lyons and P.E. Sulewski, *Physical Review Letters* **62**, 2736-2739 (1989).

[63] C.M. Canali and S.M. Girvin, *Physical Review B* **45**, 7127-7161 (1992).

[64] S. Sugai, M. Sato, T. Kobayashi, J. Akimistsu, T. Ito, H. Takagi, S. Uchida, S. Hosoya, T. Kajitani and T. Fukuda, *Physical Review B* **42**, 1045-1047 (1990).

[65] C. Kittel, *Introduction to Solid State Physics* (Wiley, New York, 1986).

[66] R.J. Birgeneau, *private communication* (1993).

[67] G. Sawatzky, *private communication* (1993).

[68] C.X. Li, M. Pompa, S.D. Longa and A. Bianconi, *Physica C* **178**, 421-431 (1991).

[69] R.A. Cowley, W.J.L. Buyers, P. Martel and R.W.H. Stevenson, *Physical Review Letters* **23**, 86-89 (1969).

[70] C. Kittel, *Quantum Theory of Solids* (Wiley, New York, 1987).

[71] C.M. Canali, S.M. Girvin and M. Wallin, *Physical Review B* **45**, 10131-10134 (1992).

[72] B. Keimer, N. Belk, R.J. Birgeneau, A. Cassanho, C.Y. Chen, M. Greven, M.A. Kastern, A. Aharony, Y. Endoh, R.W. Erwin and G. Shirane, *Physical Review B* **46**, 14034-14053 (1992).

[73] C.M. Canali and M. Wallin, *Physical Review B* **48**, 3264-3280 (1993).

[74] N. Kojima, M. Kawarazaki, I. Mogi, M. Takeda, G. Kido and Y. Nakagawa, *Physical Review B* **47**, 15086-15090 (1993).

[75] S. Freeman and J.J. Hopfield, *Physical Review Letters* **21**, 910-913 (1968).

[76] J.F. Annett, R.M. Martin, A.K. McMahan and S. Satpathy, *Physical Review B* **40**, 2620-2623 (1989).

[77] A.K. McMahan, *private communication.* (1993).

[78] G.A. Sawatzky, *private communication* (1993).

[79] H. Eskes, L.H. Tjeng and G.A. Sawatzky, *Physical Review B* **41**, 288-299 (1990).

[80] Jackson, *Classical Electrdynamics* (Wiley, New York, 1975).

[81] R.M. Hazen in *Properties of High Temperature Superconductors*, edited by D. Ginsburg (World Scientific, Singapore, 1990).

[82] J.B. Grant and A.K. McMahan, *Physical Review B* **46**, 8440 (1992).

[83] E.B. Stechel and D.R. Jennison, *Physical Review B* **38**, 8873-8878 (1988).

[84] H. Eskes, G.A. Sawatzky and L.F. Feiner, *Physica C* **160**, 424-430 (1989).

[85] L.A. Curtiss and S.W. Tam, *Physical Review B* **41**, 1824-1828 (1990).

[86] V.I. Kudinov, A.I. Kirilyuk, N.M. Kreines, R. Laiho and E. Lahderanta, *Physics Letters* **A151**, 358- 364 (1990).

[87] V.I. Kudinov, I.L. Chaplygin, A.I. Kirilyuk, N.M. Kreines, R. Laiho and E. Lahderanta, *Physics Letters* **A157**, 290 (1991).

[88] A. Levy Ph.D. Thesis, MIT, 1992.

[89] Y.H. Kim, S.W. Cheong and Z. Fisk, *Physical Review Letters* **67**, 2227 (1991).

[90] T. Thio, R.J. Birgeneau, A. Cassanho and M.A. Kastner, *Physical Review B* **42**, 10800- (1990).

[91] D.G. Thomas, J.J. Hopfield and W.M. Augustyniak, *Physical Review* **140**, A202-A220 (1965).

[92] M.A. Kastner and D. Monroe, *Solar Energy Materials* **8**, 41-52 (1982).

[93] M.A. Kastner in *Noncyrstalline Semiconductors*, edited by M. Pollak (CRC Press, Boca Raton, FL, 1987).

[94] J. Orenstein, M.A. Kastner and V. Vaninov, *Philosophical Magazine B* **46**, 23-62 (1982).

[95] H.P. Geserich, G. Scheiber, J. Geerk, H.C. Li, G. Linker, W. Assmus and W. Weber, *Europhysics Letters* **6**, 277-282 (1988).

[96] W. Weber, *Zeitschrift fur Physik B.* **70**, 323-329 (1988).

[97] B.X. Yang, J.M. Tranquada and G. Shirane, *Physical Review B* **38**, 174-178 (1988).

[98] M. Ain, W. Reichardt, B. Hennion, G. Pepy and B.M. Wanklyn, *Physica C* **162-164**, 1279 (1989).

[99] M. Tinkham, *Group Theory and Quantum Mechanics* (McGraw-Hill, New York, 1964).

[100] C.J. Ballhausen, *Introduction To Ligand Field Theory* (McGraw-Hill, New York, 1962.)

[101] S. Sugano, Y. Tanabe and H. Kamimura, *Multiplets of Transition-Metal Ions in Crystals* (Academic Press, New York, 1970)

[102] F. Mila, *Physical Review B* **38**, 11358-11367 (1988).

[103] M. Abramowitz and I.A. Stegun, *Handbook of Mathematical Functions* (Dover, New York).